Fuels and Materials from Sunlight and Water

Thesis by

Bryan Michael Hunter

In Partial Fulfillment of the Requirements for the degree of

Doctor of Philosophy

CALIFORNIA INSTITUTE OF TECHNOLOGY

Pasadena, California

2017

(Defended May 26, 2017)

Bryan Michael Hunter

ORCID: 0000-0001-8559-9304

To the great teachers that inspired me to become a scientist.

ACKNOWLEDGEMENTS

This thesis is the product of years of support, mentorship, and friendship from so many people. Please accept my heartfelt gratitude for all you have done—this is as much yours as it is mine.

To my advisor, Harry Gray, it has been one of the greatest personal and professional honors of my life to work for you and alongside you. You have taught me that a love for science and a love for people can come from the same place and need not be orthogonal. Thank you for bringing me to Caltech, and for your boundless scientific and non-scientific support.

There is no denying that Jay Winkler is a brilliant scientist, but he has also been a deeply valuable mentor and teacher during my time as a graduate student. Jay, thank you for constantly reminding me how to think like an experimentalist. I am proud to consider myself a member of Winkler Nation.

Mike Hill, there is no way to express my profound gratitude for all you have given me. Thank you for taking a chance on a clueless high school student many years ago and for inspiring me to study inorganic chemistry. You have, single-handedly, taught me almost everything I know in the lab, all the while cheering me on. There is no doubt that I would not be where I am today without you.

I am indebted to George Rossman, whose spectroscopic expertise is scattered throughout this document. George's immense knowledge, skill in the lab, and excitement at rolling up his sleeves and experimenting were constant reminders that he is a chemist in disguise.

None of this work would have been possible without Astrid Müller, who developed pulsed laser synthesis into a technique for the synthesis of water oxidation catalysts and characterized the iron-nickel catalyst that is the focus of this thesis. Astrid worked tirelessly to move these projects forward, with an inspiring sense of integrity and attention to detail.

Jackie Barton, the chair of my committee, went above and beyond the call of duty. Her advice and support regarding my research, proposals, and career were greatly appreciated. Doug Rees graciously stepped in following the passing of Jack Richards, and has been a wonderful committee member. I remember my conversations with Jack fondly. Interacting with these incredible scientists throughout my Caltech career has been a pleasure and an honor.

I owe a great deal of thanks to the Resnick Institute at Caltech, who believed in the importance of this work way back at the beginning. The dynamic duo, Neil Fromer and Heidi Rusina, selflessly provided guidance and helped me learn how to get my research out to the masses. I am proud to have been a Graduate Fellow of the Resnick Institute.

To the many collaborators that I have worked with during my graduate school career, your expertise is astounding. Brian Wong and his team at UC Irvine gave us the unique chance to study water oxidation in living tissues. Wolfgang Hieringer and Stanislav Záliš provided elegant computational models for complex experimental observations. Niklas Thompson finally badgered me into doing Mössbauer, which now appears to be a very fruitful addition to our studies of high-valent iron. Kent Mann, a true "legend of d^8," has been an invaluable source of advice. Tony Vlček's experiments on d^8-d^8 systems have propelled us into exciting new territory. And the Britt group at UC Davis, particularly Dave Britt, Troy

Stich, Rick Sayler, and Ryan Wall, has been a joy to collaborate with on heterogeneous water oxidation catalysts. I look forward to our continued adventures!

Thank you to the scientists and professionals at Caltech who made day-to-day research so easy. Siddharth Dasgupta, thank you for your clear vision for CCI Solar, and for believing in the work we were doing. Mike Takase and Larry Henling in the X-Ray Crystallography Facility are heroes. Mike Roy and Steve Olson (machinists) and Rick Gerhart and Brian Markowicz (glass blowers) made the equipment I could only dream about.

The CCE administrators who keep the world turning while we focus on research rarely get the credit they deserve. Amy Woodall-Ojeda, Liz Callihan, Anne Penney, and Pat Anderson, thank you for your support over the years and for lending an ear. Alison Ross, the chemistry graduate students are supremely lucky to have you, and I appreciate all you have done with the CGSC. Rick Jackson, you kept the Gray Group functioning and fed; I can't think of two more important responsibilities. Agnes Tong, you recruited me to Caltech and nurtured me through my most difficult times. I am so thankful to have you as my friend.

To the many current and former Gray Group members, thank you for sharing your time, space, and ideas with me. Peter Agbo, Carl Blumenfeld, Tania Darnton, Sarah Del Ciello, Maraia Ener, Yan Choi Lam, Judy Lattimer, Michael Lichterman, Brendon McNicholas, Chris Roske, Josef Schwan, Oliver Shafaat, and Heather Williamson all overlapped with me. I also had the great pleasure of working with several remarkable postdoctoral scholars, namely James Blakemore, Brad Brennan, Emmanuelle Despagnet-Ayoub, Wes Kramer, Mike Rose, Brian Sanders, Aaron Sattler, Wes Sattler, and Keiko Yokoyama. I also want to give special thanks to Josh Buss from the Agapie Group.

I have had the pleasure of mentoring many talented high school and undergraduate students during my time at Caltech. Through the CCI Solar SEAL program, the Oakwood School brigade made inspiring progress developing a cheap, effective ozone cleaner for spotting metal oxides. Michelle DeBoever was instrumental in setting up the program at Oakwood and keeping it running. Working with the Occidental College undergraduates who do research with Mike Hill has been a great source of joy for me. Finally, my SURF students, Mette Kjeldsen, Adelfa Vera Rosado, and Doran Pennington, worked on the projects related to this thesis. Their research is ongoing, thanks in large part to their hard work and dedication.

My Teach for America and Disney friends, Emily, Allison, Sam, Noble, Andrew, Scott, Thomas, and Zach, always know how to cheer me up when "the journey becomes, uh, bumpy." Thank you for your love and support.

Finally, I want to thank my incredible family for their contributions to this thesis. Sometimes, being together—just the six of us—was the only thing that kept me going. To my parents Tom and Sue Hunter, you have always been my biggest supporters, even though my mom still wants me to go to law school. My brother, Jason, has grown to become one of my best friends. And the more recent additions of Sydney and Aziz has rounded us out to the perfect sextet.

Aziz, you have been a source of joy, comfort, and love since I started this journey. I look, excitedly, to the future.

ABSTRACT

The urgency to develop new technologies that harness energy and natural feedstocks in a sustainable fashion has never been more apparent. With global power consumption growing at an exponential rate, only one resource is truly capable of powering the planet: the sun. Sunlight is reliable, clean, and free.

Significant resources have been pledged to develop and refine solar energy devices that convert photons into electricity (i.e. photovoltaics), but the sun's intermittency and the poor overlap of solar irradiance with global power demand a different strategy. In light of these limitations, we have proposed a device which converts solar energy into reduced chemical fuels (e.g. dihydrogen or methane) that can be indefinitely stored and easily transported. In principle, the only required inputs are sunlight, an earth-abundant feedstock such as carbon dioxide, protons (H^+), and reducing equivalents (e^-). The source of these protons and electrons must be abundant and ubiquitous—we chose water.

Despite the 2-billion-year history of plants performing water oxidation to produce molecular oxygen, protons, and electrons (Photosystem II), our understanding of this complex $4H^+/4e^-$ process has been severely limited. Only recently have high-performing, earth-abundant heterogeneous electrocatalysts been reported that can be scaled up to make functioning devices.

This dissertation describes progress on both the synthetic and mechanistic fronts in developing earth-abundant heterogeneous water oxidation catalysts for solar-driven water splitting. We have synthesized nanoparticulate Ni-Fe catalysts with the highest measured activity on flat electrodes to date. We carefully characterized these materials spectroscopically to determine that edge-site iron was active in catalysis. We then undertook novel *in-situ* spectroelectrochemical techniques in non-aqueous media to identify the active iron species, which is surprisingly a *cis*-dioxo-iron(VI) corner site. The data also indicate that geminal iron-oxo coupling may be the operative mechanism of O-O bond formation, a new scheme with potential biological relevance.

Finally, we have expanded our goal to include sustainably reducing other feedstocks, such as carbon dioxide and hydrocarbons. In doing so, we aim to make pharmaceuticals, polymers, and other high-value products from sunlight and water.

PUBLISHED CONTENT AND CONTRIBUTIONS

Darnton, T. V.;* Hunter, B. M.;* Hill, M.G.; Záliš, S.; Vlček Jr, A.; Gray, H.B. Reduced and Superreduced Diplatinum Complexes. *Journal of the American Chemical Society* **2016**, *138*, 5699. DOI: 10.1021/jacs.6b02559.

B.M.H. performed the electrochemical and spectroelectrochemical characterization, participated in developing the bonding scheme, and co-wrote the manuscript.
* Contributed equally.

Hunter, B. M.; Blakemore, J. D.; Deimund, M.; Gray, H.B.; Winkler, J. R.; Müller, A. M. Highly Active Mixed-Metal Nanosheet Water Oxidation Catalysts Made by Pulsed-Laser Ablation in Liquids. *Journal of the American Chemical Society*, **2014**, *136*, 13118. DOI: 10.1021/ja506087h.

B.M.H. characterized the nanosheet catalysts by infrared (IR) spectroscopy and participated in the writing of the manuscript.

Hunter, B. M.; Gray, H. B.; Müller, A. M. Earth-Abundant Heterogeneous Water Oxidation Catalysts. *Chemical Reviews* **2016**, *116*, 14120. DOI: 10.1021/acs.chemrev.6b00398.

B.M.H. wrote the manuscript along with the other authors.

Hunter, B. M.; Hieringer, W.; Winkler, J. R.; Gray, H. B.; Müller, A. M. Effect of interlayer anions on [NiFe]-LDH nanosheet water oxidation activity. *Energy & Environmental Science*, **2016**, *9*, 1734. DOI : 10.1039/C6EE00377J.

B.M.H. participated in the conception of the project, characterized the exchanged materials by infrared (IR) spectroscopy, and wrote the manuscript along with the other authors.

Hunter, B. M.; Kallick, J.; Kissel, J.; Herzig, M.; Manuel, C; Protsenko, D.; Wong, B. J. F.; Hill, M. G. Controlled-Potential Electromechanical Reshaping of Cartilage. *Angewande Chemie*, **2016**, *128*, 5587. DOI: 10.1002/ange.201600856.

B.M.H. participated in the inception of the method, the hypothesis of cartilage reshaping by water oxidation, and the writing of the manuscript.

Hunter, B. M.; Villahermosa, R. M.; Exstrom, C. L.; Hill, M. G.; Mann, K. R.; Gray, H. B. M-M Bond-Stretching Energy Landscapes for $M_2(dimen)_4^{2+}$ (M = Rh, Ir; dimen = 1,8-Diisocyanomenthane) Complexes. *Inorganic Chemistry*, **2012**, *51*, 6898. DOI: 10.1021/ic300716q.

B.M.H. performed the calculations, analyzed the data, and wrote the manuscript.

Záliš, S; Hunter, B. M.; Gray, H. B.; Vlček Jr, A. Electronic Structures of Reduced and Superreduced $Ir_2(1,8\text{-diisocyanomenthane})_4^{n+}$ Complexes. *Inorganic Chemistry*, **2017**, *56*, 2874. DOI: 10.1021/acs.inorgchem.6b03001.

B.M.H. contributed to the design of the project, primarily in the bonding scheme of superreduced d^8-d^8 "$6p^2$" complexes.

TABLE OF CONTENTS

LIST OF FIGURES

LIST OF TABLES

1 INTRODUCTION

1.1 Purpose and Scope

The development and characterization of the nickel-iron layered double hydroxide ([NiFe]-LDH) water oxidation catalyst forms the central theme of my graduate work and this thesis. Our understanding of this system developed rather linearly, and so this document is ordered nearly chronologically. Each chapter is designed to be self-contained; as such, there is no separate methods chapter. I hope that researchers interested in solar fuel generation will find this organization helpful as they design novel experiments.

Chapter 1 provides an introduction to earth-abundant heterogeneous water oxidation catalysts, highlighting recent advances made in the field. It also gives some biologically relevant background that I believe may be important mechanistically moving forward. Because our initial goal was to develop a solar-driven device for the synthesis of fuels, the focus is on hydrogen production.

In Chapter 2, the synthesis of the [NiFe]-LDH catalyst is reported. This catalyst displays the lowest overpotential (the difference between the thermodynamic potential for water oxidation and the experimental potential required to reach a specified current density, in our case always 10 mA/cm^2) to date on a flat electrode. Specific details regarding the pulsed laser synthetic technique are given.

Our first mechanistic study is recounted in Chapter 3, where the effects of interlayer anions are explored. Here, catalyst performance was assessed for different intercalated anions, and the "nitrate effect" in the X-ray photoelectron spectroscopy was explained by computational chemistry.

The vast majority of my graduate career was spent collecting the data appearing in Chapter 4, which represents a detailed spectroscopic study of intermediates accessible under high potentials in non-aqueous media. These experiments represent a new paradigm for studying water oxidation catalysts in which the substrate (i.e. water) is withheld and reintroduced strategically to close the catalytic cycle. Here, details of an unusual *cis*-dioxo iron(VI) active species are elucidated, and a mechanism for water oxidation in base is proposed.

Chapter 5 represents a broadening of our initial goal by incorporating new substrates for the reductive half-reaction. These studies are mostly preliminary, but show that fuels are only the beginning of the important value-added products accessible by sunlight/water conversion.

Finally, in Chapter 6, I have attempted to look ahead at the future of heterogeneous water oxidation catalysts and make some predictions based on my experiences and theory. I hope these observations will be useful to researchers in the field.

I have also included Appendix A, which is thematically linked to the main text; these experiments involve water oxidation in living cartilaginous tissue. Many of the lessons learned in Chapters 1-6 are applicable.

Appendices B-D are superficially unrelated to the remainder of the thesis, but tell a cohesive story in themselves. A case study in binuclear d^8-d^8 complexes, these experiments represent the first and last that I have performed as a graduate student.

My hope is that this repository of my time at Caltech will be useful to those who wish to follow up on the work I have done, whether in the Gray Group or elsewhere. Many of these projects I expect to continue to work on, so this thesis is, in some ways, a mechanism of closure for the "early days." I look forward to continued spirited discussions about these results.

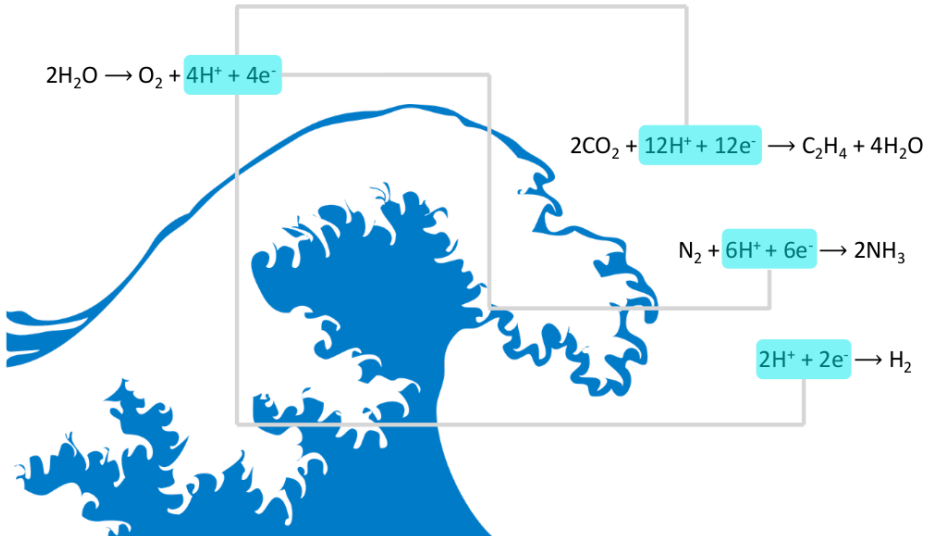

Figure 1.1. The water oxidation half-reaction provides protons (H+) and electrons (e-), which can be used to reduce a variety of abundant feedstocks to make fuels (e.g. hydrogen) and materials (e.g. ethylene and ammonia).

1.2 Why Water Oxidation?

The oxidation of water to oxygen liberates the protons and electrons required for the generation of fuels and other valuable molecules (Figure 1.1). Much progress has been made recently in designing and synthesizing scalable, heterogeneous water oxidation catalysts for solar-driven water splitting. Here, we provide an outlook on the future of such materials, with an eye toward rational design of high-performing catalysts.

The development of renewable energy systems is the greatest challenge for humanity in the 21st century.[1] All aspects of life on our planet depend on the global availability of clean and affordable energy. It is cause for concern that power consumption on earth (~13.5 TW in 2001) is expected to double by 2050 and triple by 2100.[2] We must call on the sun for survival: it is by far our largest and most reliable source of energy; it delivers an entire year's worth of energy to the earth's surface within 80 min.[3]

As fossil fuels have high energy density, we have become reliant on them for most of our needs. However, combustion of fossil fuels has detrimental effects on climate and health. In addition to global climate change attributable to rapidly increasing CO_2

concentrations in the atmosphere, excessive emissions that form smog have become a big problem in many countries. Furthermore, the dependence of industrialized nations on oil, gas, and coal and the ever-increasing demand for energy are roadblocks in efforts for world peace.[4] A paradigm shift in our current infrastructure is needed to avoid catastrophe.[5]

Fossil fuels are byproducts of eons of photosynthesis.[6] The issues we are encountering from their use arise from the large amount we combust in the relatively short timeframe of a few centuries. In light of the devastating effects and even more alarming prospects of air pollution and climate change, the need for viable energy solutions that do not interfere with our lifestyle has never been more urgent. The fight against global warming has begun, and significant amounts of funding have been pledged to combat it.[7] Yet, as developing nations become more prosperous and technology advances, worldwide demand for energy will continue to increase. This dilemma can only be solved by innovation: we will focus on earth-abundant materials tailored for carbon-neutral fuel generation, as these could lead to technologies to solve problems associated with the energy and concomitant climate crisis.

1.2.1 Potentials of Water Splitting Reactions

An attractive, carbon-neutral solution is solar-driven water splitting to produce hydrogen fuel from water[1] (Figure 1.2). All the materials needed for efficient water splitting must consist of earth-abundant elements to achieve global scalability.[8]

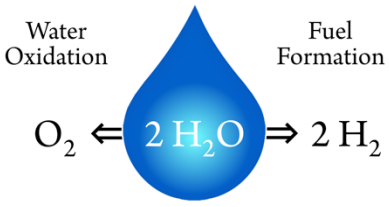

Figure 1.2. Schematic of water splitting.

The thermodynamic potential of the water splitting reaction, $2H_2O(l) \rightarrow 2H_2(g) + O_2(g)$, is $\Delta E^0 = -1.23$ V. The stepwise oxidation of water requires large overpotentials. The

overpotential of a redox reaction is the potential above the thermodynamic potential needed to overcome reaction barriers; in electrocatalysis, it is referenced to a given turnover frequency or current density. At all pH values, the standard potential for the four-electron, four-proton oxidation of water is substantially lower than that for some of the sequential one-electron steps. At pH 7, the one-electron reduction potential for the hydroxyl radical ($^{\bullet}$OH) is 2.32 V, over 1.5 V more positive than the reduction potential for the four-electron concerted reduction of dioxygen (0.815 V at pH 7).[9]

In nature, water oxidation is accomplished by photosystem II (PS II), the highly-conserved machinery for the production of plant fuel from sunlight. The water-oxidizing complex (WOC) is an inorganic calcium-manganese-oxo cluster,[10] whose structure has been studied extensively by X-ray crystallography.[11] Of critical importance is that water oxidation is carried out in a series of proton-coupled electron transfer (PCET) steps.[12] The so-called "Kok cycle" of the WOC dictates that one proton leaves the reaction center for each electron that leaves.[13] The resulting effect is a "potential leveling" scheme in which subsequent oxidation steps take place at potentials similar to the first. In the absence of PCET, charge-build up on the WOC would necessitate prohibitively high potentials for the second, third, and fourth oxidation steps.[14] A theoretical framework for PCET has been developed by Cukier[15,16] and Hammes-Schiffer.[17,18] There has been much recent work on synthetic analogues of the WOC.[19-22] In one study of note, Agapie and coworkers found that redox inactive metals modulated the reduction potentials of the Mn ions in their clusters.[23]

Depending on solution pH, water splitting proceeds by different half reactions (Figure 1.3). In aqueous acid (pH 0), the water oxidation half reaction has $E^0 = 1.23$ V, while the proton reduction half reaction has $E^0 = 0.00$ V (by modern convention, all half reaction potentials are given as the reduction potentials). At pH 14, E^0 is 0.83 V for the hydrogen evolution half reaction and 0.40 V for the water oxidation half reaction. These potentials are milder relative to the normal hydrogen electrode, which could have implications on catalyst stability and device design. It is worth noting that dioxygen reduction may compete with proton reduction under acidic conditions.

In aqueous acid:

$$2\,H_2O\,(l) \rightarrow O_2\,(g) + 4\,H^+ + 4\,e^- \qquad -E^0 = -1.23\ V$$
$$4\,H^+ + 4\,e^- \rightarrow 2\,H_2\,(g) \qquad E^0 = 0.00\ V$$
$$2\,H_2O\,(l) \rightarrow O_2\,(g) + 2\,H_2\,(g) \qquad \Delta E^0 = -1.23\ V$$

In aqueous base:

$$4\,OH^- \rightarrow O_2\,(g) + 2\,H_2O\,(l) + 4\,e^- \qquad -E^0 = -0.40\ V$$
$$4\,H_2O\,(l) + 2\,e^- \rightarrow 2\,H_2\,(g) + 4\,OH^- \qquad E^0 = -0.83\ V$$
$$2\,H_2O\,(l) \rightarrow O_2\,(g) + 2\,H_2\,(g) \qquad \Delta E^0 = -1.23\ V$$

Figure 1.3. Water splitting half reactions at low and high pH.

1.2.2 Solar Water Splitting Device Designs

Designs of solar-driven water splitting devices come in three flavors.[24] Photovoltaic–electrolyzer combinations are most mature technologically but could be surpassed by fully integrated wireless devices. Photocatalyst colloids, where the oxygen and hydrogen evolution reactions (OER and HER) occur together, have issues with the formation of explosive H_2 and O_2 mixtures. The integrated photoelectrochemical (PEC) devices, also called tandem or monolithic devices, strike a balance between the two limits. They are wireless to avoid ohmic losses, and the components for light capture and catalysis, as well as for OER and HER are separated. Decoupling the processes of light capture and catalysis offers advantages, because size matters. Optimal dimensions for light absorbers are typically on the order of a hundred nanometers. For catalysts, however, smaller is better, as chemical (redox) reactions occur on a molecular scale. Shrinking catalyst size provides more active surface sites per mass because the surface-to-volume ratio changes favorably as particles get smaller. Several investigators have discussed the advantages and disadvantages of various photoelectrochemical device designs.[25-37]

Irrespective of device design, water oxidation catalysis is crucial for harnessing solar photons. Not only water splitting but also other green chemistry transformations require the electrons and protons generated by the oxidation of our most abundant feedstock. As recent reviews summarized the design criteria and reactivities of molecular catalysts,[38-40] we focus here only on heterogeneous catalysts.

1.2.3. Materials Stability Considerations

Electrochemical equilibria of metals in aqueous solutions are well described in the Pourbaix Atlas.[41] The data compiled in this atlas show that, at high potentials, more stable earth-abundant metal oxide or hydroxide materials exist in high pH electrolyte (Figure 1.4). Anion exchange membranes (AEMs) are currently being developed to replace Nafion® as the separator between the oxygen and hydrogen evolving compartments of a tandem device.[42,43] Devices typically operate at extreme pH, *i.e.* strong aqueous base or acid.[44] It is not clear at this time if overall acidic or alkaline conditions will work better for water splitting devices, given the requirements of scalability, efficiency, and robustness.[45]

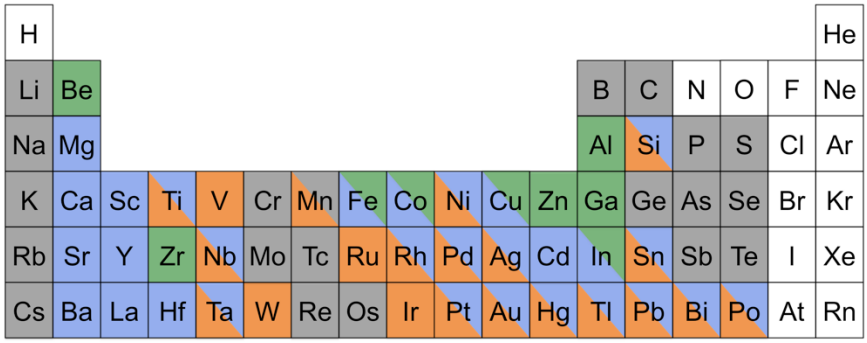

Figure 1.4. Corrosion stability of non-gaseous group 1 through 16 elements for element–water systems at 25°C under positive applied potentials, adapted from the Pourbaix Atlas.[41] Color code: stable against corrosion by innate immunity or the formation of an oxide or hydroxide layer at low (orange), around neutral (green), and high (blue) pH. Elements that corrode under applied oxidative potentials are depicted in gray. Multiple colors (blue/orange, blue/green) indicate stability over a wide pH range. The combination orange/gray is for stability at low pH but only for moderately positive potentials.

Since we know that water oxidation catalysts will be required to operate at high potentials, we have color-coded the non-gaseous group 1 through 16 elements of the periodic table that are corrosion-resistant by innate immunity or the formation of an oxide or hydroxide layer at different pH values in water (based on data from the Pourbaix Atlas;[41] Figure 1.4). Elements that are stable against corrosion under applied anodic potential and low pH are colored orange. Those that are immune to corrosion at neutral pH are depicted in green, and those that are stable at high pH are in blue. Elements that always corrode under

high anodic potentials are gray. We believe that this chart could serve as a roadmap for the development of stable water oxidation catalysts, although it should be noted that it does not take into account mixtures or alloys.

Of interest is that bismuth vanadate is stable in base, even though vanadium is orange in the table; vanadate ions by themselves are stable at high pH under anodic polarization.[41] Other binary systems show similar behavior that deviates from simple Pourbaix predictions. Although manganese is not stable in 0.1 M aqueous KOH, the $Ca_2Mn_2O_5$ oxygen-deficient perovskite is a stable water oxidation catalyst under these conditions.[46] Another strategy involves mixing base-unstable metals into nickel-containing double hydroxides. OER catalysts based on nickel double hydroxides and Cr, Mn, or Zn are stable in 0.1 M aqueous KOH even though Cr, Mn, and Zn are not independently stable in base.[47] Ternary systems also have been explored, with the perovskites $LaCrO_3$, $La_{0.7}Sr_{0.3}CrO_3$, and $La_{0.8}Sr_{0.2}CrO_3$ being stable for OER in 1 M aqueous NaOH, contrary to the prediction for Cr.[48]

Commercial water electrolyzers consist of OER and HER catalysts, and the two half reactions are separated by a membrane.[49] In high current-density systems, both catalysts are based on scarce metals, Pt for HER and IrO_2 for OER.[50] Noble metal oxides (Rh, Ir, Ru) were identified as highly active heterogeneous catalysts for water oxidation.[51] Iridium oxide (IrO_2), though not earth-abundant, was subsequently found to be one of the most active materials.[52] Further investigations demonstrated that molecular precursors can form highly active heterogeneous catalysts based on iridium oxide.[53] In related work, a quartz crystal microbalance was employed to differentiate between homogeneous and heterogeneous iridium catalysis.[54] Interestingly, Osterloh *et al.* used iridium dioxide nanocrystals as both photoanode and catalyst to split water with visible and UV light,[55] and iridium-doped metal-organic frameworks were found to be competent for water oxidation.[56] Iridium-based catalysts will not be able to provide a globally scalable solution to our energy problem because Ir is the scarcest element in earth's upper crust.[8]

1.3 Earth-Abundant Water Oxidation Catalysts

In 1972, Fujishima and Honda showed that TiO_2 was capable of splitting water as both a photoanode (light absorber providing holes, h^+) and water oxidation catalyst.[57] Although TiO_2 is not an efficient catalyst for water oxidation and its large bandgap E_g of >3.0 eV[58] limits its overlap with the solar spectrum, the use of semiconductors to absorb visible light to effect water oxidation was an important development. Even though TiO_2 has been studied intensely the past few decades, attempts to substantially enhance its light absorption properties have not met with much success.[59]

Other metal oxides, such as ZnO,[60] La:$NaTaO_3$,[61,62] WO_3,[63,64] and $SrTiO_3$,[65] have been investigated for solar-driven water splitting. All these materials have bandgaps that are too large to make good use of sunlight, thereby limiting overall solar-to-hydrogen efficiencies.[66] A few visible-light absorbers have been examined. Shifting the absorption edge of TiO_2 toward the visible region was achieved by nitrogen doping, which turned the material yellow (E_g = 2.9 eV).[67] And molecular nitrogen-intercalation decreased the bandgap of WO_3 to 1.9 eV.[68] Nevertheless, neither material met all the requirements for efficient water oxidation.[69] Shao-Horn *et al.* predicted and experimentally confirmed OER activity of a complex Ba-Co-Sr-Fe (BCSF) oxide perovskite material that compared favorably with IrO_2.[70] Electronic structure−activity relationships in similar perovskites were reported.[71] Combining a co-catalyst with active photoanode materials has become the most promising methodology, evidenced by recent work by Marschall *et al.* on layered perovskite nanofiber photoanodes with photodeposited Rh-Cr_2O_3.[72]

Bismuth vanadate ($BiVO_4$) has been identified as a promising photoanode material for solar water oxidation.[73] It has been shown to be stable against photocorrosion in aqueous electrolytes from pH 3 to 13.[74] $BiVO_4$ crystallizes in different polymorphs, with monoclinic scheelite exhibiting the highest photocatalytic water oxidation activity.[75,76] This crystalline phase of $BiVO_4$ is an *n*-type semiconductor with a direct bandgap of 2.4 eV (making it appear yellow) and a valence band edge at ~2.4 V vs. RHE (reversible hydrogen electrode) that is sufficiently positive to effect water oxidation.[58,77] Water oxidation efficiency is mainly

limited by high electron-hole recombination, inadequate water oxidation kinetics, and poor charge transport properties.[73]

Large variations of photocurrents have been reported for $BiVO_4$ photoanodes.[78-87] In recent work, we correlated morphology and chemical surface composition of this material to its photoelectrochemical performance, with the aim to differentiate contributions from different properties.[88] We devised a novel anodic electrodeposition procedure with different amounts of iodide added to the aqueous plating bath, which allowed us to prepare $BiVO_4$ films with virtually identical thicknesses but different morphologies, and we could control surface Bi content (Figure 1.5).[88]

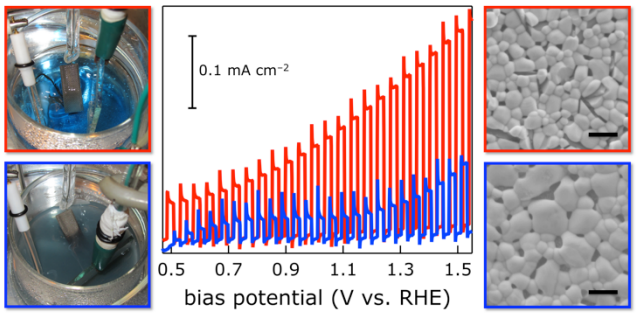

Figure 1.5. Effect of $BiVO_4$ preparation conditions on photocurrent generation (blue, without, red, with iodide in the electrodeposition bath).[88] Left: Photos of the plating baths, center: measured chopped-illumination photocurrent densities as a function of bias potential vs. the reversible hydrogen electrode (RHE), right: SEM images of the resulting $BiVO_4$ photoanodes; the scale bars are 1 μm. Experimental details are given in ref. 88.

Optimized photocurrent generation of $BiVO_4$ photoanodes resulted from intertwined material properties, whose interplay was probed by bivariate data analysis. Our data showed that a near-stoichiometric surface Bi/V ratio in combination with high-aspect-ratio crystallites, which were small enough to provide efficient charge separation yet sufficiently large to overcome mass transport limitations, led to highest photocurrent generation.[88]

1.3.1 Water Oxidation Catalysts Based on First-Row Transition Metals

Bio-inspired manganese oxides have also received considerable attention. In 1977, Morita *et al.* discovered that MnO_2 electrocatalytically evolved O_2 in alkaline aqueous electrolyte.[89] Later, Harriman *et al.* observed Mn_2O_3-catalyzed water oxidation.[51] Frei *et al.* reported water oxidation catalysis by various nanostructured Mn oxides on mesoporous silica supports, with Mn_2O_3 exhibiting highest activity.[90] Jaramillo *et al.* identified layered Na-birnessite MnO_2 as an oxygen-evolving photoanode material.[91] Dau and Kurz *et al.* prepared birnessite Mn oxides with intercalated divalent cations; they found a $Ca^{2+} > Sr^{2+} > Mg^{2+}$ order for catalytic activities.[92] Stahl *et al.* reported that activities of Mn oxides depended on the choice of oxidation method.[93] Many different Mn oxide precatalysts converted into layered structures under OER conditions, as predicted by the Mn–H_2O Pourbaix diagram.[41,94] Dau and coworkers found that cyclical electrochemical deposition of MnO_2 produced Mn^{III} sites that were active for water oxidation at pH 7.[95] Further, it was shown[96] that as-prepared α-Mn_2O_3 and Ca–Mn^{III} oxide hydrates, $CaMn_2O_4{\cdot}xH_2O$, catalyzed water oxidation in the presence of either Oxone®,[97] a two-electron oxygen-transfer oxidant (HSO_5^-), or Ce^{IV}, a one-electron oxidant. As with molecular iridium precursors, Zaharieva *et al.* found that the binuclear manganese complex $[(OH_2)(terpy)Mn(\mu\text{-}O)_2Mn(terpy)(OH_2)]^{3+}$ (terpy is 2,2';6',2''-terpyridine) was transformed into layered Mn oxide particles on clay, which served as the active water oxidation catalyst.[98] In other work of note, Jaramillo *et al.* prepared nanostructured Mn^{III} oxides that showed activity similar to noble metals for both water oxidation and oxygen reduction.[99,100]

Iron oxide water oxidation materials have been heavily studied. Iron oxides are appealing materials for globally scalable, clean energy conversion applications because of the abundance and low cost of iron. Somorjai *et al.* determined that the active optical component of an iron oxide electrode is α-Fe_2O_3.[101] Iron(III) oxide showed excellent long-term stability, but had low efficiency (0.05%) for solar conversion to H_2 and O_2.[101] The very short hole lifetime of hematite (a few picoseconds)[102] presents a major obstacle. Berlinguette *et al.* found that amorphous Fe_2O_3 showed improved water oxidation activity.[103] By doping Fe_2O_3 with silicon, Grätzel *et al.* were able to increase the conversion efficiency to a

theoretical 2.1% in a tandem device.[104] Detailed electrochemical studies on passivated iron oxide electrodes by Lyons *et al.* suggested that a physisorbed peroxide pathway is dominant and that the active site is a stabilized Fe^{VI} species.[105]

Cobalt oxide (CoO_x) is stable only at high pH under positive potentials.[41] Yet Nocera *et al.* found that a heterogeneous catalyst based on Co^{II} phosphate (CoP_i), which had been formed *in situ* during electrodeposition on indium tin oxide, was highly active for water oxidation and virtually indefinitely stable in phosphate buffer at pH 7.[106] Further work on this system demonstrated that Co^{IV} was generated at potentials at which water oxidation occurred.[107] Dau *et al.*, who found that all cobalt oxide films active for water oxidation featured edge-sharing CoO_6 octahedra, concluded that O–O bond formation occurred at the edges of the cobalt oxide clusters.[108] They noted that there is no specific "recipe" for synthesizing a catalyst that works, *e.g.* specific anions or redox-inactive cations, but that these factors play a large role in determining size and potential.

Cobalt-oxide water oxidation catalysts have received attention for more than 65 years. Initial electrochemical characterization of the behavior of cobalt metal in alkaline conditions indicated that three oxides, namely CoO, Co_2O_3, and CoO_2, were accessible under anodic bias.[109] The development of alternative structures, such as Co_3O_4, has shown increased promise (there has been success incorporating Co_3O_4 in a silica scaffold).[110] Two polymorphs of lithium cobalt oxide were synthesized by Dismukes *et al.*, and it was determined that the presence of a Co_4O_4 cubic core was indicative of water oxidation activity.[111] (We note that this cubane motif is present in PS II, albeit with manganese instead of cobalt.) Cobalt-manganese hydroxide was more active than the respective single-metal oxides.[112] Wang and coworkers were able to synthesize size-controlled Co_3O_4 nanoparticles without supporting ligands, and found that both size control and the absence of ligands that prevented species from diffusing to the surface were essential for activity.[113] In an electrochemical study, Lyons *et al.* concluded that Co^{IV} was the active species.[114]

We employed pulsed laser ablation in liquids (PLAL) as a technique for the synthesis of surfactant-free, size- and composition-controlled <5-nm cobalt oxide nanoparticles.[115] In PLAL, a high-energy laser pulse is focused on a solid target that is submerged in liquid. The pulse creates a plasma plume, which is confined at xshigh temperature and pressure by the

liquid. Extreme pressure triggers a shock wave in the confining liquid, causing the plasma to rapidly expand and cool. Nanoparticles condense out and are injected into the surrounding liquid. Our Co_3O_4 nanoparticles synthesized by PLAL had an overpotential for water oxidation of 314 mV (measured at 0.5 mA cm^{-2}), comparing favorably with the best electrodeposited cobalt oxide species; our material also featured very high mass activity of more than 10 A m^{-2} g^{-1} at 500 mV overpotential (Figure 1.6).[115]

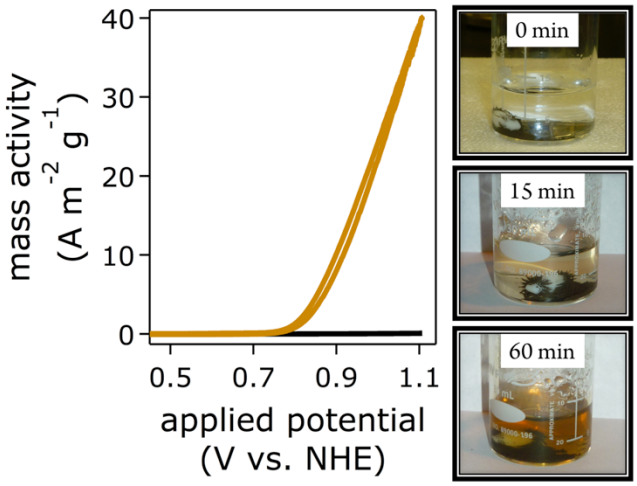

Figure 1.6. Left: Mass activity for water oxidation in 1.0 M aqueous KOH on flat graphite electrodes as a function of applied potential vs. the normal hydrogen electrode (NHE); yellow, Co_3O_4 nanoparticles synthesized by PLAL at 90 mJ $pulse^{-1}$, black, commercial 50-µm-diameter Co_3O_4 powder. Right: PLAL preparation of Co_3O_4 nanoparticles from Co powder in water at different synthesis durations.

Another first-row transition metal oxide, NiO_x, which was identified as a water oxidation catalyst by Bode in 1966,[116] was studied in depth in the 1980's.[117] Soon it was discovered that even tiny amounts of iron improved the water oxidation activity of NiO_x.[118,119] In a thorough study of iron incorporation into nickel oxide films, Boettcher *et al.* found that even accidental incorporation of iron enhanced catalytic activity.[120] Electrochemical investigations of nickel oxide electrodes by Lyons *et al.* concluded that the likeliest mechanisms involve Ni^{III} or Ni^{IV}, again in a physisorbed peroxide scheme. Lyons *et al.* did not invoke multiple oxidation states of nickel, instead using the electrode as the hole (h^+) acceptor throughout.[121] In other work, Stahl *et al.* synthesized an inverse spinel

$NiFeAlO_4$ material that had an overpotential for water oxidation of 330 mV at 0.5 mA cm^{-2} per active nickel.[122] Interestingly, the addition of a redox-inert metal enhanced the water oxidation activity of this material.

The effect of scandium on electrodeposited NiP has been explored.[123] Briefly, increasing the Sc_2O_3 composition in an amorphous NiP layer lowered the overpotential for water oxidation up to an ideal concentration of ~10%. Above ~10%, a decrease in activity was observed.

Very few vanadium-only materials have been tested for water oxidation activity. Binary and tertiary materials have been the primary focus, likely because of poor performance of vanadium oxide alone. Bismuth vanadate has been employed as a photoanode, as previously discussed; it also is catalytically active. Kudo *et al.* synthesized bismuth vanadates with varying V:Bi ratios and crystal forms that showed oxygen evolution rates from 2.5-421 μmol h^{-1} (the best performing material was in the monoclinic crystal form) under visible light irradiation.[75] The addition of copper ($BiCu_2VO_6$) reduced the bandgap, allowing greater absorption of visible light.[124] Finally, the addition of a more active metal, such as cobalt, has been shown greatly to increase the activity of vanadium-based catalysts, and binary nanoparticles, such as $Co_3V_2O_8$, have improved performance.[125]

Several chromium-based catalysts have been screened for water oxidation activity. Bockris and Otagawa measured current density in terms of real surface area for a number of perovskites at 0.3 V overpotential.[48] They found that the $La_{0.8}Sr_{0.2}CrO_3$ perovskite only passed 3.2×10^{-8} A cm^{-2}, the lowest value observed with the exception of $LaVO_3$. Solid Cr_2O_3 also has been employed as a water oxidation catalyst under supercritical conditions, with the active species believed to be chromic acid, H_2CrO_4.[126] On the other hand, small amounts of Cr_2O_3 on a $Ba_5Ta_4O_{15}$ perovskite surface produced a stable photoanode, with an oxygen evolution rate of 228 μmol h^{-1} when illuminated with a 500 W Hg immersion lamp.[127]

Copper-based water oxidation catalysts have recently attracted attention. Meyer *et al.* synthesized transparent and flexible Cu/CuO nanowire films that were active for water oxidation.[128] The CuO film prevented electrochemical corrosion of the material, although the overpotential was 580 mV at 10 mA cm^{-2}. Other groups have reported using $Cu(OH)_2$ as an inexpensive, earth-abundant material for water oxidation in base, but with similarly high

overpotentials.[129] Recently, the performance of Cu-based catalysts has been dramatically improved by *in-situ* generation of copper oxide films from a copper(II) ethylenediamine complex.[130] A current density of 10 mA cm^{-2} was obtained at an overpotential of ~475 mV in 1.0 M aqueous KOH. It also has been shown that the extent to which copper complexes perform water oxidation homogeneously *vs.* heterogeneously is pH dependent.[131] Functioning photoelectrochemical (PEC) devices have been fabricated with copper oxide/silicon photoanodes, showing good stability and electrocatalytic behavior.[132] The current work on copper-based catalysts is encouraging, but the electrocatalytic activities of these materials remain far inferior to Fe, Co, and Ni based systems.

Zinc oxide (ZnO) nanowire arrays exhibit moderate photocurrent density (0.62 mA cm^{-2} at 1.0 V *vs.* RHE under 1 sun illumination) but can be improved by the addition of Co-P_i or Ni-B co-catalysts.[133] Importantly, these materials are very stable to corrosion, showing no loss in photocurrent over prolonged testing. Choi *et al.* synthesized a spinel-type $ZnCo_2O_4$ thin film that showed a relatively low overpotential (390 mV at 10 mV cm^{-2}).[134] Although this finding underscored the advantage of incorporating more active metals, the resulting material is more active than that of Co_3O_4 electrodes prepared from the same synthesis conditions with comparable thickness and morphology. It is unclear whether zinc is playing a direct role in catalysis or simply in tuning the redox potential of the cobalt material. Similarly, it has been shown that the overpotential of ZnO can be lowered by doping with Mn, Fe, Co, and Ni.[135] The largest effect (by almost 150 mV) was seen with cobalt doping.

In other work of note, polyoxometallates based on first-row transition metals have been shown to act as heterogeneous water oxidation catalysts.[136,137] Polyoxometallates (POMs) are polyoxoanions that can contain between 5-50 transition metal centers. Because of their unusual oxidative stability, high-valent states of the metal atoms are accessible (e.g. Ni^{IV} and Cr^{V}).[138,139] Although most clusters are generally believed to be active in homogeneous solutions, Co_4POM has been shown to be a precursor to an active heterogeneous CoO_x catalyst. Other researchers have utilized POM frameworks to synthesize mesoporous structures of first-row transition metal oxides, such as Co_3O_4.[140] These types of hybrid materials are promising water oxidation catalysts.[141]

Among first-row transition metals, cobalt, iron, and nickel oxides and hydroxides are most active for water oxidation, at least in alkaline electrolytes. Because higher electrocatalytic activities have been observed in layered double hydroxides, we turn our attention to this class of materials.

1.3.2 Layered Double Hydroxides

Much recent research has focused on layered double hydroxides (LDHs), mineral-like compounds that contain a sheet of $M_1^{2+}(OH)_6$ shared-edge octahedra with M_2^{3+} atoms occupying some of the M_1 sites.[142,143] Intercalated anions balance the additional positive charge of M_2^{3+}, while layers between sheets carry water. Dai *et al.* demonstrated that a composite of α-$Ni(OH)_2$ on carbon nanotubes was efficient for water oxidation.[144] Nickel-titanium LDHs were shown by O'Hare *et al.* to be very active photocatalysts.[145]

Based on previous work on iron-doped nickel oxides, [NiFe]-LDH materials have become a target for many groups. Boettcher *et al.* suggested that layered structures are particularly useful for highly efficient water oxidation catalysis.[146] Exfoliation of [NiFe]-LDHs into individual layers led to increased water oxidation activity.[147] Other iron-containing LDHs, [MFe]-LDH nanoplatelet arrays where M is Ni, Co, or Li, have been prepared by short-time electrodeposition on foam nickel substrates; all OER overpotentials were assessed on rough supporting electrodes of unknown microscopic area.[148]

We used PLAL to synthesize [NiFe]-LDH nanosheet water oxidation catalysts.[149] The x-ray diffraction (XRD) patterns of our materials were characteristic of layered double hydroxides, since the intensities of the basal (00*l*) reflections decreased as *l* increased.[150] The observed reflections were indexed in a three-layer **3R** polytype with rhombohedral symmetry, such as in synthetic hydrotalcite (Figure 1.7).[151] The XRD data of LDH materials provide rich information on the basal spacing, the interlamellar electron density stemming from interlayer water and anions, and the nanosheet size, *i.e.* lateral diameter and stack thickness.[150]

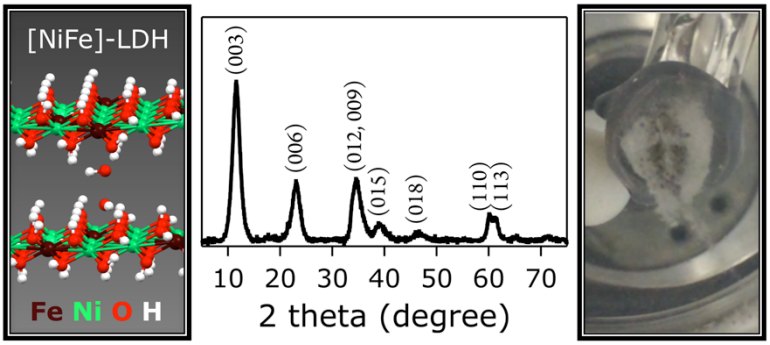

Figure 1.7. Left: Schematic illustration[152] of the structure of [NiFe]-LDH nanosheet water oxidation catalysts.[149] Center: Indexed XRD data that evidence the layered double hydroxide structure of our materials. Right: Photo of [NiFe]-LDH nanosheets during water oxidation catalysis under anodic bias in aqueous alkaline electrolyte.

The [NiFe]-LDH nanosheet water oxidation catalysts synthesized by PLAL showed outstanding performance on flat graphite electrodes; the best catalyst had 260 mV overpotential at 10 mA cm^{-2}.[149] Overpotentials of earth-abundant catalysts at 10 mA cm^{-2} typically range from 350 to 430 mV in pH 14 aqueous electrolytes[153] (Figure 1.8). We note that McCrory tested the activities of our PLAL-made Co_3O_4 water oxidation catalysts and confirmed the overpotentials we had reported.[115] His findings suggest that our overpotential assessment method was equivalent to the benchmarking technique reported by McCrory, Peters, Jaramillo, *et al.*,[153] indicating that electrocatalytic activities of different materials are directly comparable between the two laboratories.

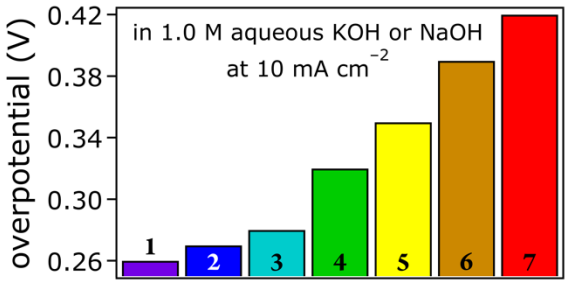

Figure 1.8. Comparison of overpotentials of our (1 to 3)[149] and other (4 to 7)[153] reported water oxidation electrocatalysts operating in 1.0 M aqueous base. The materials are Ti and La doped [NiFe]-LDH nanosheets (1), Ti doped [NiFe]-LDH nanosheets (2), [NiFe]-LDH nanosheets with 22% Fe (3), IrO_x (4), $NiFeO_x$ (5), CoO_x (6), and NiO_x (7).

Other nickel-based materials have been reported with overpotentials at current densities other than 10 mA cm^{-2}, rendering a direct comparison problematic. Adventitious nickel at concentrations as low as 17 nM was shown to catalyze water oxidation in aqueous electrolytes, with stable (tens of hours) current densities of 1 mA cm^{-2} at overpotentials as low as 540 mV at pH 9.2 and 400 mV at pH 13.[154] Thin film nickel oxide with iron impurities reached 8 mA cm^{-2} at 230 mV,[119] while β-NiOOH exhibited an overpotential of 500 mV at a current density of 5 mA cm^{-2}.[155] Nickel-borates on glassy carbon and mixed Fe-Ni oxides on carbon paper reached 1 mA cm^{-2} at overpotentials of 425 and 375 mV, respectively.[156,157] Amorphous α-$Fe_{20}Ni_{80}O_x$ on FTO glass had an overpotential of 210 mV at 0.5 mA cm^{-2}.[158] The same current density was reached at 265 mV overpotential by high surface-area nickel metal oxides,[159] and NiO_x deposited from molecular $[Ni(en)_3]^{2+}$ on glassy carbon featured an overpotential of 390 mV at 0.1 mA cm^{-2}.[160]

Other iron- and nickel-based catalysts showed higher overpotentials for water oxidation, or they were measured on high-surface-area electrodes, which leads to an enlargement of the electrode substrate surface area relative to the apparent geometric area, thereby inflating overpotential numbers. Thin-film solution-cast $Ni_{0.9}Fe_{0.1}O_x$ reached 10 mA cm^{-2} at 336 mV overpotential,[146] while electrodeposited $NiFeO_x$ reached the same current density at 360 mV.[153] A similar result was obtained with nanostructured α-$Ni(OH)_2$ (331 mV at 10 mA cm^{-2}).[161] With an iron content of 40%, thin-film electrodeposited Ni-Fe on gold yielded an overpotential of 280 mV.[162] A graphene FeNi double hydroxide material was reported on a nickel foam electrode with unspecified pore size and thus real electrode area.[163] Very recently, homogeneously dispersed Fe–Co–W oxyhydroxide gels were reported to have overpotentials of ≥315 mV on flat Au electrodes.[164]

1.3.3 Looking Forward

The overpotentials for water oxidation for many catalysts are within the range needed to construct viable devices, but there is still a need to optimize the photoanode/catalyst junction. Light capture in the presence of a catalyst remains a concern, since parasitic light absorption, reflection, and scattering by catalyst particles or layers reduce the efficiency of a device. In

addition, optical properties related to the size of the catalyst material become important, especially once devices become highly functional. Employing optimally sized catalyst particles may mitigate light reflection and scattering. These constraints dictate that catalyst mass activity must be high, since using less catalyst overall will improve device performance. Smaller catalysts such as nanoparticles, however, have a tendency to aggregate; methods must be developed for robust attachment under the demanding conditions of water oxidation. Clearly, it is difficult to pinpoint a common characteristic that makes earth-abundant water oxidation catalysts particularly active or inactive. We can say, however, that particle size and method of preparation are both centrally important. Ion and electron conductivity,[165] as well as carrier mobilities through the materials also matter.

1.4. Mechanistic Considerations

A major challenge is obtaining a clearer mechanistic picture of water oxidation. Elucidation of atomistic details during turnover is no easy feat, since most highly active earth-abundant heterogeneous catalysts are multi-metal materials. What is the site of catalysis? Are all metals catalytically active, or are some species simply necessary to tune the electronics of the system? What is the local structure? Are catalytic sites comprised of one or more metal centers? And are oxidized active sites electronically localized or delocalized? These questions are difficult to answer, particularly because catalytically active transient species are short-lived by definition. Experiments that detect such transient intermediates spectroscopically while the material is under positive potentials and immersed in electrolyte are badly needed.

1.4.1. Lessons from Nature

The vast body of research on photosynthetic oxygen evolution highlights the enormous scientific challenges associated with gaining mechanistic information of complex, heterogeneous systems during catalytic turnover. Nature's way of evolving oxygen in PS II

may serve as a mechanistic model for manmade heterogeneous water oxidation. But the mechanism of PS II catalysis is still hotly debated.

The first mechanistic proposal was set forth by Blackman and Matthaei in 1905, when they suggested that photosynthesis is a two-step process: a photochemical (light) reaction and a light-independent (dark) reaction that required elevated temperature and was thus indicative of an enzymatic reaction.[166] In the 1920's, Warburg observed that the rate of photosynthesis was inhibited by high oxygen concentrations and postulated that oxygen was produced from CO_2 during photosynthesis; this is known as the Warburg hypothesis.[167-169] Many scientists agreed with Warburg that the primary reaction in photosynthesis was the splitting of CO_2 by light into oxygen and carbon, which would subsequently be reduced to carbohydrates by water. Van Niel presented a fundamentally different view in the 1930's from his work on anaerobic sulfur bacteria. He demonstrated that photosynthesis is a light-driven redox reaction following the general equation of $CO_2 + 2H_2A + \text{photons} \rightarrow [CH_2O] + 2A + H_2O$, where $[CH_2O]$ is a carbohydrate and A an electron acceptor. Van Niel's discovery predicted that water is split into hydrogen and oxygen.[170] In 1937, Hill investigated the light-driven transfer of electrons from water to non-physiological oxidants in isolated chloroplasts and found that oxygen was generated in the absence of carbon dioxide.[171-173]

A major breakthrough came in 1941 at the dawn of radioisotope tracer studies, when ^{18}O labeling experiments by Ruben and coworkers established that oxygen in photosynthesis came from water rather than from carbon dioxide.[174] In addition to this landmark publication, Ruben and Kamen discovered the long-lived radioactive carbon isotope ^{14}C in 1940,[175] which paved the way for the elucidation of carbon pathways in photosynthetic metabolism by Calvin, for which he received the Nobel Prize in Chemistry in 1961. Isotope labeling studies remain some of the most powerful ways to elucidate the mechanisms of homogeneous and heterogeneous water oxidation catalysts. They allow for spectroscopic determination of intermediates and tracking of products from substrates.

By the mid 20th century, PS II was still a black box regarding its structure and molecular mechanism. Groundbreaking work by Joliot *et al.* in the 1960's established that the yield of oxygen evolution in the water splitting enzyme system follows a period-four oscillation upon irradiation with saturating light flashes.[176-178] In 1970, Kok developed a

kinetics scheme, known as the Kok or S-state cycle for PS II oxygen evolution (Figure 1.9).[13] Further insights into the mechanism of water oxidation on a molecular scale were enabled by the advent of gene sequencing and the discovery of the BBY preparation of a smaller, isolated PS II complex, which retained full activity for oxygen evolution.[179].

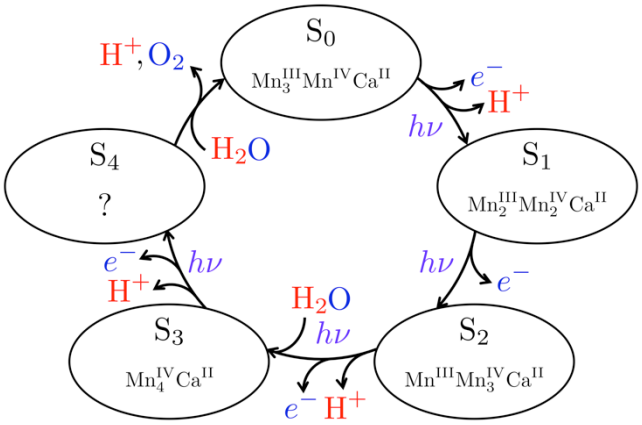

Figure 1.9. Schematic S-state cycle of the PS II WOC, including the likely oxidation states of metal ions.[13,180,181] The catalytic cycle consists of the states S_0 through S_4, where the subscript denotes the number of oxidizing equivalents abstracted from the WOC.[13] Photons ($h\nu$), electron (e^-) and proton releases, and substrate turnovers are also shown.

Great progress has been made in understanding the biochemistry of PS II, since Deisenhofer, Huber and Michel (Nobel Prize in Chemistry in 1988) determined the three-dimensional structure of a photosynthetic reaction center. Their work established the architecture of trans-membrane proteins, quinones and cytochromes. This structural information can be used analogously as the scaffold around the WOC in PS II. Work by Marcus on the theory of electron transfer reactions in chemical systems (Nobel Prize in Chemistry in 1992) inspired work by Debus, Barry, Babcock, and McIntosh in 1988, which provided the first molecular biological evidence that tyrosine radicals are involved in long-range electron transfer through P_{680}.[182,183] Importantly, the tyrosine electron carriers mediate the sequential electron transfers through the PS II protein machinery to cycle the WOC through its intermediates at moderate potentials (see section 1.2).[13,184,185]

The development of advanced electron paramagnetic resonance (EPR) and x-ray spectroscopy and diffraction techniques enabled the determination of increasingly refined

structures of the $CaMn_4O_5$ WOC.[186-189] Britt *et al.* were the first to demonstrate a $CaMn_3O_4$ cubane structure with a Mn dangler from EPR data.[190,191] Barber *et al.* obtained a 3.5 Å-resolution x-ray diffraction structure of the WOC in 2004, which confirmed Britt's cubane/Mn dangler motif, but the reported interatomic distances indicated partial reduction of the $CaMn_4O_5$ cluster by the x-ray beam.[192,193] Two years later, Messinger, Zouni, Yachandra, and co-workers examined the structure of the manganese-calcium water-splitting complex of PS II, using x-ray pulses from a femtosecond free-electron laser source; the short timescale of the x-ray pulses minimized radiation damage because diffraction data were collected before beam-induced reduction of the WOC could occur.[194] Finally, in 2011, Shen, Kamiya *et al.* reported a crystal structure of the WOC with 1.9 Å resolution and located all of the metal atoms of the Mn_4CaO_5 cluster together with all of their ligands, again verifying the Barber $CaMn_3O_4$ cube structure with a manganese dangler that is connected to the cube via an O bridge.[11]

Knowledge of the WOC structure enabled more detailed mechanistic insights into oxygen formation from water. The WOC catalyzes water oxidation to O_2 with a maximal turnover frequency of ~500 s^{-1} and a high turnover number of 10^6,[195] indicating that nature solved the difficult problems of four-electron oxidation to form molecular oxygen and simultaneous avoidance of excessive oxidative damage to the enzyme. Several key questions remained unanswered: How does the substrate for oxygen evolution bind, how does it turn over, what are the molecular intermediates? And what are the oxidation states of the individual manganese centers associated with each S state? Dismukes *et al.* established the manganese oxidation states of the S_2 state.[196] Cox, Lubitz *et al.* characterized the S_3 state (the intermediate directly prior to O–O bond formation) and reported that all manganese centers are in the IV oxidation state.[181] Three competing models predict how molecular oxygen is formed and through which pathway the S_3 state spontaneously decays to the S_0 resting state, closing the catalytic cycle.[197] Babcock proposed a metalloradical hydrogen abstraction mechanism, where S_0 is directly formed from S_3 with concomitant O_2 release.[198] Yet structural data from high-resolution x-ray experiments are not in accord with a direct O_2 generation mechanism.[11] Brudvig suggested that a single Mn^V oxo species could form an O–O bond with a Ca^{2+}-bound hydroxide or water in the S_4 transient.[199,200] But Siegbahn obtained

DFT results that favored radical O–O coupling in S_4 involving a Mn^{IV}-oxyl.[201,202] Recent work revealed that NH_3 binds at the dangler Mn site, but not in a bridging position; this finding supports both high-valent Mn–O models.[203] Molecular oxygen is released about 1 ms after the fourth photon is absorbed,[195,204] rendering structural determination of the S_4 species particularly difficult.

The lessons learned in photosynthetic WOC research should be of help in investigations of earth-abundant heterogeneous catalysts.[205] The higher stability of metal (hydr)oxide materials compared to PS II facilitates mechanistic work. Also helpful is the availability of analytical and spectroscopic methods that have been developed in the course of PS II work. Yet, even in robust materials, highly active species are short-lived and the identification of catalytic pathways remains challenging.

1.4.2. Heterogeneous Water Oxidation Catalysts

In heterogeneous catalysts, only small numbers of metal centers are active.[206] Inactive sites are likely needed to keep the material intact by providing an environment around an active site that supports high oxidation states required for water oxidation, by acting as hole reservoirs, by assisting in deprotonations, or by tuning redox potentials. Ligands assume this role in molecular catalysts, polypeptide chains in biocatalysts. In the case of water oxidation, there is intense debate if catalysis proceeds in homo- or heterogeneous fashion.[207] Robust, highly active, inorganic materials have largely regular, periodic structures, and only a few special sites are catalytically active, rendering their identification during turnover particularly challenging.

Great strides have been made with single-metal electrocatalysts, both computationally and experimentally. Rossmeisl *et al.* used density functional theory (DFT) calculations to shed light on water oxidation reactions on metal oxide surfaces that involve surface-adsorbed OOH intermediates.[208-210] Nørskov *et al.* described how computational methods provide mechanistic understanding essential for the design of new catalysts, with much emphasis on thermochemical volcano plots.[211-214] Fortunelli, Goddard, *et al.* examined OER rate-limiting steps and barriers associated with fundamental reaction steps on Pt(111)

surfaces *in silico*. They assumed a reaction pathway in which surface-adsorbed species underwent the following reactions: water dissociation, OH disproportionation, OOH formation, OOH dissociation that resulted in O_2 formation, and finally H dissolution to form an electron and solvated proton.[215] In other reports of note, Llobet *et al.* reviewed O–O bond formation pathways promoted by Ru complexes,[216] such as the "blue dimer", whose water oxidation mechanism has been studied in great detail,[217-221] and Nocera *et al.* discussed electronic design criteria for O–O bond formation *via* metal oxos.[222]

Manganese oxides support multiple metal oxidation states,[223] facilitating four-electron water oxidation. Manganese oxides occur in many different compositions and crystal phases, which affect OER activity.[224,225] Kinetics measurements on MnO_2 catalysts suggested that surface Mn^{III} sites were active.[226] The mechanism involved fast Mn oxidation coupled to deprotonation, followed by a slower chemical step.[95] The basicity of surface oxido-bridges may assist in proton abstraction from substrate water.[92] Najafpour *et al.* detected Mn^{II} and permanganate upon MnO_2 catalyzed water oxidation in the presence of Ce^{IV} ammonium nitrate.[227] Under-coordinated $Mn^{III}O_5$ units at amorphous boundaries were essential for high activity.[228] Nocera *et al.* obtained enhanced activity upon a phase-change of the birnessite MnO_2 precatalyst.[229] They also discovered that different mechanisms were operative, depending on pH: a one-electron one-proton PCET pathway dominated in alkaline conditions, whereas Mn^{III} disproportionation occurred in acid.[230]

Work by Zaharieva and Dau *et al.* has shown that disordering of initially more crystalline birnessite structures led to better catalytic performance. Similarly, amorphous cobalt, iron, and nickel oxides exhibited higher activities than crystalline bulk counterparts.[103,158,231] Amorphization may not be necessary in small, nanoparticulate materials, where lattice strains from rearrangements during turnover may be dissipated due to favorably large surface-to-volume ratios.

Mechanisms of cobalt oxide catalyzed water oxidation have also been studied. A possible mechanism based on reports outlined below is shown in Figure 1.10. Currently, there is broad consensus that two cofacial surface Co(O)OH moieties undergo two initial oxidations and deprotonations to generate terminal Co^{IV} oxos. Substrate water turnover likely produces a surface-bound peroxo species, which converts to a superoxo intermediate that

may be bridging. Addition of a second water molecule, together with loss of the fourth proton and electron, leads to O_2 release.

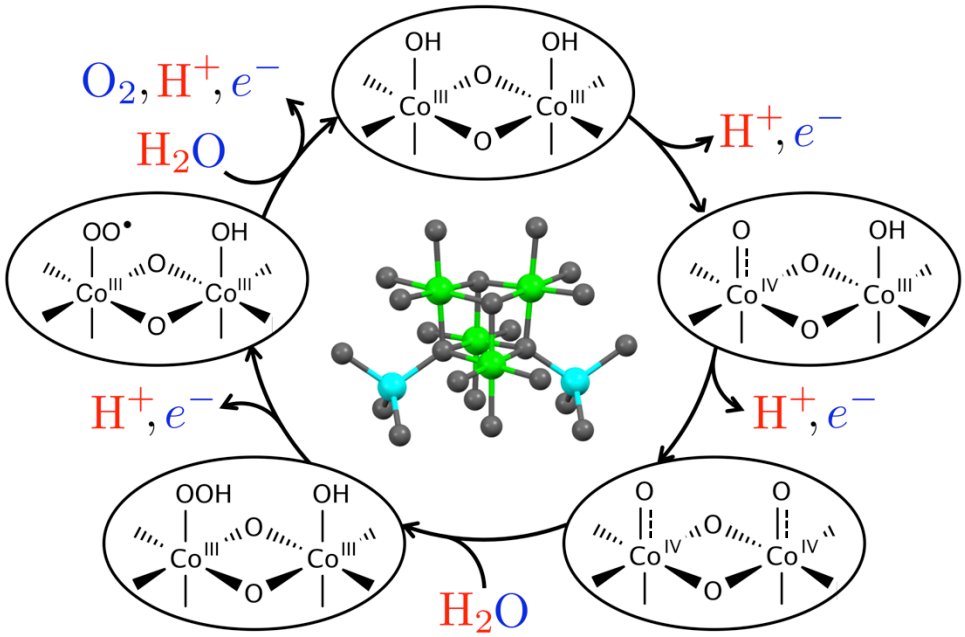

Figure 1.10. Possible mechanism of cobalt oxide catalyzed water oxidation. The Co_3O_4 structure[232] is depicted in the center; colors: Co^{II} (cyan), Co^{III} (green), O (gray).

Using DFT calculations, Van Voorhis *et al.* predicted energetics and barriers for water oxidation in a Co_4O_4 cubane cluster.[233] They suggested a mechanism in which the resting state, a (surface) μ-oxo-bridged Co^{III} hydroxide dimer, underwent metal oxidations. Radical coupling of two cofacial Co^{IV} oxo groups formed an O–O single bond. Two substrate turnover steps followed by proton transfer closed the catalytic cycle. In contrast, computations by Berlinguette and Baik *et al.* favored a mononuclear biradicaloid mechanism.[234] Siegbahn *et al.*, who performed calculations on several Co oxide model clusters, pointed out that cobalt (in contrast to manganese in PS II) prefers low-spin coupling in the relevant high oxidation states, forcing a change of electronic structure during O–O bond formation. They postulated that a Co^{IV}-oxyl radical would be needed for reactivity,[235] similar to their proposed mechanism for PS II.[201,202] Dismukes *et al.* showed that one of the studied clusters, the "Dismukes Co_4O_4 cubane", did not react with water; instead, two

hydroxide ions led to O_2 formation by an inner-sphere mechanism.[236] Water oxidation may be catalyzed by Co^{II} impurities in $Co^{III}{}_4O_4$ cubanes.[237] In other work of note, Tilley *et al.* found spectroscopic evidence for a highly oxidized terminal oxo intermediate in a Co_4O_4 cubane model compound; turnover required hydroxide.[238]

Nocera, Britt *et al.* detected Co^{IV} species by *in-situ* EPR and x-ray techniques in water oxidation catalysts generated *via* electrodeposition from aqueous solutions containing phosphate and Co^{II} (CoP_i).[107,239] Phosphorus NMR data supported the idea that electrocatalytically active CoP_i resembled an LDH with phosphate ions located in the interlamellar galleries.[240] Frei *et al.* identified oxidized Co species in Co_3O_4 nanocatalysts during turnover by *in-situ* infrared spectroscopy.[241] In other work, time-dependent redox titration experiments on CoP_i by Bard *et al.* indicated that both Co^{III} and Co^{IV} oxidized water, with pseudo-first-order rate constants of 0.19 and >2 s^{-1}, respectively.[242]

Obtaining structural and mechanistic details of heterogeneous catalysts during turnover is more straightforward with monometallic materials. But activities of multi-metallic, earth-abundant catalysts are much higher, presumably because redox potentials and catalytic pathways are fine-tuned by involving multiple metal species. For example, at a water oxidation overpotential of 280 mV, PLAL-made Co_3O_4 nanoparticles exhibited a current density of only 0.1 mA cm^{-2}, whereas [NiFe]-LDH nanosheets reached 10 mA cm^{-2}; both materials, which we investigated under virtually the same conditions in strong aqueous base on flat graphite supporting electrodes, had 100% faradaic efficiency.[115,149]

Some progress has been made in studies of even more complex materials. Bockris *et al.* investigated the mechanism of oxygen evolution on perovskites and found that OH desorption was the rate-limiting step.[243] Shao-Horn *et al.* observed amorphization of select, highly active perovskite OER catalysts.[244,245] Surface reorganization, electronic structure, and participation of lattice oxygen in the mechanism were assessed to rationalize trends in OER activities of cobaltite perovskites.[246,247]

Layered materials, especially [NiFe]-LDHs with approximately 20 to 40% Fe, have recently attracted much attention (see also previous section). They consist of slabs of $Ni^{II}(OH)_6$ edge-shared octahedra with Fe^{III} centers substituting at Ni sites. Anions in the interlamellar space between the stacked slabs balance additional positive charges that arise

from Fe^{III} occupying Ni^{II} sites; water is also intercalated.[142] Hence, Ni^{II} and Fe^{III} constitute the resting state of this catalyst. Corrigan and Boettcher *et al.* noted that Fe is required for high water oxidation activity,[118-120] suggesting that iron must be a component of the active site. Based on mechanisms occurring in nature and monometallic heterogeneous catalysts, oxidation states higher than in the resting state must be generated during turnover.

Yet Friebel and Bell *et al.* identified mononuclear Fe^{III} as the active site by DFT calculations and *operando* x-ray absorption spectroscopy (XAS) experiments on electrodeposited [$Ni^{II}Fe^{III}$]-LDH catalysts in strong aqueous base. They observed edge shapes that were unusual for octahedrally coordinated Fe^{III} and a shortening of the Fe–O distance but excluded Fe^{IV} based on their data. Instead they invoked inductive ligand effects, where oxidized Ni ions withdrew charge from O ligands shared with Fe centers, thus disfavoring Fe^{III} oxidation; a small amount of tetrahedrally coordinated Fe^{III} may also have been present.[248] Higher-valent Fe species were likely too short-lived under turnover conditions in this highly active catalyst to be detected by XAS, where the signal was overwhelmingly that of inactive Fe^{III}.

Stahl *et al.* used *operando* Mössbauer spectroscopy during water oxidation catalysis in alkaline aqueous electrolyte and identified Fe^{III} and Fe^{IV} in isotopically enriched [NiFe]-LDH materials, which were synthesized hydrothermally. Data acquisition times ranged from 18 to 24 hours. The Fe^{IV} species appeared when applied anodic potentials were high enough for water oxidation, and Fe^{IV} remained for many hours even after the applied potential was lowered below the onset of catalysis. Therefore, the detected Fe^{IV} was not deemed kinetically competent to serve as the site of water oxidation;[249] in other words, Fe^{IV} was not on path of the [NiFe]-LDH catalytic cycle.

Bard *et al.* observed "fast" and "slow" kinetics in electrodeposited [NiFe]-LDH films by surface interrogation scanning electrochemical microscopy (SI-SECM).[250] This technique allows for spatially resolved quantitative detection of redox-active surface species, without spectroscopic identification of individual intermediates. Time-dependent redox titrations revealed associated kinetics; notably, unusually high densities of catalytically participating metal sites (~300 atoms nm^{-2}) were observed, indicating fast hole conduction through

[NiFe]-LDH. For comparison, similar SI-SECM studies on Co_3O_4 and IrO_2 yielded densities of 11 and 25 nm^{-2}, respectively.[242,251]

We recently investigated the effect of interlayer anions on water oxidation activity of PLAL-made [NiFe]-LDH nanosheets in strong aqueous base (Figure 1.11). We found that carbonate replaced other interlayer anions in alkaline aqueous electrolyte in ambient air. Carbonate is of course ubiquitous and self-buffered in strong aqueous base in ambient air, as it is favored by dissolution speciation of CO_2 at high pH.[252] We discovered that carbonate-containing [NiFe]-LDH nanosheets were much more active and stable than corresponding nitrate-catalysts, which we assessed in carbonate-free electrolyte in an inert atmosphere.[253] Hence, all water oxidation electrocatalysis in high pH aqueous electrolyte in ambient air occurs in the presence of carbonate, which facilitates catalytic turnover.

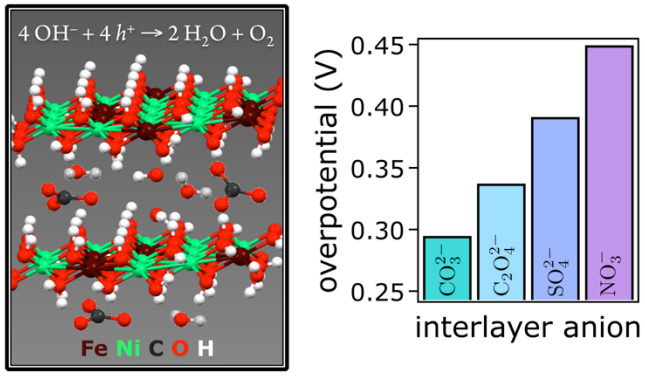

Figure 1.11. Schematic of a $[Ni^{II}Fe^{III}]$-LDH structure in strong aqueous base (left). Overpotentials of [NiFe]-LDH catalysts with the formula $[Ni_{0.78}Fe_{0.22}(OH)_2](A^{m-})_{(0.22-n)/m}(OH^-)_n \bullet xH_2O$ and different interlayer anions A^{m-} at 1.0 mA cm^{-2} (adapted from ref. 253; right).

We observed a sigmoidal dependence of OER activity on anion basicity. In plots of overpotentials, which we determined in carbonate-free electrolyte, as a function of the pK_a values of the conjugate acids of the interlayer anions, we found an apparent pK_a of (3.4±0.7) during turnover. Mechanistically, our results imply that interlayer anions act as Brønsted bases that assist deprotonation or Lewis bases, which lower oxidation potentials at the active site. The apparent pK_a of 3.4 suggests that a higher-valent metal oxo species is a catalytically active intermediate.[253]

We also have probed the likely sites of water oxidation (*i.e.* at edges or within the [NiFe]-LDH nanosheets). XPS data in combination with DFT calculations suggested that a previously unassigned N 1s species in the precatalyst, which correlated with higher water oxidation activity,[149] was nitrite bound through its N-atom to *edge-site iron*.[253] Further support for water oxidation occurring at edge sites came from our observation that catalytic activity did not correlate with basal spacings of various [NiFe]-LDH nanosheet materials, which we had prepared with different interlayer anions; slab-to-slab distances would only matter if reactants and products had to diffuse through the interlamellar galleries. Our findings indicate that edge-site Fe plays a major role in water oxidation catalysis in [NiFe]-LDH nanosheets.[253]

Why does iron improve the water oxidation activity of many mixed-metal oxide/hydroxide catalysts? Could it be related to the ease of generation of high-valent oxos on the left side of the oxo wall?[254] Is it really that simple? Surely manganese should be well suited for water oxidation if a high-valent metal-oxo center were the only criterion. But we know that inorganic and biological manganese oxo clusters differ greatly in water oxidation activity. Why is the manganese-calcium cluster in PS II so much better than purely inorganic Mn compounds? We think it likely that noncovalent peptide-cluster interactions elevate the reduction potentials of the various Ca-Mn-oxo redox states, making water oxidation energetically feasible. Of course, multiple oxidizing equivalents (holes) must be coupled to the active center (or centers) to support the removal of electrons from initially generated "oxidized-oxo" (peroxo?) intermediates to promote the reductive elimination of oxygen. In PS II, the required holes can be stored within the cluster complex itself; in a heterogeneous Fe-Ni catalyst, we suggest that hole transfer from electro- (or photo-) generated oxidized nickel centers to nearby iron active sites would produce Fe-oxos capable of oxidizing water.

In summary, water oxidation is essential for the storage of solar energy in chemical fuels. Catalysts for this critical four-electron-four-proton reaction must be highly active, robust, and based on non-precious elements to enable global scalability. Mechanistic work suggests that high-valent metal-oxo centers that are accessible at moderate anodic potentials promote electrocatalytic activity. Importantly, the availability of holes in the vicinity surface-accessible sites also enhances the performance of catalytic materials.

1.5. Parting Shots

In this chapter, we have covered recent advances in the design, synthesis, and performance of heterogeneous catalysts that potentially could be functional components of globally scalable devices for the production of solar fuels. We discussed the catalytic properties of mixed-metal materials, with emphasis on robust Ni-Fe layered double hydroxide nanosheet catalysts that exhibit exceptional activities; and we pointed out that strategic incorporation of anions into these layered catalysts improved both stability and activity. We emphasized the challenges associated with the design of acid-stable earth-abundant catalysts, and offered proposals for elements that could be incorporated in functional systems.

We highlighted how lessons from nature in combination with identification of catalytic intermediates in manmade materials aid the development of superior catalysts. We believe that further advances in this field will depend to a large measure on the success of mechanistic work, unraveling the details of the complicated proton-coupled electron transfer processes needed for efficient water oxidation.

Moving forward, we must develop innovative ways to meet our energy demand in a scalable, environmentally benign fashion. In one relevant area, we are encouraged that great strides have been made in developing potentially scalable heterogeneous water oxidation catalysts for the harnessing of solar photons to synthesize chemical fuels.

1.6. Abbreviations

AEM, alkaline exchange membrane; A^{m-}, anion; DFT, density functional theory; E^0, thermodynamic potential; E_g, bandgap; e^-, electron; en, ethylenediamine; EPR, electron paramagnetic resonance; *g*, gaseous; HER, hydrogen evolution reaction; *hv*, photon; h^+, hole; *l*, liquid, Miller index; LDH, layered double hydroxide; NHE, normal hydrogen electrode; OER, oxygen evolution reaction; PCET, proton-coupled electron transfer; PEC, photoelectrochemical; P_i, phosphate; PLAL, pulsed-laser ablation in liquids; PS II, photosystem II; RHE, reversible hydrogen electrode; SI-SECM, surface interrogation scanning electrochemical microscopy; WOC, water-oxidizing complex; XAS, x-ray absorption spectroscopy; XPS, x-ray photoelectron spectroscopy; XRD, x-ray diffraction.

1.7. References and Notes

(1) Gray, H. B. Powering the Planet with Solar Fuel. *Nature Chem.* **2009,** *1* (1), 7.

(2) Lewis, N. S.; Nocera, D. G. Powering the Planet: Chemical Challenges in Solar Energy Utilization. *Proc. Natl. Acad. Sci. U. S. A.* **2006,** *103* (43), 15729-15735.

(3) *International Energy Agency, World Energy Outlook 2015*.

(4) Lewis, N. S.; Crabtree, G. Basic Research Needs for Solar Energy Utilization: Report of the Basic Energy Sciences Workshop on Solar Energy Utilization, April 18–21, 2005. *US Department of Energy Office of Basic Energy Sciences* **2005**.

(5) Davis, S. J.; Caldeira, K.; Matthews, H. D. Future CO_2 Emissions and Climate Change from Existing Energy Infrastructure. *Science* **2010,** *329* (5997), 1330-1333.

(6) Vinyard, D. J.; Ananyev, G. M.; Dismukes, G. C. Photosystem II: the Reaction Center of Oxygenic Photosynthesis. *Annu. Rev. Biochem.* **2013,** *82*, 577-606.

(7) http://www.breakthroughenergycoalition.com

(8) Haxel, G. B.; Hedrick, J. B.; Orris, G. J.; Stauffer, P. H.; Hendley II, J. W. "Rare Earth Elements: Critical Resources for High Technology," USGS, 2002.

(9) Wood, P. M. The Potential Diagram for Oxygen at pH 7. *Biochem. J.* **1988,** *253* (1), 287-289.

(10) Britt, R. D. In *Oxygenic Photosynthesis: The Light Reactions*; Ort, D. R.;Yocum, C. F.;Heichel, I. F., Eds.; Springer Netherlands: Dordrecht, 1996.

(11) Umena, Y.; Kawakami, K.; Shen, J.-R.; Kamiya, N. Crystal Structure of Oxygen-Evolving Photosystem II at a Resolution of 1.9 Å. *Nature* **2011,** *473* (7345), 55-60.

(12) Meyer, T. J.; Huynh, M. H. V.; Thorp, H. H. The Possible Role of Proton-Coupled Electron Transfer (PCET) in Water Oxidation by Photosystem II. *Angew. Chem. Int. Edit.* **2007,** *46* (28), 5284-5304.

(13) Kok, B.; Forbush, B.; McGloin, M. Cooperation of Charges in Photosynthetic O_2 Evolution–I. A Linear Four Step Mechanism. *Photochem. Photobiol.* **1970,** *11* (6), 457-475.

(14) Brudvig, G. W. Water Oxidation Chemistry of Photosystem II. *Phil. Trans. R. Soc. Lond. B: Biol. Sci.* **2008,** *363* (1494), 1211-1219.

(15) Cukier, R. Mechanism for Proton-Coupled Electron-Transfer Reactions. *J. Phys. Chem.* **1994,** *98* (9), 2377-2381.

(16) Cukier, R. Proton-Coupled Electron Transfer through an Asymmetric Hydrogen-Bonded Interface. *J. Phys. Chem.* **1995,** *99* (43), 16101-16115.

(17) Hammes-Schiffer, S. Theoretical Perspectives on Proton-Coupled Electron Transfer Reactions. *Acc. Chem. Res.* **2001,** *34* (4), 273-281.

(18) Hammes-Schiffer, S. Introduction: Proton-Coupled Electron Transfer. *Chem. Rev.* **2010,** *110* (12), 6937-6938.

(19) Kanady, J. S.; Tsui, E. Y.; Day, M. W.; Agapie, T. A Synthetic Model of the Mn_3Ca Subsite of the Oxygen-Evolving Complex in Photosystem II. *Science* **2011,** *333* (6043), 733-736.

(20) Zhang, C.; Chen, C.; Dong, H.; Shen, J.-R.; Dau, H.; Zhao, J. A Synthetic Mn_4Ca-Cluster Mimicking the Oxygen-Evolving Center of Photosynthesis. *Science* **2015,** *348* (6235), 690-693.

(21) Borovik, A. S. Bioinspired Hydrogen Bond Motifs in Ligand Design: the Role of Noncovalent Interactions in Metal Ion Mediated Activation of Dioxygen. *Acc. Chem. Res.* **2005,** *38* (1), 54-61.

(22) Vrettos, J. S.; Limburg, J.; Brudvig, G. W. Mechanism of Photosynthetic Water Oxidation: Combining Biophysical Studies of Photosystem II with Inorganic Model Chemistry. *BBA-Bioenergetics* **2001,** *1503* (1), 229-245.

(23) Tsui, E. Y.; Tran, R.; Yano, J.; Agapie, T. Redox-Inactive Metals Modulate the Reduction Potential in Heterometallic Manganese–Oxido Clusters. *Nature Chem.* **2013,** *5* (4), 293-299.

(24) McKone, J. R.; Lewis, N. S.; Gray, H. B. Will Solar-Driven Water-Splitting Devices See the Light of Day? *Chem. Mater.* **2013,** *26* (1), 407-414.

(25) Parkinson, B. On the Efficiency and Stability of Photoelectrochemical Devices. *Acc. Chem. Res.* **1984,** *17* (12), 431-437.

(26) Khaselev, O.; Turner, J. A. A Monolithic Photovoltaic-Photoelectrochemical Device for Hydrogen Production via Water Splitting. *Science* **1998,** *280* (5362), 425-427.

(27) Newman, J.; Hoertz, P. G.; Bonino, C. A.; Trainham, J. A. Review: an Economic Perspective on Liquid Solar Fuels. *J. Electrochem. Soc.* **2012,** *159* (10), A1722-A1729.

(28) Tachibana, Y.; Vayssieres, L.; Durrant, J. R. Artificial Photosynthesis for Solar Water-Splitting. *Nat. Photonics* **2012,** *6* (8), 511-518.

(29) Osterloh, F. E. Inorganic Nanostructures for Photoelectrochemical and Photocatalytic Water Splitting. *Chem. Soc. Rev.* **2013,** *42* (6), 2294-2320.

(30) Pinaud, B. A.; Benck, J. D.; Seitz, L. C.; Forman, A. J.; Chen, Z.; Deutsch, T. G.; James, B. D.; Baum, K. N.; Baum, G. N.; Ardo, S.et al. Technical and Economic Feasibility of Centralized Facilities for Solar Hydrogen Production via Photocatalysis and Photoelectrochemistry. *Energy Environ. Sci.* **2013,** *6* (7), 1983-2002.

(31) Döscher, H.; Geisz, J. F.; Deutsch, T. G.; Turner, J. A. Sunlight Absorption in Water–Efficiency and Design Implications for Photoelectrochemical Devices. *Energy Environ. Sci.* **2014,** *7* (9), 2951-2956.

(32) Gu, S.; Xu, B.; Yan, Y. Electrochemical Energy Engineering: a New Frontier of Chemical Engineering Innovation. *Annu. Rev. Chem. Biomol. Eng.* **2014,** *5*, 429-454.

(33) Luo, J.; Im, J.-H.; Mayer, M. T.; Schreier, M.; Nazeeruddin, M. K.; Park, N.-G.; Tilley, S. D.; Fan, H. J.; Grätzel, M. Water Photolysis at 12.3% Efficiency via Perovskite Photovoltaics and Earth-Abundant Catalysts. *Science* **2014,** *345* (6204), 1593-1596.

(34) Chen, Y.; Sun, K.; Audesirk, H.; Xiang, C.; Lewis, N. S. A Quantitative Analysis of the Efficiency of Solar-Driven Water-Splitting Device Designs Based on Tandem Photoabsorbers Patterned with Islands of Metallic Electrocatalysts. *Energy Environ. Sci.* **2015,** *8* (6), 1736-1747.

(35) Dumortier, M.; Haussener, S. Design Guidelines for Concentrated Photo-Electrochemical Water Splitting Devices Based on Energy and Greenhouse Gas Yield Ratios. *Energy Environ. Sci.* **2015,** *8* (11), 3069-3082.

(36) Verlage, E.; Hu, S.; Liu, R.; Jones, R. J. R.; Sun, K.; Xiang, C.; Lewis, N. S.; Atwater, H. A. A Monolithically Integrated, Intrinsically Safe, 10% Efficient, Solar-Driven Water-Splitting System Based on Active, Stable Earth-Abundant Electrocatalysts in Conjunction with Tandem III-V Light Absorbers Protected by Amorphous TiO_2 Films. *Energy Environ. Sci.* **2015,** *8* (11), 3166-3172.

(37) Doscher, H.; Young, J. L.; Geisz, J. F.; Turner, J. A.; Deutsch, T. G. Solar-to-Hydrogen Efficiency: Shining Light on Photoelectrochemical Device Performance. *Energy Environ. Sci.* **2016,** *9* (1), 74-80.

(38) Kärkäs, M. D.; Verho, O.; Johnston, E. V.; Åkermark, B. Artificial Photosynthesis: Molecular Systems for Catalytic Water Oxidation. *Chem. Rev.* **2014,** *114* (24), 11863-12001.

(39) Blakemore, J. D.; Crabtree, R. H.; Brudvig, G. W. Molecular Catalysts for Water Oxidation. *Chem. Rev.* **2015,** *115* (23), 12974-13005.

(40) Kärkäs, M.; Åkermark, B. Water Oxidation using Earth-Abundant Transition Metal Catalysts: Opportunities and Challenges. *Dalton Trans.* **2016,** *45* (37), 14421-14461.

(41) Pourbaix, M. *Atlas of Electrochemical Equilibria in Aqueous Solutions*; Pergamon Press: New York, 1966.

(42) Leng, Y.; Chen, G.; Mendoza, A. J.; Tighe, T. B.; Hickner, M. A.; Wang, C.-Y. Solid-State Water Electrolysis with an Alkaline Membrane. *J. Am. Chem. Soc.* **2012,** *134* (22), 9054-9057.

(43) Varcoe, J. R.; Atanassov, P.; Dekel, D. R.; Herring, A. M.; Hickner, M. A.; Kohl, P. A.; Kucernak, A. R.; Mustain, W. E.; Nijmeijer, K.; Scott, K. Anion-Exchange Membranes in Electrochemical Energy Systems. *Energy Environ. Sci.* **2014,** *7* (10), 3135-3191.

(44) Walter, M. G.; Warren, E. L.; McKone, J. R.; Boettcher, S. W.; Mi, Q.; Santori, E. A.; Lewis, N. S. Solar Water Splitting Cells. *Chem. Rev.* **2010,** *110* (11), 6446-6473.

(45) Load changes, as they occur in sun-light-driven devices because of the diurnal nature of solar illumination, will be another major consideration regarding optimal pH conditions.

(46) Kim, J.; Yin, X.; Tsao, K.-C.; Fang, S.; Yang, H. $Ca_2Mn_2O_5$ as Oxygen-Deficient Perovskite Electrocatalyst for Oxygen Evolution Reaction. *J. Am. Chem. Soc.* **2014,** *136* (42), 14646-14649.

(47) Diaz-Morales, O.; Ledezma-Yanez, I.; Koper, M. T.; Calle-Vallejo, F. Guidelines for the Rational Design of Ni-Based Double Hydroxide Electrocatalysts for the Oxygen Evolution Reaction. *ACS Catal.* **2015,** *5* (9), 5380-5387.

(48) Bockris, J. O.; Otagawa, T. The Electrocatalysis of Oxygen Evolution on Perovskites. *J. Electrochem. Soc.* **1984,** *131* (2), 290-302.

(49) Mauritz, K. A.; Moore, R. B. State of Understanding of Nafion. *Chem. Rev.* **2004,** *104* (10), 4535-4586.

(50) Carmo, M.; Fritz, D. L.; Mergel, J.; Stolten, D. A Comprehensive Review on PEM Water Electrolysis. *Int. J. Hydrogen Energy* **2013,** *38* (12), 4901-4934.

(51) Harriman, A.; Pickering, I. J.; Thomas, J. M.; Christensen, P. A. Metal Oxides as Heterogeneous Catalysts for Oxygen Evolution under Photochemical Conditions. *J. Chem. Soc., Faraday Trans. I* **1988,** *84* (8), 2795-2806.

(52) Chen, X.; Chen, G.; Yue, P. L. Stable $Ti/IrO_x–Sb_2O_5–SnO_2$ Anode for O_2 Evolution with Low Ir Content. *J. Phys. Chem. B* **2001,** *105* (20), 4623-4628.

(53) Blakemore, J. D.; Schley, N. D.; Olack, G. W.; Incarvito, C. D.; Brudvig, G. W.; Crabtree, R. H. Anodic Deposition of a Robust Iridium-Based Water-Oxidation Catalyst from Organometallic Precursors. *Chem. Sci.* **2011,** *2* (1), 94-98.

(54) Schley, N. D.; Blakemore, J. D.; Subbaiyan, N. K.; Incarvito, C. D.; D'Souza, F.; Crabtree, R. H.; Brudvig, G. W. Distinguishing Homogeneous from Heterogeneous Catalysis in Electrode-Driven Water Oxidation with Molecular Iridium Complexes. *J. Am. Chem. Soc.* **2011,** *133* (27), 10473-10481.

(55) Frame, F. A.; Townsend, T. K.; Chamousis, R. L.; Sabio, E. M.; Dittrich, T.; Browning, N. D.; Osterloh, F. E. Photocatalytic Water Oxidation with Nonsensitized IrO_2 Nanocrystals under Visible and UV Light. *J. Am. Chem. Soc.* **2011,** *133* (19), 7264-7267.

(56) Wang, C.; Xie, Z.; deKrafft, K. E.; Lin, W. Doping Metal–Organic Frameworks for Water Oxidation, Carbon Dioxide Reduction, and Organic Photocatalysis. *J. Am. Chem. Soc.* **2011,** *133* (34), 13445-13454.

(57) Fujishima, A.; Honda, K. Electrochemical Photolysis of Water at a Semiconductor Electrode. *Nature* **1972,** *238* (5358), 37-38.

(58) Walsh, A.; Yan, Y.; Huda, M. N.; Al-Jassim, M. M.; Wei, S.-H. Band Edge Electronic Structure of $BiVO_4$: Elucidating the Role of the Bi s and V d Orbitals. *Chem. Mater.* **2009,** *21* (3), 547-551.

(59) Prévot, M. S.; Sivula, K. Photoelectrochemical Tandem Cells for Solar Water Splitting. *J. Phys. Chem. C* **2013,** *117* (35), 17879-17893.

(60) Liu, M.; Nam, C.-Y.; Black, C. T.; Kamcev, J.; Zhang, L. Enhancing Water Splitting Activity and Chemical Stability of Zinc Oxide Nanowire Photoanodes with Ultrathin Titania Shells. *J. Phys. Chem. C* **2013,** *117* (26), 13396-13402.

(61) Kato, H.; Asakura, K.; Kudo, A. Highly Efficient Water Splitting into H_2 and O_2 over Lanthanum-Doped $NaTaO_3$ Photocatalysts with High Crystallinity and Surface Nanostructure. *J. Am. Chem. Soc.* **2003,** *125* (10), 3082-3089.

(62) Lau, L. C.; Lee, K. T. The Effect of Band Engineering of Semiconductors on Photocatalytic Water Splitting: A Review. *IJRET* **2013,** *2* (11), 195-206.

(63) Mi, Q.; Zhanaidarova, A.; Brunschwig, B. S.; Gray, H. B.; Lewis, N. S. A Quantitative Assessment of the Competition between Water and Anion Oxidation at WO_3 Photoanodes in Acidic Aqueous Electrolytes. *Energy Environ. Sci.* **2012,** *5* (2), 5694-5700.

(64) Miseki, Y.; Sayama, K. High-Efficiency Water Oxidation and Energy Storage Utilizing Various Reversible Redox Mediators under Visible Light over Surface-Modified WO_3. *RSC Adv.* **2014,** *4* (16), 8308-8316.

(65) Kawasaki, S.; Nakatsuji, K.; Yoshinobu, J.; Komori, F.; Takahashi, R.; Lippmaa, M.; Mase, K.; Kudo, A. Epitaxial Rh-Doped $SrTiO_3$ Thin Film Photocathode for Water Splitting under Visible Light Irradiation. *Appl. Phys. Lett.* **2012,** *101* (3), 033910.

(66) Bolton, J. R.; Strickler, S. J.; Connolly, J. S. Limiting and Realizable Efficiencies of Solar Photolysis of Water. *Nature* **1985,** *316* (6028), 495-500.

(67) Sakthivel, S.; Janczarek, M.; Kisch, H. Visible Light Activity and Photoelectrochemical Properties of Nitrogen-Doped TiO_2. *J. Phys. Chem. B* **2004,** *108* (50), 19384-19387.

(68) Mi, Q.; Ping, Y.; Li, Y.; Cao, B.; Brunschwig, B. S.; Khalifah, P. G.; Galli, G. A.; Gray, H. B.; Lewis, N. S. Thermally Stable N_2-Intercalated WO_3 Photoanodes for Water Oxidation. *J. Am. Chem. Soc.* **2012,** *134* (44), 18318-18324.

(69) A TiO_2 bandgap of 2.9 eV is still too large for efficient light absorption; and tungsten oxide is not stable in alkaline media in which highly active, earth-abundant water oxidation catalysts operate.

(70) Suntivich, J.; May, K. J.; Gasteiger, H. A.; Goodenough, J. B.; Shao-Horn, Y. A Perovskite Oxide Optimized for Oxygen Evolution Catalysis from Molecular Orbital Principles. *Science* **2011,** *334* (6061), 1383-1385.

(71) Liu, H.; Moré, R.; Grundmann, H.; Cui, C.; Erni, R.; Patzke, G. R. Promoting Photochemical Water Oxidation with Metallic Band Structures. *J. Am. Chem. Soc.* **2016,** *138* (5), 1527-1535.

(72) Hildebrandt, N. C.; Soldat, J.; Marschall, R. Layered Perovskite Nanofibers via Electrospinning for Overall Water Splitting. *Small* **2015,** *11* (17), 2051-2057.

(73) Park, Y.; McDonald, K. J.; Choi, K.-S. Progress in Bismuth Vanadate Photoanodes for use in Solar Water Oxidation. *Chem. Soc. Rev.* **2013,** *42* (6), 2321-2337.

(74) Abdi, F. F.; Firet, N.; Dabirian, A.; van de Krol, R. Spray-Deposited Co-Pi Catalyzed $BiVO_4$: a Low-Cost Route towards Highly Efficient Photoanodes. *MRS Proceedings* **2012,** *1446*, 7-12.

(75) Kudo, A.; Omori, K.; Kato, H. A Novel Aqueous Process for Preparation of Crystal Form-Controlled and Highly Crystalline $BiVO_4$ Powder from Layered Vanadates at Room Temperature and Its Photocatalytic and Photophysical Properties. *J. Am. Chem. Soc.* **1999,** *121* (49), 11459-11467.

(76) Tokunaga, S.; Kato, H.; Kudo, A. Selective Preparation of Monoclinic and Tetragonal $BiVO_4$ with Scheelite Structure and Their Photocatalytic Properties. *Chem. Mater.* **2001,** *13* (12), 4624-4628.

(77) Kudo, A.; Ueda, K.; Kato, H.; Mikami, I. Photocatalytic O_2 Evolution under Visible Light Irradiation on $BiVO_4$ in Aqueous $AgNO_3$ Solution. *Catal. Lett.* **1998,** *53* (3-4), 229-230.

(78) Abdi, F. F.; Firet, N.; van de Krol, R. Efficient $BiVO_4$ Thin Film Photoanodes Modified with Cobalt Phosphate Catalyst and W-doping. *ChemCatChem* **2013,** *5* (2), 490-496.

(79) Alarcon-Llado, E.; Chen, L.; Hettick, M.; Mashouf, N.; Lin, Y.; Javey, A.; Ager, J. W. $BiVO_4$ Thin Film Photoanodes Grown by Chemical Vapor Deposition. *Phys. Chem. Chem. Phys.* **2014,** *16* (4), 1651-1657.

(80) Berglund, S. P.; Flaherty, D. W.; Hahn, N. T.; Bard, A. J.; Mullins, C. B. Photoelectrochemical Oxidation of Water Using Nanostructured $BiVO_4$ Films. *J. Phys. Chem. C* **2011,** *115* (9), 3794-3802.

(81) Chen, L.; Alarcón-Lladó, E.; Hettick, M.; Sharp, I. D.; Lin, Y.; Javey, A.; Ager, J. W. Reactive Sputtering of Bismuth Vanadate Photoanodes for Solar Water Splitting. *J. Phys. Chem. C* **2013,** *117* (42), 21635-21642.

(82) Choi, S. K.; Choi, W.; Park, H. Solar Water Oxidation using Nickel-Borate Coupled $BiVO_4$ Photoelectrodes. *Phys. Chem. Chem. Phys.* **2013,** *15* (17), 6499-6507.

(83) Jeong, H. W.; Jeon, T. H.; Jang, J. S.; Choi, W.; Park, H. Strategic Modification of $BiVO_4$ for Improving Photoelectrochemical Water Oxidation Performance. *J. Phys. Chem. C* **2013,** *117* (18), 9104-9112.

(84) Kim, T. W.; Choi, K. S. Nanoporous $BiVO_4$ Photoanodes with Dual-Layer Oxygen Evolution Catalysts for Solar Water Splitting. *Science* **2014,** *343* (6174), 990-994.

(85) Sayama, K.; Wang, N.; Miseki, Y.; Kusama, H.; Onozawa-Komatsuzaki, N.; Sugihara, H. Effect of Carbonate Ions on the Photooxidation of Water over Porous $BiVO_4$ Film Photoelectrode under Visible Light. *Chem. Lett.* **2010,** *39* (1), 17-19.

(86) Seabold, J. A.; Choi, K.-S. Efficient and Stable Photo-Oxidation of Water by a Bismuth Vanadate Photoanode Coupled with an Iron Oxyhydroxide Oxygen Evolution Catalyst. *J. Am. Chem. Soc.* **2012,** *134* (4), 2186-2192.

(87) Su, J.; Guo, L.; Yoriya, S.; Grimes, C. A. Aqueous Growth of Pyramidal-Shaped $BiVO_4$ Nanowire Arrays and Structural Characterization: Application to Photoelectrochemical Water Splitting. *Cryst. Growth Des.* **2009,** *10* (2), 856-861.

(88) Sinclair, T. S.; Hunter, B. M.; Winkler, J. R.; Gray, H. B.; Müller, A. M. Factors Affecting Bismuth Vanadate Photoelectrochemical Performance. *Mater. Horiz.* **2015,** *2* (3), 330-337.

(89) Morita, M.; Iwakura, C.; Tamura, H. The Anodic Characteristics of Manganese Dioxide Electrodes Prepared by Thermal Decomposition of Manganese Nitrate. *Electrochim. Acta* **1977,** *22* (4), 325-328.

(90) Jiao, F.; Frei, H. Nanostructured Manganese Oxide Clusters Supported on Mesoporous Silica as Efficient Oxygen-Evolving Catalysts. *Chem. Commun.* **2010,** *46* (17), 2920-2922.

(91) Pinaud, B. A.; Chen, Z.; Abram, D. N.; Jaramillo, T. F. Thin Films of Sodium Birnessite-Type MnO_2: Optical Properties, Electronic Band Structure, and Solar Photoelectrochemistry. *J. Phys. Chem. C* **2011,** *115* (23), 11830-11838.

(92) Wiechen, M.; Zaharieva, I.; Dau, H.; Kurz, P. Layered Manganese Oxides for Water-Oxidation: Alkaline Earth Cations Influence Catalytic Activity in a Photosystem II-Like Fashion. *Chem. Sci.* **2012,** *3* (7), 2330-2339.

(93) Pokhrel, R.; Goetz, M. K.; Shaner, S. E.; Wu, X.; Stahl, S. S. The "Best Catalyst" for Water Oxidation Depends on the Oxidation Method Employed: A Case Study of Manganese Oxides. *J. Am. Chem. Soc.* **2015,** *137* (26), 8384-8387.

(94) Najafpour, M. M.; Sedigh, D. J. Water Oxidation by Manganese Oxides, a New Step towards a Complete Picture: Simplicity is the Ultimate Sophistication. *Dalton Trans.* **2013,** *42* (34), 12173-12178.

(95) Zaharieva, I.; Chernev, P.; Risch, M.; Klingan, K.; Kohlhoff, M.; Fischer, A.; Dau, H. Electrosynthesis, Functional, and Structural Characterization of a Water-Oxidizing Manganese Oxide. *Energy Environ. Sci.* **2012,** *5* (5), 7081-7089.

(96) Najafpour, M. M.; Ehrenberg, T.; Wiechen, M.; Kurz, P. Calcium Manganese(III) Oxides ($CaMn_2O_4 \cdot xH_2O$) as Biomimetic Oxygen-Evolving Catalysts. *Angew. Chem. Int. Edit.* **2010,** *49* (12), 2233-2237.

(97) Kurz, P.; Berggren, G.; Anderlund, M. F.; Styring, S. Oxygen Evolving Reactions Catalysed by Synthetic Manganese Complexes: A Systematic Screening. *Dalton Trans.* **2007,** *2007* (38), 4258-4261.

(98) Najafpour, M.; Moghaddam, A. N.; Dau, H.; Zaharieva, I. Fragments of Layered Manganese Oxide are the Real Water Oxidation Catalyst after Transformation of Molecular Precursor on Clay. *J. Am. Chem. Soc.* **2014,** *136* (20), 7245-7248.

(99) Gorlin, Y.; Jaramillo, T. F. A Bifunctional Nonprecious Metal Catalyst for Oxygen Reduction and Water Oxidation. *J. Am. Chem. Soc.* **2010,** *132* (39), 13612-13614.

(100) Gorlin, Y.; Lassalle-Kaiser, B.; Benck, J. D.; Gul, S.; Webb, S. M.; Yachandra, V. K.; Yano, J.; Jaramillo, T. F. In Situ X-ray Absorption Spectroscopy Investigation of a Bifunctional Manganese Oxide Catalyst with High Activity for Electrochemical Water Oxidation and Oxygen Reduction. *J. Am. Chem. Soc.* **2013,** *135* (23), 8525-8534.

(101) Turner, J.; Hendewerk, M.; Parmeter, J.; Neiman, D.; Somorjai, G. The Characterization of Doped Iron Oxide Electrodes for the Photodissociation of Water Stability, Optical, and Electronic Properties. *J. Electrochem. Soc.* **1984,** *131* (8), 1777-1783.

(102) Joly, A. G.; Williams, J. R.; Chambers, S. A.; Xiong, G.; Hess, W. P.; Laman, D. M. Carrier Dynamics in α-Fe2O3 (0001) Thin Films and Single Crystals Probed by Femtosecond Transient Absorption and Reflectivity. *J. Appl. Phys.* **2006,** *99* (5), 053521.

(103) Smith, R. D. L.; Prévot, M. S.; Fagan, R. D.; Zhang, Z.; Sedach, P. A.; Siu, M. K. J.; Trudel, S.; Berlinguette, C. P. Photochemical Route for Accessing Amorphous Metal Oxide Materials for Water Oxidation Catalysis. *Science* **2013,** *340* (6128), 60-63.

(104) Cesar, I.; Kay, A.; Gonzalez Martinez, J. A.; Grätzel, M. Translucent Thin Film Fe_2O_3 Photoanodes for Efficient Water Splitting by Sunlight: Nanostructure-Directing Effect of Si-Doping. *J. Am. Chem. Soc.* **2006,** *128* (14), 4582-4583.

(105) Lyons, M. E. G.; Brandon, M. P. The Oxygen Evolution Reaction on Passive Oxide Covered Transition Metal Electrodes in Aqueous Alkaline Solution. Part III - Iron. *Int. J. Electrochem. Sci.* **2008,** *3* (12), 1463-1503.

(106) Kanan, M. W.; Nocera, D. G. In Situ Formation of an Oxygen-Evolving Catalyst in Neutral Water Containing Phosphate and Co^{2+}. *Science* **2008,** *321* (5892), 1072-1075.

(107) McAlpin, J. G.; Surendranath, Y.; Dincă, M.; Stich, T. A.; Stoian, S. A.; Casey, W. H.; Nocera, D. G.; Britt, R. D. EPR Evidence for Co(IV) Species Produced During Water Oxidation at Neutral pH. *J. Am. Chem. Soc.* **2010,** *132* (20), 6882-6883.

(108) Risch, M.; Klingan, K.; Ringleb, F.; Chernev, P.; Zaharieva, I.; Fischer, A.; Dau, H. Water Oxidation by Electrodeposited Cobalt Oxides—Role of Anions and Redox-Inert Cations in Structure and Function of the Amorphous Catalyst. *ChemSusChem* **2012,** *5* (3), 542-549.

(109) El Wakkad, S. E. S.; Hickling, A. The Anodic Behaviour of Metals. Part VI.-Cobalt. *T. Faraday Soc.* **1950,** *46* (0), 820-824.

(110) Pandey, A. D.; Jia, C.; Schmidt, W.; Leoni, M.; Schwickardi, M.; Schüth, F.; Weidenthaler, C. Size-Controlled Synthesis and Microstructure Investigation of Co_3O_4 Nanoparticles for Low-Temperature CO Oxidation. *J. Phys. Chem. C* **2012,** *116* (36), 19405-19412.

(111) Gardner, G. P.; Go, Y. B.; Robinson, D. M.; Smith, P. F.; Hadermann, J.; Abakumov, A.; Greenblatt, M.; Dismukes, G. C. Structural Requirements in Lithium Cobalt Oxides for the Catalytic Oxidation of Water. *Angew. Chem. Int. Edit.* **2012,** *51* (7), 1616-1619.

(112) Song, F.; Hu, X. Ultrathin Cobalt–Manganese Layered Double Hydroxide Is an Efficient Oxygen Evolution Catalyst. *J. Am. Chem. Soc.* **2014,** *136* (47), 16481-16484.

(113) Grzelczak, M.; Zhang, J.; Pfrommer, J.; Hartmann, J.; Driess, M.; Antonietti, M.; Wang, X. Electro- and Photochemical Water Oxidation on Ligand-free Co_3O_4 Nanoparticles with Tunable Sizes. *ACS Catal.* **2013,** *3* (3), 383-388.

(114) Lyons, M. E. G.; Brandon, M. P. The Oxygen Evolution Reaction on Passive Oxide Covered Transition Metal Electrodes in Aqueous Alkaline Solution. Part II - Cobalt. *Int. J. Electrochem. Sci.* **2008,** *3* (12), 1425-1462.

(115) Blakemore, J. D.; Gray, H. B.; Winkler, J. R.; Müller, A. M. Co_3O_4 Nanoparticle Water-Oxidation Catalysts Made by Pulsed-Laser Ablation in Liquids. *ACS Catal.* **2013,** *3* (11), 2497-2500.

(116) Bode, H.; Dehmelt, K.; Witte, J. Zur Kenntnis der Nickelhydroxidelektrode—I. Über das Nickel(II)-Hydroxidhydrat. *Electrochim. Acta* **1966,** *11* (8), 1079-IN1071.

(117) Oliva, P.; Leonardi, J.; Laurent, J. F.; Delmas, C.; Braconnier, J. J.; Figlarz, M.; Fievet, F.; Guibert, A. d. Review of the Structure and the Electrochemistry of Nickel Hydroxides and Oxy-Hydroxides. *J. Power Sources* **1982,** *8* (2), 229-255.

(118) Młynarek, G.; Paszkiewicz, M.; Radniecka, A. The Effect of Ferric Ions on the Behaviour of a Nickelous Hydroxide Electrode. *J. Appl. Electrochem.* **1984,** *14* (2), 145-149.

(119) Corrigan, D. A. The Catalysis of the Oxygen Evolution Reaction by Iron Impurities in Thin Film Nickel Oxide Electrodes. *J. Electrochem. Soc.* **1987,** *134* (2), 377-384.

(120) Trotochaud, L.; Young, S. L.; Ranney, J. K.; Boettcher, S. W. Nickel-Iron Oxyhydroxide Oxygen-Evolution Electrocatalysts: the Role of Intentional and Incidental Iron Incorporation. *J. Am. Chem. Soc.* **2014,** *136* (18), 6744-6753.

(121) Lyons, M. E. G.; Brandon, M. P. The Oxygen Evolution Reaction on Passive Oxide Covered Transition Metal Electrodes in Aqueous Alkaline Solution. Part I - Nickel. *Int. J. Electrochem. Sci.* **2008,** *3* (12), 1386-1424.

(122) Chen, J. Y. C.; Miller, J. T.; Gerken, J. B.; Stahl, S. S. Inverse Spinel $NiFeAlO_4$ as a Highly Active Oxygen Evolution Electrocatalyst: Promotion of Activity by a Redox-Inert Metal Ion. *Energy Environ. Sci.* **2014,** *7* (4), 1382-1386.

(123) Niedbala, J.; Budniok, A.; Surowka, J.; Gierlotka, D. Electrolytic Oxygen Evolution on Ni-P-Sc_2O_3 Composite Layers. *Thin Solid Films* **1996,** *287* (1-2), 164-168.

(124) Liu, H.; Nakamura, R.; Nakato, Y. Bismuth-Copper Vanadate $BiCu_2VO_6$ as a Novel Photocatalyst for Efficient Visible-Light-Driven Oxygen Evolution. *ChemPhysChem* **2005,** *6* (12), 2499-2502.

(125) Xing, M.; Kong, L.-B.; Liu, M.-C.; Liu, L.-Y.; Kang, L.; Luo, Y.-C. Cobalt Vanadate as Highly Active, Stable, Noble Metal-Free Oxygen Evolution Electrocatalyst. *J. Mater. Chem. A* **2014,** *2* (43), 18435-18443.

(126) Aki, S. N. V. K.; Ding, Z.-Y.; Abraham, M. A. Catalytic Supercritical Water Oxidation: Stability of Cr_2O_3 Catalyst. *AIChE J.* **1996,** *42* (7), 1995-2004.

(127) Soldat, J.; Busser, G. W.; Muhler, M.; Wark, M. Cr_2O_3 Nanoparticles on $Ba_5Ta_4O_{15}$ as a Noble-Metal-Free Oxygen Evolution Co-Catalyst for Photocatalytic Overall Water Splitting. *ChemCatChem* **2016,** *8* (1), 153-156.

(128) Du, J.; Chen, Z.; Ye, S.; Wiley, B. J.; Meyer, T. J. Copper as a Robust and Transparent Electrocatalyst for Water Oxidation. *Angew. Chem., Int. Ed.* **2015,** *54* (7), 2073-2078.

(129) Cui, S.; Liu, X.; Sun, Z.; Du, P. Noble Metal-Free Copper Hydroxide as an Active and Robust Electrocatalyst for Water Oxidation at Weakly Basic pH. *ACS Sustainable Chemistry & Engineering* **2016,** *4* (5), 2593-2600.

(130) Liu, X.; Cui, S.; Qian, M.; Sun, Z.; Du, P. In Situ Generated Highly Active Copper Oxide Catalysts for the Oxygen Evolution Reaction at Low Overpotential in Alkaline Solutions. *Chem. Commun.* **2016,** *52* (32), 5546-5549.

(131) Prevedello, A.; Bazzan, I.; Dalle Carbonare, N.; Giuliani, A.; Bhardwaj, S.; Africh, C.; Cepek, C.; Argazzi, R.; Bonchio, M.; Caramori, S.et al. Heterogeneous and Homogeneous Routes in Water Oxidation Catalysis Starting from Cu^{II} Complexes with Tetraaza Macrocyclic Ligands. *Chem. - Asian J.* **2016,** *11* (8), 1281-1287.

(132) Shi, Y.; Gimbert-Surinach, C.; Han, T.; Berardi, S.; Lanza, M.; Llobet, A. CuO-Functionalized Silicon Photoanodes for Photoelectrochemical Water Splitting Devices. *ACS Appl. Mater. Interfaces* **2016,** *8* (1), 696-702.

(133) Jiang, C.; Moniz, S. J. A.; Khraisheh, M.; Tang, J. Earth-Abundant Oxygen Evolution Catalysts Coupled onto ZnO Nanowire Arrays for Efficient Photoelectrochemical Water Cleavage. *Chem. - Eur. J.* **2014,** *20* (40), 12954-12961.

(134) Kim, T. W.; Woo, M. A.; Regis, M.; Choi, K.-S. Electrochemical Synthesis of Spinel Type $ZnCo_2O_4$ Electrodes for Use as Oxygen Evolution Reaction Catalysts. *J. Phys. Chem. Lett.* **2014,** *5* (13), 2370-2374.

(135) Jang, D. M.; Kwak, I. H.; Kwon, E. L.; Jung, C. S.; Im, H. S.; Park, K.; Park, J. Transition-Metal Doping of Oxide Nanocrystals for Enhanced Catalytic Oxygen Evolution. *J. Phys. Chem. C* **2015,** *119* (4), 1921-1927.

(136) Pope, M. T.; Müller, A. Polyoxometalate Chemistry: an Old Field with New Dimensions in Several Disciplines. *Angew. Chem. Int. Edit.* **1991,** *30* (1), 34-48.

(137) Sumliner, J. M.; Lv, H.; Fielden, J.; Geletii, Y. V.; Hill, C. L. Polyoxometalate Multi-Electron-Transfer Catalytic Systems for Water Splitting. *Eur. J. Inorg. Chem.* **2014,** *2014* (4), 635-644.

(138) Gouzerh, P.; Che, M. From Scheele and Berzelius to Müller. *Actual. Chim.* **2006,** (298), 1.

(139) Pope, M. T.; Kortz, U. In *Encyclopedia of Inorganic and Bioinorganic Chemistry*; John Wiley & Sons, Ltd, 2011.

(140) Armatas, G. S.; Katsoulidis, A. P.; Petrakis, D. E.; Pomonis, P. J.; Kanatzidis, M. G. Nanocasting of Ordered Mesoporous Co_3O_4-Based Polyoxometalate Composite Frameworks. *Chem. Mater.* **2010,** *22* (20), 5739-5746.

(141) Lv, H.; Geletii, Y. V.; Zhao, C.; Vickers, J. W.; Zhu, G.; Luo, Z.; Song, J.; Lian, T.; Musaev, D. G.; Hill, C. L. Polyoxometalate Water Oxidation Catalysts and the Production of Green Fuel. *Chem. Soc. Rev.* **2012,** *41* (22), 7572-7589.

(142) Duan, X.; Evans, D. G. *Layered Double Hydroxides*; Springer Science & Business Media, 2006.

(143) Fan, G.; Li, F.; Evans, D. G.; Duan, X. Catalytic Applications of Layered Double Hydroxides: Recent Advances and Perspectives. *Chem. Soc. Rev.* **2014,** *43* (20), 7040-7066.

(144) Gong, M.; Li, Y.; Wang, H.; Liang, Y.; Wu, J. Z.; Zhou, J.; Wang, J.; Regier, T.; Wei, F.; Dai, H. An Advanced Ni–Fe Layered Double Hydroxide Electrocatalyst for Water Oxidation. *J. Am. Chem. Soc.* **2013,** *135* (23), 8452-8455.

(145) Zhao, Y.; Li, B.; Wang, Q.; Gao, W.; Wang, C. J.; Wei, M.; Evans, D. G.; Duan, X.; O'Hare, D. NiTi-Layered Double Hydroxides Nanosheets as Efficient Photocatalysts for Oxygen Evolution from Water using Visible Light. *Chem. Sci.* **2014,** *5* (3), 951-958.

(146) Trotochaud, L.; Ranney, J. K.; Williams, K. N.; Boettcher, S. W. Solution-Cast Metal Oxide Thin Film Electrocatalysts for Oxygen Evolution. *J. Am. Chem. Soc.* **2012,** *134* (41), 17253-17261.

(147) Song, F.; Hu, X. Exfoliation of Layered Double Hydroxides for Enhanced Oxygen Evolution Catalysis. *Nat. Commun.* **2014,** *5*, 4477-4486.

(148) Li, Z.; Shao, M.; An, H.; Wang, Z.; Xu, S.; Wei, M.; Evans, D. G.; Duan, X. Fast Electrosynthesis of Fe-Containing Layered Double Hydroxide Arrays toward Highly Efficient Electrocatalytic Oxidation Reactions. *Chem. Sci.* **2015,** *6* (11), 6624-6631.

(149) Hunter, B. M.; Blakemore, J. D.; Deimund, M.; Gray, H. B.; Winkler, J. R.; Müller, A. M. Highly Active Mixed-Metal Nanosheet Water Oxidation Catalysts Made by Pulsed-Laser Ablation in Liquids. *J. Am. Chem. Soc.* **2014,** *136* (38), 13118-13121.

(150) Evans, D. G.; Slade, R. C. Structural Aspects of Layered Double Hydroxides. *Struct. Bond.* **2006,** *119*, 1-87.

(151) Stanimirova, T. S.; Kirov, G.; Dinolova, E. Mechanism of Hydrotalcite Regeneration. *J. Mater. Sci. Lett.* **2001,** *20* (5), 453-455.

(152) The depicted LDH structure is based on that of α-$Ni(OH)_2$ reported in the American Mineralogist Crystal Structure Database (AMCSD) #0015759.

(153) McCrory, C. C. L.; Jung, S.; Peters, J. C.; Jaramillo, T. F. Benchmarking Heterogeneous Electrocatalysts for the Oxygen Evolution Reaction. *J. Am. Chem. Soc.* **2013,** *135* (45), 16977-16987.

(154) Roger, I.; Symes, M. D. Efficient Electrocatalytic Water Oxidation at Neutral and High pH by Adventitious Nickel at Nanomolar Concentrations. *J. Am. Chem. Soc.* **2015,** *137* (43), 13980-13988.

(155) Yeo, B. S.; Bell, A. T. In Situ Raman Study of Nickel Oxide and Gold-Supported Nickel Oxide Catalysts for the Electrochemical Evolution of Oxygen. *J. Phys. Chem. C* **2012,** *116* (15), 8394-8400.

(156) Dincă, M.; Surendranath, Y.; Nocera, D. G. Nickel-Borate Oxygen-Evolving Catalyst that Functions under Benign Conditions. *Proc. Natl. Acad. Sci. U. S. A.* **2010,** *107* (23), 10337-10341.

(157) Landon, J.; Demeter, E.; İnoğlu, N.; Keturakis, C.; Wachs, I. E.; Vasić, R.; Frenkel, A. I.; Kitchin, J. R. Spectroscopic Characterization of Mixed Fe–Ni Oxide Electrocatalysts for the Oxygen Evolution Reaction in Alkaline Electrolytes. *ACS Catal.* **2012,** *2* (8), 1793-1801.

(158) Smith, R. D. L.; Prévot, M. S.; Fagan, R. D.; Trudel, S.; Berlinguette, C. P. Water Oxidation Catalysis: Electrocatalytic Response to Metal Stoichiometry in Amorphous Metal Oxide Films Containing Iron, Cobalt, and Nickel. *J. Am. Chem. Soc.* **2013,** *135* (31), 11580-11586.

(159) Li, X.; Walsh, F. C.; Pletcher, D. Nickel Based Electrocatalysts for Oxygen Evolution in High Current Density, Alkaline Water Electrolyzers. *Phys. Chem. Chem. Phys.* **2011,** *13* (3), 1162-1167.

(160) Singh, A.; Chang, S. L. Y.; Hocking, R. K.; Bach, U.; Spiccia, L. Highly Active Nickel Oxide Water Oxidation Catalysts Deposited from Molecular Complexes. *Energy Environ. Sci.* **2013,** *6* (2), 579-586.

(161) Gao, M.; Sheng, W.; Zhuang, Z.; Fang, Q.; Gu, S.; Jiang, J.; Yan, Y. Efficient Water Oxidation Using Nanostructured α-Nickel-Hydroxide as an Electrocatalyst. *J. Am. Chem. Soc.* **2014,** *136* (19), 7077-7084.

(162) Louie, M. W.; Bell, A. T. An Investigation of Thin-Film Ni–Fe Oxide Catalysts for the Electrochemical Evolution of Oxygen. *J. Am. Chem. Soc.* **2013,** *135* (33), 12329-12337.

(163) Long, X.; Li, J.; Xiao, S.; Yan, K.; Wang, Z.; Chen, H.; Yang, S. A Strongly Coupled Graphene and FeNi Double Hydroxide Hybrid as an Excellent Electrocatalyst for the Oxygen Evolution Reaction. *Angew. Chem. Int. Edit.* **2014,** *53* (29), 7584-7588.

(164) Zhang, B.; Zheng, X.; Voznyy, O.; Comin, R.; Bajdich, M.; García-Melchor, M.; Han, L.; Xu, J.; Liu, M.; Zheng, L.et al. Homogeneously Dispersed Multimetal Oxygen-Evolving Catalysts. *Science* **2016,** *352* (6283), 333-337.

(165) Burke, M. S.; Enman, L. J.; Batchellor, A. S.; Zou, S.; Boettcher, S. W. Oxygen Evolution Reaction Electrocatalysis on Transition Metal Oxides and (Oxy)hydroxides: Activity Trends and Design Principles. *Chem. Mater.* **2015,** *27* (22), 7549-7558.

(166) Blackman, F. F.; Matthaei, G. L. C. A Quantitative Study of Carbon Dioxide Assimilation and Leaf Temperature in Natural Illumination. *Proc. Roy. Soc., B* **1905,** *76*, 402-460.

(167) Warburg, O. Über die Geschwindigkeit der photochemischen Kohlensäurezersetzung in lebenden Zellen. *Biochem. Zeit.* **1919,** *100*, 230-270.

(168) Warburg, O. Über die Geschwindigkeit der photochemischen Kohlensäurezersetzung in lebenden Zellen II. *Biochem. Zeit.* **1919,** *103*, 188-217.

(169) Warburg, O. Theorie der Kohlensäureassimilation. *Naturwiss.* **1921,** *9* (18), 354-358.

(170) van Niel, C. B. On the Morphology and Physiology of the Purple and Green Sulphur Bacteria. *Arch. Microbiol.* **1932,** *3* (1), 1-112.

(171) Hill, R. Oxygen Evolved by Isolated Chloroplasts. *Nature* **1937,** *139*, 881-882.

(172) Hill, R. Oxygen Produced by Isolated Chloroplasts. *Proc. R. Soc. Lond. B Biol. Sci.* **1939,** *127* (847), 192-210.

(173) Hill, R.; Scarisbrick, R. Production of Oxygen by Illuminated Chloroplasts. *Nature* **1940,** *146*, 61-62.

(174) Ruben, S.; Randall, M.; Kamen, M.; Hyde, J. L. Heavy Oxygen (O^{18}) as a Tracer in the Study of Photosynthesis. *J. Am. Chem. Soc.* **1941,** *63* (3), 877-879.

(175) Ruben, S.; Kamen, M. D. Radioactive Carbon of Long Half-Life. *Phys. Rev.* **1940,** *57* (6), 549.

(176) Joliot, P. Cinétiques des Réactions Liées a l'Émission d'Oxygène Photosynthétique. *BBA-Biophysics* **1965,** *102* (1), 116-134.

(177) Joliot, P.; Joliot, A. A Polarographic Method for Detection of Oxygen Production and Reduction of Hill Reagent by Isolated Chloroplasts. *BBA-Bioenergetics* **1968,** *153* (3), 625-634.

(178) Bennoun, P.; Joliot, A. Etude de la Photooxydation de l'Hydroxylamine par les Chloroplastes d'Epinards. *BBA-Bioenergetics* **1969,** *189* (1), 85-94.

(179) Berthold, D. A.; Babcock, G. T.; Yocum, C. F. A Highly Resolved, Oxygen-Evolving Photosystem II Preparation from Spinach Thylakoid Membranes. *FEBS Lett.* **1981,** *134* (2), 231-234.

(180) Klauss, A.; Haumann, M.; Dau, H. Alternating Electron and Proton Transfer Steps in Photosynthetic Water Oxidation. *Proc. Natl. Acad. Sci. U. S. A.* **2012,** *109* (40), 16035-16040.

(181) Cox, N.; Retegan, M.; Neese, F.; Pantazis, D. A.; Boussac, A.; Lubitz, W. Electronic Structure of the Oxygen-Evolving Complex in Photosystem II Prior to OO Bond Formation. *Science* **2014,** *345* (6198), 804-808.

(182) Debus, R.; Barry, B.; Sithole, I.; Babcock, G. T.; McIntosh, L. Directed Mutagenesis Indicates that the Donor to P 680^{+} in Photosystem II is Tyrosine-161 of the D1 Polypeptide. *Biochemistry* **1988,** *27* (26), 9071-9074.

(183) Debus, R. J.; Barry, B. A.; Babcock, G. T.; McIntosh, L. Site-Directed Mutagenesis Identifies a Tyrosine Radical Involved in the Photosynthetic Oxygen-Evolving System. *Proc. Natl. Acad. Sci. U. S. A.* **1988,** *85* (2), 427-430.

(184) Britt, R. D.; Campbell, K. A.; Peloquin, J. M.; Gilchrist, M. L.; Aznar, C. P.; Dicus, M. M.; Robblee, J.; Messinger, J. Recent Pulsed EPR Studies of the Photosystem II Oxygen-Evolving Complex: Implications as to Water Oxidation Mechanisms. *BBA-Bioenergetics* **2004,** *1655*, 158-171.

(185) Nugent, J. H. A.; Ball, R. J.; Evans, M. C. W. Photosynthetic Water Oxidation: the Role of Tyrosine Radicals. *BBA-Bioenergetics* **2004,** *1655*, 217-221.

(186) Britt, R. D. Oxygen Evolution. *Adv. Photosynth.* **1996,** *4* (Oxygenic Photosynthesis: The Light Reactions), 137-164.

(187) Britt, R. D. Electron Spin Echo Methods in Photosynthesis Research. *Adv. Photosynth.* **1996,** *3* (Biophysical Techniques in Photosynthesis), 235-253.

(188) Britt, R. D.; Force, D. A.; Campbell, K. A.; Randall, D. W.; Gilchrist, L. M.; Clemens, K. L.; Gingell, D. M.; Peloquin, J. M.; Pham, D. P.; Debus, R. J. Progress in Characterization of the Photosystem II Oxygen Evolving Complex using Advanced EPR Methods. *ACS Symp. Ser.* **1998,** *692* (Spectroscopic Methods in Bioinorganic Chemistry), 272-285.

(189) Sauer, K.; Yachandra, V. K.; Britt, R. D.; Klein, M. P. The Photosynthetic Water Oxidation Complex Studied by EPR and X-ray Absorption Spectroscopy. In *Manganese Redox Enzymes*; Pecoraro, V. L., Ed.; VCH Publishers: New York, 1992; pp 141-175.

(190) Britt, R. D.; Peloquin, J. M.; Campbell, K. A. Pulsed and Parallel-Polarization EPR Characterization of the Photosystem II Oxygen-Evolving Complex. *Annu. Rev. Biophys. Biomol. Struct.* **2000,** *29*, 463-495.

(191) Peloquin, J. M.; Britt, R. D. EPR/ENDOR Characterization of the Physical and Electronic Structure of the OEC Mn Cluster. *BBA-Bioenergetics* **2001,** *1503* (1-2), 96-111.

(192) Ferreira, K. N.; Iverson, T. M.; Maghlaoui, K.; Barber, J.; Iwata, S. Architecture of the Photosynthetic Oxygen-Evolving Center. *Science* **2004,** *303* (5665), 1831-1838.

(193) Barber, J. Crystal Structure of the Oxygen-Evolving Complex of Photosystem II. *Inorg. Chem.* **2008,** *47* (6), 1700-1710.

(194) Yano, J.; Kern, J.; Sauer, K.; Latimer, M. J.; Pushkar, Y.; Biesiadka, J.; Loll, B.; Saenger, W.; Messinger, J.; Zouni, A. Where Water is Oxidized to Dioxygen: Structure of the Photosynthetic Mn4Ca Cluster. *Science* **2006,** *314* (5800), 821-825.

(195) Cox, N.; Pantazis, D. A.; Neese, F.; Lubitz, W. Biological Water Oxidation. *Acc. Chem. Res.* **2013,** *46* (7), 1588-1596.

(196) Dismukes, G. C.; Siderer, Y. Intermediates of a Polynuclear Manganese Center Involved in Photosynthetic Oxidation of Water. *Proc. Natl. Acad. Sci. U. S. A.* **1981,** *78* (1), 274-278.

(197) Britt, R. D.; Oyala, P. H. One Step Closer to O_2. *Science* **2014,** *345* (6198), 736-736.

(198) Hoganson, C. W.; Babcock, G. T. A Metalloradical Mechanism for the Generation of Oxygen from Water in Photosynthesis. *Science* **1997,** *277* (5334), 1953-1956.

(199) Limburg, J.; Szalai, V. A.; Brudvig, G. W. A Mechanistic and Structural Model for the Formation and Reactivity of a Mn^{V}=O Species in Photosynthetic Water Oxidation. *J. Chem. Soc., Dalton Trans.* **1999,** (9), 1353-1362.

(200) Limburg, J.; Vrettos, J. S.; Liable-Sands, L. M.; Rheingold, A. L.; Crabtree, R. H.; Brudvig, G. W. A Functional Model for OO Bond Formation by the O_2-Evolving Complex in Photosystem II. *Science* **1999,** *283* (5407), 1524-1527.

(201) Siegbahn, P. E. Water Oxidation Mechanism in Photosystem II, Including Oxidations, Proton Release Pathways, O–O Bond Formation and O_2 Release. *BBA-Bioenergetics* **2013,** *1827* (8), 1003-1019.

(202) Siegbahn, P. E. M. Theoretical Studies of O−O Bond Formation in Photosystem II. *Inorg. Chem.* **2008,** *47* (6), 1779-1786.

(203) Oyala, P. H.; Stich, T. A.; Debus, R. J.; Britt, R. D. Ammonia Binds to the Dangler Manganese of the Photosystem II Oxygen-Evolving Complex. *J. Am. Chem. Soc.* **2015,** *137* (27), 8829-8837.

(204) Yano, J.; Yachandra, V. Mn_4Ca Cluster in Photosynthesis: Where and How Water is Oxidized to Dioxygen. *Chem. Rev.* **2014,** *114* (8), 4175-4205.

(205) Barber, J. Photosynthetic Energy Conversion: Natural and Artificial. *Chem. Soc. Rev.* **2009,** *38* (1), 185-196.

(206) Small portions of catalytic species are active when the species are very short-lived and hot, so that one catalytic pathway kinetically outcompetes other reaction paths; larger portions of active sites may exist when turnover is inefficient and slow.

(207) Artero, V.; Fontecave, M. Solar Fuels Generation and Molecular Systems: Is it Homogeneous or Heterogeneous Catalysis? *Chem. Soc. Rev.* **2013,** *42* (6), 2338-2356.

(208) Rossmeisl, J.; Qu, Z. W.; Zhu, H.; Kroes, G. J.; Nørskov, J. K. Electrolysis of Water on Oxide Surfaces. *J. Electroanal. Chem.* **2007,** *607* (1–2), 83-89.

(209) Man, I. C.; Su, H.-Y.; Calle-Vallejo, F.; Hansen, H. A.; Martínez, J. I.; Inoglu, N. G.; Kitchin, J.; Jaramillo, T. F.; Nørskov, J. K.; Rossmeisl, J. Universality in Oxygen Evolution Electrocatalysis on Oxide Surfaces. *ChemCatChem* **2011,** *3* (7), 1159-1165.

(210) Rossmeisl, J.; Logadottir, A.; Nørskov, J. K. Electrolysis of Water on (Oxidized) Metal Surfaces. *Chem. Phys.* **2005,** *319* (1), 178-184.

(211) Nørskov, J. K.; Bligaard, T.; Rossmeisl, J.; Christensen, C. H. Towards the Computational Design of Solid Catalysts. *Nature Chem.* **2009,** *1* (1), 37-46.

(212) Nørskov, J. K.; Rossmeisl, J.; Logadottir, A.; Lindqvist, L.; Kitchin, J. R.; Bligaard, T.; Jónsson, H. Origin of the Overpotential for Oxygen Reduction at a Fuel-Cell Cathode. *J. Phys. Chem. B* **2004,** *108* (46), 17886-17892.

(213) Viswanathan, V.; Hansen, H. A.; Nørskov, J. K. Selective Electrochemical Generation of Hydrogen Peroxide from Water Oxidation. *J. Phys. Chem. Lett.* **2015,** *6* (21), 4224-4228.

(214) Vojvodic, A.; Nørskov, J. K. Optimizing Perovskites for the Water-Splitting Reaction. *Science* **2011,** *334* (6061), 1355-1356.

(215) Fortunelli, A.; Goddard Iii, W. A.; Sementa, L.; Barcaro, G. Optimizing the Oxygen Evolution Reaction for Electrochemical Water Oxidation by Tuning Solvent Properties. *Nanoscale* **2015,** *7* (10), 4514-4521.

(216) Romain, S.; Vigara, L.; Llobet, A. Oxygen−Oxygen Bond Formation Pathways Promoted by Ruthenium Complexes. *Acc. Chem. Res.* **2009,** *42* (12), 1944-1953.

(217) Chronister, C. W.; Binstead, R. A.; Ni, J.; Meyer, T. J. Mechanism of Water Oxidation Catalyzed by the μ-Oxo Dimer $[(bpy)_2(OH_2)Ru^{III}ORu^{III}(OH_2)(bpy)_2]^{4+}$. *Inorg. Chem.* **1997,** *36* (18), 3814-3815.

(218) Gersten, S. W.; Samuels, G. J.; Meyer, T. J. Catalytic Oxidation of Water by an Oxo-Bridged Ruthenium Dimer. *J. Am. Chem. Soc.* **1982,** *104* (14), 4029-4030.

(219) Hurst, J. K.; Zhou, J.; Lei, Y. Pathways for Water Oxidation Catalyzed by the $[(bpy)_2Ru(OH_2)]_2O^{4+}$ ion. *Inorg. Chem.* **1992,** *31* (6), 1010-1017.

(220) Gilbert, J. A.; Eggleston, D. S.; Murphy, W. R.; Geselowitz, D. A.; Gersten, S. W.; Hodgson, D. J.; Meyer, T. J. Structure and Redox Properties of the Water-Oxidation Catalyst $[(bpy)_2(OH_2)RuORu(OH_2)(bpy)_2]^{4+}$. *J. Am. Chem. Soc.* **1985,** *107* (13), 3855-3864.

(221) Liu, F.; Concepcion, J. J.; Jurss, J. W.; Cardolaccia, T.; Templeton, J. L.; Meyer, T. J. Mechanisms of Water Oxidation from the Blue Dimer to Photosystem II. *Inorg. Chem.* **2008,** *47* (6), 1727-1752.

(222) Betley, T. A.; Wu, Q.; Van Voorhis, T.; Nocera, D. G. Electronic Design Criteria for O−O Bond Formation via Metal−Oxo Complexes. *Inorg. Chem.* **2008,** *47* (6), 1849-1861.

(223) Sherman, D. M. The Electronic Structures of Manganese Oxide Minerals *Am. Mineral.* **1984,** *69*, 788-799.

(224) Gorlin, Y.; Nordlund, D.; Jaramillo, T. F. The Role of Heat Treatment in Enhanced Activity of Manganese Oxides for the Oxygen Reduction and Evolution Reactions. *ECS Trans.* **2013,** *58* (1), 735-750.

(225) Najafpour, M. M.; Renger, G.; Hołyńska, M.; Moghaddam, A. N.; Aro, E.-M.; Carpentier, R.; Nishihara, H.; Eaton-Rye, J. J.; Shen, J.-R.; Allakhverdiev, S. I. Manganese Compounds as Water-Oxidizing Catalysts: From the Natural Water-Oxidizing Complex to Nanosized Manganese Oxide Structures. *Chem. Rev.* **2016,** *116* (5), 2886-2936.

(226) Morita, M.; Iwakura, C.; Tamura, H. The Anodic Characteristics of Massive Manganese Oxide Electrode. *Electrochim. Acta* **1979,** *24* (4), 357-362.

(227) Najafpour, M. M.; Kompany-Zareh, M.; Zahraei, A.; Jafarian Sedigh, D.; Jaccard, H.; Khoshkam, M.; Britt, R. D.; Casey, W. H. Mechanism, Decomposition Pathway and New Evidence for Self-Healing of Manganese Oxides as Efficient Water Oxidizing Catalysts: New Insights. *Dalton Trans.* **2013,** *42* (40), 14603-14611.

(228) Mattioli, G.; Zaharieva, I.; Dau, H.; Guidoni, L. Atomistic Texture of Amorphous Manganese Oxides for Electrochemical Water Splitting Revealed by Ab Initio Calculations Combined with X-ray Spectroscopy. *J. Am. Chem. Soc.* **2015,** *137* (32), 10254-10267.

(229) Huynh, M.; Shi, C.; Billinge, S. J. L.; Nocera, D. G. Nature of Activated Manganese Oxide for Oxygen Evolution. *J. Am. Chem. Soc.* **2015,** *137* (47), 14887-14904.

(230) Huynh, M.; Bediako, D. K.; Nocera, D. G. A Functionally Stable Manganese Oxide Oxygen Evolution Catalyst in Acid. *J. Am. Chem. Soc.* **2014,** *136* (16), 6002-6010.

(231) Indra, A.; Menezes, P. W.; Sahraie, N. R.; Bergmann, A.; Das, C.; Tallarida, M.; Schmeißer, D.; Strasser, P.; Driess, M. Unification of Catalytic Water Oxidation and Oxygen Reduction Reactions: Amorphous Beat Crystalline Cobalt Iron Oxides. *J. Am. Chem. Soc.* **2014,** *136* (50), 17530-17536.

(232) Smith, W. L.; Hobson, A. D. The Structure of Cobalt Oxide, Co_3O_4. *Acta Cryst. B* **1973,** *29* (2), 362-363.

(233) Wang, L.-P.; Van Voorhis, T. Direct-Coupling O_2 Bond Forming a Pathway in Cobalt Oxide Water Oxidation Catalysts. *J. Phys. Chem. Lett.* **2011,** *2* (17), 2200-2204.

(234) Crandell, D. W.; Ghosh, S.; Berlinguette, C. P.; Baik, M. H. How a $[Co^{IV}=O]^{2+}$ Fragment Oxidizes Water: Involvement of a Biradicaloid $[CoII–(\cdot O\cdot)]^{2+}$ Species in Forming the O–O Bond. *ChemSusChem* **2015,** *8* (5), 844-852.

(235) Li, X.; Siegbahn, P. E. Water Oxidation Mechanism for Synthetic Co-Oxides with Small Nuclearity. *J. Am. Chem. Soc.* **2013,** *135* (37), 13804-13813.

(236) Smith, P. F.; Hunt, L.; Laursen, A. B.; Sagar, V.; Kaushik, S.; Calvinho, K. U. D.; Marotta, G.; Mosconi, E.; De Angelis, F.; Dismukes, G. C. Water Oxidation by the $[Co_4O_4(OAc)_4(py)_4]^+$ Cubium is Initiated by OH^- Addition. *J. Am. Chem. Soc.* **2015,** *137* (49), 15460-15468.

(237) Ullman, A. M.; Liu, Y.; Huynh, M.; Bediako, D. K.; Wang, H.; Anderson, B. L.; Powers, D. C.; Breen, J. J.; Abruña, H. D.; Nocera, D. G. Water Oxidation Catalysis by Co(II) Impurities in $Co(III)_4O_4$ Cubanes. *J. Am. Chem. Soc.* **2014,** *136* (50), 17681-17688.

(238) Nguyen, A. I.; Ziegler, M. S.; Oña-Burgos, P.; Sturzbecher-Hohne, M.; Kim, W.; Bellone, D. E.; Tilley, T. D. Mechanistic Investigations of Water Oxidation by a Molecular Cobalt Oxide Analogue: Evidence for a Highly Oxidized Intermediate and Exclusive Terminal Oxo Participation. *J. Am. Chem. Soc.* **2015,** *137* (40), 12865-12872.

(239) Kanan, M. W.; Yano, J.; Surendranath, Y.; Dinca, M.; Yachandra, V. K.; Nocera, D. G. Structure and Valency of a Cobalt−Phosphate Water Oxidation Catalyst Determined by In Situ X-Ray Spectroscopy. *J. Am. Chem. Soc.* **2010,** *132* (39), 13692-13701.

(240) Harley, S. J.; Mason, H. E.; McAlpin, J. G.; Britt, R. D.; Casey, W. H. A (31) P NMR Investigation of the CoPi Water-Oxidation Catalyst. *Chemistry* **2012,** *18* (34), 10476-10479.

(241) Zhang, M.; de Respinis, M.; Frei, H. Time-Resolved Observations of Water Oxidation Intermediates on a Cobalt Oxide Nanoparticle Catalyst. *Nature Chem.* **2014,** *6* (4), 362-367.

(242) Ahn, H. S.; Bard, A. J. Surface Interrogation of CoP(i) Water Oxidation Catalyst by Scanning Electrochemical Microscopy. *J. Am. Chem. Soc.* **2015,** *137* (2), 612-615.

(243) Bockris, J. O.; Otagawa, T. Mechanism of Oxygen Evolution on Perovskites. *J. Phys. Chem.* **1983,** *87* (15), 2960-2971.

(244) May, K. J.; Carlton, C. E.; Stoerzinger, K. A.; Risch, M.; Suntivich, J.; Lee, Y.-L.; Grimaud, A.; Shao-Horn, Y. Influence of Oxygen Evolution during Water Oxidation on the Surface of Perovskite Oxide Catalysts. *J. Phys. Chem. Lett.* **2012,** *3* (22), 3264-3270.

(245) Risch, M.; Grimaud, A.; May, K. J.; Stoerzinger, K. A.; Chen, T. J.; Mansour, A. N.; Shao-Horn, Y. Structural Changes of Cobalt-Based Perovskites upon Water Oxidation Investigated by EXAFS. *J. Phys. Chem. C* **2013,** *117* (17), 8628-8635.

(246) Kim, H.; Park, J.; Park, I.; Jin, K.; Jerng, S. E.; Kim, S. H.; Nam, K. T.; Kang, K. Coordination Tuning of Cobalt Phosphates towards Efficient Water Oxidation Catalyst. *Nat. Commun.* **2015,** *6*.

(247) Mefford, J. T.; Rong, X.; Abakumov, A. M.; Hardin, W. G.; Dai, S.; Kolpak, A. M.; Johnston, K. P.; Stevenson, K. J. Water Electrolysis on $La_{1-x}Sr_xCoO_{3-\delta}$ Perovskite Electrocatalysts. *Nat. Commun.* **2016,** *7*, 11053.

(248) Friebel, D.; Louie, M. W.; Bajdich, M.; Sanwald, K. E.; Cai, Y.; Wise, A. M.; Cheng, M.-J.; Sokaras, D.; Weng, T.-C.; Alonso-Mori, R.et al. Identification of Highly Active Fe Sites in (Ni,Fe)OOH for Electrocatalytic Water Splitting. *J. Am. Chem. Soc.* **2015,** *137* (3), 1305-1313.

(249) Chen, J. Y. C.; Dang, L.; Liang, H.; Bi, W.; Gerken, J. B.; Jin, S.; Alp, E. E.; Stahl, S. S. Operando Analysis of NiFe and Fe Oxyhydroxide Electrocatalysts for Water Oxidation: Detection of Fe^{4+} by Mössbauer Spectroscopy. *J. Am. Chem. Soc.* **2015,** *137* (48), 15090-15093.

(250) Ahn, H. S.; Bard, A. J. Surface Interrogation Scanning Electrochemical Microscopy of $Ni_{1-x}Fe_xOOH$ ($0 < x < 0.27$) Oxygen Evolving Catalyst: Kinetics of the "fast" Iron Sites. *J. Am. Chem. Soc.* **2015,** *138* (1), 313-318.

(251) Arroyo-Currás, N.; Bard, A. J. Iridium Oxidation as Observed by Surface Interrogation Scanning Electrochemical Microscopy. *J. Phys. Chem. C* **2015,** *119* (15), 8147-8154.

(252) Greenwood, N. N.; Earnshaw, A. *Chemistry of the Elements*, 1984, p. 368.

(253) Hunter, B. M.; Hieringer, W.; Winkler, J. R.; Gray, H. B.; Müller, A. M. Effect of Interlayer Anions on [NiFe]-LDH Nanosheet Water Oxidation Activity. *Energy Environ. Sci.* **2016,** *9* (5), 1734-1743.

(254) Winkler, J. R.; Gray, H. B. Electronic Structures of Oxo-Metal Ions. *Struct. Bond.* **2012,** *142*, 17-28.

2 HIGHLY ACTIVE MIXED-METAL NANOSHEET WATER OXIDATION CATALYSTS MADE BY PULSED-LASER ABLATION IN LIQUIDS (PLAL)

Adapted with permission from Hunter, B. M.; Blakemore, J. D.; Deimund, M.; Gray, H. B.; Winkler, J. R.; Müller, A. M. Highly Active Mixed-Metal Nanosheet Water Oxidation Catalysts Made by Pulsed-Laser Ablation in Liquids. *Journal of the American Chemical Society* **2014**, *136*, 13118. DOI: 10.1021/ja506087h.

2.1. Summary

Surfactant-free mixed-metal hydroxide water oxidation nanocatalysts were synthesized by pulsed-laser ablation in liquids. In a series of [Ni-Fe]-layered double hydroxides with intercalated nitrate and water, $[Ni_{1-x}Fe_x(OH)_2](NO_3)_y(OH)_{x-y}\bullet nH_2O$, higher activity was observed as the amount of Fe decreased to 22%. Addition of Ti^{4+} and La^{3+} ions further enhanced electrocatalysis, with a lowest overpotential of 260 mV at 10 mA cm^{-2}. Electrocatalytic water oxidation activity increased with the relative proportion of a 405.1 eV N 1s (XPS binding energy) species in the nanosheets.

2.2. Catalysts Made by Pulsed Laser Ablation in Liquids

Conversion of solar energy into storable fuels in a sustainable way will be essential to meet future global energy demands. Worldwide scalability requires materials to be made from earth-abundant elements. Splitting water into oxygen and hydrogen with only sunlight as energy input is seen as a particularly attractive route.[1] But such systems for the production of solar fuels will require robust, highly active catalysts.[2-4]

Most widely used water oxidation catalysts are based on rare metals such as Ru and Ir.[5,6] First-row transition metal oxides and hydroxides continue to attract attention because of their low cost and stability in base.[7-14] The overpotentials of earth-abundant catalysts at 10

mA cm^{-2} typically range from 350 to 430 mV in pH 14 aqueous electrolytes.[15,16] In recent work, Yan showed that hollow spheres of α-$Ni(OH)_2$ catalyzed water oxidation in base with an overpotential of 331 mV at 10 mA cm^{-2} on glassy carbon working electrodes.[17]

Here we report surfactant-free, highly active $[Ni_{1-x}Fe_x(OH)_2](NO_3)_y(OH)_{x-y}\bullet nH_2O$ nanosheet water oxidation catalysts with admixed ions. Our best catalyst had an overpotential of 260 mV at 10 mA cm^{-2} on flat highly-ordered pyrolytic graphite working electrodes. We attribute the higher activity to unique morphological and structural properties, which were synthetically accessible by the use of pulsed-laser ablation in liquids (PLAL). In PLAL, nanoparticles are formed by very rapid cooling of a plasma comprised of elements from the solid ablation target and the surrounding liquid. This condensation process, which is kinetically controlled, produces predominantly crystalline nanomaterials.[18] PLAL offers size and composition control through a wide range of tunable experimental parameters.[19]

With PLAL, mixed-metal nanomaterials with tailored compositions can be prepared readily by adding metal ions into the aqueous ablation liquid. We intentionally incorporated different amounts of Fe into our α-$Ni(OH)_2$ nanocatalysts, as variable concentrations of Fe in electrodeposited nickel (oxy)hydroxides have been shown to improve electrocatalytic activity.[20-25] We also added Ti^{4+} and La^{3+} ions to the ablation liquid and screened the resulting materials for water oxidation activity.

Eight mixed-metal catalysts were synthesized using PLAL by varying ablation targets, metal ion type and concentrations, and laser pulse energies (see section 2.3 for experimental details, all ablation solutions contained nitrate). The nanomaterials were prepared with Fe concentrations ranging from 22 to 95% of the total metal content (Table 2.1). We identified their compositions spectroscopically; and, notably, they all exhibited high electrocatalytic oxygen-evolution activities in basic electrolytes.

Powder X-ray diffraction (XRD) measurements (2.4) indicate that the Fe-rich nanoparticles **1**-**3** are poorly crystalline; the Ni-rich nanoparticles **4**-**8** display diffraction patterns consistent with layered double hydroxide (LDH) structures. XRD data indicate minor contributions from Fe(O)OH;[26] **6** also contained the crystalline spinel $NiFe_2O_4$,[27] and Ti-based oxides were present in **7** and **8**. LDHs have the general formula

$[M_{1-x}M'_x(OH)_2](A^{m-})_{x/m}\bullet nH_2O$; the structures are comprised of sheets of $[M_{1-x}M'_x(OH)_2]^{x+}$ edge-shared octahedra. Cationic charges arising from M'^{3+} in the sheets are balanced by intercalated hydrated anions (A^{m-}).[28-30]

Table 2-1: Preparation conditions of catalysts **1** to **8** and concentrations of Fe with respect to total metal content.

Catalyst	Solid target	Added ions	Ion concentration (M)	Pulse energy (mJ)	Fe (% metal content)[a]
1	Ni	Fe	0.1	90	95
2	Ni	Fe	0.01	90	86
3	Fe	Ni	0.1	90	70
4	Fe	Ni	1.0	90	36
5	Fe	Ni	3.0	90	22
6	Fe	Ni	3.0	210	30
7	Fe	Ni Ti	3.0 0.015	210	23
8	Fe	Ni Ti La	3.0 0.015 0.023	210	29

[a] Determined by XPS.

X-ray photoelectron spectroscopy (XPS) was employed to obtain binding energies of Ni 2p and Fe 2p core levels in **1**-**8**; these energies are indicative of $Ni(OH)_2$ and (hydrous) iron oxides (2.4). In addition, Mössbauer[31,29] and x-ray absorption[32-34] spectroscopic data indicate that Fe is incorporated as Fe^{3+} in place of Ni^{2+} in [Ni-Fe]-LDHs. Two well-resolved N 1s peaks appear in the XP spectra of nanoparticles **4**-**8**, with binding energies of 407.3 and 405.1 eV. The higher binding-energy feature (407.3 eV) is assigned to nitrate.[35-40] The 2.2 eV reduction in N 1s binding energy for the second feature could arise from nitrate in an

unusual electronic environment, although a lower oxidation state (*e.g.*, NO_2, NO_2^-) cannot be ruled out. Infrared spectra are consistent with the presence of a second type of NO_x species (2.4). Infrared and Raman data (2.4) support the presence of intercalated nitrate anions in the LDH structure.[41] On the basis of these data, the predominant crystalline material in **4-8** can be assigned to the [Ni-Fe]-LDH $[Ni_{1-x}Fe_x(OH)_2](NO_3)_y(OH)_{x-y}\bullet nH_2O$ (Figure 2.1).

Nanoparticle sizes were obtained from transmission electron micrographs (TEM), and crystalline domain sizes were determined by Scherrer analysis of XRD data. Lateral sizes ranged from ~7 to 22 nm (Table 2-2). Catalysts **1** to **5** consisted of nanosheets, as expected for layered structures. Analysis of TEM and XRD data for **6** revealed that two types of nanoparticles were formed; smaller, more spherical (6.5 ± 0.8) nm particles are attributed to the spinel $NiFe_2O_4$, and larger (13 ± 1) nm sheets are assigned to the LDH $[Ni_{1-x}Fe_x(OH)_2](NO_3)_y(OH)_{x-y}\bullet nH_2O$. Also, differences in TEM contrast, shape, and size were found for **7** and **8**.[42] Specific surface areas of catalysts **5** to **8** determined by Brunauer-Emmett-Teller (BET) measurements are in agreement with particle sizes derived from TEM data. Catalysts **6** to **8**, which were synthesized at 210 mJ pulse energy, had similar BET surface areas (193±1 $m^2\ g^{-1}$), whereas **5**, prepared at 90 mJ/pulse, exhibited a slightly higher surface area (220 $m^2\ g^{-1}$).[43]

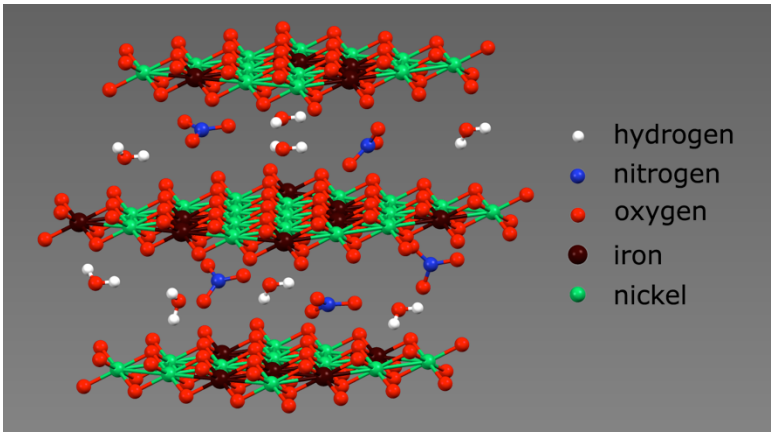

Figure 2.1. Schematic structural representation of the [Ni-Fe]-LDH, $[Ni_{1-x}Fe_x(OH)_2](NO_3)_y(OH)_{x-y}\bullet nH_2O$.

We assessed electrocatalytic oxygen-evolution activity in 1 M aqueous KOH.[44] Faradaic yields of oxygen evolution for **5**, **6** and **8** were all essentially 100%. Steady-state Tafel data were measured to obtain overpotentials; virtually identical mass loadings were used in all electrochemical experiments (all current densities are reported per geometric area). Importantly, chronoamperometry data showed that the catalytic activity of nanoparticles **5-8** was maintained for more than 5 hours (2.5).

The electrocatalytic activities of materials **1** to **5**, synthesized at virtually the same pulse energy, steadily increased with decreasing Fe content (Figure 2.16). Catalyst **5** (22% Fe relative to total metal content) performed best in the [Ni-Fe]-LDH materials, with an overpotential of 280 mV at 10 mA cm^{-2}. Incorporation of less than 22% Fe relative to total metal content was limited by the solubility of Ni nitrate in the aqueous ablation liquid. XRD data for **5**, collected before and after 30 min of anodic polarization, confirmed that the crystallinity of the [Ni-Fe]-LDH material was retained (Figure 2.8). The Fe content of our best performing catalyst is in agreement with Dai's report.[34] It differs, however, from findings for amorphous materials, which performed best with 40% Fe.[45]

We made catalyst **6** employing virtually the same precursor conditions as for **5**, but with a pulse energy of 210 instead of 90 mJ. We have shown before with cobalt oxide that pulse energy can be used to control particle size.[19] Varying pulse energy in the synthesis of more complex mixed-metal materials led to particles with different compositions (Figure 2.2). While **5** consisted mainly of crystalline [Ni-Fe]-LDH, **6** was mixed crystalline [Ni-Fe]-LDH/$NiFe_2O_4$. Catalyst **6** showed inferior activity for water oxidation relative to **5**, presumably because the active [Ni-Fe]-LDH was diluted by the spinel oxide. This finding suggests that crystalline $[Ni_{1-x}Fe_x(OH)_2](NO_3)_y(OH)_{x-y}\bullet nH_2O$ is the more active species in our materials for catalytic water oxidation. IR spectra of **5** and **6** are consistent with $[Ni_{1-x}Fe_x(OH)_2](NO_3)_y(OH)_{x-y}\bullet nH_2O$ with high interstitial water and nitrate content.[46-48] The positions of peaks in the IR spectrum of catalyst **5** indicated the incorporation of Fe into the α-$Ni(OH)_2$ lattice (2.3).[49]

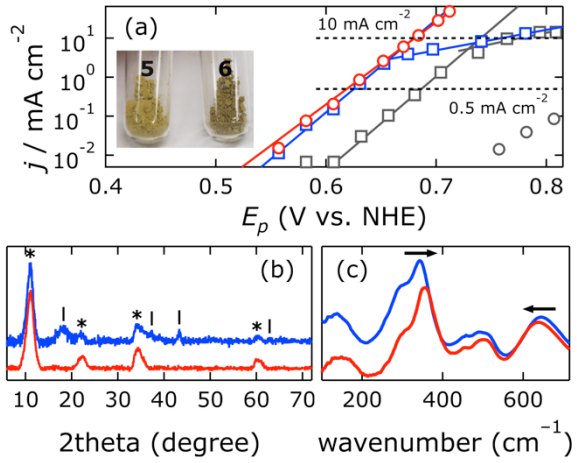

Figure 2.2. (a) Tafel plots of current density (j) as a function of electrode polarization potential (E_p) (red, **5**; blue, **6**; gray squares, Ni oxide electrodeposited according to ref. 50; gray circles, bare electrode), and a photograph of **5** and **6**; (b) XRD data: * $[Ni_{1-x}Fe_x(OH)_2](NO_3)_y(OH)_{x-y}\bullet nH_2O$, | $NiFe_2O_4$ spinel; (c) IR spectra (red, **5**; blue, **6**).

The precise nature of the electrocatalytically active species in Fe–Ni–O catalysts has been much discussed.[51,52,45,53] In work on crystalline Fe–Ni–O thin films, Boettcher suggested (Fe,Ni)(O)OH was the catalytically active phase.[24,25] Whereas Dai found that crystalline α-(Fe,Ni)$(OH)_2$ had highest activity with an Fe:Ni ratio of 5:1,[34,54] Hu demonstrated higher intrinsic activity of exfoliated LDHs with a nominal Fe:Ni ratio of 1:3.[55] In other work of note, O'Hare demonstrated that NiTi layered double hydroxide nanosheets were effective visible-light-driven water oxidation photocatalysts with $AgNO_3$ as sacrificial electron acceptor.[56]

We found that addition of Lewis-acidic Ti^{4+} and La^{3+} ions to the ablation liquid improved catalytic activity relative to our most active [Fe-Ni]-LDH catalyst (**5**). We synthesized catalysts **7** and **8** using virtually the same precursor conditions as for **5**, but with Ti^{4+} (**7**) or Ti^{4+} and La^{3+} (**8**) added to the ablation solution (Table 2-1). XRD data revealed that both catalysts were primarily [Ni-Fe]-LDH materials (2.4). Oxides containing added elements were also present; TiO_2 and Fe_2TiO_4 were found in **7**, whereas crystalline Ni_3TiO_5 and $La(Ni,Fe)O_3$ were detected in **8**. The spinel oxide $NiFe_2O_4$ was absent from both **7** and **8**. XPS data showed that **8** contained 1% La relative to total metal content. Both catalysts

were more active than LDHs **5** and **6**, with **7** and **8** exhibiting the lowest overpotentials at 10 mA cm^{-2} of 270 and 260 mV, respectively (2.5).

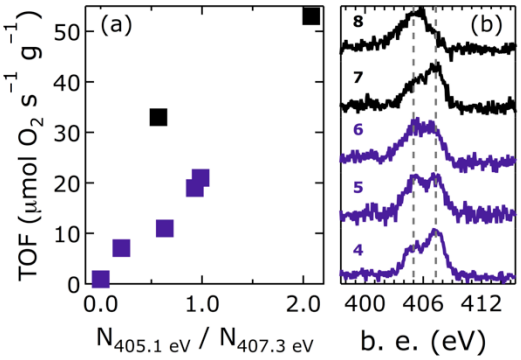

Figure 2.3. (a) TOF vs. $N_{405.1\ eV}/N_{407.3\ eV}$ (purple, neat Fe–Ni-based catalysts; black, **7** and **8**); (b) XPS data of catalysts **4** to **8** (the gray dashed lines mark the N 1s binding energies (405.1 and 407.3 eV)).

Highly active, surfactant-free, mixed transition metal hydroxide water oxidation nanoparticle catalysts can be made by PLAL. We spectroscopically identified a crystalline [Ni-Fe]-LDH as the catalytically most active material. We discovered that turnover frequency (TOF) correlated with the ratio of two nitrogen species detected by XPS in the as-synthesized catalysts (Figure 2.3). Addition of Ti^{4+} and La^{3+} ions further enhanced activity (reaching 10 mA cm^{-2} at an overpotential of 260 mV). On a flat electrode, this is the lowest overpotential reported to date for mixed metal oxide catalysts.

2.3. General Experimental Conditions and Apparatus

2.3.1. Materials and Methods. Nanomaterial synthesis by pulsed laser ablation in liquids was performed in the Beckman Institute Laser Resource Center at California Institute of Technology. X-ray photoelectron spectroscopy was carried out at the Molecular Materials Research Center (Beckman Institute at California Institute of Technology). Transmission

electron micrographs were collected at the Beckman Resource Center for Transmission Electron Microscopy (California Institute of Technology).

All chemicals were used as received. Deionized water was obtained from a Barnstead Diamond Nanopure system and had a resistivity of ≥16 MΩ cm^{-1}.

2.3.2. Synthesis. Mixed metal nanomaterials were synthesized using the method of pulsed laser ablation in liquids (PLAL). Suspensions of iron (Alfa, −200 mesh, 99+%) or nickel (Alfa, −150+200 mesh, 99.8%) powders were stirred in 10 mL aqueous metal nitrate solutions using a magnetic stirrer in a 30 mL glass beaker at room temperature in ambient air. For ablation, 0.5 g iron powder or 2.0 g nickel powder were used. With iron as ablation target, the liquid consisted of 10 mL pH 10.0 water (adjusted with potassium hydroxide, Mallinckrodt) with nickel nitrate ($Ni(NO_3)_2 \cdot 6H_2O$, Alfa, 98%) concentrations of 0.1 M, 1.0 M, and 3.0 M. With nickel as ablation target, the liquid was 10 mL water with iron nitrate ($Fe(NO_3)_3 \cdot 9H_2O$, Alfa, 98.0–101.0%) concentrations of 0.01 M and 0.1 M. Nanomaterials with more than two metals were made from 0.5 g iron powder suspended in 10 mL of a solution of 3.0 M nickel nitrate and 0.015 M titanium(IV) oxide bis(acetylacetonate) (Strem, >95%) in 10 mL pH 10.0 water (adjusted with KOH). Some solutions also contained 0.023 M lanthanum nitrate ($La(NO_3)_3 \cdot 6H_2O$, Sigma-Aldrich, ≥99%). Beakers and stir bars were thoroughly cleaned with *aqua regia* before use.

A 355 nm, 8 ns pulse laser beam, provided by the third harmonic of a 10 Hz Q-switched Nd:YAG laser (Spectra-Physics Quanta-Ray PRO-Series), was focused 0.5 mm below the surface of the liquid with a 100 mm focal length plano-convex quartz lens. Each sample was irradiated for 60 min. Laser pulse energies were either 90 or 210 mJ/pulse.

After synthesis, nanoparticle suspensions were separated from the metallic ablation targets using a strong magnet. Solid nanoparticulate powders were obtained by centrifugation and washing with water until the supernatant did not show any metal nitrate absorption. The nanoparticles were then washed twice with acetone (EMD, OmniSolv®) and dried under vacuum. A high precision balance (Sartorius CPA225D) was used to weigh the nanoparticle powders. Around 5 mg material were suspended in water to make 2 mg

mL^{-1} suspensions; 20 μL of these were drop cast on freshly-cleaved highly-ordered pyrolytic graphite (HOPG) working electrodes and dried in ambient air under a heat lamp at 50°C, resulting in a catalyst loading of 40 μg.

Electrodeposited nickel oxide catalyst was prepared according to established procedure. In detail, we dissolved 2.18 g $Ni(NO_3)_2 \cdot 6H_2O$ in 5 mL water and added this solution to 75 mL rapidly stirred 0.1 M pH 9.20 aqueous sodium borate buffer, which immediately became turbid. The sodium borate buffer was made from sodium tetraborate ($Na_2B_4O_7 \cdot 10H_2O$, Baker, 101.4%) and its pH was adjusted by adding boric acid (H_3BO_3, Mallinckrodt, 99.9%). The filtrate of the suspension was used as the electrolyte; the working electrode was a freshly cleaved HOPG electrode. An Ag/AgCl/3.0 M NaCl reference electrode (Bioanalytical Systems, Inc.; measured to be +0.212 V vs NHE) and a Ni gauze (Alfa) counter electrode were used. We passed 51 mC charge with an applied voltage of 1.312 V vs. NHE; faradaically, we deposited 530 nmol Ni, which corresponds to 40 μg NiO. Before catalytic activity testing the electrodeposited films were thoroughly washed with water.

2.3.3. Physical Characterization. X-ray photoelectron spectra (XPS) were taken using a Surface Science Instruments M-probe surface spectrometer. Monochromatic Al Kα radiation (1486.6 eV) was used to excite electrons from the samples, which had been drop-cast on clean Cu foil and dried in ambient air at room temperature. The sample chamber was maintained at $<5\times10^{-9}$ Torr. Survey scans from 0 to 1000 eV were carried out to identify the elements present in the nanoparticles. Binding energies were referenced to the C 1s peak arising from adventitious carbon, taken to have a binding energy of 284.8 eV. High-resolution spectra were collected for the Fe 2p, Ni 2p, Ti 2p, La 3d, N 1s, and O 1s regions. Quantitative peak areas were derived after Shirley background subtraction and using relative sensitivity factors. Binding energies were obtained from the same peak fits. Quantitative XPS analysis was performed with CasaXPS (Version 2.3.16 PR 1.6).

X-ray diffraction (XRD) data were collected with a Bruker D2 PHASER diffractometer. Monochromatic Cu Kα radiation (1.5418 Å; tube power 30 kV, 10 mA) was

used; the instrument was equipped with 0.1° divergence, 1.5° Soller, and 0.6 mm detector slits, and had a 3-mm secondary anti-scatter screen. Diffracted radiation was collected with a Lynxeye detector. The instrument resolution was 0.05° in 2θ, and the counting time was 3 seconds per step, resulting in a total scan time of about 75 min for each sample. Solid samples were deposited with vaseline (X-Alliance GmbH) on a zero-diffraction silicon plate (MTI Corporation). XRD background subtraction, Scherrer and pattern analysis were performed with the Bruker DIFFRAC.SUITE software coupled to the International Centre for Diffraction Data powder diffraction file database (ICDD, PDF-2 Release 2012).

Raman spectra of neat solid catalysts were collected at room temperature in ambient air with a Renishaw M1000 micro-Raman spectrometer. A 50× magnification objective and a 50-μm slit, resulting in 4 cm^{-1} resolution, were used. The laser excitation wavelength was 514.3 nm (Cobolt Fandango™ 100 laser), the power at the sample was 213 μW (1% laser power, measured with a Thorlabs PM100USB power meter), and depolarized scattered light was detected. The excitation intensity was chosen as to prevent radiation damage of the nanoparticulate powders; collected spectra did not change during repeated scans. The radiation damage threshold was approximated to be at a laser intensity that was three times higher than that applied. Application of 10% laser power through a 50× magnification objective led to immediate radiation damage, and a dark spot was visible on the sample when viewed through the microscope. Focusing the 10% power laser beam through a 20× magnification objective led to gradual sample degradation over multiple scans, which was also observed by visual inspection with the microscope. The instrument's autofocus function was used to maximize the signal-to-noise ratio. The accumulation time was 10 s, and 8 scans were averaged for each sample. The measured Raman shifts were calibrated against a Si standard. Spectra were compared to reference spectra from the RRUFF database, which were collected with 532 nm excitation and depolarized detection.

Attenuated total reflectance infrared spectra of neat nanoparticulate powders were collected with a Thermo Nicolet iS50 FT-IR spectrometer, equipped with a Pike Technologies GladiATR accessory plate and an uncooled pyroelectric deuterated triglycine sulfate (DTGS) detector. In the 50 to 700 cm^{-1} range, a far-infrared multilayer beamsplitter

was used and a measured water vapor spectrum was subtracted from the data; in the 400 to 4000 cm^{-1} range, a KBr beamsplitter was used. Spectra of the solid nanoparticulate powders were collected at room temperature in ambient air, and 132 scans were averaged for each sample.

Transmission electron microscopy (TEM) measurements were performed with an FEI Tecnai T-12. For each material, 2 μL of a suspension of 2 mg mL^{-1} nanoparticles in water were drop cast on a 200 mesh Cu grid coated with Formvar carbon (Ted Pella), which was placed on a Kimwipe. The nanoparticles were dispersed on the hydrophobic grid surface by adding 10 μL isopropanol. The average diameter of the nanoparticles was determined using the ImageJ software.

Specific surface areas were determined by Brunauer-Emmett-Teller (BET) measurements, using a Quantachrome Autosorb iQ instrument. Adventitious adsorbates were removed under vacuum by heating approximately 40 mg of each catalyst powder at a rate of 10 K min^{-1} from room temperature to 423 K, holding it there for 1 hour, followed by heating to 573 K at a rate of 10 K min^{-1}, where it remained for 6 hours, and subsequent cooling to room temperature. Virtually identical sizes of catalysts before and after heating for BET analysis were found by TEM imaging. Multipoint argon adsorption-desorption isotherms were collected at 87.45 K, and the specific surface areas were calculated with the instrument's built-in software, based on the BET equation.

2.3.4. Electrochemical Characterization. Cyclic voltammetry, Tafel, and chronoamperometry data were collected at room temperature. For all electrochemical measurements, the electrolyte was aqueous 1.0 M pH 14.0 KOH (Mallinckrodt); an Hg/HgO reference electrode (CH Instruments), a Ni gauze (Alfa) counter electrode, and HOPG working electrodes with 40 μg catalyst on them were used. Working electrodes for cyclic voltammetry, faradaic oxygen yield, and chronoamperometry data consisted of upward-facing HOPG (GraphiteStore, surface area: 0.09 cm^2) electrodes. Working electrodes were cleaned by sonication for 10 min in concentrated hydrochloric acid, washed with water, and their surfaces were polished using 400 and 600 grit sandpaper, after which the graphite was cleaved with adhesive tape to obtain a fresh HOPG surface for each catalyst.

Cyclic voltammograms were measured at 10 mV s^{-1} scan rate with a Gamry Reference 600 potentiostat. Tafel data were recorded using a rotating disk electrode (RDE) apparatus. Measurements were carried out in a 100 mL three-neck round-bottom flask with a Pine MSR variable speed rotator used at 1,500 rpm and a Princeton Applied Research Parstat 4000 potentiostat. The dwell time at each applied potential point was 5 min to reach steady-state conditions. The disk electrode was made of HOPG with stabilizing epoxy around its side (surface area: 0.13 cm^2). The current density *versus* potential data were post-measurement corrected for uncompensated resistance losses (see below). All potentials reported here are relative to the normal hydrogen electrode (NHE), and current densities are per geometric area.

The ohmic drop (uncompensated resistance, R_u) was experimentally determined for an HOPG working electrode, either blank or with 40 μg nanoparticulate catalyst loading, using a Gamry Reference 600 potentiostat and its built-in "measure R_u" utility that uses the current interrupt method. The working electrode was swept between 0.107 and 0.907 V vs. NHE and R_u values were collected. The averages of 3 R_u values were plotted as a function of applied potential, and the data were fit with a line (Figure 2.4).

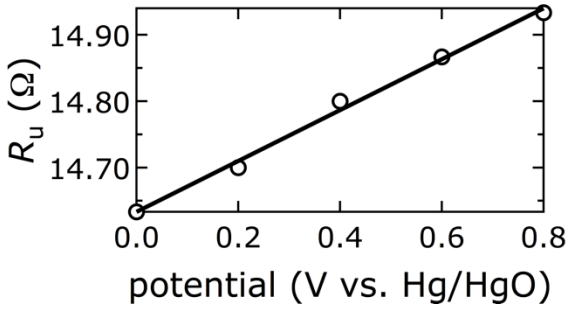

Figure 2.4. Determination of R_u for post-measurement iR drop correction; circles, measured data; line, linear fit.

Manual post-measurement iR drop correction was performed, because automatic iR-correction is inherently problematic for high-surface-area materials. In detail, the true

polarization potential E_p was calculated from the applied potential E_a, the measured current i, and the uncompensated resistance R_u as $E_p = E_a - iR_u$.

Faradaic yields of oxygen evolution data were collected with a gas-tight electrochemical cell. A glass cell was filled with 65 mL electrolyte, leaving 59 mL headspace, in which the O_2 concentration was measured. A potential of 0.857 V vs. NHE was applied for 30 min, using a Gamry 600 potentiostat. The electrolysis chamber was water-jacketed and kept at a constant temperature of (22.0±0.5)°C to ensure a stable response from the O_2 sensor. In a typical experiment, based on the charge transferred, we expected 284 µL of O_2 evolved and detected 297 µL. This confirmed essentially 100 % oxygen evolution within the error (10%) of our method.

Long-term stability measurements were performed using a Gamry 600 potentiostat and a working electrode, onto which 40 µg catalyst had been drop cast from a 2 mg mL^{-1} suspension that also contained 80 µg mL^{-1} Nafion 117 (Aldrich). Nafion was added for chronoamperometry experiments to improve the mechanical stability of catalyst films on HOPG during oxygen evolution. A potential of 0.654 V vs. NHE was applied for 5.5 hours and the current was recorded.

Data analysis and graphing was performed with Igor Pro 6.34 (Wavemetrics).

2.4. Physical Characterization

2.4.1. X-Ray Photoelectron Spectra. XPS data were collected to identify nanoparticle compositions by peak integrations of high-resolution spectra of the Fe 2p, Ni 2p, O 1s, N 1s, Ti 2p, and La 3d regions, where applicable. The regions were chosen as to collect data on transitions with the highest x-ray ionization cross-sections. Since the x-ray ionization cross-section of Ti 2p is a factor of 5.4 lower than that of La 3d, and 1.5 times less Ti^{4+} than La^{3+} was added to the ablation liquid, no Ti photoelectrons were detected. We deliberately did not attempt to quantify oxygen content from XPS data because the

amount of this element is regularly overestimated; oxygen also occurs in other sources, such as adventitious carbon species and oxides of the underlying copper substrate.

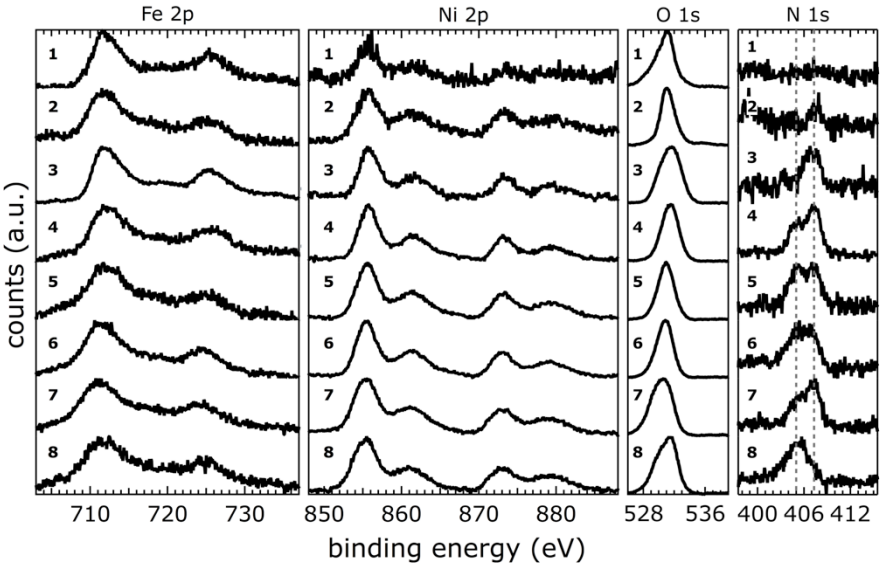

Figure 2.5. XPS data of catalysts **1** to **8** in the Fe 2p, Ni 2p, O 1s, and N 1s regions. The gray dashed lines are at the N 1s binding energies at 405.1 and 407.3 eV.

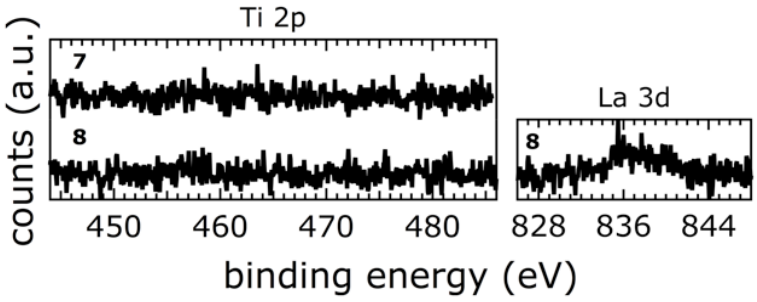

Figure 2.6. XPS data of catalysts **7** and **8** in the Ti 2p and La 3d regions.

The Fe 2p core level spectra of catalysts **1** to **8** showed peaks consistent with iron oxides and oxyhydroxides,[57] with Fe $2p_{3/2}$ binding energies close to 710.9 eV. It is not

possible to distinguish the different Fe phases in our materials from Fe 2p XPS data, as various iron oxides and oxyhydroxides, such as FeO, Fe_2O_3, Fe_3O_4, and Fe(O)OH, have similar Fe core-level binding energies and spectral shapes.[57] The Ni 2p core-level binding energies of catalysts **1** to **8** were indicative of $Ni(OH)_2$ or Ni(O)OH,[58,59] with Ni $2p_{3/2}$ binding energies close to 855.7 eV. The O 1s spectra of **1** to **8** exhibited, among contributions from adventitious oxygen species, two peaks centered around 528.8 eV and 531.4 eV, as expected for Fe or Ni oxide and hydroxide species, respectively.[58] The N 1s core level spectra of catalysts **1** to **8** showed two peaks with binding energies at 407.3 eV and 405.1 eV.

2.4.2. X-Ray Diffraction Data. XRD data were collected to determine crystalline phases and crystallite sizes by Scherrer analysis. Note that peak widths were determined by factoring in multiple diffraction lines from the corresponding PDF, where applicable. Overlapping diffraction lines may give rise to peaks that appear broader in the total intensity spectra. As a result, peak broadness in the total intensity spectrum does not necessarily correlate to the actual crystalline domain size. The XRD data were fit by the automatic search/match function of the Bruker software DIFFRAC.SUITE, using a database based on macroscopic crystals. Peak positions were in agreement with known XRD patterns as follows. The Fe-rich catalysts were amorphous, **1** and **3** completely so, and **2** predominantly so, with some broad peaks that were assigned to poorly crystallized Fe_3O_4 (powder diffraction file (PDF) # 00-019-0629) and γ-Fe_2O_3 (PDF 00-039-1346). XRD data of the more Ni-rich catalysts **4** to **8** showed mainly the crystalline layered double hydroxide (LDH) $[Ni_{1-x}Fe_x(OH)_2](NO_3)_y(OH)_{x-y}\bullet nH_2O$ (PDF 00-038-0715, α-(Fe,Ni)$(OH)_2$) and a minor contribution from crystalline Fe(O)OH (PDF 00-029-0713). We could not observe any *β*-$Ni(OH)_2$ (PDF 00-014-0117) in our catalysts. Catalyst **6** additionally contained crystalline $NiFe_2O_4$ (PDF 01-076-6119). In **7** and **8**, minerals containing added elements were also present; TiO_2 (PDF 01-082-1123) and Fe_2TiO_4 (PDF 00-034-0177) were detected in **7**, whereas crystalline Ni_3TiO_5 (PDF 00-030-0865) and La(Ni,Fe)O_3 (PDF 01-088-0637) were found in **8**.

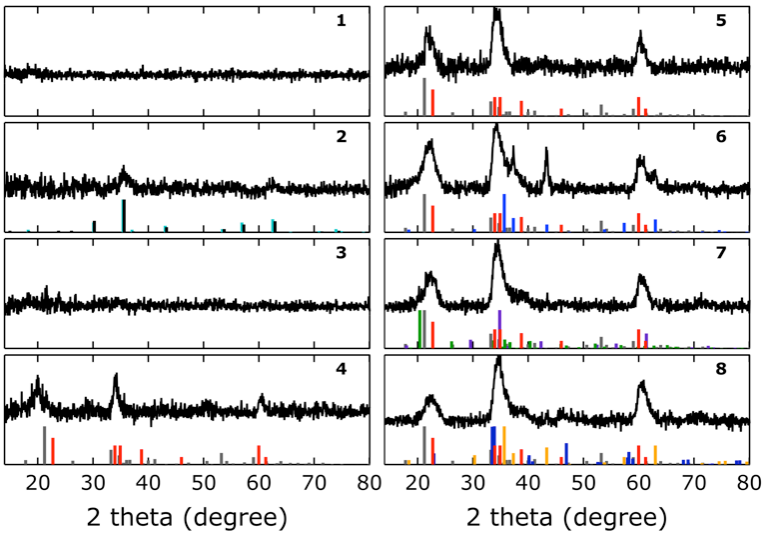

Figure 2.7. XRD data of catalysts **1** to **8**. Normalized fixed slit intensities of known macroscopic crystals are displayed as vertical lines: black, γ-Fe_2O_3; cyan, Fe_3O_4; red, α-(Fe,Ni)$(OH)_2$; gray, Fe(O)OH; blue, $NiFe_2O_4$; green, TiO_2; purple, Fe_2TiO_4; yellow, Ni_3TiO_5; dark blue, $La(Ni,Fe)O_3$.

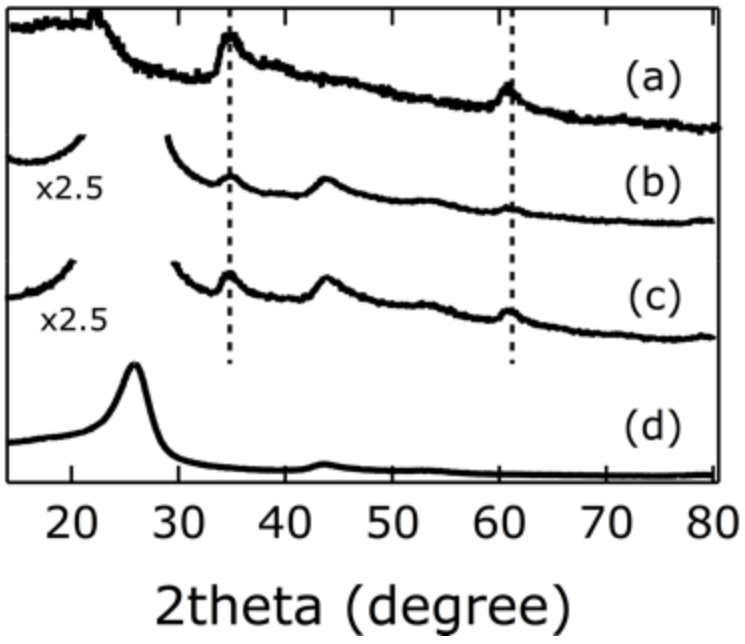

Figure 2.8. XRD data of catalyst **5** after anodization, (a) on Si, (b) on carbon cloth after 30 min anodization in 1.0 M pH 14.0 aqueous KOH at 0.807 V vs NHE, (c) on carbon cloth before anodization; bare carbon cloth (d).

2.4.3. Transmission Electron Micrographs. TEM images were taken to obtain nanoparticle sizes. Our intention was to avoid blocking catalytically active surface sites; therefore, our nanoparticles were synthesized by PLAL without any surfactants. They naturally aggregated in aqueous suspensions. We prepared very dilute samples on TEM grids, resulting in only a few (aggregated) nanoparticles being imaged per frame. Note that frame-filling nanoparticle patterns will only form by self-assembly of surfactant-capped nanoparticles due to repulsive or attractive forces between surfactant molecules.[60]

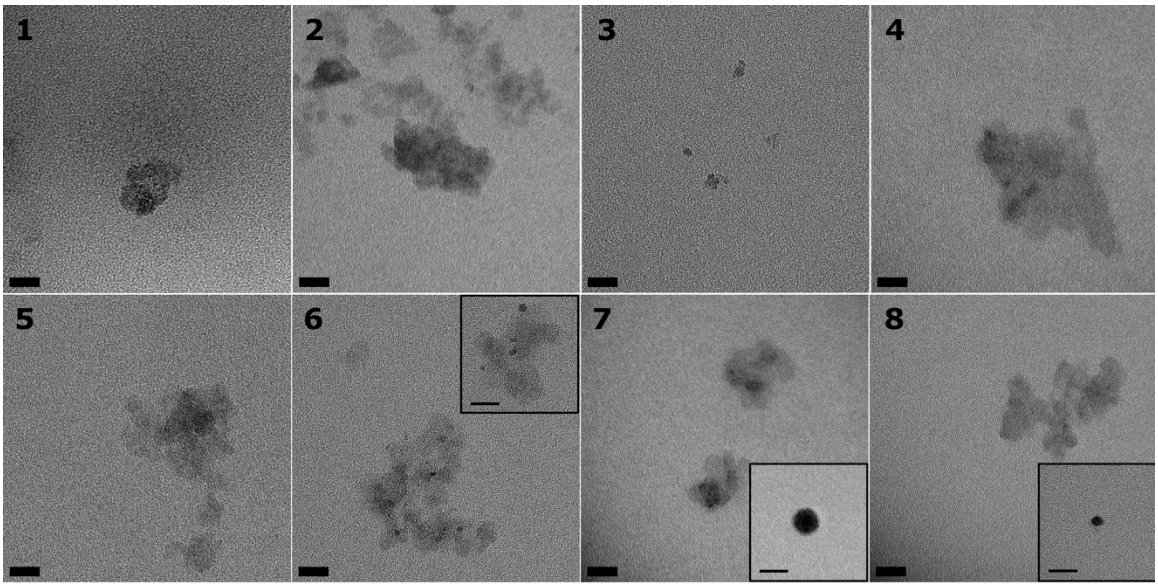

Figure 2.9. TEM images of water oxidation catalysts **1** to **8**. The insets show particles that imaged with a higher contrast. All scale bars are 20 nm.

Nanocatalyst compositions and sizes are summarized in Table 2-2. Compositions were derived from XPS peak area quantification. Scherrer analysis of XRD data for catalysts **4** to **8** was used to obtain crystalline domain sizes (materials **1** to **3** were poorly crystallized); the corresponding crystalline phases are given in parentheses. Nanoparticle sizes were determined by TEM image analysis.

Analysis of TEM and XRD data of **6** suggested that smaller, (6.5 ± 0.8) nm particles could be attributed to $NiFe_2O_4$, and larger (13 ± 1) nm nanosheets could be assigned to the

layered double hydroxide $[Ni_{1-x}Fe_x(OH)_2](NO_3)_y(OH)_{x-y}\bullet nH_2O$. It became evident from inspection of TEM images of **6** that the smaller ($NiFe_2O_4$) nanoparticles exhibited more contrast, consistent with a more spherical shape, than the larger $[Ni_{1-x}Fe_x(OH)_2](NO_3)_y(OH)_{x-y}\bullet nH_2O$ sheets. The spinel $NiFe_2O_4$ crystallizes in the cubic system,[61] rendering the formation of nanoparticles with radial symmetry likely. The double hydroxide $[Ni_{1-x}Fe_x(OH)_2](NO_3)_y(OH)_{x-y}\bullet nH_2O$, however, crystallizes as a layered structure,[62] leading to axially elongated nanosheets. Likewise, differences in TEM contrast, shape, and size were found for catalysts **7** and **8**.

Table 2-2: Catalyst metal contents, concentrations of both nitrogen species with respect to total metal content, crystalline domain sizes, and nanoparticle sizes.

Catalyst	% Metal			% Nitrogen (405.1 eV binding energy)	% Nitrogen (407.3 eV binding energy)	Crystalline Domain Size (nm)	Nanoparticle Size (nm)
	Fe	Ni	La				
1	95	5	–	0	0	–	22 ± 3
2	86	14	–	0	8	–	10 ± 2
3	70	30	–	1	6	–	7.7 ± 2
4	36	64	–	6	10	12 ± 3 (LDH)	14 ± 2
5	22	78	–	5	5	9 ± 2 (LDH)	12 ± 2
6	30	70	–	5	5	13 ± 3 (LDH) 6.1 ± 0.5 (spinel)	13 ± 2 6.5 ± 0.8
7	23	77	–	3	5	12 ± 3 (LDH)	13 ± 2 19 ± 2
8	29	70	1	8	4	14 ± 4 (LDH)	14 ± 2 8.7 ± 1

2.4.4. Brunauer-Emmett-Teller Data. BET data were collected to obtain surface areas of the more active water oxidation catalysts **5** to **8**.

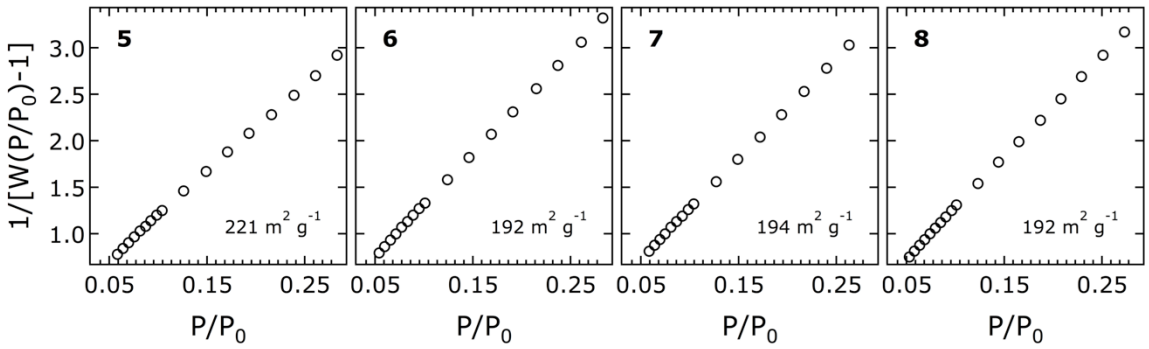

Figure 2.10. BET data of catalysts **5** to **8**; P/P_0 denotes the relative pressure, and W is the weight of the adsorbed argon.

2.4.5. Raman Spectra. The Raman spectra of **1** to **3** showed a broad feature centered at around 650 cm^{-1}. In this region, Raman shifts of ferrous-ferric oxides, such as magnetite[63] or ferrihydrite,[64] occur. The broadness observed for **1** to **3**, however, strongly suggests the presence of structurally ill-defined, poorly crystalized materials. The Raman spectra of **4** to **8** were compared to a reference spectrum of mineralogical α-$(Fe,Ni)(OH)_2$ and showed good agreement. The strong peaks in the spectra of **4** to **8** at ~1050 cm^{-1} were assigned to inter-layer nitrate ions, consistent with peaks that have previously been observed in electrochemically deposited α-$Ni(OH)_2$ thin films.[65] MacDougall reported that only *α*-$Ni(OH)_2$ contained measurable nitrate, as formation of crystalline *β*-$Ni(OH)_2$ occurred with the concurrent loss of interstitial layering; the *β*-polymorph did not accommodate interstitial ions because of tighter crystal packing.[65]

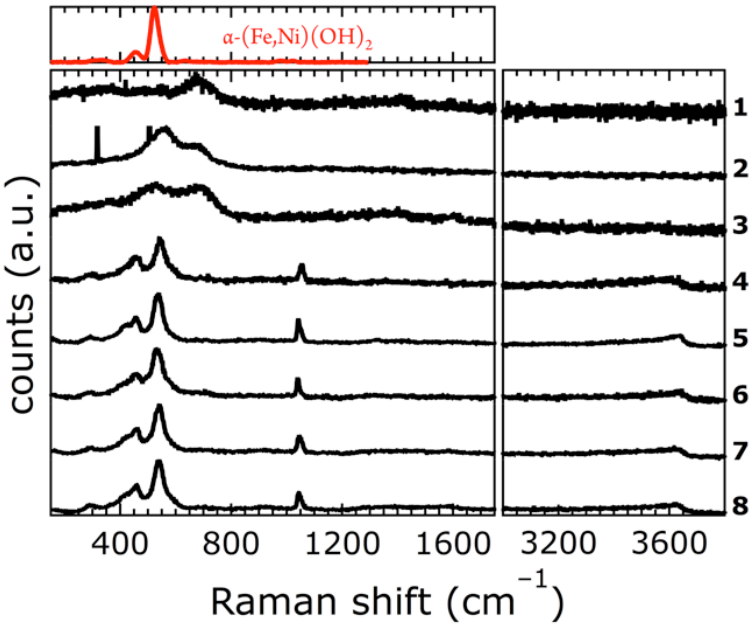

Figure 2.11. Raman spectra of catalysts **1** to **8** (black). The sharp spikes in the spectrum of **2** are from cosmic ray events. Also depicted is a reference spectrum of mineralogical α-(Fe,Ni)$(OH)_2$ (red, collected with 532 nm excitation).

Which $Ni(OH)_2$ phase is catalytically most active is still subject of intense debate. During water oxidation, α-$Ni(OH)_2$ is oxidized to γ-Ni(O)OH, whereas β-$Ni(OH)_2$ is transformed into β-Ni(O)OH; both oxyhydroxides are reduced back to their starting hydroxides during electrochemical cycling.[66-68] It has been a long-held view that β-$Ni(OH)_2$ is more active for oxygen evolution. Studies of electrodeposited amorphous α-$Ni(OH)_2$ and its ageing to β-$Ni(OH)_2$ in basic electrolytes suggested that oxygen evolution occurred at lower onset potential for β-$Ni(OH)_2$/β-Ni(O)OH.[66,69-75] Yachandra and Nocera challenged this notion by correlating structure to activity in a nickel-borate oxygen evolution catalyst.[51] Dai established that crystalline Fe-doped α-$Ni(OH)_2$ on carbon nanotubes is more active than the equivalent β-phase material.[34] And Yan recently synthesized phase-controlled crystalline α- and β-$Ni(OH)_2$ materials and found that the α-polymorph was more active for water oxidation.[76] Our results support the recent findings that α-$Ni(OH)_2$ is highly active for water oxidation.

2.4.6. Infrared Spectra. Infrared (IR) spectra were collected to shed more light on the compositions of catalysts **5** and **6**. The IR spectra of **5** and **6** showed broad peaks with maxima at 340, 500, and 640 cm^{-1}. The δ(OH) band at 640 cm^{-1} is very sensitive to the amount of water intercalated between the α-$Ni(OH)_2$ layers. Bands, attributed to OH– bending motions, typically appear at ~650 cm^{-1} for $Ni(OH)_2$ with high water content and thus indicate the presence of the α-polymorph. In contrast, for the β-polymorph, the band is shifted to ~520 cm^{-1}. Additionally, the α-polymorph shows broad absorption in the ν(OH) region (3400–3600 cm^{-1}), whereas the β-polymorph features a sharp band at 3640 cm^{-1}.[77] The location and broadness of the δ(OH) and ν(OH) bands in our catalysts **5** and **6** led us to conclude that $[Ni_{1-x}Fe_x(OH)_2](NO_3)_y(OH)_{x-y}\bullet nH_2O$ was the predominant material. The band at 1340 cm^{-1} was further evidence of interstitial nitrates.[78]

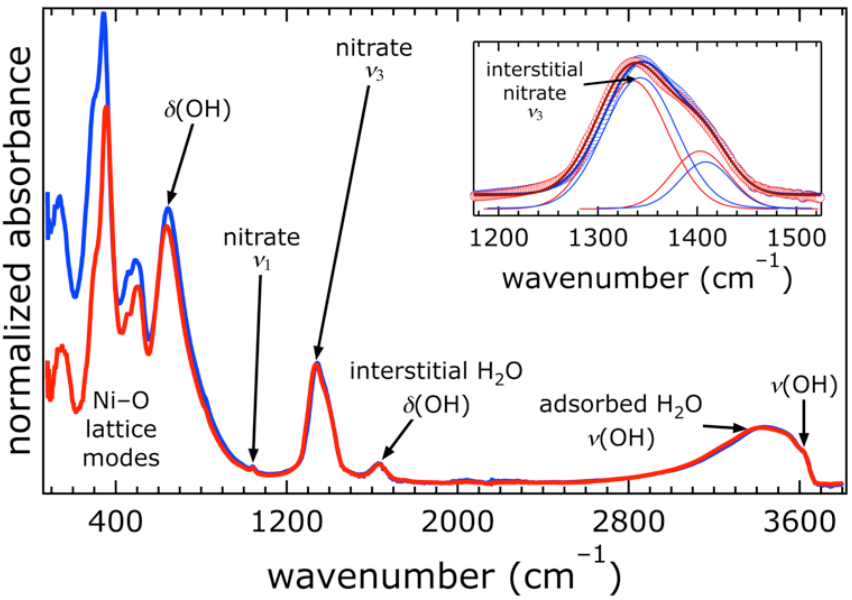

Figure 2.12. Infrared spectra of catalysts **5** (red) and **6** (blue) with band assignments. The inset shows a magnification of the nitrate (ν_3) region: open circles, data; thick lines, overall fits; thin lines, Gaussian peak fits. The band was best fit by two Gaussian distributions, indicating the presence of two distinct species.

The spectrum of $Ni(OH)_2$ with iron incorporation was qualitatively determined from published transmission-mode IR spectra.[70,78] Two materials were used in this analysis: (1)

almost exclusively $Ni(OH)_2$ and (2) one of mixed (Ni,Fe) composition, due to aging in KOH for 72 hours. The compositions of these materials were determined by XRD and Mössbauer spectroscopy in the original study.[78]

The IR spectra were digitized from an electronic (PDF) copy of the original manuscript using UN-SCAN-IT v.5.2 software. Transmission values (digitized *y*-values) were aligned with the wavelength (digitized *x*-values) for both spectra, omitting points where digitization was not complete for both.

The spectrum of (2) was shifted down vertically by assuming that the common feature at 495 cm^{-1} is isosbestic in transmission. The spectrum of (1) was scaled by a factor consistent with a second isosbestic point at 670 cm^{-1}. The absorbance spectra of the two samples was then calculated using $A(x) = 2 - \log[T(x)]$, where $A(x)$ is the absorbance and $T(x)$ is the decimal transmission at the wavelength x.

Finally, the spectrum of mixed (Ni,Fe) 'oxyhydroxide' was approximated by subtracting the absorbance spectrum of (1) from (2). It is plotted as a red dotted line in Figure 2.13, alongside the normalized absorbance spectrum of (1), graphed as a blue dotted line.

It is important to note that, in the absence of an absolute transmission value, these spectra are only qualitative. They do, however, clearly indicate the direction that the peaks shift upon incorporation of iron into the nickel phase. The growth of features at ~400 cm^{-1} and ~600 cm^{-1} relative to the features at ~350 cm^{-1} and ~650 cm^{-1} is indicative of iron incorporation into the nickel phase. This trend has been observed previously.[79-81]

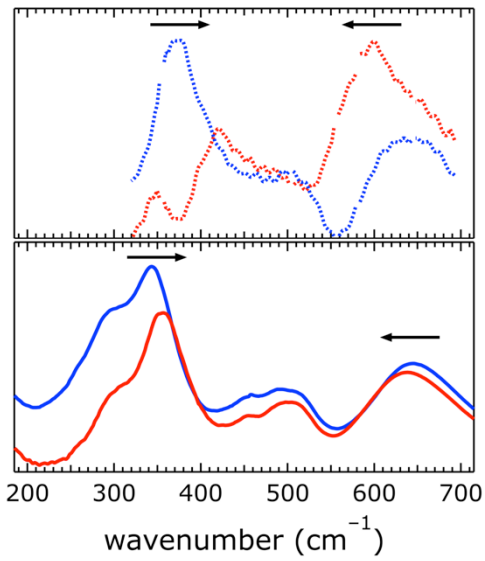

Figure 2.13. Infrared spectra (solid lines) of catalysts 5 (red) and 6 (blue) with spectral deconvolutions (dotted lines).

2.5. Electrochemical Characterization

Electrochemical activity of the nanoparticulate catalysts was assessed by cyclic voltammetry and Tafel data; long-term stability was measured by chronoamperometry.

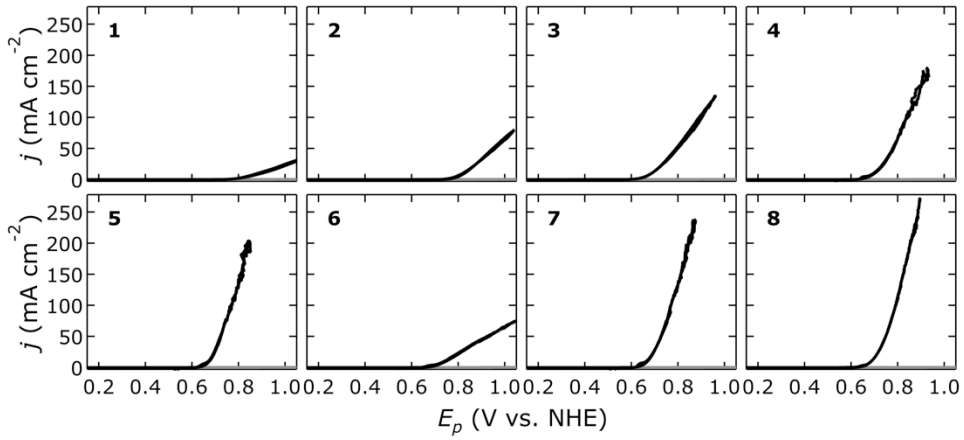

Figure 2.14. Cyclic voltammograms of catalysts **1** to **8**; j, current density, E_p, polarization potential. The disjointed segments in the measured data occurred due to bubble release from the electrode surface.

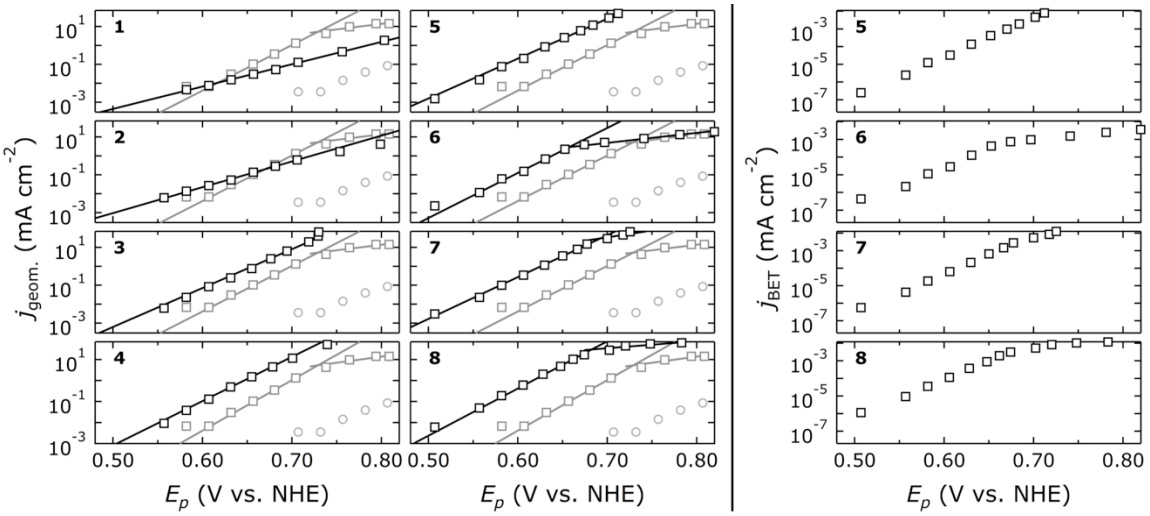

Figure 2.15. Tafel data of catalysts **1** to **8** (black squares); *j*, current density, E_p, polarization potential. For comparison, Tafel data of electrodeposited nickel oxide (gray squares, equivalent mass loading) and bare HOPG (gray circles) are also plotted. The solid lines are fits. Left, current data of **1** to **8** normalized to geometric electrode areas; right, current data of **5** to **8** normalized to BET surface areas.

Plotting the overpotential at 10 mA cm^{-2} vs. the Ni content in the catalyst (from XPS data) shows that the highest water oxidation activity was obtained with the highest Ni content (78%) in the material.

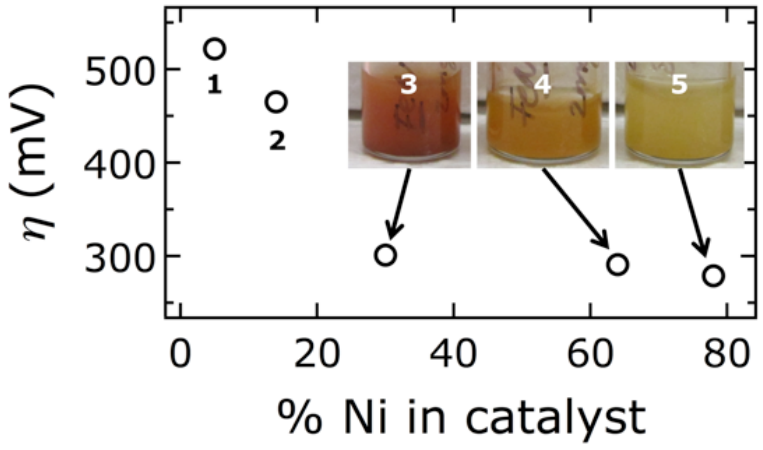

Figure 2.16. Overpotential η for water oxidation at 10 mA cm^{-2} vs. Ni content for catalysts **1** to **5**. Depicted in the photos are catalysts **3** to **5** in aqueous suspension to visualize their different colors.

Chronoamperometry data showed that catalytic activity of catalysts **5**, **6**, and **8** was maintained for more than 5 hours. The current fluctuations were due to formation and release of oxygen bubbles from the electrode surface.

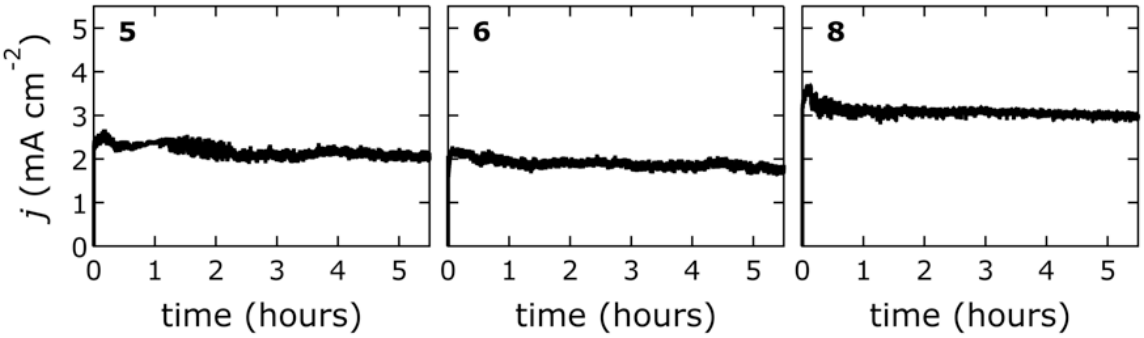

Figure 2.17. Current density *j* as a function of time data of catalysts **5**, **6** and **8**; the applied potential was 0.654 V vs. NHE.

A summary of catalytic activity data is provided in Table 2-3.

Table 2-3: Overpotentials, η, at current densities of 0.5 and 10 mA cm^{-2}, Tafel slopes A, and turnover frequencies (TOF) per gram of catalyst at 250 mV and 300 mV overpotential of catalysts **1** to **8** and electrodeposited Ni oxide for comparison.

Catalyst	η (@ 0.5 mA cm^{-2}) (mV)	η (@ 10 mA cm^{-2}) (mV)	A (mV/dec)	TOF @ η = 250 mV (μmol O_2 s^{-1} g^{-1})	TOF @ η = 300 mV (μmol O_2 s^{-1} g^{-1})
1	360	520	84.7 ± 2.1	0.23	0.89
2	300	470	73.3 ± 1.0	0.94	4.6
3	240	300	48.7 ± 0.7	7.1	78
4	230	290	47.5 ± 1.3	11	130
5	220	280	47.6 ± 0.6	21	220
6	220	350	42.0 ± 0.9 190 ± 11.6	19	42
7	210	270	45.2 ± 0.7 139 ± 35.6	33	290
8	200	260	44.7 ± 2.0 294 ± 90.6	53	290
Ni oxide	280	370	41.5 ± 0.6 170 ± 52.0	0.63	10

A comparison with published Fe–Ni-based water oxidation catalysts is provided in Table 2-4. Direct comparability of catalytic activity is in general problematic because of variations in mass loading, film thickness, intricate details of the electrochemical measurements, such as electrode substrate, rotation speed, and dwell time to reach steady-state conditions or scan rates; also, overpotentials were recorded at different current densities. Nevertheless, we compiled published data and compared them with our catalysts made by

PLAL. When measured at a current density of 10 mA cm^{-2} on a flat electrode substrate, our best catalyst had the lowest overpotential.

Table 2-4: Comparison of overpotentials η (at given current densities) of this work with reported catalysts. Electrode substrate materials are also given because only flat working electrode substrates allow for a meaningful comparison of electrocatalyst performance.

Catalyst	Electrode substrate	Current density (mA cm^{-2})	η (mV)	Reference
8	Flat HOPG	10	260	this work
5	Flat HOPG	10	280	this work
Thin-film solution-cast $Ni_{0.9}Fe_{0.1}O_x$	Au/Ti-coated quartz crystal	10	336	82
Nanostructured α-$Ni(OH)_2$	Glassy carbon	10	331	76
Electrodeposited $NiFeO_x$	Glassy carbon	10	360	15
Thin-film electrodeposited Ni-Fe (40% Fe)	Gold	10	280	45
Graphene FeNi double hydroxide hybrid	Ni foam, unspecified pore size*	10	220	83
Thin film nickel oxide with iron impurities	Nickel foil	8	230	20
Ni-Fe layered double hydroxide nanoplates	Carbon fiber paper	5	290	34
β-NiOOH	Nickel, polished with μm-sized alumina powders	5	500	84
Mixed Fe-Ni oxides	Carbon paper	1	375	85

Catalyst	Electrode substrate	Current density (mA cm^{-2})	η (mV)	Reference
Nickel-borate	Glassy carbon	1	425	50
Amorphous α-$Fe_{20}Ni_{80}O_x$	FTO glass	0.5	210	86
High surface-area nickel metal oxides	Nickel or steel microdiscs	0.5	265	87
$NiFeAlO_4$ inverse spinel	Glassy carbon	0.1	380	53
NiO_x deposited from molecular $[Ni(en)_3]^{2+}$	Glassy carbon	0.1	390	88

* The high porosity of nickel foam leads to an enlargement of the electrode substrate surface area relative to the apparent geometric area, inflating current densities that are normalized to the geometric electrode area.

2.6. Summary

In this chapter, several high-performing, earth-abundant water oxidation catalysts were presented. The technique of pulsed-laser ablation in liquids (PLAL), a medium-throughput method for synthesizing materials generally not accessible on the phase diagram, could be a valuable tool for materials chemists.

Chapters 3 and 4 deal exclusively with material **5**, described above as $[Ni_{1-x}Fe_x(OH)_2](NO_3)_y(OH)_{x-y}\bullet nH_2O$, where $x = 0.22$. These studies deal primarily with the *mechanism* of water oxidation in aqueous alkaline solutions, so complicated alloys containing titanium and lanthanum were not considered. Chapter 3 focuses on the structural properties of the catalyst and couples these with computational analysis, while Chapter 4 describes spectroscopic signatures detected *in situ*.

2.7. References and Notes

(1) Gray, H. B. *Nature Chem.* **2009**, *1*, 7.

(2) Lewis, N. S.; Nocera, D. G. *Proc. Natl. Acad. Sci. U. S. A.* **2006**, *103*, 15729.

(3) Walter, M. G.; Warren, E. L.; McKone, J. R.; Boettcher, S. W.; Mi, Q.; Santori, E. A.; Lewis, N. S. *Chem. Rev.* **2010**, *110*, 6446.

(4) McKone, J. R.; Lewis, N. S.; Gray, H. B. *Chem. Mater.* **2013**, *26*, 407.

(5) Trasatti, S. *Electrochim. Acta* **1984**, *29*, 1503.

(6) Man, I. C.; Su, H.-Y.; Calle-Vallejo, F.; Hansen, H. A.; Martínez, J. I.; Inoglu, N. G.; Kitchin, J.; Jaramillo, T. F.; Nørskov, J. K.; Rossmeisl, J. *ChemCatChem* **2011**, *3*, 1159.

(7) Gilbert, J. A.; Eggleston, D. S.; Murphy, W. R.; Geselowitz, D. A.; Gersten, S. W.; Hodgson, D. J.; Meyer, T. J. *J. Am. Chem. Soc.* **1985**, *107*, 3855.

(8) Limburg, J.; Brudvig, G. W.; Crabtree, R. H. *J. Am. Chem. Soc.* **1997**, *119*, 2761.

(9) Ruettinger, W.; Yagi, M.; Wolf, K.; Bernasek, S.; Dismukes, G. C. *J. Am. Chem. Soc.* **2000**, *122*, 10353.

(10) Dau, H.; Limberg, C.; Reier, T.; Risch, M.; Roggan, S.; Strasser, P. *ChemCatChem* **2010**, *2*, 724.

(11) Yin, Q.; Tan, J. M.; Besson, C.; Geletii, Y. V.; Musaev, D. G.; Kuznetsov, A. E.; Luo, Z.; Hardcastle, K. I.; Hill, C. L. *Science* **2010**, *328*, 342.

(12) Wiechen, M.; Zaharieva, I.; Dau, H.; Kurz, P. *Chem. Sci.* **2012**, *3*, 2330.

(13) Du, P.; Eisenberg, R. *Energy Environ. Sci.* **2012**, *5*, 6012.

(14) Singh, A.; Spiccia, L. *Coord. Chem. Rev.* **2013**, *257*, 2607.

(15) McCrory, C. C. L.; Jung, S.; Peters, J. C.; Jaramillo, T. F. *J. Am. Chem. Soc.* **2013**, *135*, 16977.

(16) Yang recently reported a highly active graphene FeNi double hydroxide hybrid on Ni foam working electrodes (Long, X.; Li, J.; Xiao, S.; Yan, K.; Wang, Z.; Chen, H.; Yang, S. *Angew. Chem., Int. Ed. Engl.* **2014**, *53*, 7584), although the high porosity of the electrode substrate leads to a surface area enlargement, inflating current densities that were normalized to the geometric electrode area; this makes a performance comparison impossible.

(17) Gao, M.; Sheng, W.; Zhuang, Z.; Fang, Q.; Gu, S.; Jiang, J.; Yan, Y. *J. Am. Chem. Soc.* **2014**, *136*, 7077.

(18) Yang, G. W. *Prog. Mater. Sci.* **2007**, *52*, 648.

(19) Blakemore, J. D.; Gray, H. B.; Winkler, J. R.; Müller, A. M. *ACS Catal.* **2013**, *3*, 2497.

(20) Corrigan, D. A. *J. Electrochem. Soc.* **1987**, *134*, 377.

(21) Risch, M.; Klingan, K.; Heidkamp, J.; Ehrenberg, D.; Chernev, P.; Zaharieva, I.; Dau, H. *Chem. Commun.* **2011**, *47*, 11912.

(22) Li, X.; Walsh, F. C.; Pletcher, D. *Phys. Chem. Chem. Phys.* **2011**, *13*, 1162.

(23) Lyons, M. E. G.; Cakara, A.; O'Brien, P.; Godwin, I.; Doyle, R. L. *Int. J. Electrochem. Sci.* **2012**, *7*, 11768.

(24) Trotochaud, L.; Ranney, J. K.; Williams, K. N.; Boettcher, S. W. *J. Am. Chem. Soc.* **2012**, *134*, 17253.

(25) Trotochaud, L.; Young, S. L.; Ranney, J. K.; Boettcher, S. W. *J. Am. Chem. Soc.* **2014**, *136*, 6744.

(26) Powder diffraction file no. 00-029-0713 (ICDD, 2012).

(27) Powder diffraction file no. 01-076-6119 (ICDD, 2012).

(28) Demourgues-Guerlou, L.; Fournès, L.; Delmas, C. *J. Solid State Chem.* **1995**, *114*, 6.

(29) Axmann, P.; Glemser, O. *J. Alloys Compd.* **1997**, *246*, 232.

(30) Trolard, F.; Bourrié, G. In *Clay Minerals in Nature - Their Characterization, Modification and Application*; Valaskova, M., Ed.; InTech: Ostrava, Czech Republic, 2012.

(31) Corrigan, D. A.; Conell, R. S.; Fierro, C. A.; Scherson, D. A. *J. Phys. Chem.* **1987**, *91*, 5009.

(32) Balasubramanian, M.; Melendres, C. A.; Mini, S. *J. Phys. Chem. B* **2000**, *104*, 4300.

(33) Landon, J.; Demeter, E.; İnoğlu, N.; Keturakis, C.; Wachs, I. E.; Vasić, R.; Frenkel, A. I.; Kitchin, J. R. *ACS Catal.* **2012**, *2*, 1793.

(34) Gong, M.; Li, Y.; Wang, H.; Liang, Y.; Wu, J. Z.; Zhou, J.; Wang, J.; Regier, T.; Wei, F.; Dai, H. *J. Am. Chem. Soc.* **2013**, *135*, 8452.

(35) Wagner, C. D.; Riggs, W. M.; Davies, L. E.; Moulder, J. F.; Mullenberg, G. E. *Handbook of X-Ray Photoelectron Spectroscopy*; Perkin-Elmer Corporation: Eden Prairie, MN, 1979.

(36) Bandis, C.; Scudiero, L.; Langford, S. C.; Dickinson, J. T. *Surf. Sci.* **1999**, *442*, 413.

(37) Wei, M.; Xu, X.; Wang, X.; Li, F.; Zhang, H.; Lu, Y.; Pu, M.; Evans, D. G.; Duan, X. *Eur. J. Inorg. Chem.* **2006**, *2006*, 2831.

(38) Baltrusaitis, J.; Jayaweera, P. M.; Grassian, V. H. *Phys. Chem. Chem. Phys.* **2009**, *11*, 8295.

(39) Wang, X.; Deng, R.; Kulkarni, S. A.; Wang, X.; Pramana, S. S.; Wong, C. C.; Gratzel, M.; Uchida, S.; Mhaisalkar, S. G. *J. Mater. Chem. A* **2013**, *1*, 4345.

(40) Nanayakkara, C. E.; Jayaweera, P. M.; Rubasinghege, G.; Baltrusaitis, J.; Grassian, V. H. *J. Phys. Chem. A* **2013**, *118*, 158.

(41) Frost, R. L.; Erickson, K. L.; Kloprogge, T. J. *Spectrochim. Acta A* **2005**, *61*, 2919.

(42) Co-crystallization of several crystal phases cannot be excluded in such small size domains.

(43) We note that, strictly speaking, BET surface areas are not necessarily equivalent to electroactive surface areas.

(44) Pourbaix, M. *Atlas of Electrochemical Equilibria in Aqueous Solutions*; Pergamon Press: New York, 1966.

(45) Louie, M. W.; Bell, A. T. *J. Am. Chem. Soc.* **2013**, *135*, 12329.

(46) Oliva, P.; Leonardi, J.; Laurent, J. F.; Delmas, C.; Braconnier, J. J.; Figlarz, M.; Fievet, F.; Guibert, A. d. *J. Power Sources* **1982**, *8*, 229.

(47) Kermarec, M.; Carriat, J. Y.; Burattin, P.; Che, M.; Decarreau, A. *J. Phys. Chem.* **1994**, *98*, 12008.

(48) Hall, D. S.; Lockwood, D. J.; Poirier, S.; Bock, C.; MacDougall, B. R. *J. Phys. Chem. A* **2012**, *116*, 6771.

(49) Hannoyer, B.; Ristić, M.; Popović, S.; Musić, S.; Petit, F.; Foulon, B.; Dalipi, S. *Mater. Chem. Phys.* **1998**, *55*, 215.

(50) Dincă, M.; Surendranath, Y.; Nocera, D. G. *Proc. Natl. Acad. Sci. U. S. A.* **2010**, *107*, 10337.

(51) Bediako, D. K.; Lassalle-Kaiser, B.; Surendranath, Y.; Yano, J.; Yachandra, V. K.; Nocera, D. G. *J. Am. Chem. Soc.* **2012**, *134*, 6801.

(52) Smith, R. D. L.; Prévot, M. S.; Fagan, R. D.; Trudel, S.; Berlinguette, C. P. *J. Am. Chem. Soc.* **2013**, *135*, 11580.

(53) Chen, J. Y. C.; Miller, J. T.; Gerken, J. B.; Stahl, S. S. *Energy Environ. Sci.* **2014**, *7*, 1382.

(54) For a comparison of activities see Table 2-4.

(55) Song, F.; Hu, X. *Nat. Commun.* **2014**, *5*.

(56) Zhao, Y.; Li, B.; Wang, Q.; Gao, W.; Wang, C. J.; Wei, M.; Evans, D. G.; Duan, X.; O'Hare, D. *Chem. Sci.* **2014**, *5*, 951.

(57) Temesghen, W.; Sherwood, P. *Anal. Bioanal. Chem.* **2002**, *373*, 601.

(58) X-ray Photoelectron Spectroscopy Database 20, Version 4.1 (National Institute of Standards and Technology, Gaithersburg, 2012); http://srdata.nist.gov/xps/.

(59) Biesinger, M. C.; Payne, B. P.; Lau, L. W. M.; Gerson, A.; Smart, R. S. C. *Surf. Interface Anal.* **2009**, *41*, 324.

(60) You, S. S.; Rashkov, R.; Kanjanaboos, P.; Calderon, I.; Meron, M.; Jaeger, H. M.; Lin, B. *Langmuir* **2013**, *29*, 11751.

(61) Powder diffraction file no. 01-076-6119 (ICDD, 2012).

(62) Powder diffraction file no. 00-038-0715 (ICDD, 2012).

(63) Shebanova, O. N.; Lazor, P. *J. Solid State Chem.* **2003**, *174*, 424.

(64) Mazzetti, L.; Thistlethwaite, P. J. *J. Raman Spectrosc.* **2002**, *33*, 104.

(65) Hall, D. S.; Lockwood, D. J.; Poirier, S.; Bock, C.; MacDougall, B. R. *J. Phys. Chem. A* **2012**, *116*, 6771.

(66) Bode, H.; Dehmelt, K.; Witte, J. *Electrochim. Acta* **1966**, *11*, 1079.

(67) McBreen, J. In *Handbook of Battery Materials*; Besenhard, J. O., Ed.; Wiley-VCH: Weinheim, 1999.

(68) Michael E. G Lyons, M. P. B. *Int. J. Electrochem. Sci.* **2008**, *3*, 1386.

(69) Lu, P. W. T.; Srinivasan, S. *J. Electrochem. Soc.* **1978**, *125*, 1416.

(70) Oliva, P.; Leonardi, J.; Laurent, J. F.; Delmas, C.; Braconnier, J. J.; Figlarz, M.; Fievet, F.; Guibert, A. d. *J. Power Sources* **1982**, *8*, 229.

(71) Bernard, M. C.; Bernard, P.; Keddam, M.; Senyarich, S.; Takenouti, H. *Electrochim. Acta* **1996**, *41*, 91.

(72) Kim, M. S.; Kim, K. B. *J. Electrochem. Soc.* **1998**, *145*, 507.

(73) Wehrens-Dijksma, M.; Notten, P. H. L. *Electrochim. Acta* **2006**, *51*, 3609.

(74) Louie, M. W.; Bell, A. T. *J. Am. Chem. Soc.* **2013**, *135*, 12329.

(75) Li, Y.-F.; Selloni, A. *ACS Catal.* **2014**, *4*, 1148.

(76) Gao, M.; Sheng, W.; Zhuang, Z.; Fang, Q.; Gu, S.; Jiang, J.; Yan, Y. *J. Am. Chem. Soc.* **2014**, *136*, 7077.

(77) Kermarec, M.; Carriat, J. Y.; Burattin, P.; Che, M.; Decarreau, A. *J. Phys. Chem.* **1994**, *98*, 12008.

(78) Hannoyer, B.; Ristić, M.; Popović, S.; Musić, S.; Petit, F.; Foulon, B.; Dalipi, S. *Mater. Chem. Phys.* **1998**, *55*, 215.

(79) White, W. B.; DeAngelis, B. A. *Spectrochim. Acta A* **1967**, *23*, 985.

(80) Musić, S.; Popović, S.; Dalipi, S. *J. Mater. Sci.* **1993**, *28*, 1793.

(81) Rajendran, S.; Rao, V. S. *J. Mater. Sci.* **1994**, *29*, 5673.

(82) Trotochaud, L.; Ranney, J. K.; Williams, K. N.; Boettcher, S. W. *J. Am. Chem. Soc.* **2012**, *134*, 17253.

(83) Long, X.; Li, J.; Xiao, S.; Yan, K.; Wang, Z.; Chen, H.; Yang, S. *Angew. Chem., Int. Ed. Engl.* **2014**, *53*, 7584.

(84) Yeo, B. S.; Bell, A. T. *J. Phys. Chem. C* **2012**, *116*, 8394.

(85) Landon, J.; Demeter, E.; İnoğlu, N.; Keturakis, C.; Wachs, I. E.; Vasić, R.; Frenkel, A. I.; Kitchin, J. R. *ACS Catal.* **2012**, *2*, 1793.

(86) Smith, R. D. L.; Prévot, M. S.; Fagan, R. D.; Trudel, S.; Berlinguette, C. P. *J. Am. Chem. Soc.* **2013**, *135*, 11580.

(87) Li, X.; Walsh, F. C.; Pletcher, D. *Phys. Chem. Chem. Phys.* **2011**, *13*, 1162.

(88) Singh, A.; Chang, S. L. Y.; Hocking, R. K.; Bach, U.; Spiccia, L. *Energy Environ. Sci.* **2013**, *6*, 579.

3 EFFECT OF INTERLAYER ANIONS ON [NiFe]-LDH NANOSHEET WATER OXIDATION ACTIVITY

Adapted from Hunter, B. M.; Hieringer, W.; Winkler, J. R.; Gray, H. B.; Müller, A. M. Effect of Interlayer Anions on [NiFe]-LDH Nanosheet Water Oxidation Activity. *Energy & Environmental Science* **2016**, *9*, 1734. DOI : 10.1039/C6EE00377J.

3.1. Summary

We synthesized nickel-iron layered double hydroxide ([NiFe]-LDH) nanosheets with different interlayer anions to probe their role in water oxidation catalysis. In alkaline electrolyte in ambient air, carbonate rapidly replaced other interlayer anions and catalytic activity was highest. Electrocatalytic water oxidation in virtually carbonate-free alkaline electrolyte revealed that activity was a function of anion basicity. Our [NiFe]-LDH nanosheets, prepared by pulsed laser ablation in liquids, were regenerated in carbonate-containing aqueous KOH. Anion binding motifs were assessed by x-ray photoelectron spectroscopy in combination with density functional theory calculations, suggesting that nitrite species bound to edge-site Fe in the precatalyst correlated with higher water oxidation activity.

3.2. Introduction

The global supply of sustainable fuels affects every aspect of human life. Electrocatalytic water splitting ($2H_2O \rightarrow 2H_2 + O_2$) is a promising approach towards transportable, carbon-neutral hydrogen fuel. The water oxidation half reaction is more demanding because it involves four electron and proton transfer steps,[1, 2] for which highly active, earth-abundant catalysts are needed.

Layered double hydroxides (LDHs), materials based on mineral structures readily found in nature, have been shown to be active for water oxidation.[3-22] We recently reported that a [NiFe]-LDH nanomaterial synthesized by pulsed laser ablation in liquids (PLAL) is among the best water oxidation catalysts made of earth abundant elements.[20]

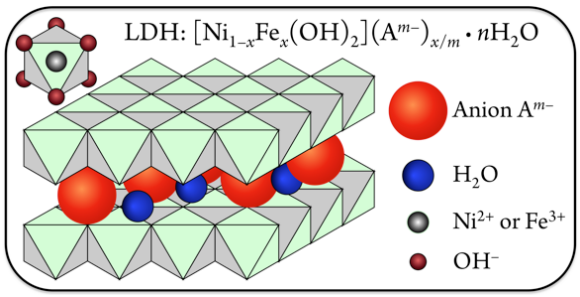

Figure 3.1. Schematic illustration of the [NiFe]-LDH structure. Anions and water are present in the interlayer space, and Ni^{2+} or Fe^{3+} ions are surrounded by six hydroxides in distorted octahedral coordination (upper left).

The structures of these nanosheet precatalysts were analyzed by x-ray diffraction (XRD) and Raman spectroscopy.[20] The [NiFe]-LDH materials consist of sheets of edge-shared nickel oxide octahedra, with varying amounts of ferric iron substituting at nickel sites. Hydroxide ligands extend into the interlayer space, which also contains water. The excess positive charges of Fe^{3+} substituting for Ni^{2+} are balanced by interlayer anions[23] (Figure 3.1).

The affinities for various mono- and divalent anions were established for [MgAl]-LDH hydrotalcite materials, which are structurally similar to our [NiFe]-LDHs. Data derived from anion-exchange isotherms revealed that divalent anions generally had higher ion selectivity than monovalent ones. The ion-exchange equilibrium constants followed the sequence $CO_3^{2-} > SO_4^{2-} > OH^- > F^- > Cl^- > I^-$.[24] Some hydroxide ions are likely always present in the interlayer galleries because OH^- partakes in strong interlamellar hydrogen bonding networks with the interlayer water, the ionic radius of hydroxide is very similar to that of water, and hydroxide is required to form the basic layers.[25] Moreover, given the large slab hydroxide and intercalated water content of LDHs, the experimental determination of minute amounts of interlayer OH^- ions is not practical. Nevertheless, we were interested in the identity of non-hydroxide interlayer anions in [NiFe]-LDHs during turnover in aqueous base in ambient air and their effects on water oxidation activity.

We exploited the benefits of PLAL as a synthetic method to investigate the role of interlayer anions in [NiFe]-LDH water oxidation catalysts. PLAL produces small, mono-

dispersed, surfactant-free nanoparticles.[26] The small size (<25 nm) allowed for the complete metathesis of interlayer anions simply by soaking in aqueous solutions. In addition, by modifying the anion content of the ablation liquid, we were able to synthesize species with different interlayer ions.

3.3. Experimental Section

3.3.1. Materials and Methods. Nanomaterial synthesis by pulsed laser ablation in liquids was performed in the Beckman Institute Laser Resource Center at California Institute of Technology. X-ray photoelectron spectroscopy was carried out at the Molecular Materials Research Center (Beckman Institute at California Institute of Technology).

All chemicals were used as received. Deionized water was obtained from a Barnstead Diamond Nanopure system and had a resistivity of ≥16 MΩ cm^{-1}. Data analysis and graphing was performed with Igor Pro 6.37 (Wavemetrics).

3.3.2. Synthesis. PLAL[26] was used to synthesize [NiFe]-LDH nanosheets.[20] Suspensions of 0.5 g iron (Alfa, −200 mesh) powder were stirred in 10 mL aqueous nickel salt solutions, using a magnetic stirrer in a 30 mL glass beaker at room temperature in ambient air. Metal salt solutions consisted of 3.0 M nickel nitrate ($Ni(NO_3)_2 \cdot 6H_2O$, Alfa), or 2.5 M nickel chloride ($NiCl_2 \cdot 6H_2O$, JT Baker) and 0.5 M nickel nitrate, or 1.5 M each nickel sulfate ($NiSO_4 \cdot 6H_2O$, EMD) and nickel nitrate. The limited solubilities of nickel chloride and sulfate required addition of nickel nitrate to keep the total nickel concentration of all three solutions at 3.0 M. The material resulting from use of 3.0 M aqueous nickel nitrate solution is henceforward called [NiFe]-(NO_3^-)-LDH. Beakers and stir bars were thoroughly cleaned with *aqua regia* before use. A 355 nm, 8 ns pulse length, 90 mJ/pulse laser beam, provided by the third harmonic of a 10 Hz Q-switched Nd:YAG laser (Spectra-Physics Quanta-Ray PRO-Series), was focused 0.5 mm below the surface of the liquid with a 100 mm focal length plano-convex quartz lens. Each sample was irradiated for 60 min. After synthesis,

unreacted iron ablation target powder was separated from the nanoparticle suspensions using a rare-earth magnet. Solid nanopowders were obtained by centrifugation and washing with water until the supernatant did not show any nickel salt absorption. The nanoparticles were then washed twice with 3 mL acetone (EMD, OmniSolv®) and dried under vacuum.

Anion exchange was effected by suspending 10 mg [NiFe]-(NO_3^-)-LDH nanosheets in 2 mL 1.0 M aqueous alkali salt solutions and letting the rigorously vortexed nanopowder soak for 45 min; the soaking time was 10 min for aqueous KOH solutions. The salts were K_2CO_3, KOH, KCl, NaF (all Mallinckrodt), Na_2SO_4 (EMD), $NaClO_4 \cdot 1H_2O$ (Fisher Scientific), KI, KBF_4, K_3PO_4, and $K_2C_2O_4 \cdot 1H_2O$ (all Sigma-Aldrich). For exchange as a function of solution pH, 1.5 mg [NiFe]-(NO_3)-LDH were dispersed in 1.0 mL 1.0 M (pH 14.0), 1.0×10^{-3} M (pH 11.0), or 1×10^{-6} M (pH 8.0) aqueous KOH solutions for 5 min. Anion-exchanged [NiFe]-LDH powders were obtained by centrifugation and washing first three times with 5 mL water and then twice with 3 mL acetone; the powders were dried under vacuum.

3.3.3. Physical Characterisation. X-ray photoelectron spectra (XPS) were collected using a Surface Science Instruments M-probe surface spectrometer. Monochromatic Al Kα radiation (1486.6 eV) was used to excite electrons from the samples, which had either been deposited as dry powders on double-sided adhesive carbon tape (EM Sciences) or drop-cast from aqueous suspension on clean Cu foil and dried in ambient air at room temperature; we did not find different results for the two sample mounting methods. The sample chamber was maintained at $<5\times10^{-9}$ Torr. Survey scans from 0 to 1000 eV were performed to identify the elements present in the nanoparticles. Binding energies were referenced to the C 1s peak arising from adventitious carbon, taken to have a binding energy of 284.8 eV.[27] High-resolution spectra were collected for all materials for the Fe 2p, Ni 2p, C 1s, N 1s, and O 1s regions. In addition, depending on the elemental composition of the material, high-resolution spectra were taken in the Cl 2s, S 2s, I 3d, B 1s, F 1s, and P 2s regions. Quantitative peak areas were derived after Shirley background subtraction[28]

and using relative sensitivity factors. Binding energies were obtained from the same peak fits. Quantitative XPS analysis was performed with CasaXPS (Version 2.3.16 PR 1.6).

XRD data were collected with a Bruker D2 PHASER diffractometer. Monochromatic Cu Kα radiation (1.5418 Å; tube power 30 kV, 10 mA) was used; the instrument was equipped with 0.1° divergence, 1.5° Soller, and 0.6 mm detector slits, and had a 3-mm secondary anti-scatter screen. Diffracted radiation was collected with a Lynxeye detector. The instrument resolution was 0.030° in 2θ, and the counting time was 4.5 seconds per step, resulting in a total scan time of about 3.5 hours for each sample. Solid samples were deposited with vaseline (X-Alliance GmbH) on a zero-diffraction silicon plate (MTI Corporation). XRD background subtraction and Scherrer analysis[29] were performed with the Bruker DIFFRAC.SUITE software. Reflections were analyzed using a Scherrer constant K of 0.89 and integral breadth, defined as the total area under the diffraction maximum divided by the peak intensity.[30] Basal spacings d were derived using Braggs law,[31] $n\lambda = 2d \sin(\theta)$, where the integer n equals one, λ is the wavelength of the incident light, and θ is the angle of incidence. The (003) peaks of background-subtracted XRD data were fitted with Gaussians (ESI), whose centers at 2θ were divided by two to obtain the angle of incidence required to calculate basal spacings.

Attenuated total reflectance infrared (IR) spectra of dry nanoparticulate powders were collected with a Thermo Nicolet iS50 FT-IR spectrometer, equipped with a Pike Technologies GladiATR accessory plate, an uncooled pyroelectric deuterated triglycine sulfate (DTGS) detector, and a KBr beamsplitter. Spectra of the solid nanoparticulate powders were collected at room temperature in ambient air, and 132 scans were averaged for each sample.

3.3.4. Electrochemical Characterisation. Nanosheet powders were weighed with a high precision balance (Sartorius CPA225D), and aqueous 2 mg mL^{-1} suspensions were prepared. A catalyst loading of 40 μg was used throughout this work and was obtained by

drop-casting 20 μL of these suspensions on highly-ordered pyrolytic graphite (HOPG) disks, which were dried in ambient air under a heat lamp at 50°C. The electrode disk had stabilizing epoxy around its side and a surface area of 0.20 cm^2. HOPG electrodes were cleaned by soaking for 5 min in concentrated hydrochloric acid, washed with water, and their surfaces were polished using 400 and 600 grit sandpaper, after which the graphite was cleaved with adhesive tape to obtain a fresh HOPG surface for each catalyst.

Measurements were carried out in ambient air or argon atmosphere in 100 mL three-neck round-bottom flasks, filled with 25 mL electrolyte. An Hg/HgO reference electrode (CH Instruments) and a Ni gauze (Alfa) counter electrode were used. All data were collected at room temperature, using a rotating disk electrode (RDE) setup at 1,500 rpm. Experiments in Ar atmosphere were carried out in a glove box, whose catalyst tolerates water; during oxygen evolution the catalyst was shut off, and after experiments the box was thoroughly flushed with Ar. In ambient air, a Pine MSR variable speed rotator and a Gamry Reference 600 potentiostat were used. In Ar atmosphere, a Pine WaveNow potentiostat and a (smaller) home-built RDE apparatus were employed; the rotation speed was determined to be 1,500 rpm with a laser tachometer.

In ambient air, the electrolyte was aqueous 1.0 M (pH 14.0) KOH. The electrolyte took up CO_2 from ambient air, which was dissolved as carbonate at this high pH. Even highest purity reagent grade alkali hydroxide solutions contain a minimum of 1% (~0.1 M) alkali carbonate.[32] Measurements in virtually carbonate-free electrolyte were performed under Ar atmosphere in a glove box. The electrolyte was prepared in the box from thoroughly degassed water, 1.0 M high purity KOH (Alfa, 99.98%, packaged under Ar), and 0.43 M barium hydroxide ($Ba(OH)_2 \cdot 1H_2O$, Sigma-Aldrich). The barium hydroxide was added in excess to precipitate all dissolved carbonate as $BaCO_3$, rendering the supernatant electrolyte virtually free of carbonate (see IR data below). Before use, an Hg/HgO reference electrode was equilibrated for one week in this solution. The pH of the virtually carbonate-free electrolyte was measured to be 14.6. Electrolyte from the same stock solution was used for all experiments requiring carbonate-free electrolyte.

Chronopotentiometry was performed for 3.5 hours at 1 mA cm^{-2}. Observed fluctuations in the data were due to formation and release of oxygen bubbles from the electrode surface. Cyclic voltammograms were measured at 0.1 V s^{-1} scan rate and after the working electrode had been held for 10 min at a current density of 1.0 mA cm^{-2}. The current density *versus* potential data were post-measurement corrected for uncompensated resistance losses (details are described elsewhere).[20] All polarization potentials reported here are relative to the normal hydrogen electrode (NHE), and current densities are per geometric area. Overpotentials η were calculated from polarization potentials E_p as $\eta = E_p - (1.23\ \text{V} - 0.059\ \text{V}\cdot\text{pH})$, taking into account the different pH values of electrolytes with and without carbonate.

3.3.5. Computational Methods. Density-functional theory calculations were performed with the Turbomole program package.[33] The PBE0 hybrid functional[34-36] was used throughout this work. The SV(P) basis set[37] was employed for geometry optimizations as well as for N 1s core level energy calculations. Solvent screening effects were approximately included via the conductor-like screening model (COSMO)[38, 39] with a solvent permittivity of 80. All calculations were spin-unrestricted. In this work, we imposed the lowest total spin projection $S_z = 0.5$ possible for the cluster models used in this work (one excess spin-up spin orbital in the Slater determinant). No point group symmetries were assumed. The model clusters were subjected to constrained geometry optimizations, where the atomic Ni, O, H positions of the parent LDH structure were kept fixed at the experimental positions, whereas the positions of all other atoms (Fe, additional OH groups, nitrate/nitrite anions) were optimized. Standard convergence criteria (Turbomole defaults) were used in general. Only for the calculation of the core-level binding energies, SCF convergence criteria were tightened to 10^{-7} a. u. for the energy and density matrix.

The calculation of N 1s core-level binding energies (BEs) was performed using N 1s orbital energies and with the so-called Slater transition state (STS) method.[40] Initial state contributions to core level shifts (is-CLS) were estimated as orbital energy differences of

the N 1s orbital energies ε in the chosen SCF solutions of the clusters without any core hole. Only *shifts* in core-level binding energies (core-level shifts, CLS) were relevant in this work, absolute binding energies should not be compared to experimental XPS data.

3.4. Results and Discussion

We synthesized twelve materials with different interlayer anions, either by anion exchange from nitrate-based [NiFe]-LDH nanosheets made by PLAL from nitrate-containing ablation liquid,[20] denoted [NiFe]-(NO_3^-)-LDH, or with Cl^- or SO_4^{2-} in the PLAL ablation liquid. Aqueous solutions for anion exchange contained 1.0 M BF_4^-, Cl^-, ClO_4^-, CO_3^{2-}, $C_2O_4^{2-}$, F^-, I^-, PO_4^{3-}, or SO_4^{2-}.

We discovered that all interlayer anions quickly exchanged for carbonate in 1.0 M aqueous KOH in ambient air, as evidenced by IR, XPS, and XRD data (see below). Strongly alkaline aqueous electrolyte exposed to ambient air is self-buffered regarding carbonate content, as dissolved carbonate is in steady-state equilibrium with gaseous CO_2.[41] The active catalyst was therefore the carbonate-containing species, regardless of the precatalyst composition.

3.4.1. Physical Characterization of Materials

3.4.1.1. X-Ray photoelectron spectra. We collected XPS data to identify nanoparticle compositions by peak integrations of high-resolution spectra of the Ni 2p, Fe 2p, B 1s, C 1s, N 1s, O 1s, B 1s, F 1s, Cl 2s, I 3d, P 2s, and S 2s regions, where applicable. The regions were chosen as to collect data on transitions with the highest x-ray ionization cross-sections,[42] and the data were background-subtracted.[28] We deliberately did not attempt to quantify oxygen content from XPS data because its amounts are regularly overestimated; oxygen occurs in many adventitious sources.

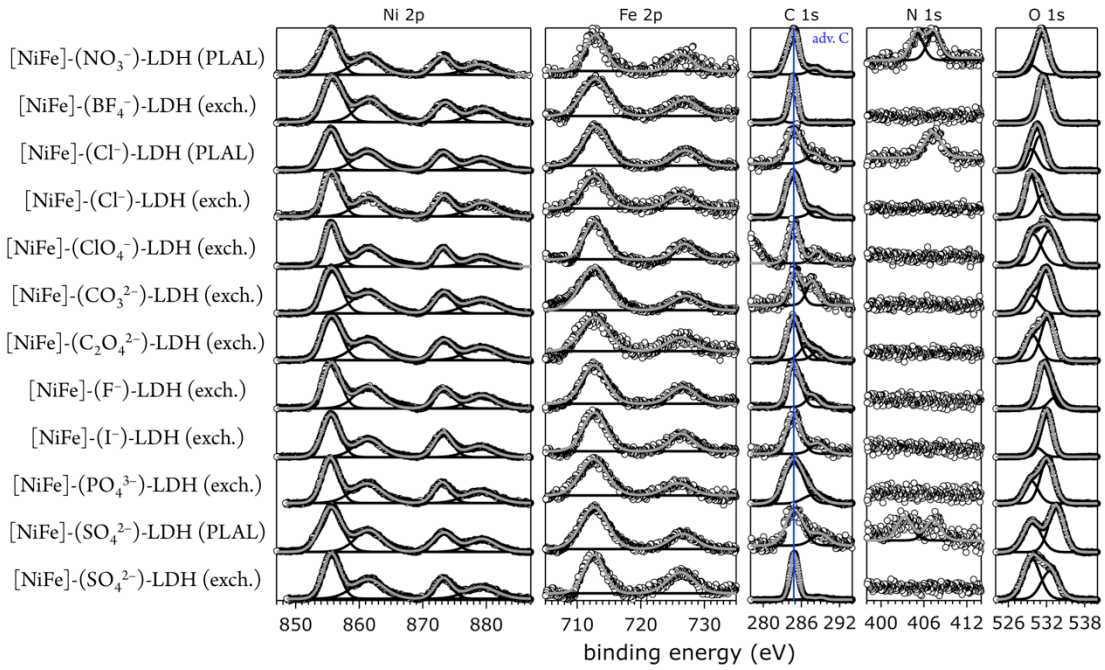

Figure 3.2. XPS data of [NiFe]-LDH nanosheets with different interlayer anions as synthesized in the Ni 2p, Fe 2p, C 1s, N 1s, and O 1s regions. The materials were prepared by pulsed-laser ablation in liquids (PLAL) or by anion exchange from [NiFe]-(NO_3^-)-LDH (exch.). Open circles, data; black lines, peak fits; grey lines, envelopes. The blue line in the C 1s panel indicates the binding of adventitious carbon.

The Ni 2p core-level binding energies of all catalysts were consistent with assignment to hydrated $Ni(OH)_2$,[43] with Ni $2p_{3/2}$ binding energies close to 855.5 eV. After exposure to 1.0 M aqueous KOH in ambient air, all [NiFe]-LDH materials featured an additional, lower binding-energy peak in the Ni $2p_{3/2}$ core level region, consistent with NiO.[44, 45] The Fe 2p core level spectra of all catalysts showed peaks attributable to iron oxides and oxyhydroxides,[13, 46] with Fe $2p_{3/2}$ binding energies close to 711.9 eV. Various iron oxides and oxyhydroxides, such as FeO, Fe_2O_3, Fe_3O_4, and FeOOH, have similar Fe core-level binding energies and spectral shapes.[46] Therefore, it is impossible to distinguish different Fe phases in our materials from Fe 2p XPS data. All materials contained 22% Fe relative to the total metal content.

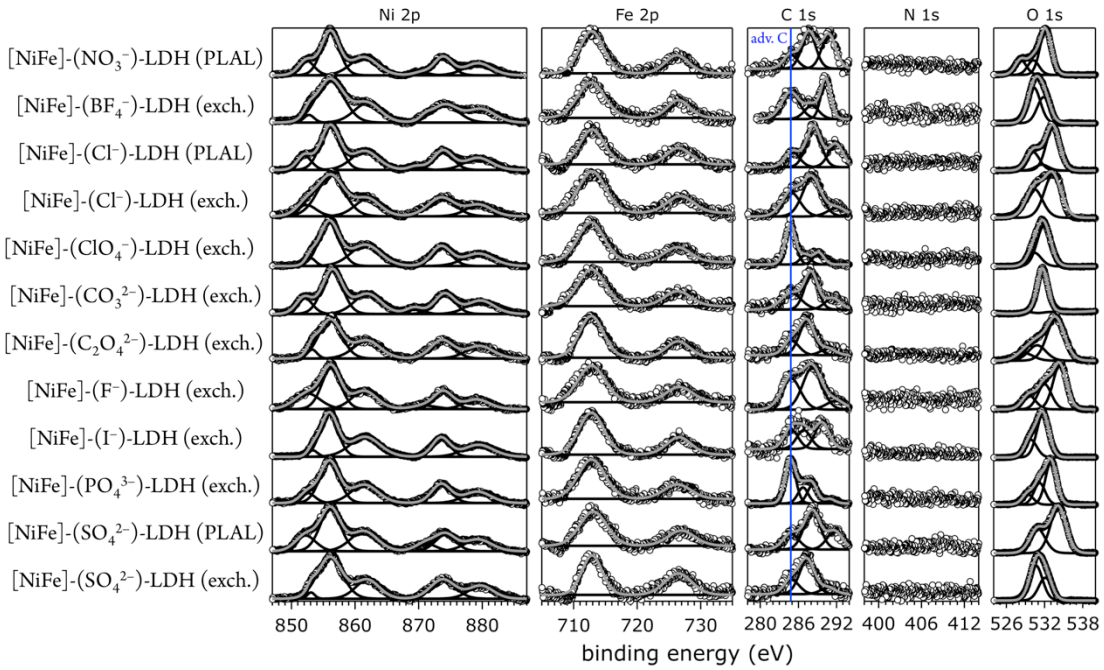

Figure 3.3. XPS data of [NiFe]-LDH nanosheets with different interlayer anions after suspension in 1.0 M aqueous KOH in ambient air in the Ni 2p, Fe 2p, C 1s, N 1s, and O 1s regions. The materials were prepared by pulsed-laser ablation in liquids (PLAL) or by anion exchange from [NiFe]-(NO_3^-)-LDH (exch.). Open circles, data; black lines, peak fits; grey lines, envelopes. The blue line in the C 1s panel indicates the binding energy of adventitious carbon.

The N 1s core level spectra of [NiFe]-(NO_3^-)-LDH, [NiFe]-(Cl^-)-LDH made by PLAL and [NiFe]-(SO_4^{2-})-LDH made by PLAL showed peaks with binding energies around 407.3 eV, consistent with nitrate.[47] In addition, [NiFe]-(SO_4^{2-})-LDH made by PLAL exhibited an N 1s peak at 403.5 eV, attributable to nitrite.[48] As reported by us before, PLAL-synthesized [NiFe]-(NO_3^-)-LDH featured in addition to the nitrate signal an N 1s peak centered at 405.1 eV.[20] After exposure to 1.0 M aqueous KOH in ambient air, we could no longer detect any peaks in the N 1s core level region, indicating that all nitrogen species were readily exchanged by other anions. The O 1s spectra were consistent with Fe or Ni oxide and hydroxide species.[44] Contributions attributable to oxygen-containing anions[44] and from adventitious sources were also present. The C 1s spectra of as-synthesized [NiFe]-LDH materials with different interlayer anions showed mostly the presence of adventitious carbon, whereas those of nanosheets that had been exposed to 1.0

M aqueous KOH in ambient air exhibited additional peaks, which were consistent with more highly oxidized carbon.[44] High-resolution XP spectra of anionic hetero-atoms (other than Ni, Fe, C, N, or O) showed that the initially present anions were lost after exposure to pH 14 aqueous KOH solution in ambient air (Figure 3.4). Quantification of non-metal atom content in the as-synthesized [NiFe]-LDH materials is summarized in Table 3-1. Additional hydroxide ions may have been present to balance the overall charge in the materials.

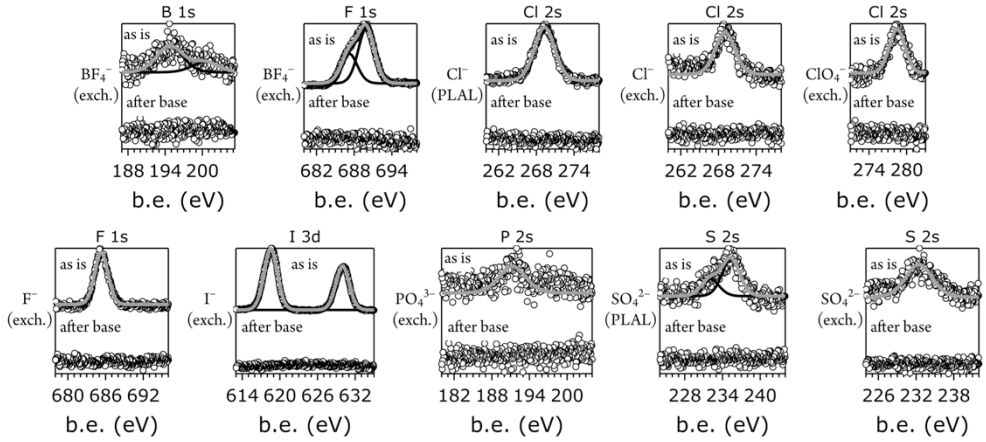

Figure 3.4. XPS data of [NiFe]-LDH nanosheets with different interlayer anions as synthesized (as is) and after suspension in 1.0 M aqueous KOH in ambient air (after base) in the B 1s, F 1s, Cl 2s, I 3d, P 2s, and S 2s regions, where applicable; b.e., binding energy. Open circles, data; black lines, peak fits; grey lines, envelopes.

Table 3-1: Summary of XPS data analysis of [NiFe]-(A^{m-})-LDH materials with different interlayer anions A^{m-}, prepared by pulsed-laser ablation in liquids (PLAL) or by anion exchange from [NiFe]-(NO_3^-)-LDH (exch.). Portion of anion elements with respect to total metal content; the relative error is ± 10 %.

Material	XPS line	% Non-metal atoms
[NiFe]-(NO_3^-)-LDH (PLAL)	N 1s	10
[NiFe]-(BF_4^-)-LDH (exch.)	B 1s F 1s	18 72
[NiFe]-(Cl^-)-LDH (PLAL)	Cl 2s N 1s	16 4.7
[NiFe]-(Cl^-)-LDH (exch.)	Cl 2s	21
[NiFe]-(ClO_4^-)-LDH (exch.)	Cl 2s	10
[NiFe]-(CO_3^{2-})-LDH (exch.)	C 1s	20
[NiFe]-($C_2O_4^{2-}$)-LDH (exch.)	C 1s	20
[NiFe]-(F^-)-LDH (exch.)	F 1s	18
[NiFe]-(I^-)-LDH (exch.)	I 3d	19
[NiFe]-(PO_4^{3-})-LDH (exch.)	P 2s	8.0
[NiFe]-(SO_4^{2-})-LDH (PLAL)	S 2s N 1s	10 4.2
[NiFe]-(SO_4^{2-})-LDH (exch.)	S 2s	17

Knowing that all nitrogen species of the as-synthesized [NiFe]-(NO_3^-)-LDH nanosheets were replaced by carbonate in strong aqueous base in ambient air, we exposed [NiFe]-(NO_3^-)-LDH to aqueous KOH solutions with pH values of 8.0, 11.0, and 14.0 and took XP spectra (Figure 3.5). For comparison, we also collected XP spectra of commercial $Ni(NO_3)_2 \cdot 6H_2O$, whose N 1s region featured a single peak centered at 407.4 eV, consistent with previous reports for metal nitrate.[48] The observed C 1s signal for $Ni(NO_3)_2 \cdot 6H_2O$ was attributable to adventitious carbon, and the O 1s peak was consistent with a transition metal nitrate.[44] Its Ni $2p_{3/2}$ peak was centered at 857.0 eV as expected,[44] and no peaks in the Fe 2p core level region were observed.

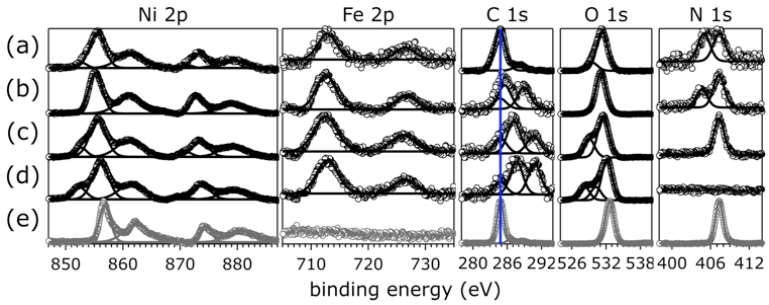

Figure 3.5. XPS data of [NiFe]-(NO_3^-)-LDH (as synthesized, a) and exchanged in different pH aqueous KOH solutions (b, pH 8.0; c, pH 11.0; d, pH 14.0). Depicted in grey are data of commercial $Ni(NO_3)_2 \bullet 6H_2O$ (e). The blue line in the C 1s panel indicates the binding energy of adventitious carbon. Open circles, data; lines, peak fits.

We found that all nitrogen species of the original material were gradually exchanged into carbon species with higher C 1s binding energy than adventitious carbon. As the solution pH rose, the N 1s peak centered at 405.1 eV disappeared before that at 407.3 eV. After exposure to pH 14.0 solution in ambient air, no nitrogen species were detectable (Figure 3.5). Instead the material took up carbonate from the aqueous base (see also IR spectra below). Quantification of XPS signals as a function of solution pH showed a linear decline of N 1s and a concomitant increase of C 1s signals (Figure 3.6). In aqueous KOH solutions at room temperature with pH values above 10, the predominant species resulting from dissolution of ambient CO_2 is carbonate, whereas at pH 8.0 dissolved inorganic carbon speciation favors HCO_3^- over CO_3^{2-} ions.[41] The observed C 1s signals of

[NiFe]-LDH materials after exposure to different pH aqueous KOH solutions were consistent with transition metal bicarbonates and carbonates.[44]

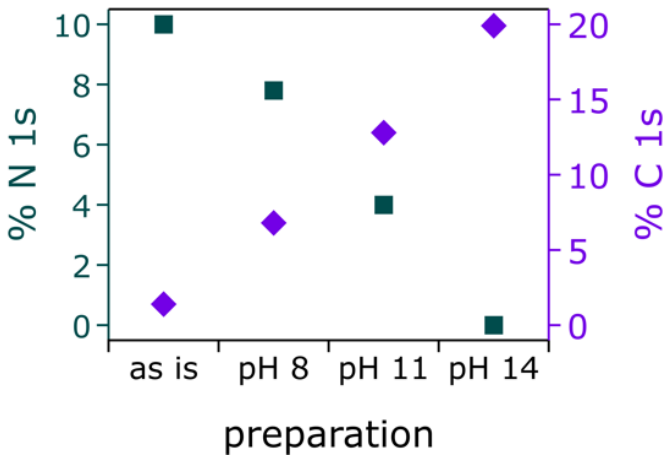

Figure 3.6. Quantification of the N 1s (teal) and C 1s (purple) regions of [NiFe]-(NO_3^-)-LDH (as is) and exchanged in different pH aqueous KOH solutions in percent with respect to the total metal content.

3.4.1.2. X-Ray diffraction data. XRD data were collected to determine crystalline phases, basal spacings by Bragg's law[31] analysis, and crystallite sizes by Scherrer analysis.[29] XRD data of [NiFe]-LDH nanosheets with different interlayer anions as synthesized (as is) and after suspension in 1.0 M aqueous KOH in ambient air are depicted in Figure 3.7.

All materials showed XRD patterns characteristic for layered double hydroxides.[23] The intensities of the basal (00*l*) reflections decrease as *l* increases. The intensity ratio of the (006) and (003) reflections is a measure of the interlamellar electron density. Loss of water in the interlayer galleries, associated with reduction in interlamellar electron density, has been reported to lead to less intense (006) reflections with respect to (003) diffractions.[49]

All XRD peaks were significantly broadened, owing to small crystallite size and stacking faults. The XRD data of [NiFe]-(ClO_4^-)-LDH (exch., as synthesized) and [NiFe]-(SO_4^{2-})-LDH (PLAL, as synthesized) materials showed non-uniform ("saw-tooth")

broadening of (*h*0*l*) reflections, which are indicative of turbostratic disorder.[25] The observed reflections were indexed in a three-layer **3R** polytype with rhombohedral symmetry, such as in synthetic hydrotalcite[50] (Figure 3.8).

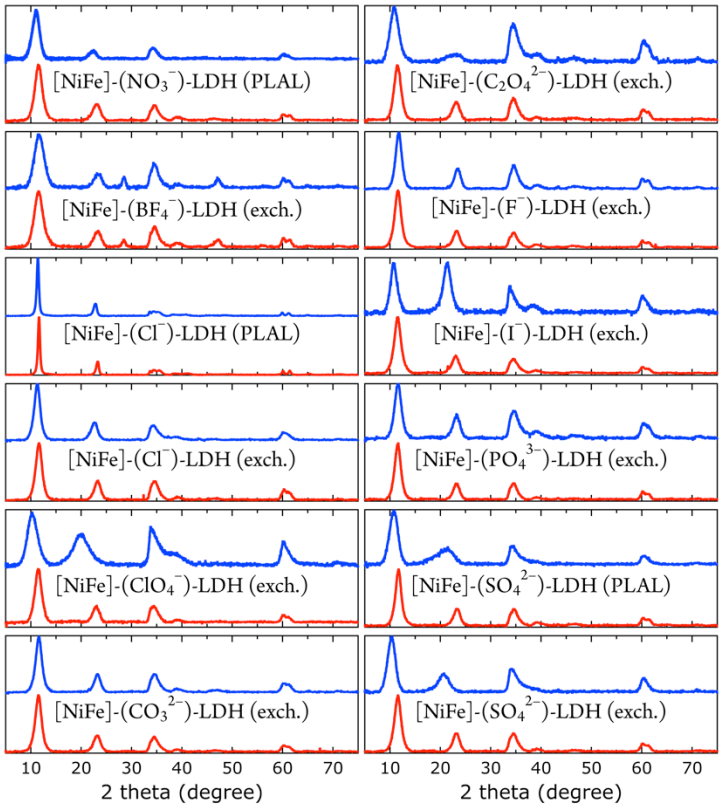

Figure 3.7. XRD data of [NiFe]-LDH nanosheets with different interlayer anions as synthesized (blue) and after suspension in 1.0 M aqueous KOH in ambient air (red).

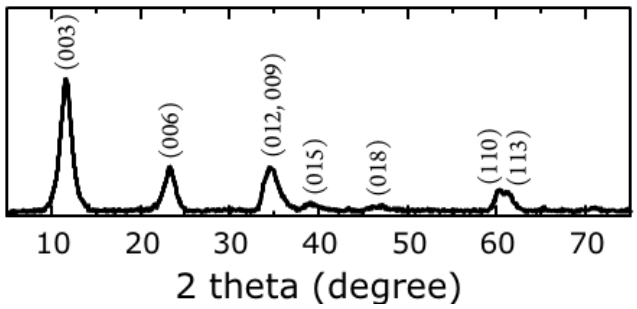

Figure 3.8. XRD data of [NiFe]-(CO_3^{2-})-LDH nanosheets with indices of reflection.

Table 3-2: Crystalline domain sizes from Scherrer analysis of [NiFe]-(A^{m-})-LDH materials with different intercalated anions A^{m-}, prepared by PLAL or by anion exchange from [NiFe]-(NO_3^-)-LDH (exch.), as synthesized and after exposure to 1.0 M aqueous KOH. The error in all dimensions is ± 13 %.

A^{m-} (prep.)	thickness (nm) as synth.	thickness (nm) after base	diameter (nm) as synth.	diameter (nm) after base
NO_3^- (PLAL)	4	4.4	13	13
BF_4^- (exch.)	3.9	3.9	14	12
Cl^- (PLAL)	12	13	21	23
Cl^- (exch.)	4.8	4.7	13	14
ClO_4^- (exch.)	3.2	4.5	12	12
CO_3^{2-} (exch.)	4.8	4.6	12	13
$C_2O_4^{2-}$ (exch.)	3.6	4.6	10	13
F^- (exch.)	3.9	4.7	11	14
I^- (exch.)	4.7	4.5	12	13
PO_4^{3-} (exch.)	4.5	4.8	11	14
SO_4^{2-} (PLAL)	3.8	5.2	12	14
SO_4^{2-} (exch.)	3.8	4.7	10	13

We obtained crystallite sizes from Scherrer analysis[29] of our XRD data (Table 3-2). Crystalline domain sizes in the *a* and *c* unit cell directions were derived from broadening of the (110) and (00*l*) (*l* = 3, 6) reflections, respecively.[25] In case of [NiFe]-(ClO_4^-)-LDH (exch., as synthesized) and [NiFe]-(SO_4^{2-})-LDH (PLAL, as synthesized) materials, only (003) reflections were used to determine nanosheet thicknesses, as the asymmetric line shape of the (006) reflections hampered proper analysis. The unit cell directions *a* and *c* correspond to lateral size (diameter) and nanosheet thickness, respectively. Most materials had very similar size. However, the [NiFe]-(Cl^-)-LDH (PLAL) materials, both as synthesized and after suspension in 1.0 M aqueous KOH in ambient air, exhibited significantly narrower peaks, indicating larger crystallite sizes.

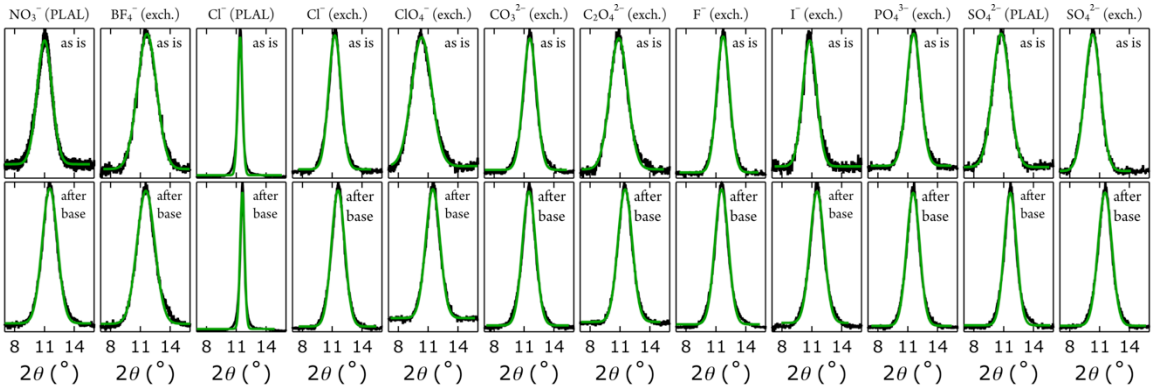

Figure 3.9. Gaussian fits (green) of the (001) peaks (black) of XRD data of [NiFe]-LDH nanosheets with different interlayer anions.

Gaussian fits of the (003) peaks (Figure 3.9) were performed to obtain the angle of incidence required to calculate basal spacings. The fits had an average error in 2θ of ± 0.05°, resulting in a basal spacing error of ± 0.03 Å. The derived basal spacings of [NiFe]-(A^{m-})-LDH materials with different intercalated anions A^{m-}, prepared by PLAL or by anion exchange from [NiFe]-(NO_3^-)-LDH (exch.), are depicted in Figure 3.10.

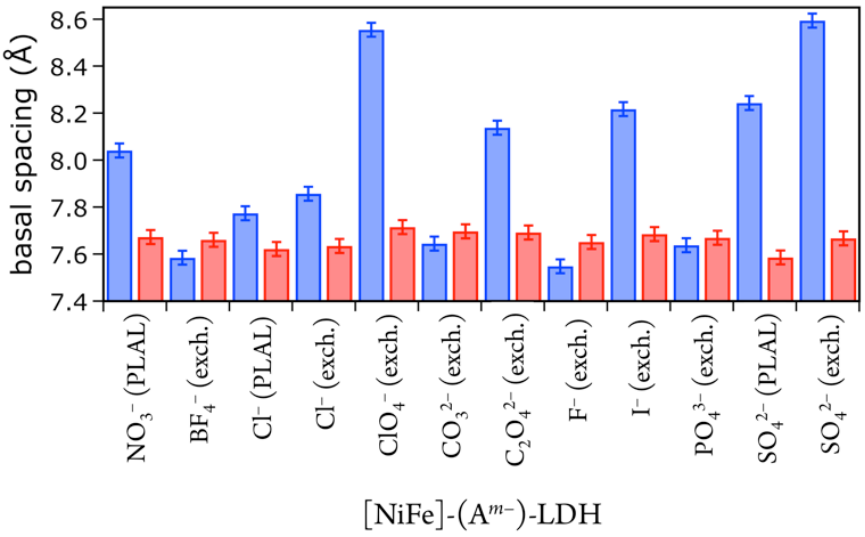

Figure 3.10. Basal spacings of [NiFe]-LDH nanosheets with different interlayer anions as synthesized (blue) and after suspension in 1.0 M aqueous KOH in ambient air (red).

We correlated the basal spacings of [NiFe]-LDH materials with the ionic radii of the anions. Non-spherical anions occupy interlamellar galleries of LDH materials at various angles, and their arrangement depends on many factors.[24,25,51] Therefore, we limited our analysis to the spherical halogen anions. We found a linear correlation of measured basal spacing with anionic radii. Our observation indicates that the anions did indeed reside in the interlayer galleries of our LDH materials.

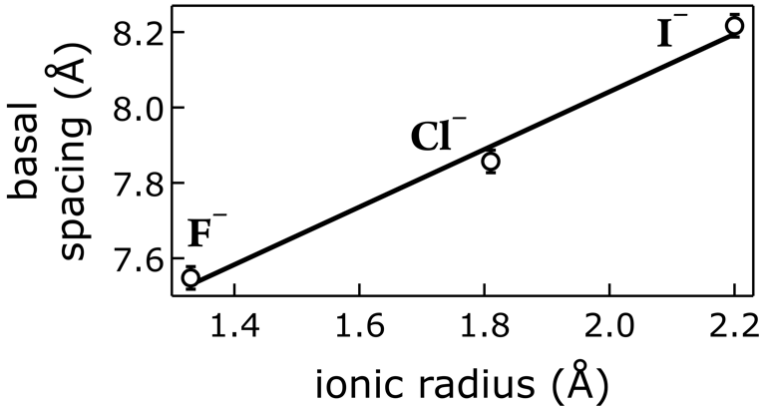

Figure 3.11. Correlation of ionic radii[52] of intercalated halogen anions A^{m-} with basal spacings of [NiFe]-(A^{m-})-LDH materials.

3.4.1.3. Infrared data. IR spectra were collected to shed more light on the identity of interlayer anions in our [NiFe]-LDH water oxidation catalysts. Layered double hydroxides have a huge affinity towards carbonate incorporation.[53, 54] Given the ubiquitous presence of carbonate in aqueous base in ambient air, spectroscopic evidence for virtually carbonate-free materials is paramount. The IR bands in the 1200–1600 cm^{-1} region are characteristic for alkali carbonate (one narrow peak at 1400 cm^{-1}) or nitrate (two broader bands centered around 1400 cm^{-1}).[55]

Our [NiFe]-(NO_3^-)-LDH nanosheets turned into [NiFe]-(CO_3^{2-})-LDH materials in strong aqueous base in ambient air (Figure 3.12). We confirmed the identity of interlayer carbonate by collecting IR data after soaking [NiFe]-(NO_3^-)-LDH in 0.1 M aqueous K_2CO_3 solution.

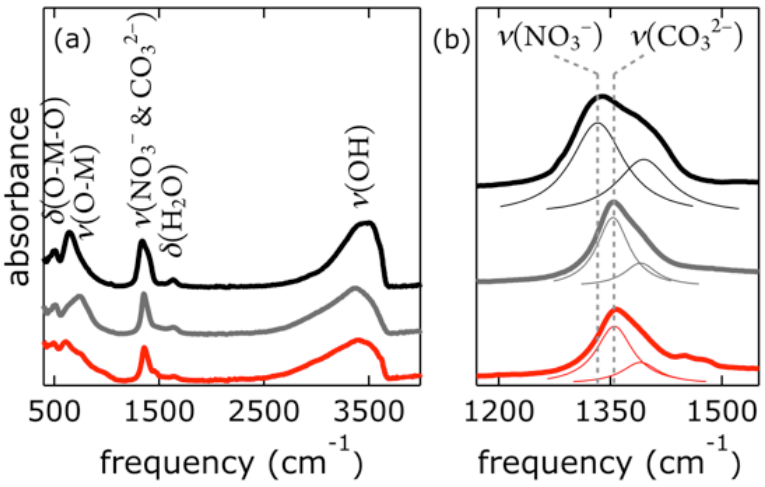

Figure 3.12. Infrared spectra of [NiFe]-(NO_3^-)-LDH nanosheets as synthesized (black), after being suspended in 0.1 M aqueous K_2CO_3 solution (grey), and after being suspended in 0.1 M aqueous KOH (red); (a) full spectra, (b) magnification of the region characteristic for NO_3^- and CO_3^{2-}, Lorentzian fits are depicted as thin lines.

One way of de-carbonation is precipitation of dissolved carbonate with Ba^{2+} as $BaCO_3$.[56] We used this method in inert atmosphere (Figure 3.13), using $Ba(OH)_2$, as to not introduce anions other than hydroxide. All attempts to achieve carbonate-free electrolyte in ambient air failed (Figure 3.13). Virtually carbonate-free electrolyte was prepared under Ar as described above. In the glove box, we dispersed [NiFe]-(NO_3^-)-LDH in this electrolyte, let it settle overnight, and removed the supernatant. Still in Ar atmosphere, we dispersed the resulting material in water, let it settle overnight, removed the supernatant, and repeated this procedure twice. After the last supernatant removal, we let the material dry in the glove box. The IR spectrum (Figure 3.14) of this material clearly shows the characteristic redshift and broadening of the nitrate with respect to the carbonate band, indicating that we succeeded to exclude carbonate from our [NiFe]-(NO_3^-)-LDH and electrolyte in the glove box.

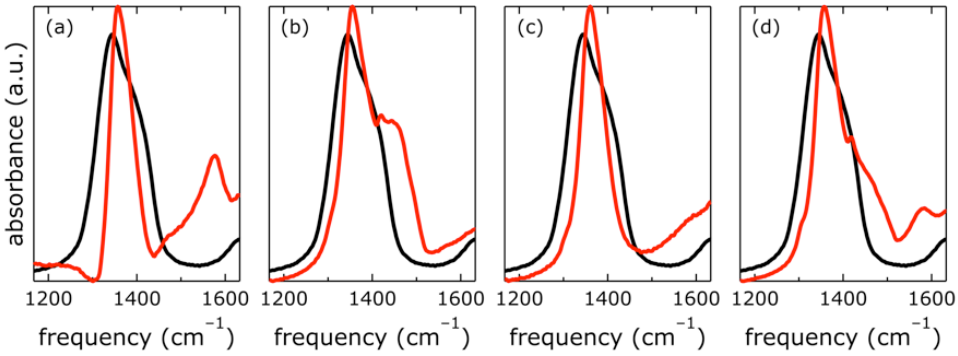

Figure 3.13. Infrared spectra of [NiFe]-(NO_3^-)-LDH nanosheets as synthesized (black) and after being suspended in 0.1 M aqueous KOH (red). The red spectra were taken using different suspension solution conditions: (a), in ambient air, no $Ba(OH)_2$; (b), in ambient air, with $Ba(OH)_2$; (c), in glove box, no $Ba(OH)_2$; (d), in glove box, with $Ba(OH)_2$. All samples were subsequently worked up in ambient air.

The nitrate peak in the infrared spectrum of the as-synthesized [NiFe]-(NO_3^-)-LDH nanosheets was broader than that observed for the [NiFe]-(NO_3^-)-LDH nanosheets which had been soaked in carbonate-free aqueous base. We attributed this to a change in the morphology of the material at high pH. This is in agreement with the dramatic changes observed in the OH and Ni—O lattice regions upon exposure to highly alkaline solutions.

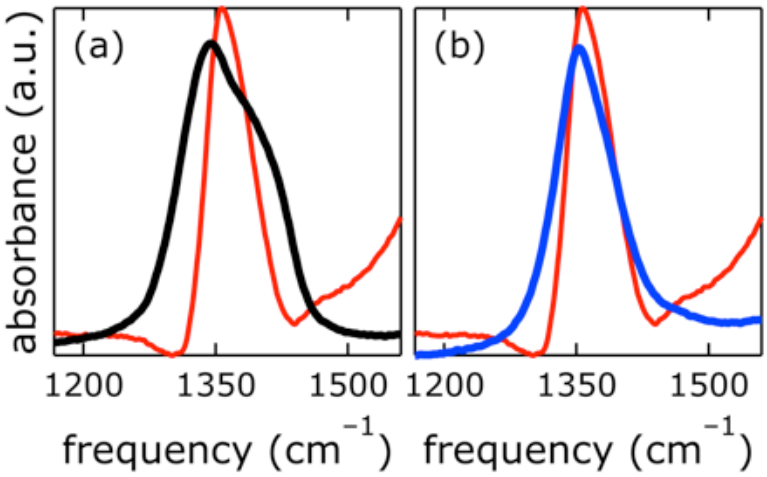

Figure 3.14. Infrared spectra of [NiFe]-(NO_3^-)-LDH nanosheets as synthesized (black), after being suspended in carbonate-free strong base electrolyte in Ar atmosphere as described above (blue), and after being suspended in 0.1 M aqueous KOH in ambient air (red).

3.4.1.4 Electrochemical Characterization. We prepared 1.0 M aqueous KOH electrolyte in a virtually CO_2-free atmosphere (glove box) and scrubbed the solution of any residual dissolved carbonate by saturating with barium hydroxide. IR data confirmed that the [NiFe]-LDH catalysts did not take up carbonate under these conditions (see above). Constant current electrolysis was used to assess long-term water oxidation activity; measured potentials were converted to overpotentials η to facilitate comparison between electrolytes with and virtually without carbonate. In Figure 3.15, the overpotentials as a function of time are shown for [NiFe]-(NO_3^-)-LDH in alkaline electrolytes with and without carbonate. The [NiFe]-(CO_3^{2-})-LDH catalyst performed better than the [NiFe]-(NO_3^-)-LDH, indicating that interlayer anions matter during water oxidation catalysis.

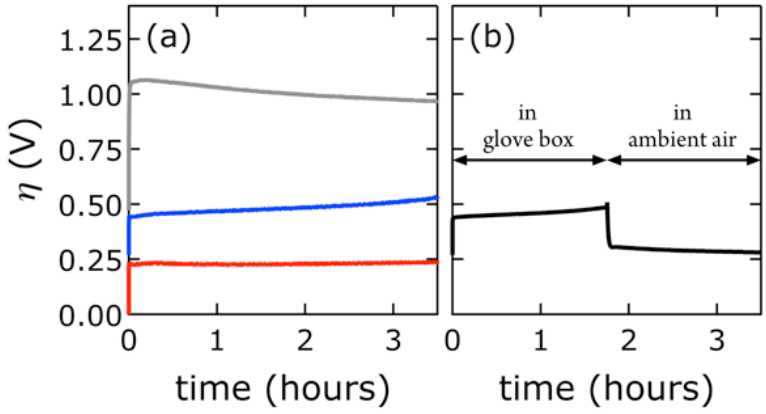

Figure 3.15. Constant current electrolysis of [NiFe]-(NO_3^-)-LDH (PLAL) at 1 mA cm^{-2}. Measured applied potentials were converted to overpotentials η to account for the different pH values of alkaline electrolytes with and virtually without carbonate. (a) Synthesized nanosheets were exposed to only one electrolyte: virtually carbonate free (glove box, blue), with carbonate (ambient air, red). The grey curve corresponds to the bare graphite electrode. (b) [NiFe]-(NO_3^-)-LDH electrode was first anodically polarized in virtually carbonate-free electrolyte (glove box), then brought into ambient air and further polarized in electrolyte with carbonate.

Interestingly, after water oxidation catalysis with [NiFe]-(NO_3^-)-LDH catalyst in virtually carbonate-free alkaline electrolyte, most of the activity of the material recovered when the electrode was removed from the glove box, and the electrolysis was continued in aqueous base in ambient air (Figure 3.15b). Enhanced catalytic activity was observed

instantaneously as [NiFe]-(CO_3^{2-})-LDH was formed. The [NiFe]-LDH nanosheets were regenerated in aqueous base in ambient air, and high activity was detected even after initial catalytic turnover without any carbonate (3.15b). Differences in electrochemical response of the bare graphite electrode in carbonate-free and carbonate-containing electrolytes were insignificant (Figure 3.16).

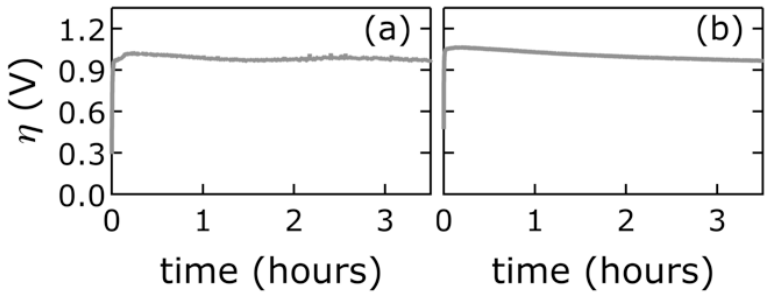

Figure 3.16. Constant current voltammograms of bare graphite electrodes in carbonate-containing (a) and virtually carbonate-free (b) electrolytes.

We probed all twelve materials in a virtually carbonate-free alkaline electrolyte to assess the effects of different interlayer anions (other than hydroxide) in the precatalysts on water oxidation catalysis. We obtained overpotential values at 1 mA cm^{-2} current density after 10 min of catalytic turnover. At the chosen current density most catalysts exhibited appreciable stability under anodic polarization. We compared activities in carbonate-free and carbonate-containing alkaline electrolytes. In all cases, catalytic activity in aqueous base in ambient air was superior (Figure 3.18).

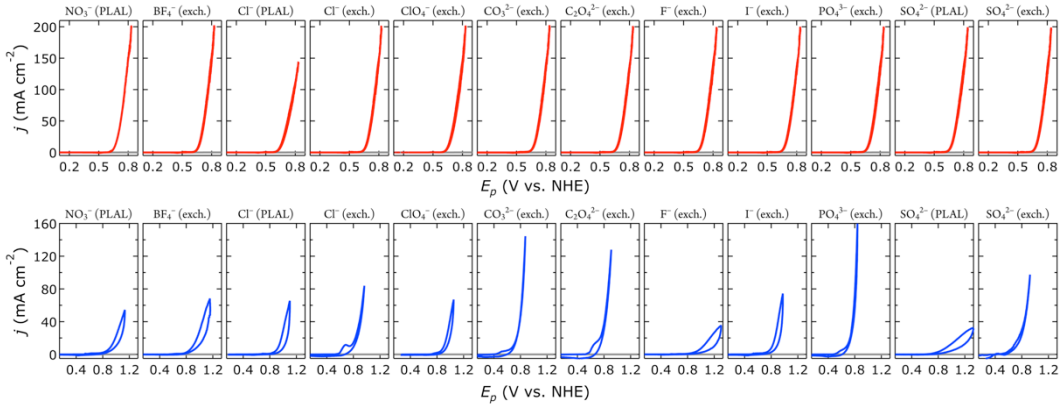

Figure 3.17. Cyclic voltammograms of [NiFe]-LDH materials with different interlayer anions in virtually carbonate-free electrolyte in a glove box (blue) and after suspension in 1.0 M aqueous KOH in ambient air (red). Cyclic voltammetry data of bare HOPG are shown in grey.

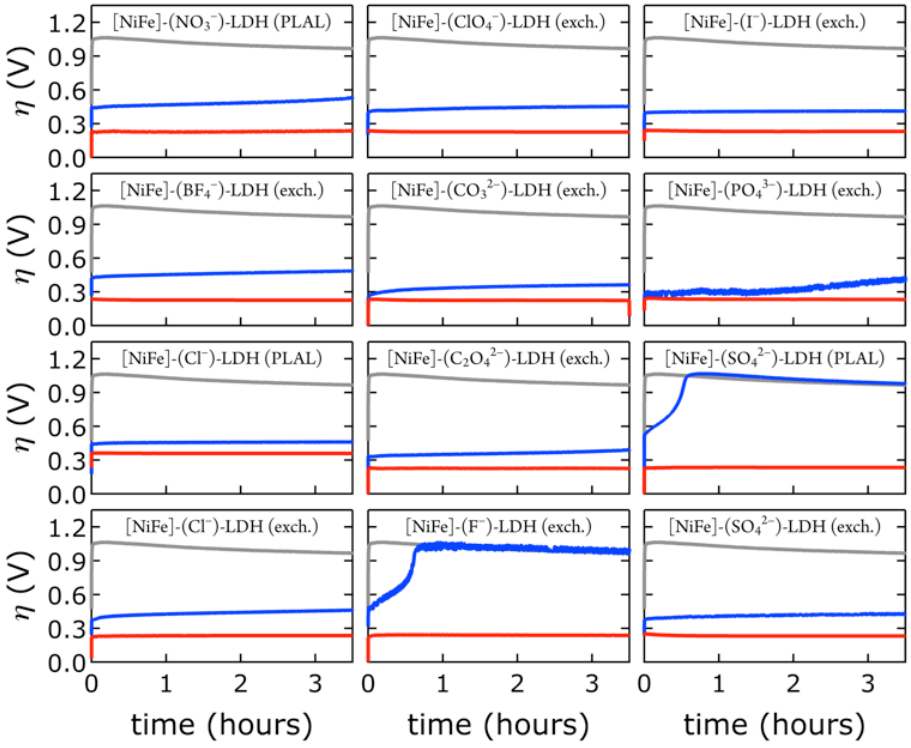

Figure 3.18. Constant current electrolysis of [NiFe]-LDH materials with different interlayer anions in virtually carbonate-free electrolyte in a glove box (blue) and after suspension in 1.0 M aqueous KOH in ambient air (red). Chronopotentiometry data of bare HOPG are shown in grey. All data were collected at a constant current density of 1 mA cm^{-2}.

After exposure to carbonate-containing electrolyte (1.0 M aqueous KOH in ambient air), all materials immediately featured low, very similar overpotentials, consistent with formation of [NiFe]-(CO_3^{2-})-LDH materials; only the [NiFe]-(Cl^-)-LDH material synthesized by PLAL, which consisted of larger nanosheets (see Table 3-2), exhibited slightly inferior performance. Likewise, the cyclic voltammograms of all materials after exposure to 1.0 M aqueous KOH in ambient air were very similar; again, the [NiFe]-(Cl^-)-LDH synthesized by PLAL showed slightly less current density (Figure 3.17). All materials exhibited remarkable stability over several hours in carbonate-containing (self-buffered) alkaline electrolyte.

3.4.2. Data Correlations

We tried to find correlations of electrochemical data, such as overpotentials and prewave peak positions, with the materials' structural and chemical characteristics, such as basal spacing, intrasheet $[NiFe](OH)_2$ structure, and interlayer anion basicity. Data of unstable materials, such as [NiFe]-(F^-)-LDH (exch.) and [NiFe]-(SO_4^{2-})-LDH (PLAL), were not included into correlations. Only small amounts of the initially deposited [NiFe]-(F^-)-LDH (exch.) and [NiFe]-(SO_4^{2-})-LDH (PLAL) materials were visible on the HOPG electrode after chronopotentiometry experiments.

We derived overpotentials of [NiFe]-LDH materials with different interlayer anions from chronopotentiometry data, which were collected in virtually carbonate-free electrolyte (glove box). They are plotted as a function of the pK_a values of the conjugate acids of the interlayer anions (Table 3-3) in Figure 3.19.

Table 3-3: Anions, conjugate acids, and pK_a values of conjugate acids of anions with references.

Anion	Conjugate acid	pK_a	Reference
NO_3^-	HNO_3	–1.3	59
BF_4^-	HBF_4	–0.44	60
Cl^-	HCl	–9.3	61
ClO_4^-	$HClO_4$	1.77	62
CO_3^{2-}	HCO_3^-	10.25	62
$C_2O_4^{2-}$	$HC_2O_4^-$	4.19	62
F^-	HF	3.45	62
I^-	HI	0.77	62
PO_4^{3-}	HPO_4^{2-}	12.67	62
SO_4^{2-}	HSO_4^-	1.92	62

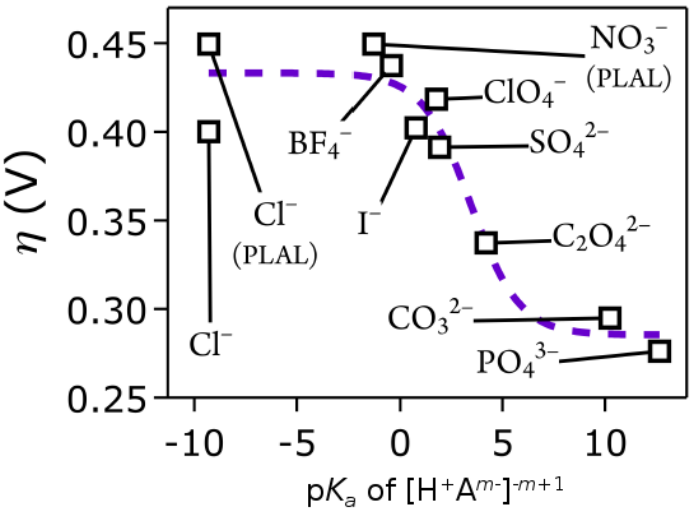

Figure 3.19. Overpotentials η of [NiFe]-LDH materials with different interlayer anions A^{m-} derived from constant current electrolysis at 1 mA cm^{-2} in virtually carbonate-free electrolyte as a function of anion basicity. Bare anion labels denote materials prepared by exchange from [NiFe]-(NO_3^-)-LDH.

We discovered a strong correlation between water oxidation activity and the pK_a values of the conjugate acids of the interlayer anions; there is sigmoidal behavior with a midpoint of 3.4 ± 0.7 (Figure 3.19).

Mechanistically, this behavior suggests a base-assisted deprotonation step during turnover. The apparent pK_a, determined electrochemically, may be related to the pK_a of a higher-valent metal-oxo species, which is typically much lower than 7. This effect manifests as an "oxo wall" between the Fe and Co triads of the periodic table.[57] Transition metals to the left of the wall make stable oxo complexes, whereas those to the right are too basic and are easily attacked by electrophiles. Different Lewis basicities, which would lower the potential required to reach the necessary Fe and/or Ni oxidation states, could also be at play.

Our discovery of the sigmoidal dependence of water oxidation activity on anion basicity is perhaps surprising, given that there is 1 M OH^- in the electrolyte. Hydroxide is of course also a good base. It is unclear, however, how much hydroxide resides in the interlayer galleries. Our results imply that the di- and tri-valent anions outcompeted hydroxide presence in the interlayer space. This is consistent with previous reports on anion affinities in LDHs (see above).[24] Our observation that the [NiFe]-(CO_3^{2-})-LDH catalyst regenerated in carbonate-containing aqueous base and showed exceptional robustness supports our conclusion that this higher-valent anion was strongly bound and played an active role during turnover. We cannot exclude that in the regime of lower activity, where we have monovalent interlayer anions (to the left in Figure 3.19), the catalysis is governed by hydroxide-mediated deprotonation. It is important to note, however, that catalytic activity can be enhanced by di- and tri-valent anions. The higher charge of multivalent anions makes them stronger proton acceptors and electron donors than monovalent anions. It is possible that a strongly bound proton acceptor is required to reduce the activation barrier for water oxidation.

We tried to correlate Ni-based redox features to interlayer anion basicity to assess if more electron-rich anions would lead to electronic changes in the nickel hydroxide layers. We deliberately chose the reduction wave of the cyclic voltammograms for analysis as the

oxidation prewave was partly obscured by the catalytic wave, rendering an accurate determination of the peak maximum problematic. This is illustrated in Figure 3.20 (a). We did not observe a clear correlation of the central polarization potential of the reduction waves of [NiFe]-LDH nanosheets with interlayer anions exhibiting different basicities or overpotential.

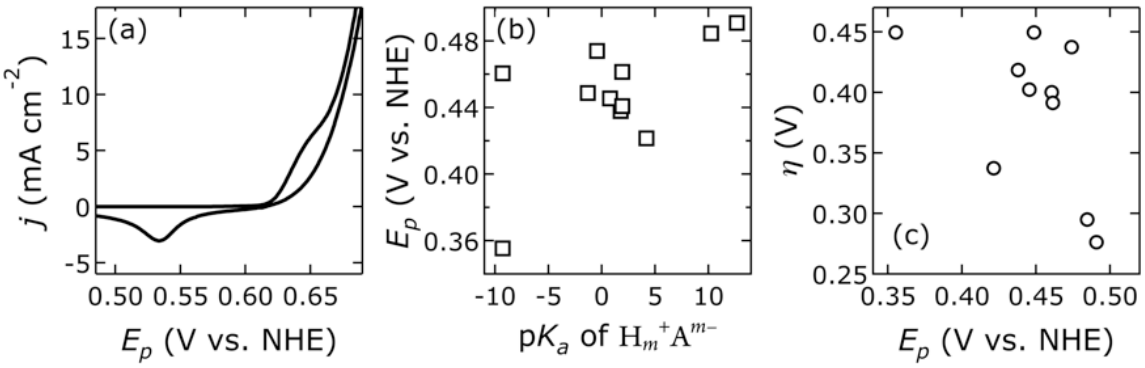

Figure 3.20. Magnified pre-water-oxidation-wave region of a representative cyclic voltammogram of [NiFe]-LDH nanosheets (a). Central polarization potential E_p of the reduction wave of [NiFe]-LDH nanosheets with different interlayer anions, collected in virtually carbonate-free electrolyte, as a function of anion basicity (b), and overpotential η as a function of E_p (c).

In addition, we investigated if the measured overpotentials depended on the intrasheet $[NiFe](OH)_2$ structure. To this end, we took IR spectra of our [NiFe]-(NO_3^-)-LDH nanosheets that had been soaked in different pH aqueous KOH solutions and analyzed lines, which are characteristic for OH-deformations; the broad bands centered around 500 cm^{-1} are Ni–O lattice modes[5] (Figure 3.21 left). The ratios of two such lines as a function of solution pH showed sigmoid behavior with a midpoint of approximately 12 (Figure 3.21 right).

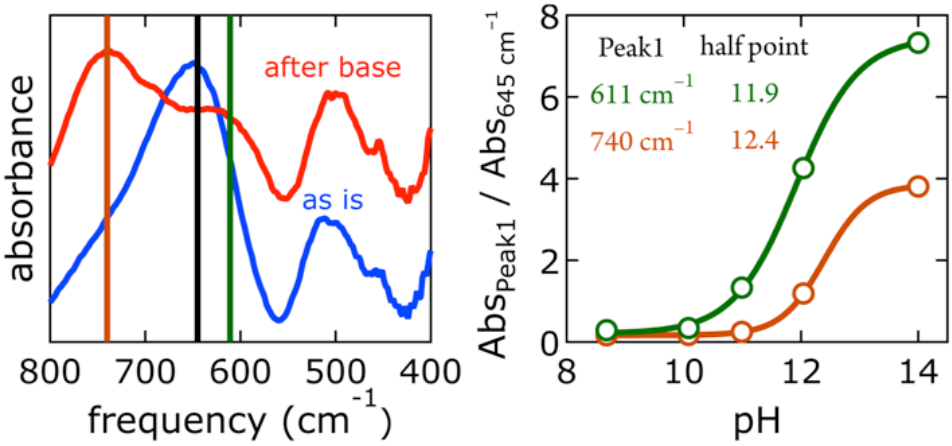

Figure 3.21. Left: IR spectra of [NiFe]-(NO_3^-)-LDH nanosheets as synthesized (as is) and after suspension in 1.0 M aqueous KOH in ambient air (after base). The vertical lines indicate the peaks that were analyzed. Right: Titration curves as a function of solution pH.

We emphasize that we did not find that catalytic activity was a function of $Ni^{3+/2+}$ prewave position,[58] indicating that the $Ni^{3+/2+}$ couple is not the rate-determining step for water oxidation. Likewise**,** measured overpotentials did not depend on the slab [NiFe]$(OH)_2$ structure, as evidenced by analysis of the IR spectra; intensities of characteristic OH-deformation modes as a function of soaking solution pH showed sigmoidal behavior with a midpoint of approximately 12, whereas overpotentials vs. pK_a values from anion-conjugate-acid data had a midpoint of 3.4 ± 0.7, indicating that intrasheet structural changes were unrelated to observed activities.

Perhaps surprisingly, measured overpotentials also did not depend on the basal spacings. In Figure 3.22, overpotentials of [NiFe]-LDH materials with different interlayer anions, collected in virtually carbonate-free electrolyte (glove box), are plotted as a function of the materials' basal spacings. Layer-to-layer spacings would only matter if reactants and products had to diffuse though the interlamellar galleries for redox reactions mediated by (central) intrasheet species. Clearly, this is not the case for our materials.

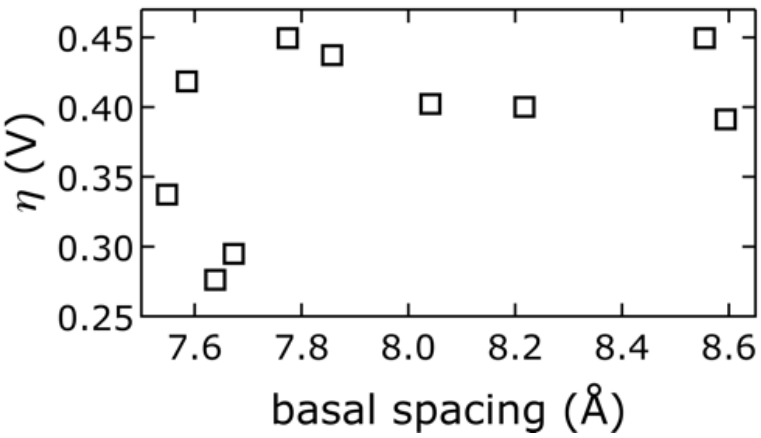

Figure 3.22. Observed overpotentials η at 10 min from chronopotentiometry data collected in virtually carbonate-free electrolyte (glove box) as a function of the basal spacing of [NiFe]-LDH materials with different interlayer anions.

3.4.3. Density functional theory calculations

We recently reported two distinct N 1s signals in the XPS data of PLAL-synthesized [NiFe]-(NO_3^-)-LDH precatalysts.[20] One peak was centered at 407.3 eV, attributable to nitrate,[47] and the other at 405.1 eV, which we tentatively ascribed to nitrate or nitrite in an unusual chemical environment. Curiously, the turnover frequency of [NiFe]-(NO_3^-)-LDH precatalysts with different Ni/Fe ratios depended on the relative proportion of the two XPS peaks.[20]

We performed DFT calculations on model LDH clusters, $[Ni_9Fe_1(OH)_{20}(NO_{2\text{ or }3})]$, to obtain information about the previously unassigned N 1s XPS signal at 405.1 eV. We wanted to find out if binding nitrate or nitrite to the [NiFe]-LDH nanosheets in various positions and binding motifs could explain the observed N 1s binding energy (BE) of 405.1 eV. This BE would require either (i) a *lowering* of the N 1s BE of nitrate by 2.2 eV or (ii) an *increase* of the N 1s BE of nitrite by 1.6 eV. We calculated N 1s core level shifts relative to a nitrate anion, which was bound by a hydrogen bridge to the top-side of the cluster. Technical details concerning the calculation of the N 1s core level binding energies and the choice of the cluster models are described above.

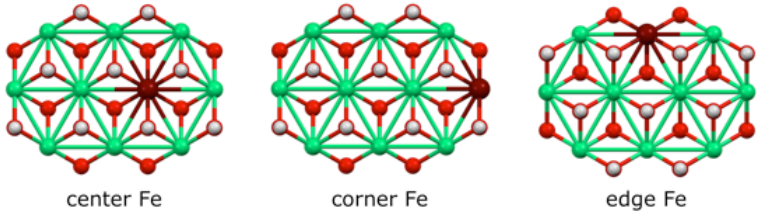

Figure 3.23. Fe sites in the basic $[Ni_9Fe_1(OH)_{18}]^{3+}$ cluster fragment. Colors: Ni green, Fe maroon, O red, H white.

We assessed the binding of nitrate and nitrite anions to different Fe sites within our prolate model clusters (central, edge at the rim along the long axis, and corner at the short-axis rim, Figure 3.23).

We also investigated different anion binding motifs: nitrate binding via one of its O atoms, nitrite binding by both O and N atom coordination (Figure 3.24).

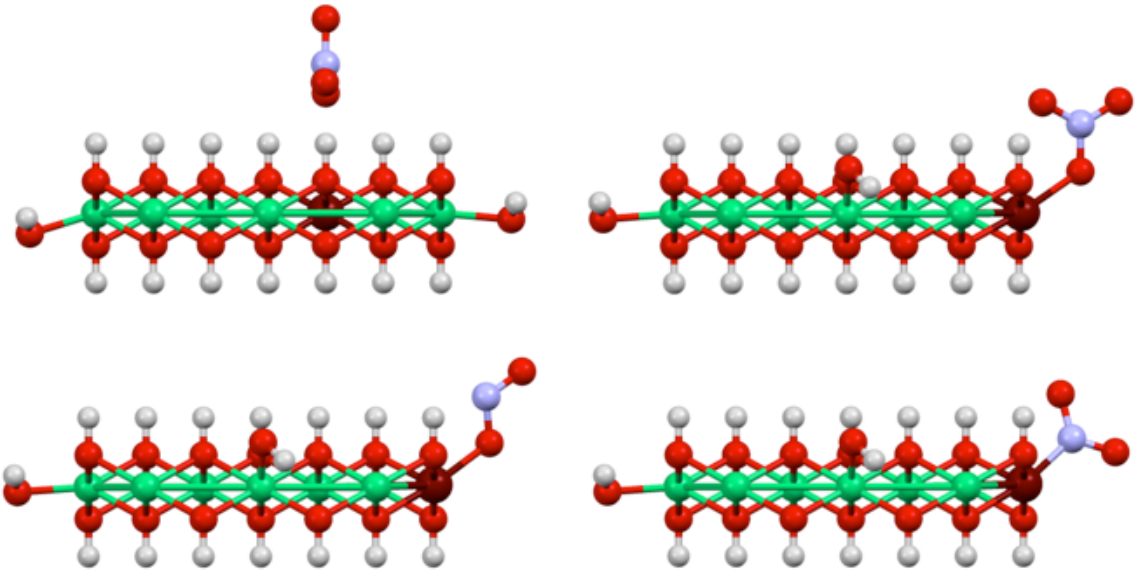

Figure 3.24. Illustration of the basic anion coordination motifs of NO_3^- (top) and NO_2^- (bottom) to $[Ni_9Fe_1(OH)_{20}]$ clusters. Only coordination to corner sites of the clusters are shown here, other sites were also investigated (Figure 3.23). The top left structure shows the reference for the calculation of core level shift from core level binding energies. Colors: Ni green, Fe maroon, N blue, O red, H white.

The experimentally observed N 1s XPS peak at 405.1 eV corresponds to a core level shift of –2.2 eV with respect to the electron binding energy of pristine nitrate at 407.4 eV.[48] Calculations of nitrate binding to the clusters yielded core level shifts that were inconsistent with the XPS signal at 405.1 eV (Figure 3.25). However, N-coordination of nitrite to edge-site Fe resulted in a core level shift of –2.1 eV, which is in very close agreement with the experimentally observed shift. Other nitrite binding motifs were not in accord with the experimental XPS data. We note that formation of nitrite was possible during our PLAL from nitrate-containing ablation solutions, as evidenced by the fact that PLAL-made [NiFe]-(SO_4^{2-})-LDH exhibited an N 1s peak at 403.5 eV, attributable to nitrite (see above).[48]

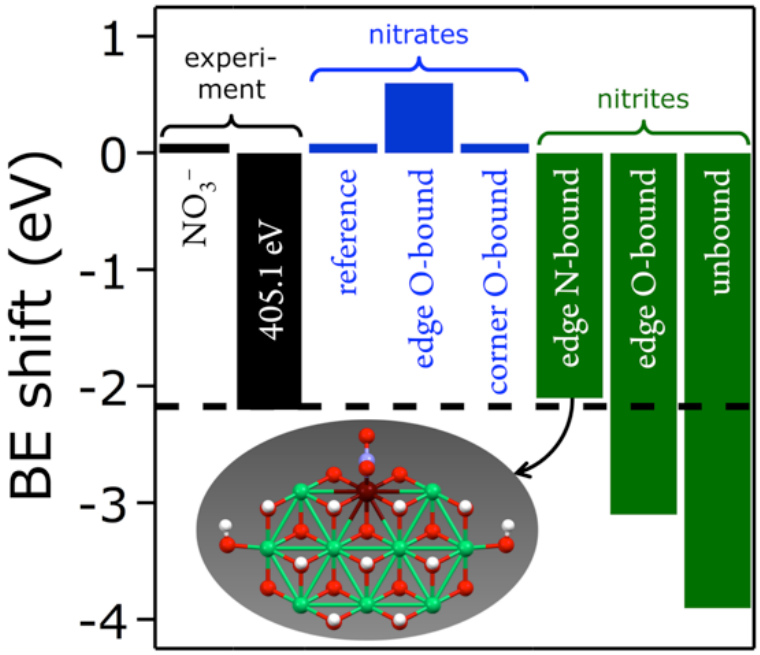

Figure 3.25. Measured (black) and calculated XPS binding energy (BE) shifts (is-CLS) for differently bound nitrates (blue) and nitrites (green) with a calculated structure that is consistent with the feature at 405.1 eV. Atom colors: Ni green, Fe maroon, N blue, O red, H white.

Assignment of the experimentally observed 405.1 eV N 1s peak of the [NiFe]-(NO_3^-)-LDH nanosheet precatalyst to nitrite bound by its N-atom to edge-site Fe suggested

that this XPS signal provided a means to quantify Fe edge sites. It also rationalized why we had previously observed higher catalytic turnover frequencies as the relative proportion of the 405.1 eV peak with respect to that at 407.3 eV increased.[20] Therefore, we conclude that edge-site Fe plays a major role in water oxidation catalyzed by our PLAL-synthesized [NiFe]-LDH nanosheets. Our calculations are consistent with our observation that the overpotentials of [NiFe]-LDH materials with different interlayer anions did not correlate with basal spacings.

3.5. Conclusions

We synthesized a series of [NiFe]-LDH nanosheets with various intercalated anions, both directly by PLAL and by anion metathesis. We found that their water oxidation activity correlated with the pK_a of the conjugate acid of the interlayer anions and propose that the anions' Brønsted or Lewis basicity plays a role in the water oxidation mechanism. Our nanocatalysts were regenerated and most active in alkaline electrolyte in ambient air, as carbonate rapidly replaced other interlayer anions. Finally, our DFT calculations suggest that a previously unassigned N 1s species in the precatalyst, which correlated with higher water oxidation activity,[20] is consistent with nitrite bound by its N-atom to edge-site iron. This finding implies that iron sites at the edges of our [NiFe]-LDH nanosheets are active in water oxidation catalysis.

3.6. References and Notes

(1) H. B. Gray, *Nature Chem.*, 2009, **1**, 7-7.

(2) N. S. Lewis and D. G. Nocera, *Proc. Natl. Acad. Sci. U. S. A.*, 2006, **103**, 15729-15735.

(3) Y. Lee, J. H. Choi, H. J. Jeon, K. M. Choi, J. W. Lee and J. K. Kang, *Energy Environ. Sci.*, 2011, **4**, 914-920.

(4) M. Gong, Y. Li, H. Wang, Y. Liang, J. Z. Wu, J. Zhou, J. Wang, T. Regier, F. Wei and H. Dai, *J. Am. Chem. Soc.*, 2013, **135**, 8452-8455.

(5) B. Li, Y. Zhao, S. Zhang, W. Gao and M. Wei, *ACS Appl. Mater. Interfaces*, 2013, **5**, 10233-10239.

(6) Y. Zhang, B. Cui, C. Zhao, H. Lin and J. Li, *Phys. Chem. Chem. Phys.*, 2013, **15**, 7363-7369.

(7) X. Zou, A. Goswami and T. Asefa, *J. Am. Chem. Soc.*, 2013, **135**, 17242-17245.

(8) S. J. Kim, Y. Lee, D. K. Lee, J. W. Lee and J. K. Kang, *J. Mater. Chem. A*, 2014, **2**, 4136-4139.

(9) Y. Li, L. Zhang, X. Xiang, D. Yan and F. Li, *J. Mater. Chem. A*, 2014, **2**, 13250-13258.

(10) D. Tang, Y. Han, W. Ji, S. Qiao, X. Zhou, R. Liu, X. Han, H. Huang, Y. Liu and Z. Kang, *Dalton Trans.*, 2014, **43**, 15119-15125.

(11) O. Diaz-Morales, I. Ledezma-Yanez, M. T. M. Koper and F. Calle-Vallejo, *ACS Catal.*, 2015, **5**, 5380-5387.

(12) I. J. Godwin and M. E. G. Lyons, *Electrochem. Commun.*, 2013, **32**, 39-42.

(13) M. Gong, Y. Li, H. Wang, Y. Liang, J. Z. Wu, J. Zhou, J. Wang, T. Regier, F. Wei and H. Dai, *J. Am. Chem. Soc.*, 2013, **135**, 8452-8455.

(14) M. Gao, W. Sheng, Z. Zhuang, Q. Fang, S. Gu, J. Jiang and Y. Yan, *J. Am. Chem. Soc.*, 2014, **136**, 7077-7084.

(15) F. Song and X. Hu, *Nat. Commun.*, 2014, **5**, 4477-4486.

(16) L. Trotochaud, S. L. Young, J. K. Ranney and S. W. Boettcher, *J. Am. Chem. Soc.*, 2014, **136**, 6744-6753.

(17) Y. Zhao, B. Li, Q. Wang, W. Gao, C. J. Wang, M. Wei, D. G. Evans, X. Duan and D. O'Hare, *Chem. Sci.*, 2014, **5**, 951-958.

(18) C. G. Morales-Guio, M. T. Mayer, A. Yella, S. D. Tilley, M. Grätzel and X. Hu, *J. Am. Chem. Soc.*, 2015, **137**, 9927-9936.

(19) M. W. Louie and A. T. Bell, *J. Am. Chem. Soc.*, 2013, **135**, 12329-12337.

(20) B. M. Hunter, J. D. Blakemore, M. Deimund, H. B. Gray, J. R. Winkler and A. M. Müller, *J. Am. Chem. Soc.*, 2014, **136**, 13118-13121.

(21) M. S. Burke, L. J. Enman, A. S. Batchellor, S. Zou and S. W. Boettcher, *Chem. Mater.*, 2015, **27**, 7549-7558.

(22) M. S. Burke, M. G. Kast, L. Trotochaud, A. M. Smith and S. W. Boettcher, *J. Am. Chem. Soc.*, 2015, **137**, 3638-3648.

(23) X. Duan and D. G. Evans, *Layered double hydroxides*, Springer Science & Business Media, 2006.

(24) S. Miyata, *Clays Clay Miner.*, 1983, **31**, 305-311.

(25) D. G. Evans and R. C. Slade, *Struct. Bond.*, 2006, **119**, 1-87.

(26) J. D. Blakemore, H. B. Gray, J. R. Winkler and A. M. Müller, *ACS Catal.*, 2013, **3**, 2497-2500.

(27) T. L. Barr and S. Seal, *J. Vac. Sci. Technol. A*, 1995, **13**, 1239-1246.

(28) D. A. Shirley, *Phys. Rev. B*, 1972, **5**, 4709-4714.

(29) P. Scherrer, *Nachr. Ges. Wiss. Göttingen*, 1918, **26**, 98-100.

(30) J. I. Langford and A. J. C. Wilson, *J. Appl. Crystallogr.*, 1978, **11**, 102-113.

(31) W. H. Bragg and W. L. Bragg, *Proc R. Soc. Lond. A*, 1913, **88**, 428-438.

(32) J. E. S. Han and T. Y. Chao, *Ind. Eng. Chem. Anal. Ed.*, 1932, **4**, 229-232.

(33) R. Ahlrichs, F. Furche, C. Hättig, W. M. Klopper, M. Sierka and F. Weigend, *Turbomole program package, version 6.6*, Karlsruhe, Germany, since 1989 (http://www.turbomole.com).

(34) C. Adamo and V. Barone, *J. Chem. Phys.*, 1999, **110**, 6158-6170.

(35) M. Ernzerhof and G. E. Scuseria, *J. Chem. Phys.*, 1999, **110**, 5029-5036.

(36) J. P. Perdew, M. Ernzerhof and K. Burke, *J. Chem. Phys.*, 1996, **105**, 9982-9985.

(37) F. Weigend and R. Ahlrichs, *Phys. Chem. Chem. Phys.*, 2005, **7**, 3297-3305.

(38) A. Klamt and G. Schüürmann, *J. Chem Soc., Perkin Trans. 2*, 1993, 799.

(39) A. Schäfer, A. Klamt, D. Sattel, J. C. Lohrenz and F. Eckert, *Phys. Chem. Chem. Phys.*, 2000, **2**, 2187-2193.

(40) J. C. Slater, *Adv. Quantum Chem.*, 1972, **6**, 92.

(41) N. N. Greenwood and A. Earnshaw, *Chemistry of the Elements*, 1984.

(42) R. N. King, *ESCA Binding Energy Chart*, Surface Science Instruments, Mountain View, CA.

(43) A. N. Mansour and C. A. Melendres, *Surf. Sci. Spectra*, 1994, **3**, 247-254.

(44) *NIST X-ray Photoelectron Spectroscopy Database*, X-ray Photoelectron Spectroscopy Database 20, Version 4.1 (National Institute of Standards and Technology, Gaithersburg, 2012); http://srdata.nist.gov/xps/.

(45) M. C. Biesinger, B. P. Payne, L. W. M. Lau, A. Gerson and R. S. C. Smart, *Surf. Interface Anal.*, 2009, **41**, 324-332.

(46) W. Temesghen and P. Sherwood, *Anal. Bioanal. Chem.*, 2002, **373**, 601-608.

(47) C. E. Nanayakkara, P. M. Jayaweera, G. Rubasinghege, J. Baltrusaitis and V. H. Grassian, *J. Phys. Chem. A*, 2013, **118**, 158-166.

(48) J. Baltrusaitis, P. M. Jayaweera and V. H. Grassian, *Phys. Chem. Chem. Phys.*, 2009, **11**, 8295-8305.

(49) C. Vaysse, L. Guerlou-Demourgues and C. Delmas, *Inorg. Chem.*, 2002, **41**, 6905-6913.

(50) T. S. Stanimirova, G. Kirov and E. Dinolova, *J. Mater. Sci. Lett.*, 2001, **20**, 453-455.

(51) S. Carlino, *Solid State Ionics*, 1997, **98**, 73-84.

(52) D. R. Lide, *CRC Handbook of Chemistry and Physics*, CRC Press, Boca Raton, FL, USA, 72nd edn., 1991.

(53) V. Rives, *Mater. Chem. Phys.*, 2002, **75**, 19-25.

(54) T. Stanimirova, N. Piperov, N. Petrova and G. Kirov, *Clay Miner.*, 2004, **39**, 177-191.

(55) F. A. Miller and C. H. Wilkins, *Anal. Chem.*, 1952, **24**, 1253-1294.

(56) W. L. F. Armarego and D. D. Perrin, *Purification of Laboratory Chemicals*, Butterworth-Heinemann, Oxford, UK, 4th edn., 1987.

(57) J. R. Winkler and H. B. Gray, *Struct. Bond.*, 2012, **142**, 17-28.

(58) The prewaves of nickel-iron double hydroxide cyclic voltammograms have previously been assigned to the $Ni^{3+/2+}$ redox couple (Trotochaud, L.; Young, S. L.; Ranney, J. K.; Boettcher, S. W. *J. Am. Chem. Soc.* 2014, **136**, 6744-6753).

(59) J. Moir and N. Wood, *CMLS, Cell. Mol. Life Sci.*, 2001, **58**, 215-224.

(60) T. Sudakova and V. Krasnoshchekov, *Zh. Neorg. Khim.*, 1978, **23**, 1506-1508.

(61) W. E. Dasent, *Inorganic energetics: an introduction*, Cambridge University Press, Cambridge, UK, 1982. Chapter 5.

(62) D. R. Lide, *CRC Handbook of Chemistry and Physics*, CRC Press, Boca Raton, FL, USA, 72nd edn., 1991.

4 TRAPPING AN IRON(VI) WATER SPLITTING INTERMEDIATE IN NONAQUEOUS MEDIA

4.1 Summary

The sustainable and economical conversion of solar energy into storable, transportable fuels by solar-driven water splitting is a grand challenge of 21st century chemistry. The mechanisms by which heterogeneous materials perform the anodic half-reaction, water oxidation, are not well understood. In this chapter, we describe *in-situ* spectroscopic measurements in nonaqueous media designed to trap an exceptionally strong oxidant generated electrochemically from an iron-containing nickel layered double hydroxide ([NiFe]-LDH) material. Anodic polarization of this material in acetonitrile produces prominent infrared absorption features (840 and 856 cm^{-1}) that are quenched by the addition of water. These vibrational spectroscopic signatures along with a potential-dependent extremely narrow luminescence peak at 1633 nm indicate that the reactive intermediate is a *cis*-dioxo-iron(VI) species. An absorption in the Mössbauer spectrum of the material, which disappears upon exposure to alkaline acetonitrile, is consistent with population of a high-valent iron-oxo species. Importantly, chemical trapping experiments reveal that addition of H_2O to the polarized electrochemical cell produces hydrogen peroxide; and addition of HO^- generates oxygen. Re-polarization of the electrode restores the iron(VI) spectroscopic signatures, confirming that the high-valent oxo complex is active in the electrocatalytic water oxidation cycle. Our work demonstrates that *in-situ* spectroscopy in nonaqueous media offers a powerful new approach to the study of aqueous redox mechanisms.

4.2. Results

Nickel-iron layered double hydroxide ([NiFe]-LDH) nanoparticles are highly active catalysts for water oxidation at pH 14 (Figure 4.1)[1,2]. These nanocatalysts, which were synthesized by pulsed laser ablation in water[3], operate at low overpotentials for oxygen evolution on flat glassy carbon electrodes. Precisely because they are such active materials, steady-state concentrations of catalytic species are necessarily low under turnover conditions; indeed, initial experiments on [NiFe]-LDH resulted in conflicting reports on the identity of the catalytically relevant sites[4-7]. Consequently, there is little consensus about the operative mechanism for these (and other) water oxidation catalysts[8].

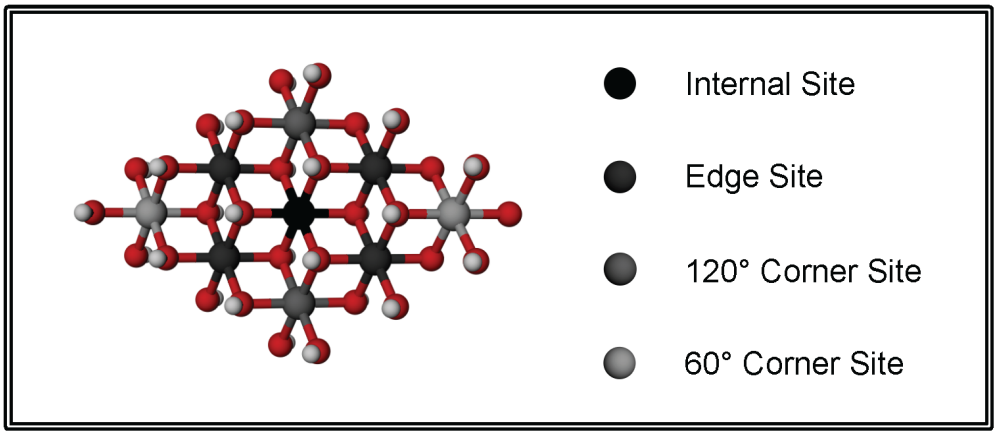

Figure 4.1. Structure of [NiFe]-LDH. In the [NiFe]-LDH material, a sheet of $Ni(OH)_6$ edge-shared octahedra contains a small amount (~20%) of iron substituting at nickel sites[9]. Different types of peripheral sites are indicated.

We have developed an alternative approach to examine reactive intermediates of highly active water-oxidation catalysts. Strasser, Dau, and coworkers suggested that the failure to observe oxidized metals in *operando* measurements on highly active [NiFe]-LDH electrodes is likely a consequence of oxygen evolution outpacing metal oxidation[7]. Under these circumstances, the steady state concentration of oxidized catalyst will be extremely

low. By using nonaqueous electrolytes (acetonitrile, nitromethane) in which the concentration of substrate (H_2O, HO^-) is reduced dramatically, the oxygen evolution rate is slowed sufficiently to permit formation of significant concentrations of reactive intermediates. Owing to the protracted reactive intermediate lifetime, we could use *in-situ* IR, UV-vis, Raman, luminescence, and Mössbauer spectroelectrochemistry to characterize a high-valent intermediate that subsequently reacted with H_2O to produce H_2O_2 and with HO^- to produce O_2. The results of our study suggest that a *cis*-dioxo-Fe(VI) species likely is an active intermediate in [NiFe]-LDH catalyzed water oxidation.

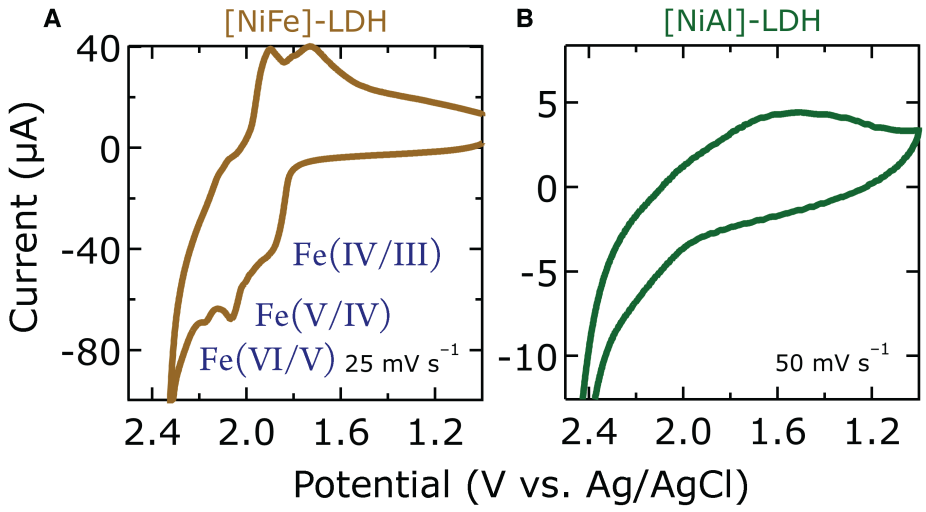

Figure 4.2. Cyclic voltammograms of [NiFe]-LDH (**A**) and [NiAl]-LDH (**B**) on glassy carbon in dry acetonitrile. $E°$(ferricenium/ferrocene) (Fc^+/Fc) was measured to be 410 mV under virtually identical conditions.

4.2.1. Electrochemistry

Under inert conditions (acetonitrile or nitromethane with 0.1 *M* [TBA]PF_6 (TBA = tetra-*n*-butylammonium) as the supporting electrolyte), cyclic voltammetry of [NiFe]-LDH films cast onto glassy carbon surfaces revealed three chemically reversible oxidations that were

absent in the iron-free analogue, [NiAl]-LDH (Figure 4.2). Because iron substitutes into the nickel-hydroxide lattice as Fe(III), we assign these oxidations to the sequential formation of Fe(IV), Fe(V), and Fe(VI), with smaller currents for each successive anodic process[10]. By reversing scans after each successive oxidation event and observing a coupled reduction, we concluded that the events were quasi-reversible on the electrochemical timescale (Figure 4.3). Closely spaced redox couples are not uncommon for proton-coupled electron transfer steps of molecular species; for example, $[Ru(II)(bpy)_2(OH_2)_2]^{2+}$ can achieve oxidation states II/III/IV/V/VI over a potential range of 0.6 V[11]. Assuming a formula of $Ni_{0.78}Fe_{0.22}(OH)_2(NO_3)_{0.22}$, we estimated from coulometry that ~0.002% of the iron sites are electrochemically active to make Fe(IV). Approximately half as many sites (0.001%) are active at the Fe(V/IV) couple, while only 0.0002% of the sites proceed to Fe(VI). The decrease in the number of electrochemically active sites at the higher potential couples is consistent with the limited number of atoms at edge and corner sites in ca. 10 nm nanosheets, suggesting that high-valent species are only formed at the perimeters of the particles.

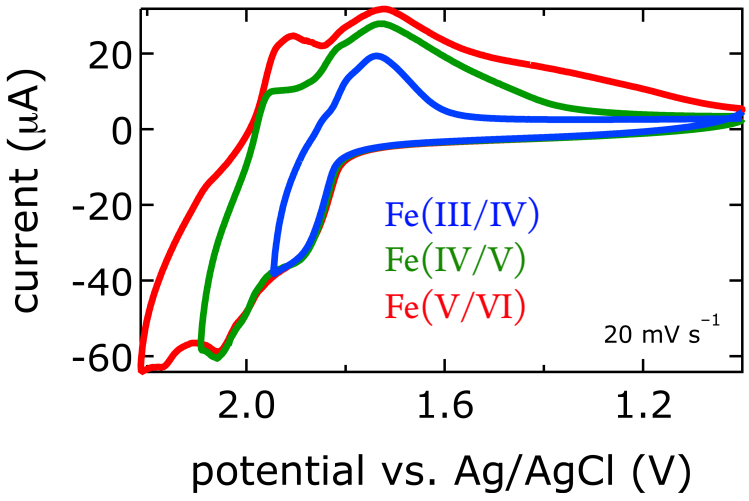

Figure 4.3. Cyclic voltammetry of [NiFe]-LDH in 0.1 M tetrabutylammonium hexafluorophosphate ([TBA]PF_6) in acetonitrile. The scans were reversed after each oxidative event, showing that each was coupled to a corresponding reduction. Scan rate was 20 mV/s.

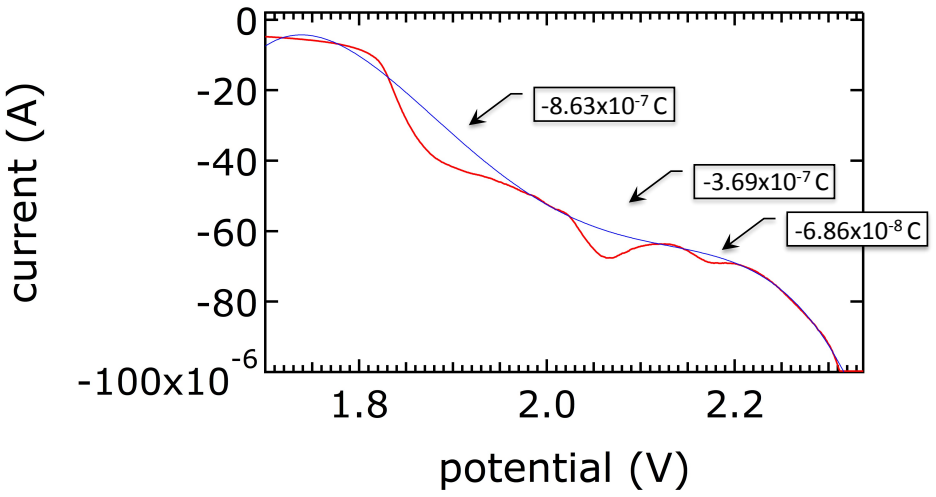

Figure 4.4. Cyclic voltammetry of [NiFe]-LDH in 0.1 M tetrabutylammonium hexafluorophosphate ([TBA]PF_6) in acetonitrile with baseline subtraction and charge passed integrated for the 3 iron-based features. Reference electrode: Ag/AgCl.

Table 4-1: Calculation of activity of iron in [NiFe]-LDH sample, based on coulometry of cyclic voltammetry.

	Charge Passed	Active Moles	% active
1st oxidation	-8.63×10^{-7}	8.94×10^{-12}	0.00237
2nd oxidation	-3.69×10^{-7}	3.82×10^{-12}	0.00101
3rd oxidation	-6.86×10^{-8}	7.11×10^{-13}	0.000188

4.2.2. Vibrational Spectroscopy

To probe the high-valent iron species, we monitored changes in the vibrational and electronic spectra of [FeNi]-LDH *via* controlled-potential spectroelectrochemistry[12]. The infrared difference spectrum recorded during bulk oxidation of [NiFe]-LDH in acetonitrile[13] exhibits prominent features at 840 and 856 cm^{-1}, with a small shoulder at 877 cm^{-1} (Figure 4.5**A**). Interestingly, the shoulder—whose intensity varied from one experiment to the next—appeared only after an induction period at a rate different from

that of the other two bands (Figure 4.5**C**). Although this oxidized intermediate was thermally stable in dry solvents, introducing "wet" electrolyte (5% water in 0.1 M [TBA]PF_6/acetonitrile) into the IR cell rapidly bleached the three main absorbances, suggesting that they correspond to an active intermediate in the water-oxidation pathway (Figure 4.5**B**)[14].

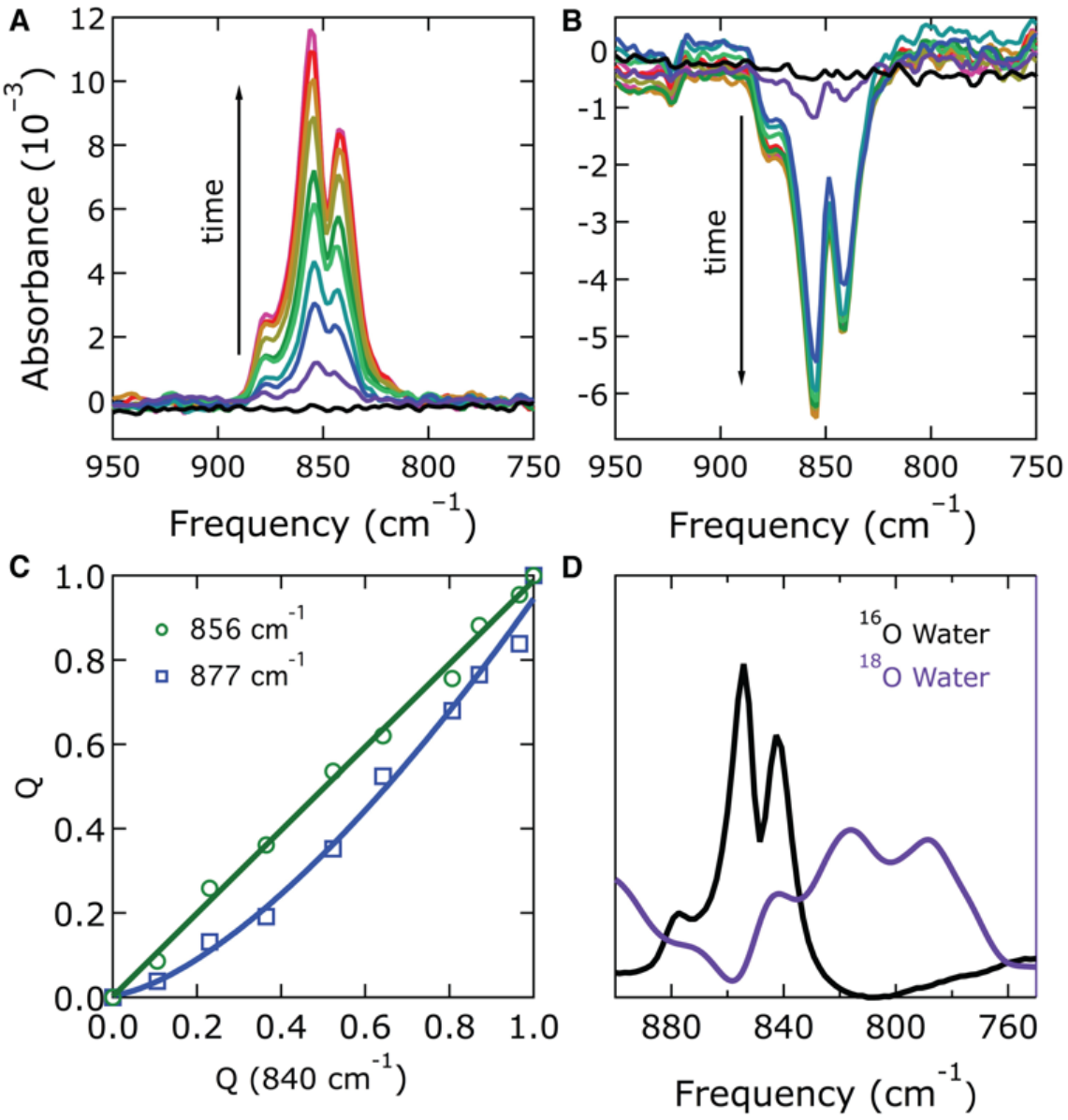

Figure 4.5. (**A**) Three-band signal growing in upon bulk oxidation in acetonitrile (2.3 V vs. Pt), 0.1 M $[TBA]PF_6$, on GC working electrode, Pt counter electrode, 30 sec. between spectra; (**B**) bleach of three-band signal upon injection of water, 30 sec. between spectra; (**C**) fractions of the final Lorentzian peak areas (Q) of the 856 and 877 cm^{-1} bands plotted versus the Q for the 840 cm^{-1} band; solid lines are fits to linear (green) and polynominal ($c_1 + c_2x^{c3}$) (blue) functions to emphasize the different trends; (**D**) exhaustive electrolysis isotope exchange in $H_2{}^{18}O$ followed by *in situ* infrared analysis.

The 840 and 856 cm^{-1} features in the spectrum are attributable to high-valent iron-oxo species. We considered the possible formation of both a mono-oxo Fe(IV)=O center[15] as well as a more highly oxidized *cis*-dioxo-Fe(VI) species—the latter by analogy to the tetraoxoferrate(VI) anion (FeO_4^{2-}). Because a mono-oxo Fe(IV)=O center would exhibit just a *single* Fe-O stretch, we assign the 840- and 856-cm^{-1} peaks to the antisymmetric and symmetric stretches of a *cis*-dioxo-Fe(VI) fragment. The symmetric and antisymmetric stretches of monomeric dioxo species are generally split by 10-30 cm^{-1}.[16-19] Using FeO_4^{2-} as a model for the putative dioxo-Fe(VI) species, DFT calculations predict considerable intensity for the Fe-O stretches in the infrared spectrum. Features corresponding to bending modes (<400 cm^{-1}) should also appear in the vibrational spectra (Figure 4.6). Subsequent *in-situ* Raman spectroelectrochemical oxidation of drop-cast [FeNi]-LDH films under virtually identical conditions revealed these bends at ~400 cm^{-1} (Figure 4.7).

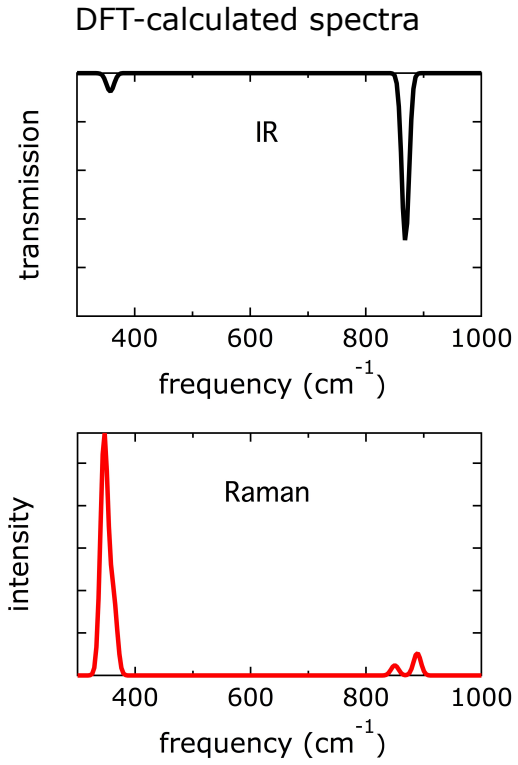

Figure 4.6. (Top) Calculated infrared spectrum for ferrate; (bottom) calculated Raman spectrum for ferrate.

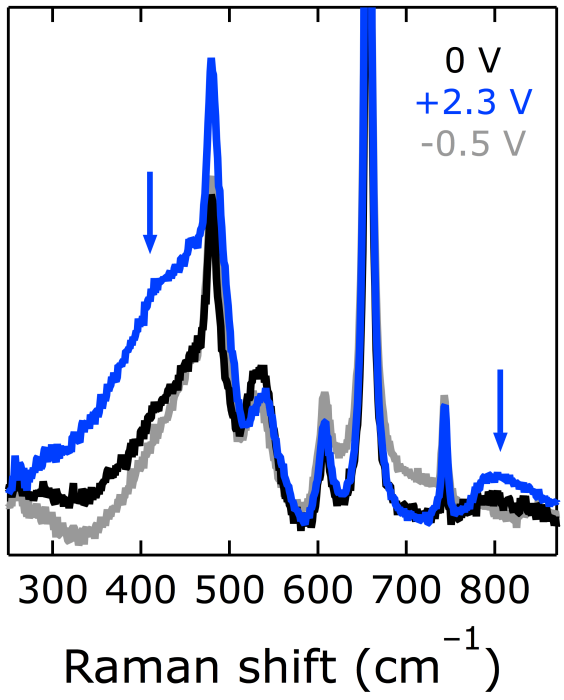

Figure 4.7. Raman spectroelectrochemistry experiment in nitromethane. Signal observed in the bending region (~400 cm^{-1}) upon polarization of the electrode at 2.3 V vs. Pt (blue). The signal is diminished upon cycling to -0.5 V vs. Pt (gray). Nitromethane, 0.1 M [TBA]PF_6, on GC working electrode, Pt counter electrode, and Pt reference electrode. The excitation wavelength was 514.3 nm.

Notably, based on its stretching frequency, we initially attributed the 875 cm^{-1} shoulder to free Fe(VI) in the form of soluble FeO_4^{2-}, which would be leached out of the material at low pH[20]. This was consistent with our observation that a purple substance sometimes appeared in the electrolyte solution after anodic polarization (Figure 4.8). Boettcher et al. previously reported that $Co_{1-x}Fe_x(OOH)$ films with $1 > x > 0.5$ slowly dissolve under water oxidation conditions[21]. It was later suggested that the dissolved species could be tetraoxoferrate(VI)[22]. Our inability to "wash out" the high-energy shoulder, however, indicated that it was due to a surface-bound moiety.

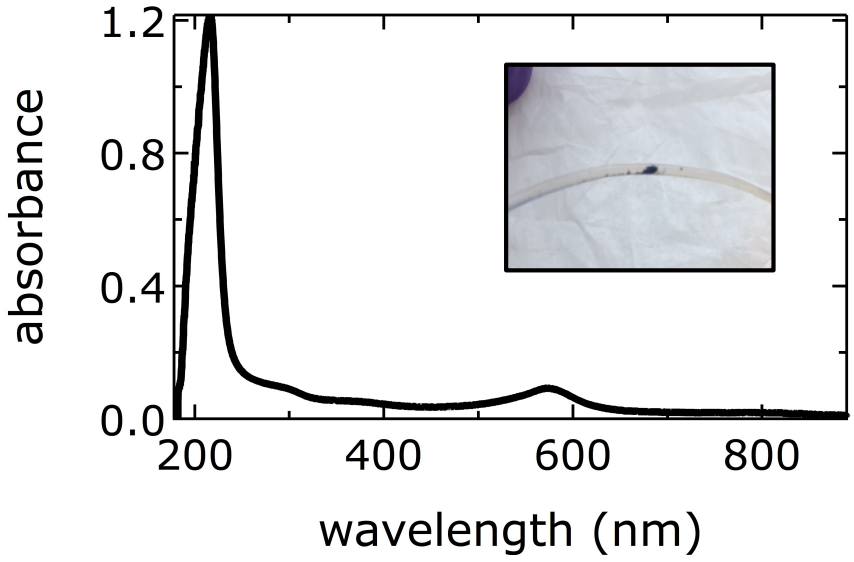

Figure 4.8. UV-visible spectrum of small volume electrolysis electrolyte following 10 minutes of anodic polarization; (Inset) typical purple substance that leaches out during spectroelectrochemistry experiments.

4.2.3. Isotope Labeling Studies

To shed additional light on these highly oxidized species, we carried out several experiments using isotopically labeled (^{18}O) water. Reproducing the 856 and 840 cm^{-1} features in the IR spectrum, we quenched the material with $H_2{}^{18}O$ water. After flushing the spectroelectrochemistry cell with 0.1 M $[TBA]PF_6$ in acetonitrile, we once again carried out a controlled-potential oxidation under non-turnover conditions. The difference spectrum between the initial and final high-valent species revealed bleaches in absorption at 878, 860, and 835 cm^{-1} and increases in absorption at 851 and 844 cm^{-1} (Figure 4.9).

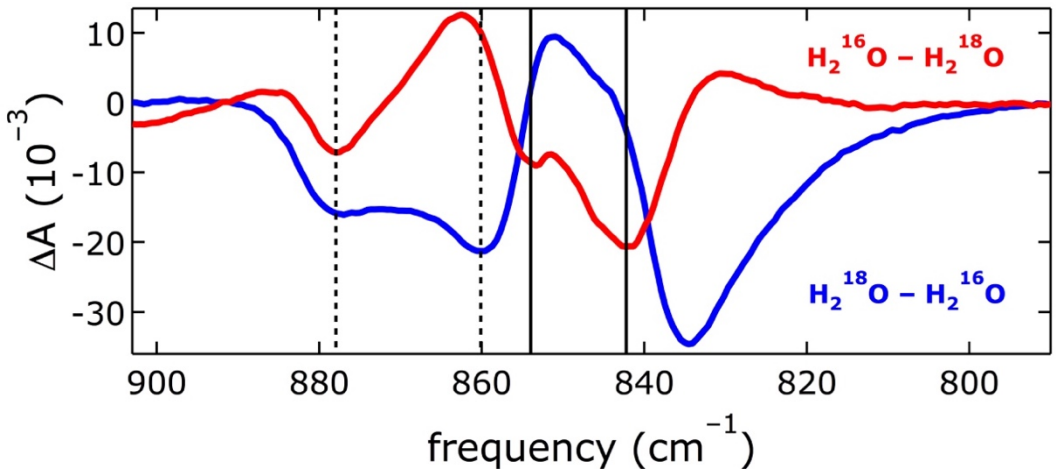

Figure 4.9. Partial isotope exchange experiment. Electrode was polarized at 2.3 V vs. Pt in acetonitrile, background taken, and quenched with 5% $H_2{}^{18}O$ in acetonitrile. Re-polarization at 2.3 V produced the blue trace ($H_2{}^{18}O$ – $H_2{}^{16}O$). A second background was taken and the electrode was quenched with 5% $H_2{}^{16}O$ in acetonitrile. Re-polarization at 2.3 V produced the red trace ($H_2{}^{16}O$ – $H_2{}^{18}O$).

Attempting to achieve full incorporation of ^{18}O into the active sites within the [NiFe]-LDH lattice, we carried out electrocatalytic water oxidation at a drop-cast film using $H_2{}^{18}O$, pH 14 for 30 minutes. We then transferred the modified electrode to the IR spectroelectrochemical cell, and performed a bulk oxidation (2.3 V *vs.* Pt, 0.1 M [TBA]PF_6 in acetonitrile) under non-catalytic conditions. The spectrum of the oxidized material was similar to that of the original high-valent species, but shifted by ~40 cm^{-1} to lower energy, consistent with complete exchange of ^{16}O with ^{18}O (Figure 4.5**D**). Due to the complete exchange, it is apparent that oxygen atoms are incorporated into the [NiFe]-LDH lattice during catalytic dioxygen evolution. These results strongly suggest that the sites we probed were directly involved in water oxidation. Notably, we found that the high-energy shoulder also was shifted by ~40 cm^{-1}, fully consistent with a side-bound peroxide[23].

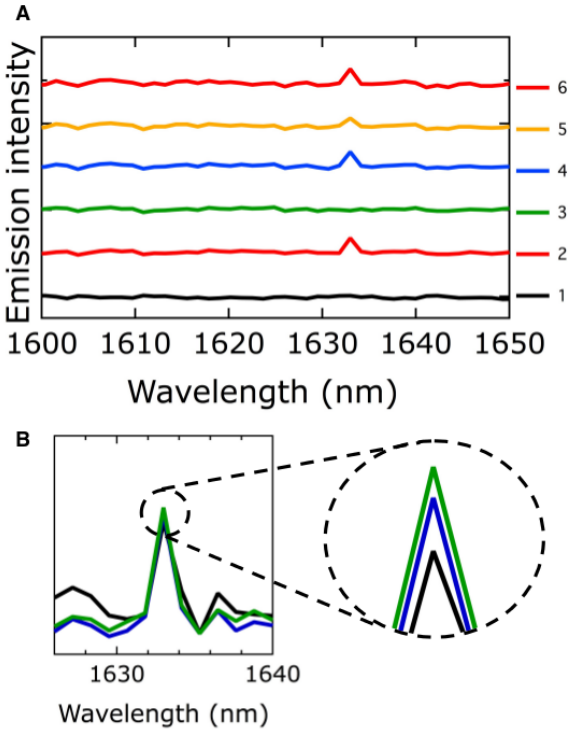

Figure 4.10. Near-infrared electrochemical luminescence measurements. (**A**) Controlled-potential steady-state luminescence cycled from (1) 0 V to (2) 2.3 V to (3) -0.5 V to (4) 2.3 V to (5) -0.5 V to (6) 2.3 V, all vs. a Pt wire pseudo-reference. (**B**) Time-course measurements of luminescence intensity at 1633 nm; 3 min. (black), 6 min. (blue), 9 min. (green).

4.2.4. Luminescence Spectroscopy

Tetraoxoferrate(VI) exhibits a narrow luminescence peak at ca. 6200 cm^{-1} (1613 nm), assigned to the $^1E \rightarrow {}^3A_2$ spin-flip transition[24]. We sought to detect an analogous Fe(VI) signature by spectroelectrochemical luminescence. Upon anodic polarization, a very narrow, weak signal appeared at 6124 cm^{-1} (1633 nm); the feature returned to baseline by biasing the electrode at -0.5 V. A second cycle reproduced the signal, although it did not entirely vanish under cathodic bias (Figure 4.10**A**(5)), consistent with features observed in the IR spectrum during redox cycling. Notably, the intensity of the luminescence increased with electrolysis time in a fashion similar to that of the infrared bands.

4.2.5. Oxygen Detection Studies/STOIR-O_2

To determine whether the species we were detecting spectroscopically was on the path to making oxygen, we sought to detect whether dioxygen was produced upon the addition of substrate (water).

We first performed bulk electrolyses in "wet" acetonitrile, with the addition of either 1% water or 1% 1 M KOH aqueous solution. The potential was set at 2.2 V vs Pt, and held until 2.5 x 10^{-2} C of charge was passed. The electrolyte solution was then assayed with an Amplex® Red hydrogen peroxide fluorescence assay (Figure 4.11). From the fluorescence intensity, we concluded that the high valent species produced hydrogen peroxide when quenched with water at pH 7, but no H_2O_2 was produced when quenched with water at pH 14.

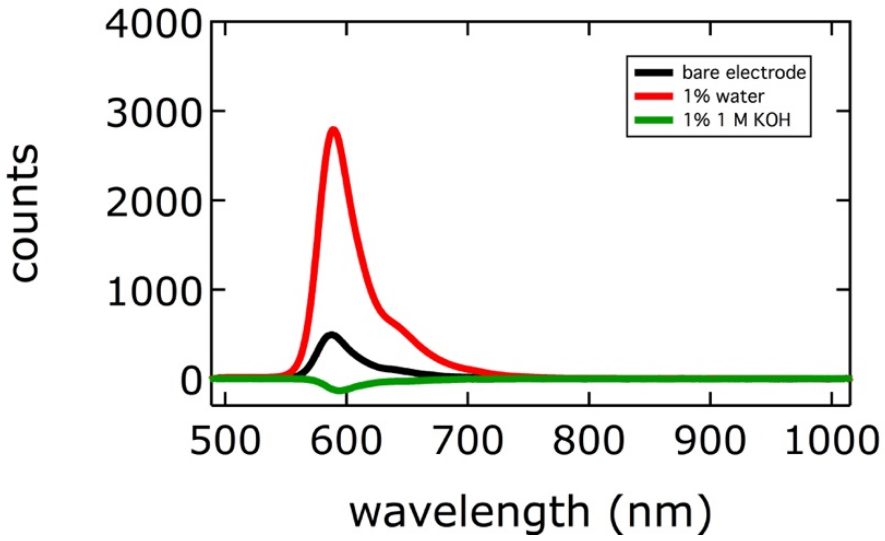

Figure 4.11. Steady-state fluorescence detection of hydrogen peroxide using Amplex® Red reagent. Fluorescence intensity is directly proportional to peroxide concentration. Fluorescence from the stock electrolyte solution has been subtracted, giving rise to a small "negative" region around 600 nm for the green trace.

To confirm that the oxidation product under alkaline conditions was O_2, we utilized an irreversible O_2-binding iridium complex, $Ir(dppe)_2Cl$ (dppe = 1,2-bis(diphenylphosphino)ethane)[25,26], to capture the small amount of O_2 produced upon quenching the polarized electrode. In this experiment, carbon fiber paper electrodes were transferred to an anaerobic optical cuvette containing $Ir(dppe)_2Cl$ in an alkaline acetonitrile solution (1% aqueous KOH, 1M), the spectrum of which had been recorded prior to exposure to the electrodes. Bleaching of the iridium complex absorption bands at 382, 442, and 512 nm indicated O_2 binding. We found that only electrodes containing catalyst that had been polarized at high potential (2 V *vs.* Pt) induced bleaching of the iridium absorption features. (Figures 4.12-4.15). Because the catalytic cycle was halted at the active species, this quenching experiment trapped a single turnover of O_2. In a typical experiment, we detected ~ 100 nmol of O_2, far greater than our detection limit. Based on the amount of oxygen produced, we estimate the number of active sites to be less than 5%. The failure of electrodes biased at lower potentials (*i.e.* 1 V *vs.* Pt) to produce O_2 indicated that the species we spectroscopically characterized was the *lowest potential intermediate active for water oxidation in non-aqueous media*.

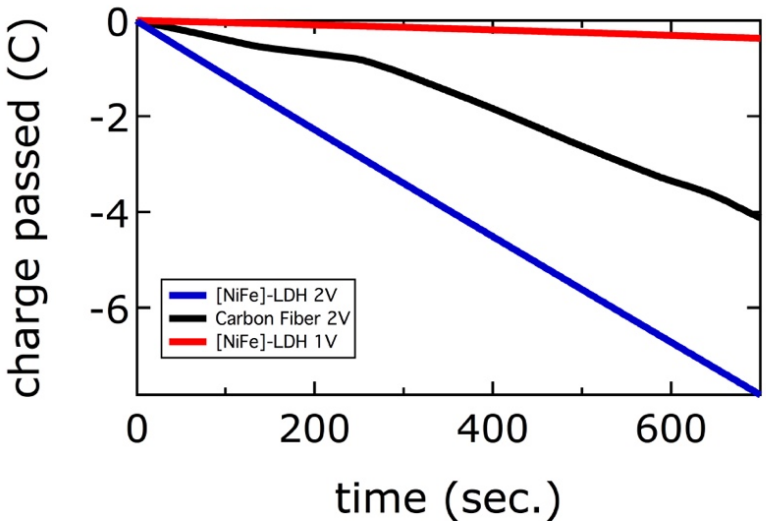

Figure 4.12. Chronocoulometric traces for STOIR-O_2 experiments.

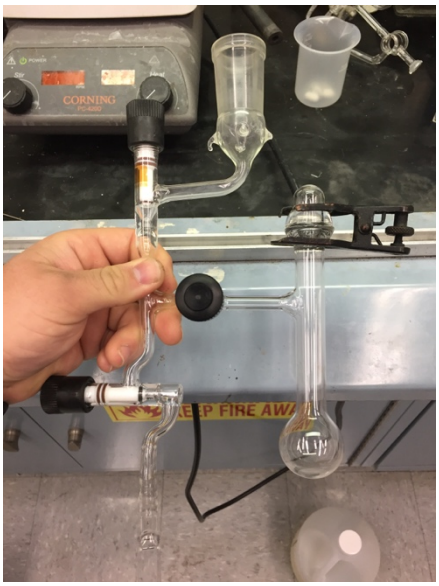

Figure 4.13. Custom laser cell for STOIR-O_2 experiments. Design allows the introduction of macroscopic carbon fiber electrodes while maintaining an oxygen-free atmosphere.

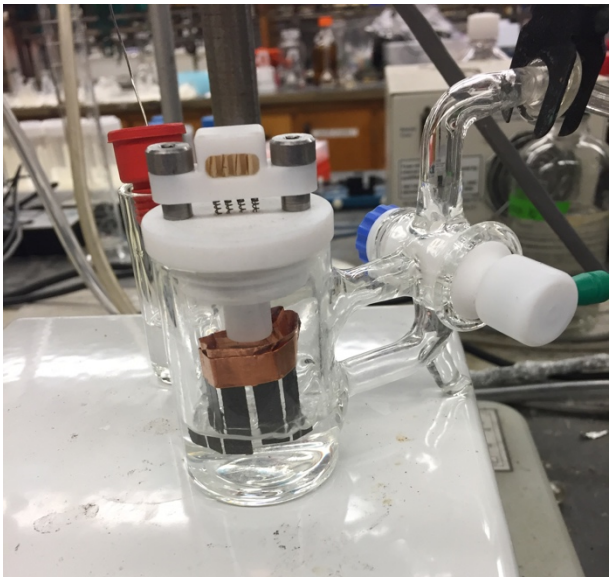

Figure 4.14. Electrochemical cell for STOIR-O_2 experiments. Electrodes are individual carbon fiber strips, held by copper tape.

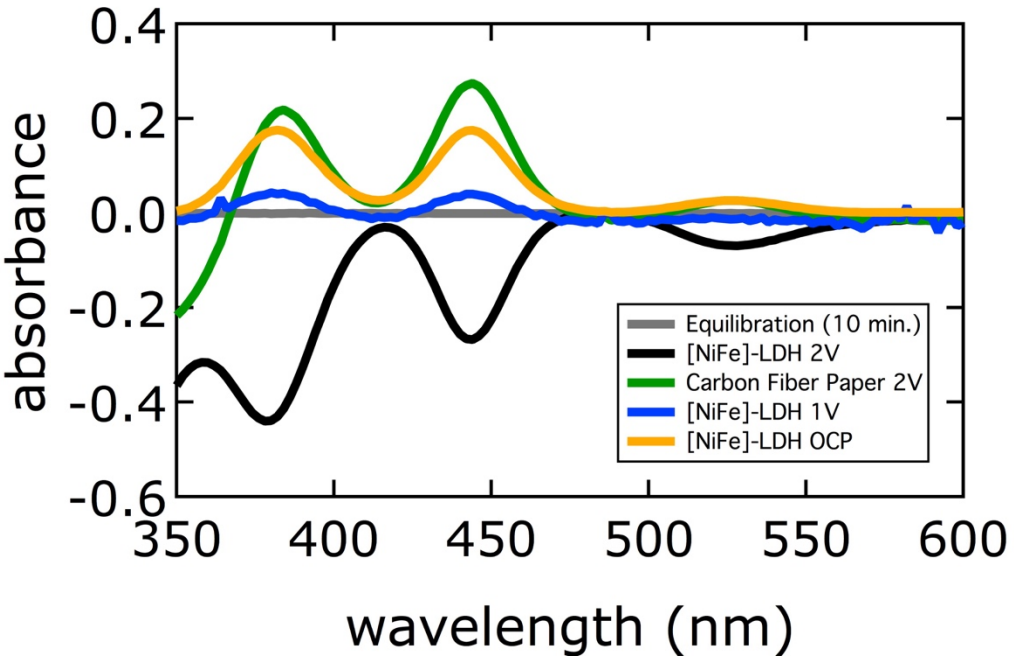

Figure 4.15. Spectra of $Ir(dppe)_2Cl$ in acetonitrile: 1% 1 M KOH, showing oxygen binding. Bleaches at 382, 442, and 512 nm are consistent with formation of an O_2 complex. Increased absorbance at those values indicate oxygen scrubbing from the solution, potentially due to oxygen deficiencies in the materials. Oxygen binding experiments were performed according to the procedure described in the text on carbon fiber electrodes polarized at: (black) 2 V *vs.* Pt (with catalyst); (green) 2 V *vs.* Pt (without catalyst); (blue) 1 V *vs.* Pt (with catalyst). A spectrum of the iridium complex in acetonitrile: 1% 1 M KOH for 10 minutes is shown in gray, and an oxygen binding experiment on the catalyst alone (no applied potential) is shown in orange.

4.2.6. Mössbauer Studies

We employed Mössbauer spectroscopy to probe the oxidation state of the high valent iron species observed at high potentials in nonaqueous media. These studies were performed on an ^{57}Fe enriched sample prepared by pulsed laser ablation in water. For nanoparticles in zero applied field the characteristic time for superparamagnetic relaxation is governed by the Néel-Brown relation,

$$\tau = \tau_0 \exp\left(\frac{E_a}{k_B T}\right),$$

where E_a is the barrier to flip the magnetization direction about the easy direction of magnetization. Thus, at very low temperatures the bulk Fe(III) will be in the slow relaxation limit ($\tau \gg 100$ ns), resulting in large internal magnetic fields and broadened, magnetically split spectra.[42] In order to be able to detect small quantities of Fe sites of catalytic relevance (~ 1-5 %), it is thus necessary to collect spectra at temperatures well above the average blocking temperature of the bulk material to obtain the narrowest possible linewidths. Given the temperature dependence of the Mössbauer-Lamb factor, this is most conveniently determined by measuring the maximum absorbance of the sample as function of temperature.

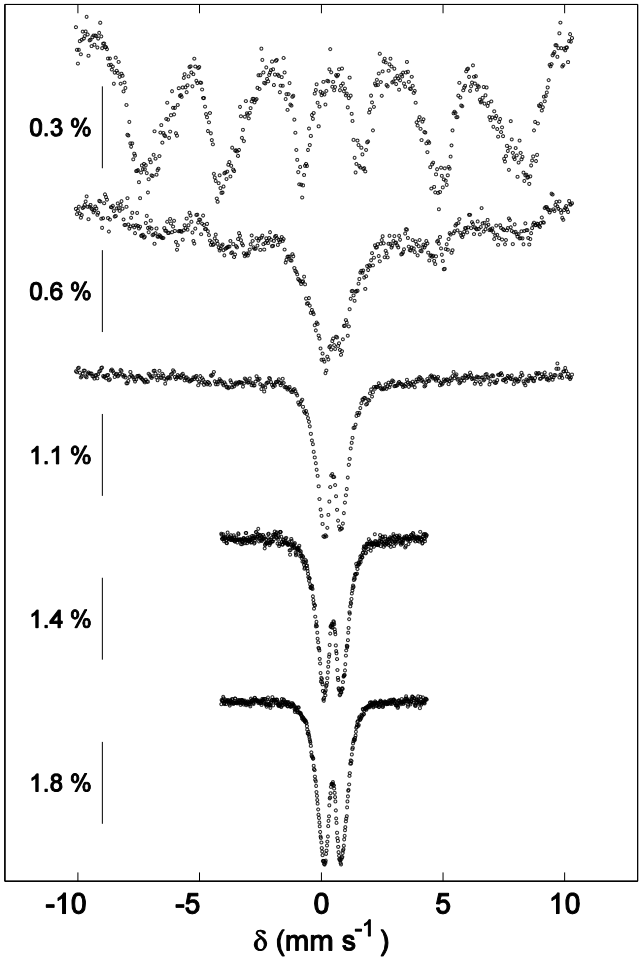

Figure 4.16. Temperature dependence of the Mössbauer signal of [Ni^{57}Fe]-LDH in zero applied field. From top to bottom, spectra were collected at 5, 15, 30, 50, and 80 K. The absorbance scale for each spectrum is indicated by the bar to the left.

As shown in Figure 4.16, we can estimate the rough blocking temperature of the bulk Fe(III) sites in the material around 15–30 K, below which the spectra display significant magnetic hyperfine splitting. Above 50 K, no resolved magnetic hyperfine splitting is observed in the spectra, but the linewidths continue to sharpen, indicative of a small percentage of very broad magnetically-split Fe(III) sites in the baseline. However, between

80 and 100 K, the maximum absorbance of the spectrum is reduced by 0.2% percent, suggesting a temperature regime where all of the Fe sites are in fast electronic relaxation.

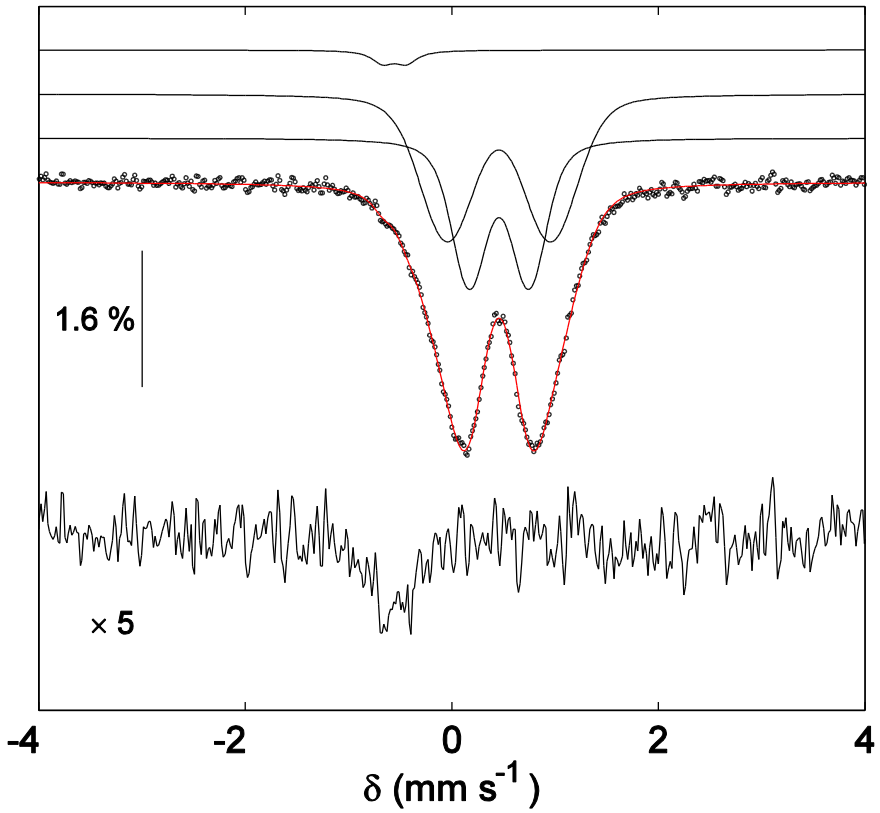

Figure 4.17. The zero field Mössbauer spectrum of [Ni^{57}Fe]-LDH collected at 100 K. The raw data are presented as open black circles, with the simulated spectrum shown in red. Individual sub-spectra are plotted as black lines above the raw data. Below is shown a subtraction of the simulated Fe(III) components from the data, showing the presence of a small amount of oxidized Fe present as a shoulder in the raw data.

The 100 K spectrum of an electrode polarized at high potential (Figure 4.17) consists of a doublet centered around 0.46 mm s^{-1}, with a clearly discernable shoulder appearing on the low energy resonance. The major signal is consistent with six-coordinate, high-spin Fe(III) in a ligand field of O-atom donors. As expected for a nanoparticle structure, the line shapes are not Lorentzian, but rather Voigt[27]. The Fe(III) signal was modeled using a

distribution of hyperfine parameters. To fully capture the observed shoulder, it was necessary to include a separate component in the simulation with $\delta = -0.51$ and $\Delta E_Q = 0.26$ mm s^{-1}. The low isomer shift of this component is consistent with the presence of a small amount (~ 2.5%) of Fe in an oxidation state greater than Fe(III)[28]. This isomer shift is also significantly more negative than that previously assigned to Fe(IV) in [NiFe]-LDH by *in-situ* Mössbauer (−0.27 mm s^{-1})[5]. Electrode polarization at lower potentials (*i.e.* 1 V *vs.* Pt) resulted in no Mössbauer spectroscopic features consistent with highly oxidized iron (Figure 4.18).

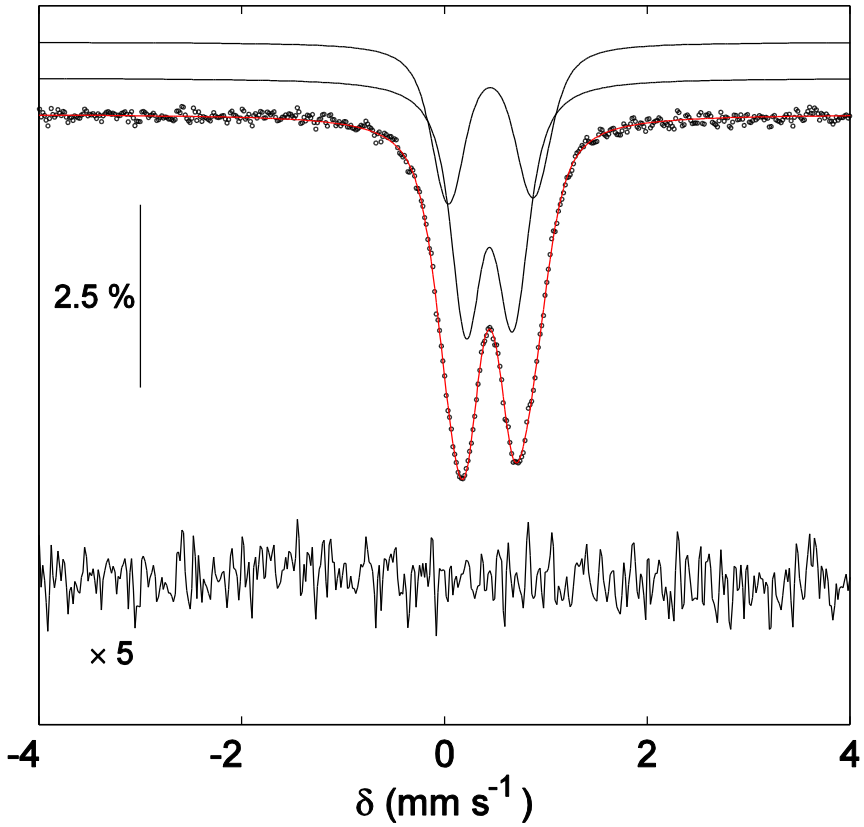

Figure 4.18. The zero field Mössbauer spectrum of [Ni^{57}Fe]-LDH, polarized at 1 V *vs.* Pt, collected at 100 K. The raw data are presented as open black circles, with the simulated spectrum shown in red. Individual sub-spectra are plotted as black lines above the raw data. Below is shown a subtraction of the simulated Fe(III) components from the data.

When a sample of catalyst initially polarized at 2 V *vs*. Pt (which showed the shoulder at $\delta = -0.51$ mm s^{-1}, described above) was removed from the spectrometer and wetted with 1% 1 M aqueous KOH in acetonitrile, the shoulder was no longer observed (Figure 4.19). Thus, the highly oxidized iron detected by Mössbauer was also incompatible (*i.e.* reactive) with aqueous base.

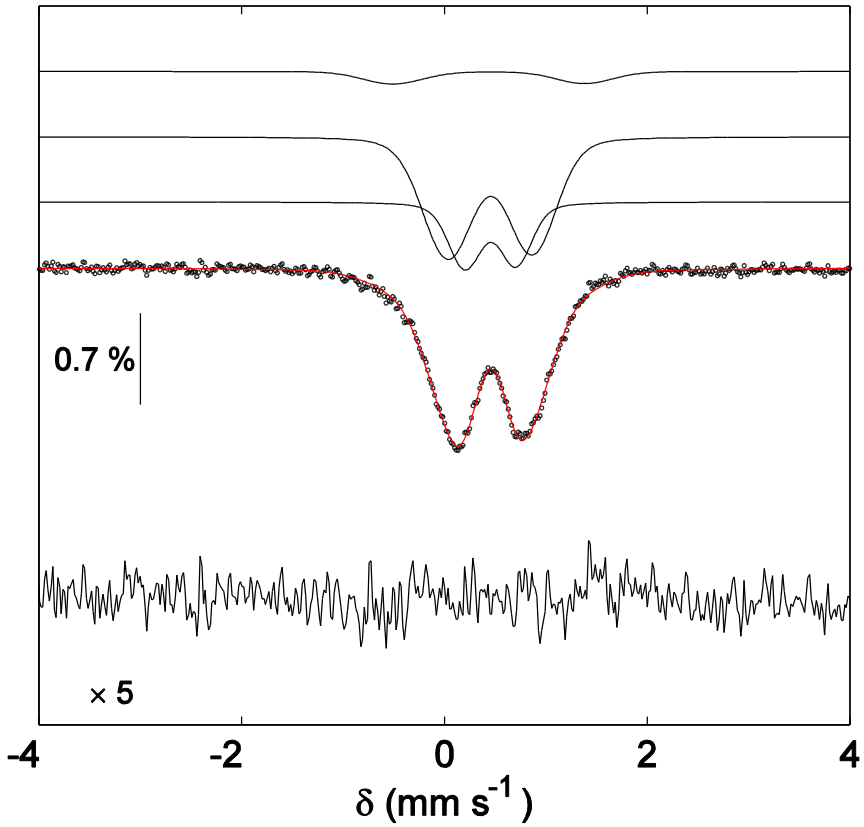

Figure 4.19. The zero field Mössbauer spectrum of [Ni^{57}Fe]-LDH, initially polarized at 2 V *vs.* Pt and then quenched in 1% 1 M aqueous KOH in acetonitrile, collected at 100 K. The raw data are presented as open black circles, with the simulated spectrum shown in red. Individual sub-spectra are plotted as black lines above the raw data. Below is shown a subtraction of the simulated Fe(III) components from the data.

We performed DFT calculations on single-site iron(VI) with three hydroxides and two oxos in which all atoms could be optimized; the apparent δ was calculated to be –0.68

mm s^{-1}. When the hydroxides were constrained to the lattice geometry, the isomer shift of Fe(VI) was calculated to be more positive, at –0.20 mm s^{-1}. A third calculation involving a 3-atom cluster of one Fe(VI) and two Al atoms yielded $\delta = -0.24$ mm s^{-1}. The computationally predicted limits for the isomer shift of iron(VI) in this environment, $-0.20 > \delta > -0.68$ mm s^{-1} (skewing more towards the negative), bound the experimentally observed isomer shift.

4.3. Mechanistic Proposal

The data are consistent with a catalytic cycle involving an Fe(VI) intermediate (Figure 4.20). Anodic bias brings the material to the so-called "γ-NiOOH" phase[29] in which Ni(III) predominates[30-34]. More positive potentials can lead either to formation of Ni(IV) or Fe(IV). Ni(IV), with a low-spin d^6 electronic configuration in octahedral coordination, cannot be stabilized by π-bonding to a terminal oxo-ligand. Fe(IV), however, with a d^4 configuration, has partially occupied $d\pi$-orbitals. In lattice sites where the Fe center has terminal hydroxide ligands, generation of the Fe(IV) state will be facilitated by deprotonation of this ligand to produce a terminal oxo. Hence, we anticipate that Fe centers in edge and corner sites are likely to be oxidized after formation of γ-NiOOH. Formation of Fe(IV)=O centers in the middle of the lattice would require disruption of triply bridging hydroxides, making the material susceptible to corrosion. Since the oxygen evolution reaction catalyzed by these materials in alkaline solution exhibits good long-term stability, we suggest that Fe(IV) formation occurs exclusively at edge and corner sites, which is compatible with the coulometry described above.

At slightly higher potentials, oxidation of Fe(IV)=O to Fe(V) or Fe(VI) occurs. These higher oxidation states can be stabilized by π-bonding to additional oxo-ligands. Only the corner sites in the LDH lattice have two or more terminal hydroxide ligands (Figure 4.1). The *trans*-dioxo geometry is preferred for a six-coordinate d^2 or d^3 metal center and neither corner site can adopt this configuration without lattice disruption.

Alternatively, reduction of the coordination number to 5 or 4 could stabilize a d^2 or d^3 configuration with *cis*-dioxo ligation. The 120° corner sites, which have just two terminal hydroxide ligands, could not reduce their coordination numbers without lattice disruption. The 60° corner sites, however, have three terminal hydroxide ligands, permitting formation of a 5-coordinate, *cis*-dioxo metal site; and in the Fe(VI) state, this 5-coordinate site would closely resemble ferrate. We note that others have proposed that tetrahedrally coordinated iron could be present under catalytic conditions[4].

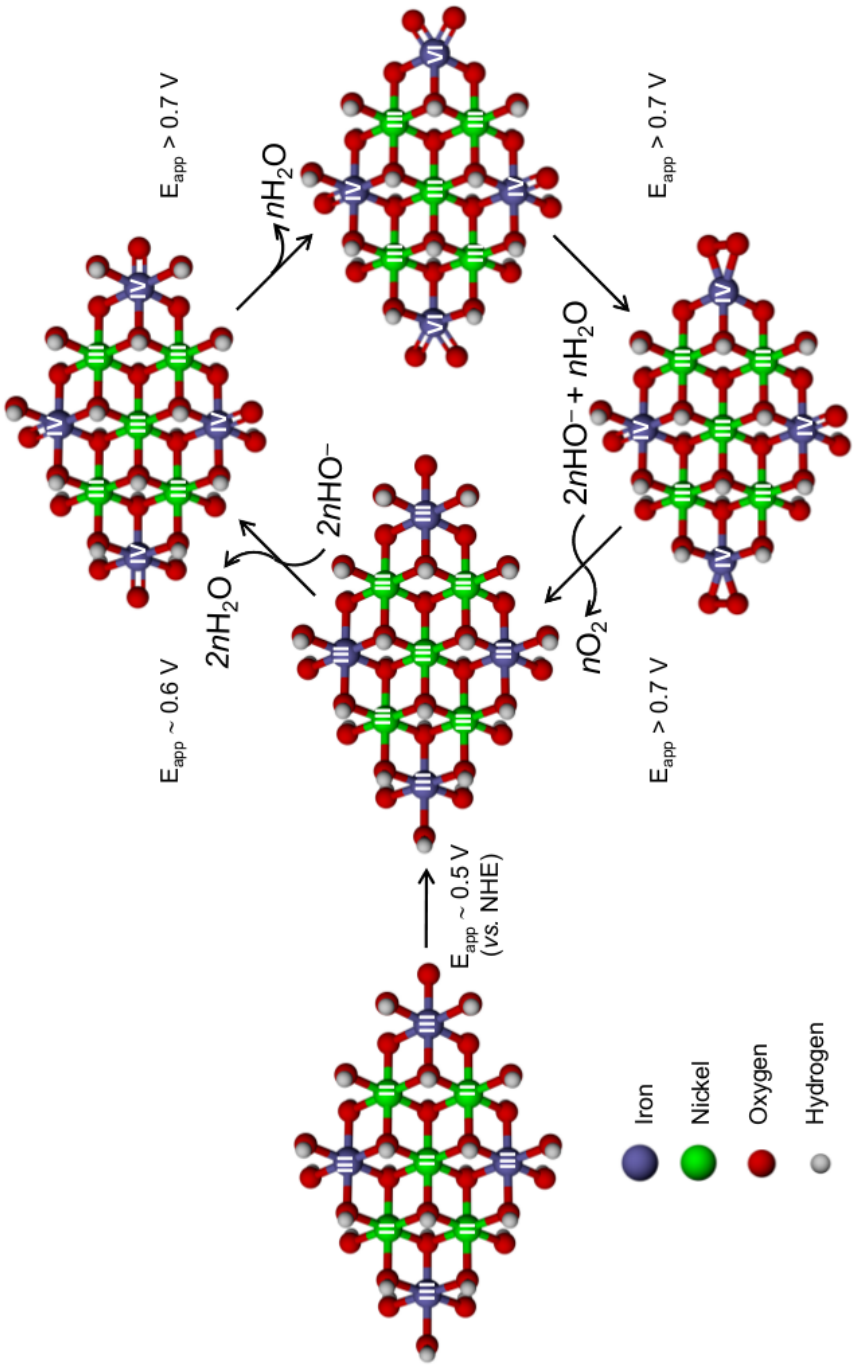

Figure 4.20. Proposed mechanism for water oxidation catalyzed by [NiFe]-LDH in alkaline solution. Oxidation states are shown as Roman numerals.

Internal redox rearrangement from a *cis*-dioxo-Fe(VI) species would produce an Fe(IV)-peroxide; the O-O stretch in this species is a plausible assignment for the high-energy peak in the infrared spectrum. Maintenance of the anodic bias, along with hydroxide binding leads to dioxygen release and reformation of γ-NiOOH. We note that ferrate and permanganate, both high-valent oxo-anions, are capable of forming O-O bonds. In our mechanism, the Ni(III) centers serve as a conduit for delivery of holes to the electrode. The high water oxidation activity of [NiFe]-LDH materials prepared by pulsed laser ablation in water may be related to the greater proportion of corner sites in nanosheets than in mesoscale materials.

Our mechanism is consistent with data on alkaline water oxidation by [NiFe]-LDH reported by other investigators. Strasser, Dau, and coworkers found a -120 mV/pH unit shift for the catalytic prewave in Ni-Fe catalysts, contrary to typical Nernstian behavior (-60 mV/pH unit) for the nickel-only material[35]. This behavior is consistent with a two proton-one electron transfer, cf. the *cis*-dioxo formation. Although Bell and coworkers concluded from X-ray absorption spectroscopy (XAS) that iron sites are not oxidized above the +3 oxidation state[4], their data are nevertheless consistent with a small amount of highly oxidized iron; at potentials effecting water oxidation *in operando*, a pronounced pre-edge appears (indicating significant *d-p* mixing) and the Fe K-edge shifts to higher energy. These trends have been observed in the XAS of potassium ferrate (K_2FeO_4), where the intensity of the pre-edge is a sensitive indicator of the oxidation state[36]. As the 1s to 3d transition is forbidden in centrosymmetric geometries, only iron in a non-octahedral or reduced coordination number environment would display such a pre-edge[37], and high-valent metal-oxo centers (*e.g.* d^2 for Fe(VI)) typically show intense pre-waves due to the short M-O bonds[38].

4.4. Conclusions

Our spectroscopic investigations in nonaqueous media suggest that nanostructuring by pulsed laser ablation in water gives a material with a high concentration of catalytic active sites. The nickel-hydroxide lattice provides a stable, corrosion-resistant host that tightly binds catalytic Fe centers, and the Ni(III)/(II) redox couple is ideally suited to the demands of water oxidation, providing both a reservoir of oxidizing equivalents and a conduit for transporting holes to the electrode. Importantly, only corner sites in the LDH lattice can accommodate the structural rearrangements necessary to produce the reactive *cis*-dioxo-Fe(VI) fragment.

4.5. Methods

Electrochemistry

Materials and procedures. [NiFe]-LDH was prepared by pulsed laser ablation in water, as described previously[1]. All measurements were performed in dried, degassed acetonitrile (HPLC grade, Fisher) that was passed through a solvent purification column. Tetra-*n*-butylammonium hexafluorophosphate ([TBA]PF_6) (Fluka) was used as received. Electrolyte solutions (0.1 M [TBA]PF_6) were prepared and stored over activated alumina and 4-Å molecular sieves.

All electrochemical experiments were performed with a CH Instruments Model 650A electrochemical analyzer. Cyclic voltammetry (CV) at ambient temperature was measured in a three-electrode configuration consisting of a highly polished glassy-carbon-disk working electrode (A = 0.07 cm^2), a Pt wire auxiliary electrode, and a 1.0 M KCl AgCl/Ag reference electrode, separated by a modified Luggin capillary. Potentials in the figures are reported vs. aqueous AgCl/Ag, not corrected for the junction potential. The ferricenium/ferrocene (Fc^+/Fc) potential was measured to be 410 mV under virtually identical conditions.

Electrodes were prepared by suspending 2 mg of [NiFe]-LDH in 1 mL of deionized water and sonicating for 15 minutes. To this suspension was added 20 μL of Nafion 117 solution (~5% in a mixture of lower aliphatic alcohols and water). The suspension was vortexed for 5 minutes. After polishing the electrode with 0.3 and 0.05 micrometer alumina successively, 20 μL of the [NiFe]-LDH was drop cast on the surface and allowed to dry under an infrared heat lamp for 20 minutes.

Small-Volume Electrolysis. A 1 cm diameter glassy carbon electrode was prepared by drop casting 80 μL of [NiFe]-LDH suspension and drying the electrode under an infrared heat lamp. Approximately 2 mL of 1 M aqueous KOH was placed in an evaporating dish and the electrode was positioned in the dish. The reference (1.0 M KCl AgCl/Ag reference electrode) was placed directly in the KOH electrolyte. A Pt wire counter electrode was in contact via a fritted glass tube.

Water oxidation was performed by passing 1 mA cm^{-2} (galvanostatic control) for 10 minutes, which turned the electrolyte purple.

The UV-visible spectrum of the resulting solution was recorded on an Ocean Optics USB 4000 spectrometer with an Ocean Optics USB-ISS-UV/VIS light source and SpectraSuite software.

Coulometry. We assume that the formula of the material is $Ni_{0.78}Fe_{0.22}(OH)_2(NO_3)_{0.22}$. Although it is known that carbonate substitutes for nitrate in aqueous base in ambient air[2], we assume that no ion exchange has occurred in acetonitrile. Further, we do not explicitly include interlayer water molecules, which we know are embedded in the interlayer from infrared spectroscopy[1].

Assuming the above formula, the MW is 105.72 g/mol. Depositing 20 μL of a 2 mg/mL solution, we expect to have 3.78×10^{-7} moles of Fe on the surface.

Infrared (IR) Spectroelectrochemistry

Infrared spectroelectrochemistry was carried out in diffuse reflectance mode using a custom-built cell.

Cell Design. The cell featured a 1 cm diameter circular glassy carbon electrode with a concentric (equidistant) platinum wire serving as a pseudo-reference electrode. The front window, made of zinc selenide (ZnSe, International Crystal Laboratories, 3 mm thick) was separated from the electrode by a 200 micrometer Teflon spacer. Inlet and outlet holes were plumbed with surgical tubing, with a platinum wire affixed to the outlet serving as an auxiliary electrode.

Electrode Preparation. A suspension of 2 mg [NiFe]-LDH in 1 mL of deionized water was made by sonicating for 15 minutes. For Nafion-containing electrodes, 20 μL of Nafion 117 solution were added to the suspension and it was vortexed for 5 minutes. Following polishing with 0.3 and 0.05 micrometer alumina, 80 μL of [NiFe]-LDH suspension was drop cast on the surface and allowed to dry under an infrared heat lamp for 15 minutes.

IR Measurements. Infrared absorption data were collected on a Thermo Nicolet Nexus FT-IR spectrometer using an LN_2-cooled MCT-A (Thermo) detector. The sample chamber was allowed to purge with nitrogen for one hour. A stand for the electrochemical cell was machined and two silver-deposited mirrors were used to guide light from the source onto the electrode surface (facing down), and reflected light to the detector. Beam alignment was performed using the spectrometer's internal He-Ne laser. A blank was recorded at no applied potential before the cell was switched on and potential was increased until maximum current flow was achieved (2.3 V vs. Pt). All spectra were background corrected.

Electrochemical Control. All potentiometric control was accomplished by a BAS model CV-27 electrochemical analyzer.

Solvent Control. Solvent flow was controlled using a gastight syringe connected to the input port of the spectroelectrochemical cell. Solvents were either acetonitrile (HPLC grade, Fisher) that had been passed through a solvent purification column and stored over activated alumina and molecular sieves, or nitromethane that had been distilled and sealed in glass ampules. Supporting electrolyte was 0.1 M tetrabutylammonium hexafluorophosphate.

For quenching experiments, a solution of 5% by weight water in acetonitrile was prepared.

Exhaustive Electrolysis in $H_2{}^{18}O$ Water. A pea-sized amount of solid potassium was added to ~20 mL of $H_2{}^{18}O$ and the pH was measured to be approximately 14. The spectroelectrochemical electrode was polarized, with the current held at 1 mA/cm^2 (galvanostatically). Oxygen bubbles were observed forming on the electrode. Electrolysis was continued for 10 minutes, after which the electrode was rinsed with deionized water and placed in the spectroelectrochemical cell. The cell was polarized *in-situ* at 2.3 V vs Pt. A high-frequency interference pattern due to the spacer thickness was removed by filtering the spectrum through a binomial smoothing algorithm with a smoothing parameter of 500. Notably, a ca. 10-fold loss in signal intensity was observed due to material coming off of the electrode surface.

Raman Spectroelectrochemistry

Raman spectroelectrochemistry was carried out in a custom-built cell.

Cell Design. The cell featured a 1 cm diameter circular glassy carbon electrode with a concentric (equidistant) platinum wire serving as a pseudo-reference electrode. The front window, made of fused silica (3 mm thick), was separated from the electrode by a 200 micrometer Teflon spacer. Inlet and outlet holes were plumbed with surgical tubing, with a platinum wire affixed to the outlet serving as an auxiliary electrode.

Electrode Preparation. A suspension of 2 mg [NiFe]-LDH in 1 mL of deionized water was made by sonicating for 15 minutes. Following polishing with 0.3 and 0.05 micrometer alumina, 80 μL of [NiFe]-LDH suspension was drop cast on the surface and allowed to dry under an infrared heat lamp for 15 minutes.

Raman Measurements. Raman data were collected on a Renishaw M1000 micro-Raman spectrometer using a 514.4 ± 0.3 nm excitation source (Cobolt Fandango 100 laser) at 10% power. A 50x long working distance objective was used. The excitation source was focused on the material deposited on the electrode, and the Raman signal (absent potential) was shown to match the Raman spectra of the as-prepared catalyst[1].

Electrochemical Control. All potentiometric control was accomplished by a CH Instruments Model 650A electrochemical analyzer.

Solvent Control. Solvent flow was controlled using a gastight syringe connected to the input port of the spectroelectrochemical cell. Solvents were either acetonitrile (HPLC grade, Fisher) that had been passed through a solvent purification column and stored over activated alumina and molecular sieves, or nitromethane that had been distilled and sealed in glass ampules. Supporting electrolyte was 0.1 M tetrabutylammonium hexafluorophosphate.

UV-Visible (UV-vis) Spectroelectrochemistry

UV-vis spectroelectrochemistry was carried out in specular reflectance mode using a custom-built cell.

Cell Design. The cell featured a 1 cm diameter circular glassy carbon electrode with a concentric (equidistant) platinum wire serving as a pseudo-reference electrode. The front window, made of fused silica (3 mm thick), was separated from the electrode by a 200 micrometer Teflon spacer. Inlet and outlet holes were plumbed with surgical tubing, with a platinum wire affixed to the outlet serving as an auxiliary electrode.

Electrode Preparation. A suspension of 2 mg [NiFe]-LDH in 1 mL of deionized water was made by sonicating for 15 minutes. Following polishing with 0.3 and 0.05 micrometer alumina, 80 μL of [NiFe]-LDH suspension was drop cast on the surface and allowed to dry under an infrared heat lamp for 15 minutes.

UV-Vis Measurements. An Ocean Optics UV-vis light source (DH-2000) and spectrometer (USB2000) were connected to the Y-arms of a bifurcated fiber-optic cable; the end of the cable was connected through a lens housing containing a semi-spherical collimating lens to the front-face window of the spectroelectrochemical cell at a 90 degree angle. A drop of mineral oil between the fiber optic and front-face fused silica window of the cell ensured refractive-index matching. Spectra were not corrected for front-face reflection. The error in intensity at an absorbance of 0.5 was less than 1%.

Electrochemical Control. All potentiometric control was accomplished using a CH Instruments Model 650A electrochemical analyzer.

Solvent Control. Solvent flow was controlled using a gastight syringe connected to the input port of the spectroelectrochemical cell. The solvent was acetonitrile (HPLC grade,

Fisher) that had been passed through a solvent purification column and stored over activated alumina and molecular sieves. Supporting electrolyte was 0.1 M tetrabutylammonium hexafluorophosphate.

Chemical Oxidation by Hydrogen Peroxide. To a suspension of 2 mg [NiFe]-LDH suspended in 1 mL of deionized water was added 100 μL of 30% hydrogen peroxide solution. The solution was placed in front of a mercury vapor lamp for 10 minutes to stimulate the production of hydroxyl radical. The UV-visible spectrum was recorded on an Ocean Optics USB 4000 spectrometer with an Ocean Optics USB-ISS-UV/VIS light source and SpectraSuite software.

Spectrum of Potassium Ferrate. Potassium ferrate was prepared as described previously[30]. The UV-visible spectrum was recorded on an Ocean Optics USB 4000 spectrometer using the SpectraSuite software. The pH was 7.

Density Functional Theory (DFT) Calculations

The structure of the ferrate (FeO_4^{2-}) anion was optimized using the Orca program package[31] with the PBE0 functional and Ahlrichs VDZ basis set[32]. The full Hessian was then calculated and the vibrational frequencies were read from the output file.
Infrared and Raman spectra were calculated using the orca_mapspc tool with 15 cm^{-1} FWHM values.

Mössbauer shifts were calculated using the method of Neese with the B3LYP functional and the CP(PPP) basis on iron, which gives the best correlation to experimental parameters for 20 control complexes, including ferrate (FeO_4^{2-})[33].

Control Experiments with "Wet" Acetonitrile

Water Oxidation. A 1 cm diameter glassy carbon electrode was prepared by drop casting 80 μL of [NiFe]-LDH suspension and drying the electrode under an infrared heat lamp. A typical three-electrode cell was used. The reference (1.0 M KCl AgCl/Ag reference electrode) compartment was separated from the working compartment by a Luggin capillary. A Pt wire counter electrode was in contact via a coarse frit. The cell was stirred.

Electrolyte was either 0.1 M tetrabutylammonium hexafluorophosphate in acetonitrile with 1% water, or 0.1 M tetrabutylammonium hexafluorophosphate in acetonitrile with 1% 1 M aqueous KOH. The working electrode potential was held constant and 2.5×10^{-2} C of charge was passed. Time elapsed was 970 seconds (bare electrode, no catalyst), 229 seconds (catalyst in 1% water) and 225 seconds (catalyst in 1% 1 M aqueous KOH).

Hydrogen Peroxide Assay. An Amplex® Red Hydrogen Peroxide/Peroxidase Assay Kit was obtained from ThermoFisher. A working solution of 100 μM Amplex® Red reagent and 0.2 U/mL HRP was prepared immediately prior to quantification. Equal volumes (1 mL) of electrolyte and working solution were mixed and incubated in the dark for 30 minutes.

Steady-State Fluorescence. Steady-state fluorescence profiles were obtained with 488.0 nm excitation (Coherent Innova 70 argon-ion laser). Luminescence was collected using an optical fiber optic and directed to a Melles Griot 13 FOS 200 spectrometer. A 488.0 nm long-pass cutoff filter was used to reject excitation light.

Luminescence Spectroelectrochemistry

Luminscence spectroelectrochemistry was carried out in specular reflectance mode using a custom-built cell.

Cell Design. The cell featured a 1 cm diameter circular glassy carbon electrode with a concentric (equidistant) platinum wire serving as a pseudo-reference electrode. The front window, made of fused silica (3 mm thick), was separated from the electrode by a 100 micrometer Teflon spacer. Inlet and outlet holes were plumbed with surgical tubing, with a platinum wire affixed to the outlet serving as an auxiliary electrode.

Electrode Preparation. A suspension of 2 mg [NiFe]-LDH in 1 mL of deionized water was made by sonicating for 15 minutes. Following polishing with 0.3 and 0.05 micrometer alumina, 80 μL of [NiFe]-LDH suspension was drop cast on the surface and allowed to dry under an infrared heat lamp for 15 minutes.

Luminescence Measurements. A 20 W Oriel Quartz Tungsten Halogen (QTH) lamp was coupled to the 100 μm-core arm of a bifurcated optical fiber. The 200 μm-core common

end of the cable was connected through a lens housing containing a semi-spherical collimating lens to the front-face window of the spectroelectrochemical cell at a 90 degree angle. The remaining 100 μm-core arm was coupled to a NIR-grade fiber bundle (10 fibers, 200 μm each) by an SMA-to-SMA coupler. The fiber bundle terminated in a linear array which directly coupled to an EG&G Princeton Applied Research Model 1235 digital triple grating spectrograph with 275 mm focal length. The detector was an EG&G Princeton Applied Research Model 1452 NIR InGaAs-InP alloy 256-element linear array. The detector was cooled to 2°C. The grating had 150 grooves/mm and was blazed at 1250 nm. The system had about 3 nm resolution in the 1600 nm region of the NIR. Integration time was 1.5 seconds per scan, and 50 scans were integrated per spectrum. In order to collect the entire region from 1100-1700 nm, a single grating change was made in the middle of acquisition, resulting in a total scan time of 2.5 minutes, plus time spent communicating with the console.

A light leakage scan was taken at 1.5 seconds integration time; this signal was subsequently subtracted from all obtained spectra. The data presented is the ratio of counts obtained under potential to counts obtained before electrolysis.

Electrochemical Control. All potentiometric control was accomplished using a CH Instruments Model 650A electrochemical analyzer.

Solvent Control. Solvent flow was controlled using a gastight syringe connected to the input port of the spectroelectrochemical cell. The solvent was acetonitrile (HPLC grade, Fisher) that had been passed through a solvent purification column and stored over activated alumina and molecular sieves. Supporting electrolyte was 0.1 M tetrabutylammonium hexafluorophosphate.

Oxygen Detection Experiments

Synthesis of Vaska's Complex—Step 1: Chlorobis(cyclooctene)iridium(I)dimer (Sigma-Aldrich) was dissolved in acetonitrile. The solution was stirred at room temperature for 10 minutes under argon. The argon flow was then stopped and CO gas was passed through the solution until a green color was observed. Four equivalents of PPh_3 were added in dichloromethane and the solution was stirred for 30 minutes as a yellow precipitate formed.

The solvent was evaporated under vacuum and the precipitate was washed with diethyl ether. The "tennis ball yellow" compound was recrystallized from DCM/hexane and stored under argon.

Synthesis of Ir(dppe)$_2$Cl—Step 2: Standard procedure was followed[25]. Briefly, two equivalents of dppe (dppe = 1,2-bis(diphenylphosphino)ethane) in benzene were added to Vaska's complex (also in benzene) under argon and stirred until a white precipitate formed. The carbonyl is then removed by heating the white solid to 100°C in a 10:1 mixture of toluene:1-propanol. The bright orange precipitate is the irreversible O_2 binding complex.

Oxygen Binding Experiments: A solution of acetonitrile with 1% 1 M aqueous KOH was thoroughly degassed by a free-pump-thaw method in a modified laser cell bulb and isolated in the cuvette. Approximately 20 mg of Ir(dppe)$_2$Cl was added to the bulb and cycled with vacuum and argon at least 10 times. The solution and the complex were mixed and a background spectrum was taken. The solution was then isolated in the cuvette. While isolated, the remainder of the cell was rinsed with acetone to ensure no complex remained; the cell was then dried under vacuum for 15 minutes to remove any remaining acetone.

Electrolysis: Five carbon fiber paper electrodes, 0.5 cm x 2 cm, were soaked in a 2 mg/1 mL suspension of [NiFe]-LDH in water for 10 minutes. The electrodes were then placed into a three-compartment electrochemical cell, supported by copper tape. The electrodes were held at 2 V *vs.* Pt for 1000 seconds before being removed and immediately dropped into the bulb of the laser cuvette (above). The bulb was cycled with vacuum and argon at least 10 times.

Spectroscopy: The solution and electrodes were "mixed" briefly (about 30 seconds), and a spectrum of the solution was taken, referenced to the background taken initially. Spectra were compared to prior studies of O_2 adducts of this complex[26].

Mössbauer Spectroscopy

Mössbauer spectra were recorded on a spectrometer from SEE Co. (Edina, MN) operating in the constant acceleration mode in a transmission geometry in zero applied magnetic field. The sample was kept in an SVT-400 cryostat form Janis (Wilmington, MA),

using either liquid He (for temperatures < 80 K) or liquid N_2 (for temperatures > 80 K) as a cryogen. The quoted isomer shifts are relative to the centroid of the spectrum of a metallic foil of α-Fe at room temperature. Samples were prepared by polarizing carbon fiber paper soaked in [Ni^{57}Fe]-LDH suspension, removing the electrodes under potential, and punching holes directly into liquid nitrogen. The frozen punches were then mounted into a Delrin cup fitted with a screw-cap. Data analysis was performed using version 4 of the program WMOSS (www.wmoss.org).

As is typical for Fe-containing nanoparticles, the Lorentzian line shape required for a single Fe absorber is not observed in the Mössbauer spectra. Rather, a distribution of local Fe environments exists in the material, resulting in a distribution of hyperfine interactions[27,42]. In the limit of fast electronic relaxation, internal fields average to zero and a distribution of quadrupole doublets is obtained. It is assumed that the quadrupole splittings are normally distributed according to,

$$P\left(\Delta E_Q\right) = \sum_{i=1}^{N} p_i G_i(\Delta E_Q),$$

where $G\left(\Delta E_Q\right)$ is Gaussian with normalization constant p_i. Assuming the isomer shifts are linearly coupled to the quadrupole splitting, the elementary quadrupole doublet is then given by,

$$D(v) = \sum_{k=-1}^{1} h_k \frac{\frac{\gamma^2}{4}}{\left(v-\delta_0-\delta_1\Delta E_Q-k\Delta E_Q/2\right)^2+\frac{\gamma^2}{4}},$$

where h_k is the Lorentzian height, γ is the width, and v is velocity. The observed spectrum is then,

$$f(v) = \int D(v)P\left(\Delta E_Q\right)d\Delta E_Q,$$

equivalent to a sum of $2N$ Voigt lineshapes. To simulate the data, the number of distributions N was gradually increased until the fitting parameters $(\gamma, \delta_0, \delta_1, h_1/h_{-1})$ became stable.

In the 100 K spectrum of [Ni^{57}Fe]-LDH polarized at 2 V *vs.* Pt, a shoulder appeared at around −0.5 mm s^{-1}. Attempting to fit this feature as an additional Fe(III) component with δ = 0.3–0.5 mm s^{-1} improved the fit marginally, but did not qualitatively capture the observed

shoulder. However, as shown in Table S-2, inclusion of a component with negative isomer shift led to a substantial improvement of the simulation.

DFT Calculations: Mössbauer shifts were calculated using the method of Neese with the B3LYP functional and the CP(PPP) basis on iron, which gave the best correlation to experimental parameters for 20 control complexes, including ferrate (FeO_4^{2-})[43].

Table 4-2: Simulation for [Ni^{57}Fe]-LDH polarized at 2 V *vs.* Pt, at 100 K using a hyperfine distribution model.

	Parameters			
	***N* = 1**	***N* = 2**	***N* = 3**	**Final fit**
$\Delta E_{Q,1}$ (mm s^{-1})	0.791	0.619	0.590	0.498
σ_1 (mm s^{-1})	0.578	0.520	0.549	0.366
p_1 (mm s^{-1})	1.078	0.546	0.603	0.305
$\Delta E_{Q,1}$ (mm s^{-1})		1.098	1.095	0.852
σ_1 (mm s^{-1})		0.956	0.576	0.648
p_1 (mm s^{-1})		0.487	0.299	0.534
$\Delta E_{Q,1}$ (mm s^{-1})			1.619	1.345
σ_1 (mm s^{-1})			0.910	0.821
p_1 (mm s^{-1})			0.125	0.173
γ (mm s^{-1})	0.431	0.267	0.228	0.250
δ_0 (mm s^{-1})	0.487	0.474	0.472	0.457
δ_1 (mm s^{-1})	−0.042	−0.028	−0.025	−0.022
h_1/h_{-1}	0.963	0.955	0.954	1.005
δ (mm s^{-1})				-0.511
ΔE_Q (mm s^{-1})				0.262
γ (mm s^{-1})				0.250
Area				0.024
Red. χ^2	1.740	0.682	0.615	0.567

Table 4-3: Simulation for [Ni^{57}Fe]-LDH, polarized at 1 V *vs.* Pt, at 100 K using a hyperfine distribution model.

	Parameters	
	***N* = 1**	***N* = 2 (Final)**
$\Delta E_{Q,1}$ (mm s^{-1})	0.606	0.470
σ_1 (mm s^{-1})	0.559	0.350
p_1 (mm s^{-1})	0.997	0.608
$\Delta E_{Q,1}$ (mm s^{-1})		0.853
σ_1 (mm s^{-1})		0.430
p_1 (mm s^{-1})		0.384
$\Delta E_{Q,1}$ (mm s^{-1})		
σ_1 (mm s^{-1})		
p_1 (mm s^{-1})		
γ (mm s^{-1})	0.297	0.277
δ_0 (mm s^{-1})	0.423	0.430
δ_1 (mm s^{-1})	0.041	0.030
h_1/h_{-1}	1.015	1.005
Red. χ^2	0.910	0.591

Table 4-4: Simulation for [Ni^{57}Fe]-LDH, after quenching, at 100 K using a hyperfine distribution model.

	Parameters		
	***N* = 1**	***N* = 2**	***N* = 3 (Final)**
$\Delta E_{Q,1}$ (mm s^{-1})	0.737	0.606	0.503
σ_1 (mm s^{-1})	0.568	0.616	0.610
p_1 (mm s^{-1})	1.044	0.497	0.243
$\Delta E_{Q,1}$ (mm s^{-1})		0.977	0.834
σ_1 (mm s^{-1})		1.116	1.011
p_1 (mm s^{-1})		0.485	0.650
$\Delta E_{Q,1}$ (mm s^{-1})			1.888
σ_1 (mm s^{-1})			1.228
p_1 (mm s^{-1})			0.081
γ (mm s^{-1})	0.423	0.224	0.133
δ_0 (mm s^{-1})	0.462	0.465	0.460
δ_1 (mm s^{-1})	−0.015	−0.020	−0.013
h_1/h_{-1}	0.930	0.915	0.922
Red. χ^2	0.854	0.608	0.562

4.6. References and Notes

1. Hunter, B. M. *et al*. Highly Active Mixed-Metal Nanosheet Water Oxidation Catalysts Made by Pulsed-Laser Ablation in Liquids. *J. Am. Chem. Soc*. **136**, 13118-13121 (2014).

2. Hunter, B. M., Hieringer, W., Winkler, J. R., Gray, H. B. & Müller, A. M. Effect of interlayer anions on [NiFe]-LDH nanosheet water oxidation activity. *Energy Environ. Sci*. **9**, 1734-1743 (2016).

3. Blakemore, J. D., Gray, H. B., Winkler, J. R. & Müller, A. M. Co_3O_4 Nanoparticle Water-Oxidation Catalysts Made by Pulsed-Laser Ablation in Liquids. *ACS Catal*. **3**, 2497-2500 (2013).

4. Friebel, D. *et al*. Identification of Highly Active Fe Sites in (Ni,Fe)OOH for Electrocatalytic Water Splitting. *J. Am. Chem. Soc*. **137**, 1305-1313 (2015).

5. Chen, J. Y. C. *et al*. Operando Analysis of NiFe and Fe Oxyhydroxide Electrocatalysts for Water Oxidation: Detection of Fe^{4+} by Mössbauer Spectroscopy. *J. Am. Chem. Soc*. **137**, 15090-15093 (2015).

6. Ahn, H. S. & Bard, A. J. Surface Interrogation Scanning Electrochemical Microscopy of $Ni_{1-x}Fe_xOOH$ ($0 < x < 0.27$) Oxygen Evolving Catalyst: Kinetics of the "fast" Iron Sites. *J. Am. Chem. Soc*. **138**, 313-318 (2016).

7. Görlin, M. *et al*. Oxygen Evolution Reaction Dynamics, Faradaic Charge Efficiency, and the Active Metal Redox States of Ni–Fe Oxide Water Splitting Electrocatalysts. *J. Am. Chem. Soc*. **138**, 5603-5614 (2016).

8. Hunter, B. M., Gray, H. B. & Müller, A. M. Earth-Abundant Heterogeneous Water Oxidation Catalysts. *Chem. Rev*. **116**, 14120-14136 (2016).

9. The [NiAl]-LDH was prepared by precipitation synthesis, resulting in much larger particles than the [NiFe]-LDH prepared by pulsed laser ablation in water. As a result, suspensions of the "nickel-only" material were prone to settling and electrode coatings were much lower. This was reflected both visibly in the electrode coverage and in the current observed in the cyclic voltammograms.

10. For [NiFe]-LDH, we observe a catalytic water oxidation current of 10 mA cm^{-2} at ~0.660 V *vs*. NHE in 1 M aqueous KOH (pH 14). In an attempt to compare this potential to the potentials measured in acetonitrile, one can correct for pH, water content of the acetonitrile solvent, and liquid-liquid junction potentials. The cathodic shift of the acetonitrile potentials to a pseudo aqueous NHE reference is estimated to be within 300 mV of the observed catalytic current in aqueous alkaline solution.

11. Huynh, M. H. V. & Meyer, T. J. Proton-Coupled Electron Transfer. *Chem. Rev.* **107**, 5004-5064 (2007).

12. The initial, “background” spectrum was recorded at an applied potential of 1.5 V—i.e., positive of the Ni-centered oxidations.

13. The potential, relative to a platinum wire, was increased until maximum current was passed, indicating that the oxidation events in the cyclic voltammogram had been reached. This occured at 2.3 V *vs*. the Pt pseudo-reference.

14. In control experiments where water oxidation was carried out in acetonitrile with 1% water or 1% 1 M aqueous KOH, the former produced a large quantity of hydrogen peroxide, whereas the latter produced an undetectable amount of hydrogen peroxide. We conclude that the product of quenching with 1% 1 M aqueous KOH in acetonitrile is dioxygen (see SI).

15. Proshlyakov, D. A., Henshaw, T. F., Monterosso, G. R., Ryle, M. J. & Hausinger, R. P. Direct Detection of Oxygen Intermediates in the Non-Heme Fe Enzyme Taurine/α-Ketoglutarate Dioxygenase. *J. Am. Chem. Soc.* **126**, 1022-1023 (2004).

16. Busca, G. Differentiation of mono-oxo and polyoxo and of monomeric and polymeric vanadate, molybdate and tungstate species in metal oxide catalysts by IR and Raman spectroscopy. *J. Raman. Spectrosc.* **33**, 348-358 (2002).

17. Xiao, Z., Gable, R. W., Wedd, A. G. & Young, C. G. Complexes Containing *cis*-$[Mo^{V}O_2]^{+}$ and *cis*-$[Mo^{V}O(OH)]^{2+}$ Centers. *J. Am. Chem. Soc.* **118**, 2912-2921 (1996).

18. Bridgeman, A. J. & Cavigliasso, G. Molecular and electronic structures of six-coordinate chloro-oxo-metalate complexes of V, Nb, Ta, Mo, and W. *J. Chem. Soc., Dalton Trans.*, 3556-3563 (2001).

19. Griffith, W. P. & Wickins, T. D. *cis*-Dioxo- and trioxo-complexes. *J. Chem. Soc. A*, 400-404 (1968).

20. We were initially surprised that a purple substance occasionally leached out of the material during in-situ infrared experiments. Under (aqueous) turnover conditions, we were reproducibly able to turn the electrolyte purple by operating the cell in a small volume of water. As the pH near the electrode dropped (due to the water oxidation half-reaction), we believe that the LDH material became unstable and Fe(VI) leached out, leading to a purple solution. The UV-visible spectrum of the resulting solution is similar to that of potassium ferrate in solution (SI). Interestingly, in-situ UV-visible spectroelectrochemical oxidation of drop cast films in 0.1 M $[TBA]PF_6$/acetonitrile showed two analogous bands (at ~500 and ~600 nm) for surface-confined species, similar to the spectrum of potassium ferrate in solution (SI).

21. Burke, M. S., Kast, M. G., Trotochaud, L., Smith, A. M. & Boettcher, S. W. Cobalt–Iron (Oxy)hydroxide Oxygen Evolution Electrocatalysts: The Role of Structure and Composition on Activity, Stability, and Mechanism. *J. Am. Chem. Soc.* **137**, 3638-3648 (2015).

22. Zou, S. *et al.* Fe (Oxy)hydroxide Oxygen Evolution Reaction Electrocatalysis: Intrinsic Activity and the Roles of Electrical Conductivity, Substrate, and Dissolution. *Chem. Mater.* **27**, 8011-8020 (2015).

23. Liang, H.-C. *et al.* Contrasting Copper–Dioxygen Chemistry Arising from Alike Tridentate Alkyltriamine Copper(I) Complexes. *J. Am. Chem. Soc.* **124**, 4170-4171 (2002).

24. Brunold, T. C., Hauser, A. & Güdel, H. U. Absorption and luminescence spectroscopy of ferrate (VI) doped into crystals of K_2MO_4 (M = S, Se, Cr, Mo). *J. Lumin.* **59**, 321-332 (1994).

25. Vaska, L., Catone, D. L. A New Series of Four-, Five-, and Six-Coordinated Iridium Complexes. *J. Am. Chem. Soc.* **88**, 5324-5325.

26. Geoffroy, G. L., Hammond, G. S., Gray, H. B. Photochemical Reductive Elimination of Oxygen, Hydrogen, and Hydrogen Chloride from Iridium Complexes. *J. Am. Chem. Soc.* **97**, 3933-3936.

27. Rancourt, D. G.; Ping, J. Y. *Nuclear Instruments and Methods in Physics Research Section B: Beam Interactions with Materials and Atoms* **1991,** *58*, 85-97.

28. The significantly higher percentage of electroactive iron in this experiment (3% *vs.* 0.0002% found previously) was due to the high surface area of the electrode material, carbon fiber paper rather than glassy carbon.

29. Klaus, S., Cai, Y., Louie, M. W., Trotochaud, L. & Bell, A. T. Effects of Fe Electrolyte Impurities on $Ni(OH)_2$/NiOOH Structure and Oxygen Evolution Activity. *J. Phys. Chem. C* **119**, 7243-7254 (2015).

30. Lyons, M. D. & Brandon, M. P. The Oxygen Evolution Reaction on Passive Oxide Covered Transition Metal Electrodes in Aqueous Alkaline Solution. Part 1-Nickel. *Int. J. Electrochem. Sci.*, 1386-1424 (2008).

31. Desilvestro, J., Corrigan, D. A. & Weaver, M. J. Characterization of Redox States of Nickel Hydroxide Film Electrodes by In Situ Surface Raman Spectroscopy. *J. Electrochem. Soc.* **135**, 885-892 (1988).

32. Oliva, P. *et al*. Review of the structure and the electrochemistry of nickel hydroxides and oxy-hydroxides. *J. Power Sources* **8**, 229-255 (1982).

33. Barnard, R., Randell, C. F. & Tye, F. L. Studies concerning charged nickel hydroxide electrodes I. Measurement of reversible potentials. *J. Appl. Electrochem.* **10**, 109-125 (1980).

34. Doyle, R. L., Godwin, I. J., Brandon, M. P. & Lyons, M. E. G. Redox and electrochemical water splitting catalytic properties of hydrated metal oxide modified electrodes. *PCCP* **15**, 13737-13783 (2013).

35. Görlin, M. *et al*. Tracking Catalyst Redox States and Reaction Dynamics in Ni—Fe Oxyhydroxide Oxygen Evolution Reaction Electrocatalysts: The Role of Catalyst Support and Electrolyte pH. *J. Am. Chem. Soc.* **139**, 2070-2082 (2017).

36. Farmand, M. *et al*. Super-iron nanoparticles with facile cathodic charge transfer. *Electrochem. Commun.* **13**, 909-912 (2011).

37. Farmand, M., Licht, S. & Ramaker, D. Studying the Reversibility of Multielectron Charge Transfer in Fe(VI) Cathodes Utilizing X-ray Absorption Spectroscopy. *J. Phys. Chem. C* **117**, 19875-19884 (2013).

38. Chandrasekaran, P. *et al*. Prediction of High-Valent K-edge Absorption Spectra by Time-Dependent Density Functional Theory. *Dalton Trans*. **40**, 11070-11079 (2011).

39. Caddick, S., Murtagh, L. & Weaving, R. Potassium Ferrate on Wet Alumina: Preparation and Reactivity. *Tetrahedron* **56**, 9365-9373 (2000).

40. Neese, F. The ORCA program system. *Wiley Interdiscip. Rev.: Comput. Mol. Sci.* **2**, 73-78 (2012).

41. Schäfer, A., Horn, H. & Ahlrichs, R. Fully optimized contracted Gaussian basis sets for atoms Li to Kr. *J. Chem. Phys.* **97**, 2571-2577 (1992).

42. Gütlich, P.; Bill, E.; Trautwein, A. X., *Mössbauer Spectroscopy and Transition Metal Chemistry*. Springer Berlin Heidelberg: New York, 2011.

43. Römelt, M., Ye, S. & Neese, F. Calibration of Modern Density Functional Theory Methods for the Prediction of ^{57}Fe Mössbauer Isomer Shifts: Meta-GGA and Double-Hybrid Functionals. *Inorg. Chem.* 48, 784-785 (2009).

5 DEVELOPMENT OF AN ELECTROCATALYTIC HYDROCARBON C-H FUNCTIONALIZATION SYSTEM USING TRAPPED FERRATE ANION (FeO_4^{2-}) ACTIVE SITES

5.1. Overview

Here, we change focus slightly from solar fuels to solar materials. Ethylene (C_2H_4) and ammonia (NH_3) are the two most energy-intensive materials produced on the planet. We believe, since they are the products of reduction of CO_2 and N_2, that they could be coupled into our solar water oxidation scheme. The electrons and protons needed to produce these highly value-added materials then would come from water, and the massive amount of energy currently used in their production would come from sunlight.

We wanted to determine the stability of our [NiFe]-LDH water oxidation catalyst in the presence of various hydrocarbon feedstocks, and we were surprised to find that the catalyst was able to *directly oxidize many C-H bonds with regioselectivity.* This chapter is dedicated to our preliminary work in this area, but much of this territory remains uncharted. The final sections are presented more as proposed research which we intend to complete in the near future.

5.2. Significance

The *selective*, catalytic activation of carbon-hydrogen bonds in simple hydrocarbons remains a significant challenge in organic chemistry. Despite marked progress over the previous decades, a general means of selectively oxidizing Csp3-H bonds using earth-abundant catalysts remains elusive to synthetic chemists. Herein we propose an electrocatalytic approach to selective C–H oxidation reactions of simple hydrocarbons through the repurposing of an earth-abundant water oxidation catalyst with a ferrate-like active site. This proposal is supported by preliminary data on the selective reaction of some simple hydrocarbons, including methane. Importantly, the selectivity of this catalyst is tuned by

modulating the applied potential, providing a unique means of control for this reaction. We initially aim to develop these preliminary hydrocarbon C–H oxidation results via exploration of both substrate tolerance and mechanism. Following this, we hope to extend this approach to other C–H functionalization reactions, such as the synthetically-relevant problem of C–H fluorination.

The importance of C–H functionalization for the field of organic synthesis is largely accepted by modern chemists, with the selective transformation of unactivated C–H bonds into other functional groups being viewed as a "holy grail" of chemical reactivity.[1-3] The reason for this is obvious: if selective C–H functionalization of simple hydrocarbons was possible and easy, the means of synthesizing almost any geometrically-possible molecule could be within reach.[4-6] Csp3–H bonds (e.g. in methane) are particularly difficult in this regard, positioning their selective functionalization as a preeminent challenge in C–H activation studies.

From the plethora of important studies detailing selective Csp3-H functionalization, several general strategies have emerged. The first approach, electrophilic activation, stems from Shilov's seminal studies with aqueous platinum chemistry.[7] Later, Bergman[8] and Graham[9] reported the basis for the second major class of activation processes: oxidative addition. Studies of d^0 metals have shown sigma-metathesis[10] to proceed readily under mild conditions and, finally, increased understanding of biological C–H functionalization reactions has revealed non-organometallic[11] C–H Activation (NOCHA) to be a highly relevant and general means of activating alkyl C–H bonds.

NOCHA comprises all processes wherein a proton and one or more electron are removed from an organic substrate in one or more steps to generate discrete, uncoordinated intermediate(s), often synthetically-versatile[12] radicals. Three subfamilies of this process are most common for the activation of Csp3–H bonds: electron transfer-proton transfer (ET-PT), proton-coupled electron transfer (PCET), and hydride transfer (HT). ET-PT is composed of two elementary steps: single electron transfer (SET) oxidation of the substrate to generate a radical cation intermediate followed by deprotonation to furnish a neutral radical (Figure 5.1a). PCET can be seen as a subset of ET-PT wherein the electron and proton move during

the same elementary step, allowing for a lower activation barrier than ET-PT in some situations (Figure 5.1b). A special case of PCET where the proton and electron transfer from the same starting orbital to the same ending orbital as a unit is called hydrogen atom transfer (HAT). HT can be seen as HAT with an extra electron, with the concerted departure of a hydride fragment generating a carbocationic intermediate (Figure 5.1c).

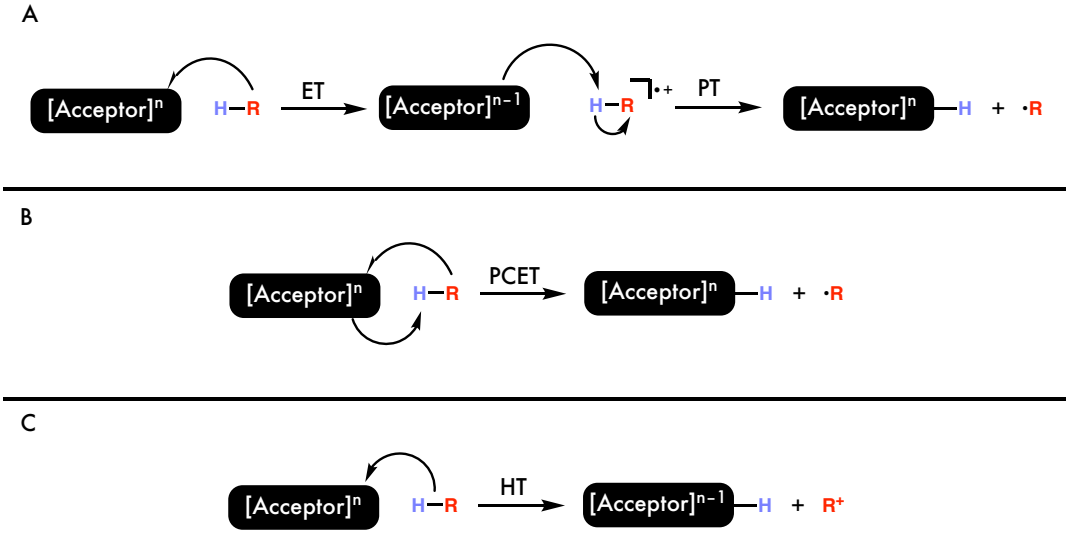

Figure 5.1. Schematic of the three non-organometallic C–H activation (NOCHA) processes relevant to Csp3–H functionalization: A) electron transfer-proton transfer (ETPT), B) proton-coupled electron transfer (PCET), and C) hydride transfer (HT). Figure reproduced with permission from Julian West.

Notably, these are common motifs in biology to functionalize unactivated C–H bonds,[13] particularly in the iron-dependent heme (e.g. P450) and non-heme enzymes.[14] These enzymes achieve C–H activation through high-valent iron-oxo species which are able to perform NOCHA outer-sphere reactions. Synthetic chemistry has been inspired by these systems, with both porphyrinoid[15,16] and non-heme[17-19] systems being devised to catalytically activate C–H. However, like their enzymatic congeners, these catalysts present several drawbacks. First is the relatively high complexity of the supporting ligands often required for reactivity, limiting the attainability of many desired catalytic frameworks. Second is the high specificity of each individual catalyst. This selectivity precludes tunability within a

single catalyst. Finally, these systems frequently decompose under reaction conditions, often through the oxidation of the ligand framework.

More robust organic oxidants include high-valent metal oxides, such as potassium permanganate ($KMnO_4$), manganese dioxide (MnO_2), chromium trioxide (CrO_3), potassium chromate (K_2CrO_4) and potassium dichromate ($K_2Cr_2O_7$).[20] The use of these reagents requires delicate control of reaction conditions to achieve reproducible results; often, competing side reactions (*e.g.* over-oxidation and acid/base chemistry) are overwhelming, especially in multistep syntheses. Furthermore, the regio- and stereospecificity is poor at elevated temperatures, limiting their utility in industrial settings. Finally, metal-based oxidants are often highly toxic; in particular, chromium and osmium are well-known carcinogens. The stoichiometric oxidation of an organic substrate often produces excessive amounts of contaminated waste.

All of the above-mentioned oxidative C–H functionalizations require stoichiometric reagents, whether strong oxidants (e.g. H_2O_2) or oxo-transfer reagents (e.g. iodosobenzene). While a terminal electron acceptor will always be required for a net-oxidative process, the possibility of using an abundant chemical species (e.g. atmospheric oxygen) would be of great interest. Recent reports from Gunnoe[21] and Baran[22] suggest that electrocatalysis may be a promising alternative to direct chemical transformations.

The development of a tunable, "green" oxidation catalyst that could be run electrochemically would be of great importance for the synthesis of pharmaceuticals and value-added chemicals. The annual worldwide production of potassium permanganate is estimated to be ~30,000 metric tons, most of which is used as an oxidant in industry.[23] Iron is both earth-abundant and environmentally benign, and the products of ferrate reduction are iron(III) oxides and hydroxides—rust.

5.3. Background

5.3.1. Ferrate

The tetrahedral[24] d^2 ferrate anion (FeO_4^{2-}) has been identified as a versatile and mild oxidant for organic substrates, similar in reactivity to permanganate (MnO_4^-). Although the syntheses of the sodium[25] and potassium[26] ferrate salts were first reported in 1951, relatively little is known about the reactivity and potential uses of ferrate.

Recent studies utilizing ferrate for waste water treatment,[27] and the identification of ferrate as a nominally homogeneous water oxidant[28] has generated renewed interest in the unusual, reactive species. Due to its relative ease of production and stability in air, potassium ferrate has been studied more extensively than the sodium, strontium, and barium salts.

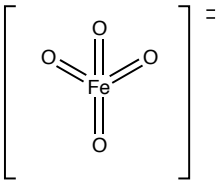

Figure 5.2. Bonding scheme for the ferrate dianion. The molecular geometry is tetrahedral.

The potassium salt is readily purified by precipitation of sodium ferrate in potassium hydroxide,[29] though a more recent technique involves the direct production of K_2FeO_4 from $Fe(NO_3)_3 \cdot 9H_2O$ in concentrated bleach.[30] Also of significant interest is the production of ferrate electrochemically, which features direct oxidation of an iron anode in saturated KOH.[31-33]

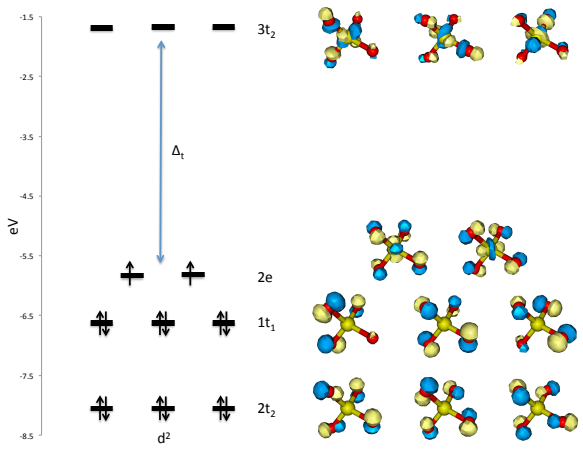

Figure 5.3. Calculated one-electron orbital levels for FeO_4^{2-} in the gas phase, showing LUMO, HOMO, HOMO-1 and HOMO-2 levels.

Güdel and coworkers have extensively studied the solid-state absorption and emission spectra of ferrate,[34-36] noting two sharp absorption features at 6209 and 9118 cm^{-1}. These are assigned to the spin-flip transitions within the e^2 manifold, namely $^3A_2 \rightarrow {}^1E$ and

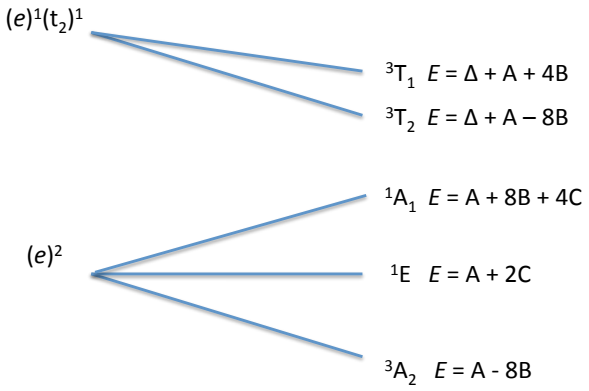

Figure 5.4. Strong-field splitting diagram for the lowest energy configurations. Matrix elements are given in terms of the Racah parameters.

$^3A_2 \rightarrow {}^1A_1$, respectively.

Although initial studies have not found that light plays a significant role in the reactivity of ferrate,[37] these excited states must be more oxidizing than the ground state by ca. 1 eV. This has led to our ongoing study of the photophysics of ferrate in an attempt to use light to promote and direct its reactivity.

The reactivity of ferrate with organic substrates is similar to that of permanganate (Figure 5.5), whereby primary and secondary alcohols and amines are converted to the corresponding aldehydes and ketones.[38] Darling et al. demonstrated regioselectivity, using ferrate to preferentially oxidize the primary alcohols in carbohydrates,[39] while Tsuda and Nakajima showed that the final product for benzyl alcohols is the corresponding aldehyde, rather than the carboxylic acid.[40] Sharma and coworkers have explored potential applications for pharmaceuticals and complex synthesis by the oxidation of sulfonamide antimicrobials, estrogens, endocrine disrupters and amino acids.[41] Recent reports indicate that $BaFeO_4$, in the presence of Lewis acids (*e.g.* $MgCl_2$, BF_3), oxidizes and chlorinates a variety of organic substrates at relatively high yields.[42]

Like potassium permanganate, the purple potassium ferrate powder remains stable in air for prolonged periods of time; in neutral or acidic conditions, however, the ferrate anion rapidly decomposes, evolving dioxygen and forming ferric hydroxide products. Aqueous stability is achieved at pH > 10, providing evidence that the protonated forms of ferrate are

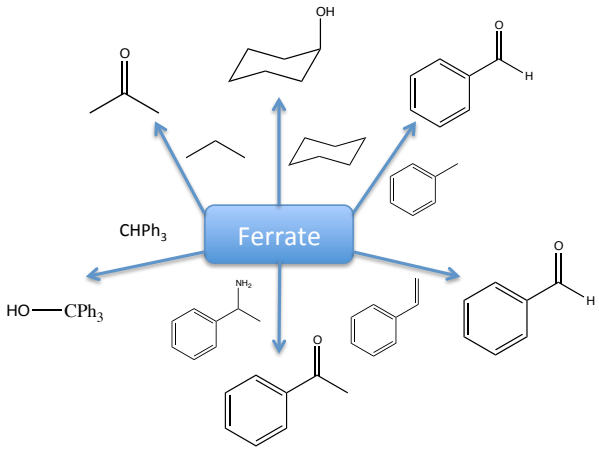

Figure 5.5. Examples of chemical oxidations by ferrate (FeO_4^{2-}).

the reactive species for water oxidation. The Fe(VI/III) reduction potential was calculated by calorimetric studies[43] for the reaction of K_2FeO_4 with $HClO_4$ and found to be 2.20 and 0.72 V versus NHE under acidic and basic conditions, respectively.[44] These values are significantly higher than the Mn(VII/IV) couple (1.679 V at pH 1, 0.588 V at pH 14), in agreement with the increased reactivity of ferrate. To date, no feasible catalytic pathway for ferrate oxidation has been proposed or developed.

At least two studies[30,44] have attempted to improve the regio- and stereoselectivity of ferrate oxidations by associating the potassium salt with microporous adsorbents

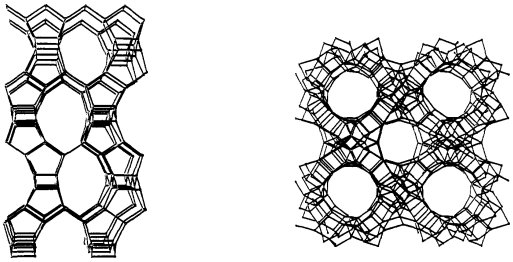

Figure 5.6. Stereoviews of the ZSM-5 zeolite framework. Reproduced from reference 24.

(aluminosilicates). Depending on the identity of the clay scaffold, yields for benzyl alcohol oxidation to benzaldehyde ranged from excellent (99%, K10 clay) to poor (1%, acidic alumina). These procedures have the primary benefit of being compatible with organic solvents, whereas potassium ferrate alone is generally insoluble. These clays have not been developed commercially (unlike those for lower-valent iron-adsorbed clays) because of the difficulty in purification of the ferrate-scaffold-product suspension. Permanganate, in contrast, has been successfully incorporated into a zeolite to produce a purely heterogeneous paradigm for organic oxidation.[45-47] Zeolites (Figure 5.6) have become attractive for catalysis over the past three decades owing to their shape discrimination, stability, ease of use, and potential for enantioselectivity.[48] The proposed work seeks to incorporate ferrate into "trapped" systems, much like the zeolite-permanganate model, and to develop a means of effecting electrocatalytic turnover for the system.

5.3.2. Thermodynamics of Ferrate Oxidations

Pulsed radiolysis studies have identified many of the intermediate products of ferrate oxidation, including the singly reduced FeO_4^{3-} species, which is a stronger oxidant than the iron(VI) species itself.[49] It is proposed that the iron(V) species is more substitutionally labile than proper ferrate, allowing substrate (*e.g.* H_2O_2) to bind to the metal center.[50] Studies of the decay kinetics of FeO_4^{3-} reveal rates in the free radical regime ($k \approx 10^7$ M^{-1} s^{-1}).[51] Additionally, the degree of protonation of the iron species is shown to be of critical importance, with the protonated forms ($HFeO_4^-$, H_2FeO_4) being the reactive species. The mechanism of stoichiometric water oxidation by ferrate at pH 1 has been probed by both stopped-flow experiments and DFT calculations.[52] Roth and coworkers propose a μ-oxo diferrate intermediate species, $[H_4Fe_2O_7]^{2+}$, with a structure similar to dichromate at low pH (Figure 5.7). They propose that O-O bond formation occurs by direct oxo-oxo coupling between neighboring iron centers, or by water attack on an electrophilic oxo. The mechanism at higher pH is less well understood, but is generally believed to be first-order in ferrate concentration with much slower rates ($k \approx 10$ M^{-1} s^{-1}), indicating an alternate mechanism is operative.[53]

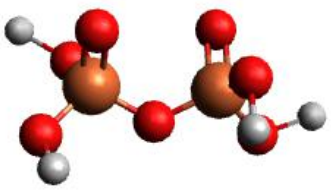

Figure 5.7. DFT-optimized structure of the proposed diferrate intermediate.

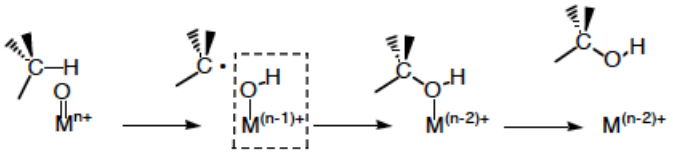

Figure 5.8. Rebound mechanism for metal-oxo C-H bond activation. The key O-H bond is indicated.

Considering the "trapped" nature of our ferrate mimics, we expect to favor a unimolecular mechanism inside the catalyst structure. Coupled with the strong pH dependence of ferrate-driven water oxidation, we propose that water oxidation catalysts may act similarly to P450's "compound I," a high-valent ferryl heme species. As the reactive intermediate in P450-mediated hydroxylation of hydrocarbons, compound I ("Fe(V)=O") is probably best described as S^{+}-Fe(IV)=O, where S^{+} is a cysteine sulfur cation radical. Oxidation by P450 proceeds by the "rebound" mechanism (Figure 5.8), wherein compound I abstracts hydrogen from the substrate, which is subsequently hydroxylated by OH• transfer from the iron center. Both ferrate and the putative Compound I feature a $^{3}A_{2}$ electronic

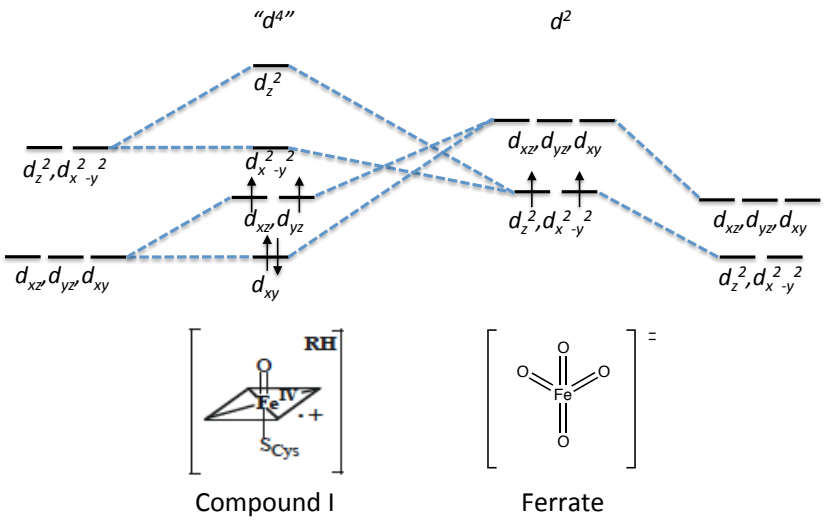

Figure 5.9. Simplified molecular orbital (MO) diagrams for the ferryl heme in Compound I of P450 (left) and FeO_4^{2-} (right).

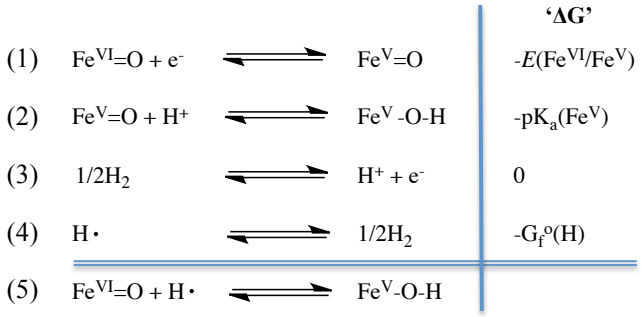

Figure 5.10. Thermodynamic cycle for determining *D*(O-H) ($-\Delta H_5$). 'ΔG' column indicates thermodynamic parameter relating to the free energy of each reaction, without constant factors (*e.g.*, $\Delta G_1 = -F\!E$).

ground state (Figure 5.9), which leads us to believe that they may exhibit similar reactivity towards substrates.

Using the hydrogen atom extraction mechanism of P450 as a *model*, we can estimate the thermodynamics of the ferrate oxidation system. Mayer has proposed that the relative strength of the $M^{(n-1)+}$-O-H bond following hydrogen atom extraction is of central importance in determining C-H activation by a metal-oxo species (Figure 5.8).[54] If the O-H bond in the one-electron reduced metal species (*D*(O-H)) is stronger than the C-H bond being broken (*D*(C-H)), the reaction can take place thermodynamically. Of primary interest, then, is the estimation of the homolytic bond dissociation energy (BDE), *D*(O-H).

The value of *D*(O-H) is equal to $-\Delta H^o$ for reaction (5) in Figure 5.10, and the thermodynamic cycle in Figure 5 can be utilized to estimate its value from empirical (*e.g.* redox couples, pK_a values) or calculated (*e.g.* free energy of formation for the hydrogen atom) parameters. Bordwell et al. have proposed[55] Eqn. 1 as an estimate of *D*(O-H), based on the cycle in Figure 5.10:

$$D(\text{O-H})\ (\text{kcal/mol}) = 23.06*[E(\text{Fe(VI)/Fe(V)})] + 1.37*pK_a(\text{Fe(V)}) + C, \qquad \text{(Eqn. 1)}$$

where C is the sum of the free energy of formation of the hydrogen atom (48.6 kcal/mol) and an 8.2-kcal $T\Delta S^o$ term. Eqn. 1 gives excellent (often ±1 kcal/mol) agreement with a multitude of literature values, and has been used by Green et al. to successfully estimate *D*(O-H) in chloroperoxidases.[56] Taking into account the increased reduction potential of ferrate versus permanganate (the calculated value of 2.20 V *vs*. NHE), and assuming that the pK_a of the

iron(V) species is similar to that of the iron(VI) species (pKa ~ 7.2),[50] *D*(O-H) = 117 kcal/mol under acidic conditions. This is clearly large enough to activate the strongest C-H bonds. Furthermore, this correctly predicts that ferrate is reactive enough to homolyze the O-H bond in water (~111 kcal/mol).

Holm and Donahue have tabulated a comprehensive series of oxo-transfer half reactions,

$$X_{(g)} + \tfrac{1}{2}O_{2(g)} \rightleftharpoons XO_{(g)}, \qquad \Delta H_{X/XO}\,(\text{kcal/mol})$$

which together can be used to determine the thermodynamic driving force for an oxygen atom transfer to occur, much like a standard reduction potential table.[57] Although not fully reproduced herein, it is interesting to note that (in the gas phase) OsO_4, a popular organic oxidant in spite of its high toxicity, features $\Delta H_{X/XO} = -12.8$ kcal/mol, and is unable to effect oxygen atom transfer to water or chlorine (25.2 and 19.2 kcal/mol, respectively). We note, however, that ferrate *does* perform oxygen atom transfer to water, further indicating its strength relative to traditional oxidizing agents and allowing us to estimate its position on Holm's tables. The only substrate on the tables less susceptible to oxygen atom transfer is oxygen itself, with the production of ozone at $\Delta H_{X/XO} = +34.1$ kcal/mol.

5.3.3. Water Oxidation Catalysts

Layered double hydroxides (LDHs), have been shown to be highly active for water oxidation.[58] We recently reported a well-defined [NiFe]-LDH nanomaterial (Figure 5.11) synthesized by pulsed laser ablation in liquids (PLAL).

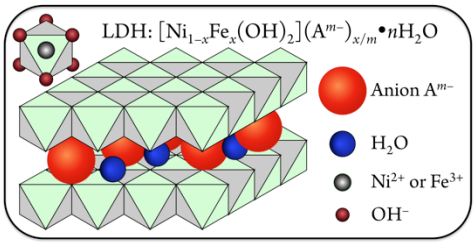

Figure 5.11. Structure of [NiFe]-LDH.

The scalable synthesis uses earth-abundant precursors and the prepared catalyst is isolated by simple centrifugation. Incorporating small amounts of titanium and lanthanum ions at the ppm level yields a material which is among the best water oxidation catalysts made of earth abundant elements ever reported.[59]

While the [NiFe]-LDH system is difficult to study *in situ* in aqueous environments due to its high water oxidation activity, it has been found that changing the solvent to a robust organic solvent (e.g. nitromethane or acetonitrile) permits the sequential generation of a variety of metastable species by increasing the applied potential to the electrode. Spectroscopic characterization of these intermediates has suggested the formation of an iron(VI) *cis*-dioxo species, similar in structure to a trapped ferrate. The proposed catalytic cycle, consistent with experimental findings, is shown in Figure 5.12. Application of a mild (~0.5 V vs NHE) potential oxidizes Ni(II) sites in the precatalyst cluster **I** to Ni(III) sites in the catalytically-relevant species **II**. Further oxidation of this cluster at a potential of ~0.6 V oxidizes the terminal and edge iron sites to Fe(IV) (species **III**). Potentials over 0.7 V generate species **IV** with ferrate-like terminal Fe(VI) centers at corner sites that are able to drop coordination number. This intermediate can then rearrange to **V**, a side-bound Fe(IV)-peroxide which liberates dioxygen upon binding of hydroxide.

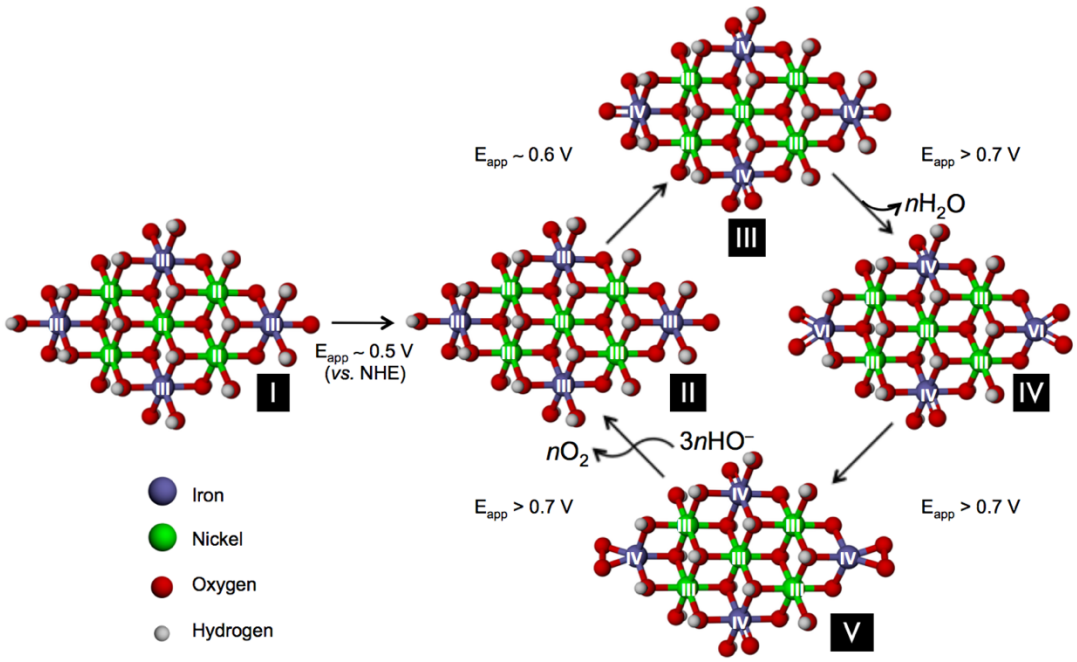

Figure 5.12. Proposed electocatalytic cycle for water oxidation with [NiFe]-LDH in base.

Spectroscopic studies of intermediates **IV** and **V** and the strategic injection of substrate water have verified the existence of a "trapped" ferrate species (Figure 5.12). Application of a +2.3 V (vs Pt in acetonitrile) potential in acetonitrile produces new infrared peaks centered at 856 and 877 cm^{-1}, consistent with a high-valent metal *cis*-dioxo motif. Addition of water to this electro-generated species results in the rapid bleaching of these features with the concomitant evolution of dioxygen. Furthermore, carrying out an extended electrolysis in the presence of $H_2{}^{18}O$ results in a characteristic shifting of these IR bands toward lower energy, providing strong evidence for 1) their correspondence to metal-oxo vibrational modes and 2) their relevance to catalysis.

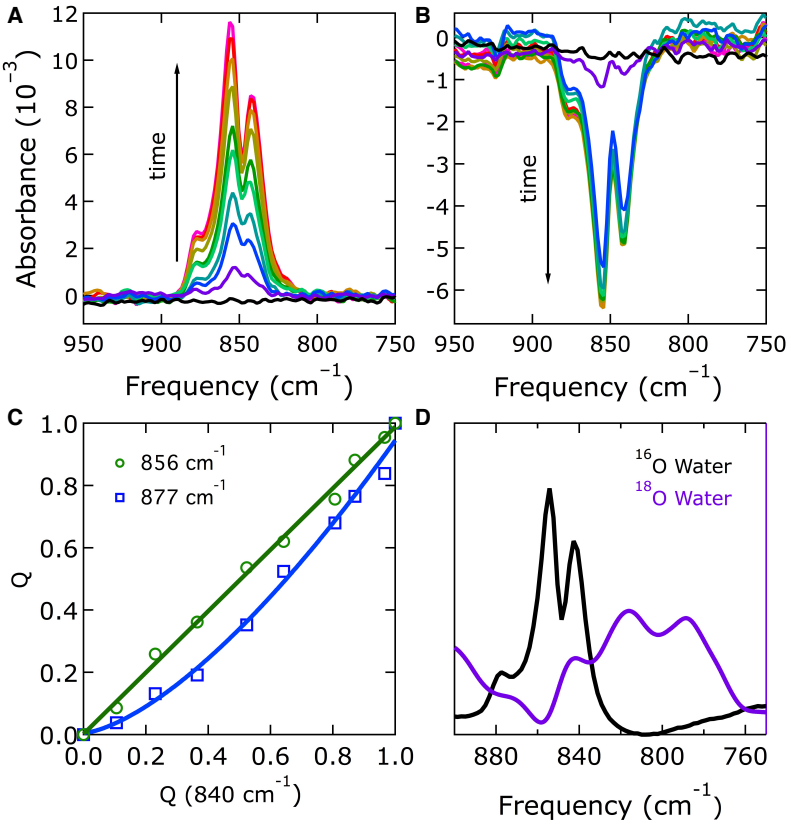

Figure 5.13. Spectroscopic evidence for the proposed intermediates. See Chapter 4.

Thus, our work suggests that the active site for water oxidation in [NiFe]-LDH nanosheets is a high-valent iron center resembling the ferrate anion (FeO_4^{2-}). The reactivity of ferrate is similar to that of permanganate,[38,39,41] with limited over-oxidation.[40] Unlike permanganate, ferrate is a poor epoxidation agent, producing instead allylic alcohols and cleaved products.[42] Taking into account the calculated reduction potential of ferrate (2.20 V *vs*. NHE), and assuming that the pK_a of the reduced Fe^{V} species is higher than that of Fe^{VI} (pKa ~ 7.2)[50], one can estimate that ferrate could activate C-H bonds as strong as 117 kcal/mol.

5.4. Methods and Materials

Standard oxidation reactions are performed in 0.1 M lithium perchlorate in acetonitrile or nitromethane with varying amounts of water (micromolar to millimolar in concentration).

The working electrode is prepared by drop-casting 120 uL of a 1mg/1mL catalyst suspension in water onto a fluorine-doped tin oxide (FTO) glass substrate. A typical three-electrode electrochemical cell is used with a platinum wire counter electrode and a silver/silver ion non-aqueous reference electrode.

Cyclic voltammetry is performed on blank FTO and catalyst-coated FTO, before and after the addition of substrate (millimolar concentration). Bulk electrolysis at a constant potential is used to generate products, which are detected by NMR (using solvent-suppression techniques) and gas chromatography coupled to mass spectrometry.

5.5. Results

5.5.1. Product Distributions for "Simple" Oxidations

We have shown that toluene oxidation in acetonitrile to benzaldehyde and benzyl alcohol is potential- and time-dependent (Figure 5.14). Of particular interest, no benzoic acid is detected.

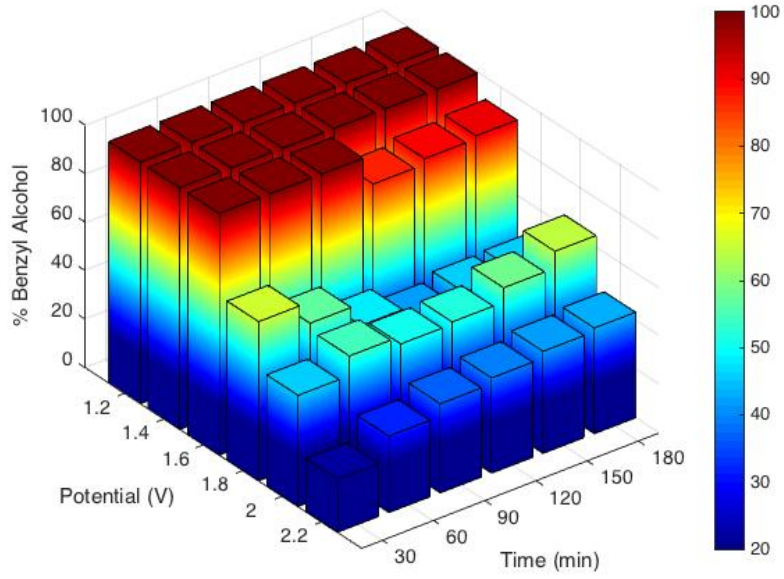

Figure 5.14. Product distribution (% benzyl alcohol relative to total benzyl alcohol and benzaldehyde produced) for [NiFe]-LDH electrolysis at various potentials and electrolysis times.

These studies, along with those involving other substrates, can be used to map the product distribution as a function of potential and electrolysis time. These "product landscapes" will serve as a roadmap for C-H activation of all types and strengths, with the goal of dialing-in a potential to obtain a desired distribution.

Other factors likely to affect product distribution are reaction (solvent) temperature, solvent composition (e.g. acetonitrile, nitromethane, etc.), catalyst loading, and substrate concentration. At low substrate concentration, for example, side reactions with solvent molecules have also been observed, leading to alternate products. These variables allow for further tuning of the system.

5.5.2. Functional Group Tolerance for "Complex" Transformations

Controlled methods to oxidize alkanes at room temperature are currently very limited and often result in over-oxidation to CO_2 and other undesired byproducts. The production of methanol from methane is a case in point. The mild oxidizing conditions employed in this system can be leveraged to favor specific products (Figure 5.15).

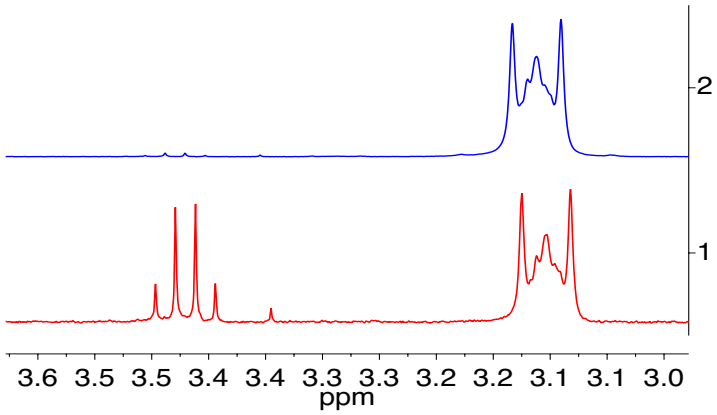

Figure 5.15. NMR spectra showing cyclohexane after bulk electrolysis (2 hours) without (top) and with (bottom) catalyst at 1.7 V vs. Ag/Ag^+ in 0.1 M $LiClO_4$ in acetonitrile. The peak at ~ 3.45 ppm corresponds to cyclohexanol. Spectra were scaled to the peak at 3.1 ppm, which is present in the electrolyte solution.

The production of allylic alcohols and ketones, important building blocks in the synthesis of organic compounds including pharmaceuticals, represents a significant challenge due to the propensity of the neighboring C=C double bond to undergo epoxidation. Preliminary data show that the double bond remains intact during oxidation for some substrates (Figure 5.16).

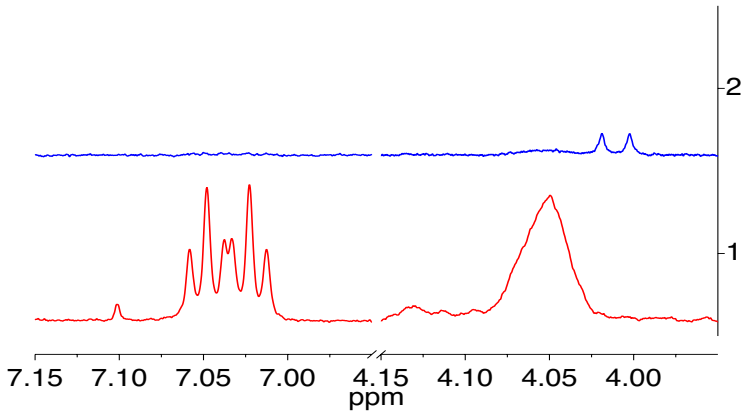

Figure 5.16. NMR spectra showing cyclohexene after bulk electrolysis (2 hours) without (top) and with (bottom) catalyst at 1.8 V vs. Ag/Ag^+ in 0.1 M $LiClO_4$ in acetonitrile. The peak at ~ 7.05 ppm corresponds to cyclohexen-one, while the peak at ~ 4.05 ppm corresponds to cyclohexen-ol.

Functional group tolerance may extend to alkynes, alcohols, ethers, epoxides, haloalkanes, aldehydes, ketones, esters, carboxylic acids, amides, amines, nitriles, imines, isocyanates, thiols, azos, and arenes.

5.5.3. Flow-Through Device for Rapid Conversion

A flow-through electrochemical device has been developed in which the flow rate and potential are easily controllable. Substrate enters the electrochemical cell through one port and product mixtures exit through a secondary port (Figure 5.17). Once the device is assembled, counter compartment (A) is filled with electrolyte solution through a port in the Teflon base. The counter electrode is a platinum wire (seen in A) fed through the Teflon base

in electrical isolation from the rest of the device. The counter compartment is separated from the working compartment by a Teflon disc fitted with a fine glass frit (B). A thin platinum wire is inlaid around the inner diameter of the Teflon disc and leaves the cell through a slot in (A) that has been coated to be nonconductive. This serves as the reference electrode. A thin (ca. 100 um) Teflon spacer (C) is sandwiched between (B) and the working electrode assembly (D), which holds the catalyst-coated FTO glass. Holes in the working electrode assembly (D) line up with the ports in (E). The threaded ring (F) screws on to (A) and is tightened to prevent leaking. Gaskets or O-rings between (A)/(B) and (D)/(E) prevent leaking. A predetermined potential is applied and substrate is pumped into one of the ports in (E), either by syringe or by peristaltic pump. In this way, substrate passes over the electrode without mixing with the electrolyte solution in the counter compartment, below. The high surface area of the electrode combined with the small volume inside the cell increases the current density and yield for a given flow rate.

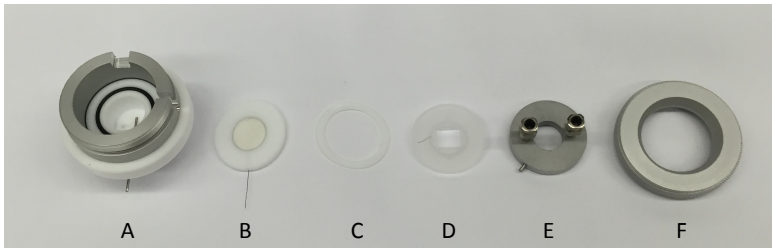

Figure 5.17. Flow-through cell (exploded view).

Figure 5.18. Assembled flow-through cell.

5.6. Future Directions

5.6.1. Specific Aims

The future of this project focuses on developing the [NiFe]-LDH water oxidation catalyst framework into an electrocatalytic hydrocarbon C-H oxidation system by exploiting the "trapped" ferrate sites present upon anodization. Simultaneously, other systems containing zeolite matrices supporting single-site ferrate anions will be designed. There are three specific aims proposed to accomplish these goals. First, accurate thermodynamic parameters must be measured *electrochemically*, both the proposed "trapped" systems and in solution. Specifically, we aim to measure E^{o}(Fe(VI/V)) in addition to observing higher oxidation states (*e.g.* Fe(VII) and Fe(VIII)). A detailed understanding of the thermodynamics of the system will help to design novel frameworks for oxidizing specific substrates, given the measured driving force. The second aim is to determine the scope of C-H electro-oxidation in "trapped" systems. The third aim is a mechanistic investigation of the viable electrocatalytic systems, with the goal of targeted improvement.

5.6.2. Aim 1: Electrochemical Measurement of Thermodynamic Properties

The electrochemistry of potassium ferrate is complicated by several factors: (1) it has limited solubility in traditional solvents; (2) its redox couple(s) are outside of the solvent window for most solvents; and (3) based on the increased oxidizing ability of Fe(V) and the terminal production of Fe(III) species, there is unlikely to be an observable, one-electron Fe(VI/V) couple.

Room temperature ionic liquids (RTILs) were developed specifically to have large electrochemical solvent windows, typically in excess of 5 V.[60] As such, they offer a significant improvement over common aqueous and organic electrolyte systems, such as tetrabutylammonium perchlorate in acetonitrile.[61] Additionally, the solubility of potassium ferrate may be improved in RTILs, such as trihexyl(tetradecyl)phosphonium bis-2,4,4-(trimethylpentyl)phosphinate (CYPHOS 104 IL). Preliminary experiments suggest that

K_2FeO_4 is somewhat soluble in propylene carbonate (PC) in the presence of the cryptand 4,7,13,16,21,24-hexaoxa-1,10-diazabicyclo[8.8.8]hexacosane, which has specificity for K^+ ions. Dry PC, frequently used in lithium-ion batteries, is reported to be stable up to 5 V *vs*. Li/Li^+.[62] Either of these solvent systems may be adequate for preliminary electrochemical investigations.

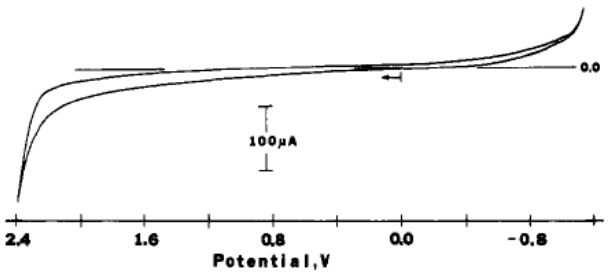

Figure 5.19. Cyclic voltammetric scan of the background at a platinum disk working electrode in 0.15 M tetrabutylammonium perchlorate-liquid sulfur dioxide at -40°C, showing typical anodic and cathodic potential limits. Reproduced from Ref. 63.

It is proposed that additional electrochemical studies are to be carried out in liquid sulfur dioxide. Tinker and Bard have reported[63] the benefits of experimentation in liquid SO_2, an aprotic, dipolar solvent with a large solvent window (Figure 5.19). Although relatively few studies involving liquid sulfur dioxide have been reported, early work demonstrated its utility in the electrolysis of various inorganic salts.[64] We are particularly interested in using SO_2 to access ferrate at higher oxidation states, potentially Fe(VII) and Fe(VIII). A gas at room temperature, isolation of electrolysis products from SO_2 is made simple by boiling off the solvent, though it should be noted that the presence of electrolyte introduces minor complications. Isolating high-valent iron species in this way would be very novel in itself, allowing for spectroscopic (*e.g.* EPR, Mössbauer) and mechanistic studies.

There are several potential challenges associated with the proposed electrochemical studies, primarily due to the fact that the one-electron redox couple may not be determinable. Since the Fe(V/IV) couple is likely to be more positive than the Fe(VI/V) couple under some conditions, ferrate may instead undergo a two-electron reduction; in this case, the simple "rebound" mechanism (*vide supra*) may be inadequate to describe the observed reactivity.

This scenario is highly dependent on the kinetics of the Fe(V) reduction or disproportionation, however, and the radical mechanism may still be operative for a two-electron oxidant. Furthermore, we predict that ferrate will be an excellent oxo-transfer agent, which may react directly with the liquid SO_2, forming SO_3. Holm's thermodynamic tables (*vide supra*) indicate that this reactivity is viable.

A possible solution to these issues is to utilize a *zeolitic framework for electrochemical measurements*. There is little precedent for extensive electrochemical studies on guest molecules embedded in zeolites, although at least one study has examined their semi-conductor nature.[65] Other groups have successfully synthesized "silver-exchanged" zeolites, in which some or all of the supporting cations are replaced by Ag^+.[66] Chronopotentiometric measurements, carried out in powdered graphite, show reversible reduction and oxidation of the silver guest ions, inferring electrical conductivity with the electrode. We propose screening of a variety of solvents, including RTILs, PC, and liquid SO_2, at a carbon-paste electrode with 50% zeolite by weight. Within the zeolite pores, higher *and* lower iron oxidation states may be stabilized, similar to the stabilizing effects of heme protein domains, possibly allowing for the isolation of the one-electron oxidized and reduced ferrate. These species are likely unstable in solution due to the formation of μ-oxo dimers.

A method for supporting potassium ferrate in a zeolite scaffold structure will be modified from that reported for potassium permanganate in Y- and β-Zeolite.[45,46] Zeolite pellets of various sizes, porosity, and structures will be added to aqueous, basic solutions of potassium ferrate and allowed to incorporate. The water will subsequently be removed from the reaction mixture under reduced pressure, and non-adsorbed potassium ferrate will be physically separated by a mesh screen. The resulting ferrate-on-zeolite material will be mixed with varying amounts of graphite (or graphite paste) to produce active catalyst that can be pressed into columns or cartridges.

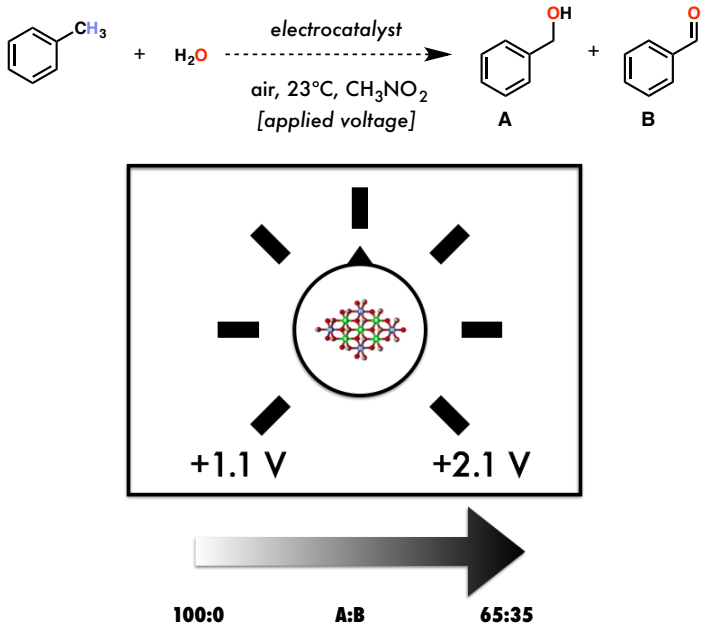

Figure 5.20. The selectivity of C–H electro-oxidation of toluene using the [NiFe]-LDH catalyst can be tuned by modulating the applied potential in nitromethane (or acetonitrile). Figure reproduced with permission from Julian West.

5.6.3. Aim 2: Scope of C-H Electro-Oxidation

Initial experiments show the [NiFe]-LDH catalyst to be highly active for the selective oxidation of simple hydrocarbons. Starting with toluene, the PCET products benzyl alcohol and benzaldehyde are produced, and the distribution can be tuned by modulating the applied potential. At low potentials (< 1.1 V vs Ag^{+}/Ag in nitromethane) only benzyl alcohol is formed, while at high (ca. 2.1 V vs Ag^{+}/Ag) potentials both benzyl alcohol and benzaldehyde are formed in a 2:1 ratio (Figure 5.20). Under all conditions no benzoic acid is formed. To the best of our knowledge, this constitutes the first example of an electrochemically tunable C–H oxidation catalyst.

Further study using cyclohexene as a substrate has shown cyclohexen-3-ol and cyclohexenone to be the sole organic oxidation products, again suggesting a NOCHA process (Figure 5.21). Interestingly, cyclohexene oxide is not formed under these conditions, a sharp

departure from many other high-valent metal-oxo systems (though common for ferrate oxidation chemistry).

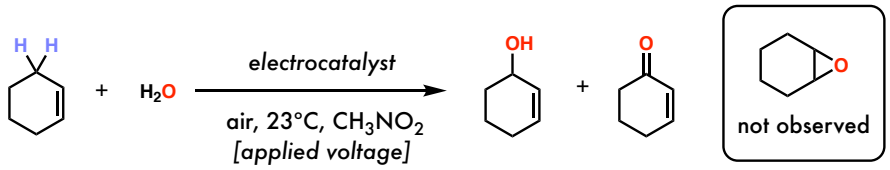

Figure 5.21. Cyclohexene is cleanly oxidized to cyclohexen-3-ol and cyclohexanone under the electrocatalytic conditions. No cyclohexene oxide is detected. Figure reproduced with permission from Julian West.

A final highly-relevant preliminary result was found in the selective oxidation of methane to methanol when the reaction was carried out in nitromethane as a solvent. This reaction has been a longstanding grand challenge in organometallic chemistry and has particular relevance to the energy security of the United States in light of the current shale gas boom.[67] We plan to further investigate and optimize the efficiency of this oxidation and those of other simple hydrocarbons, with the study proceeding in three phases of increasing complexity.

Phase I: Oxidation of simple saturated and unsaturated hydrocarbons

We plan to optimize the reaction conditions (solvent, time, potential, temperature, etc.) for the aforementioned examples and extend them to other simple hydrocarbons. We aim to include linear, branched, cyclic, and polycyclic hydrocarbons in the initial studies (Figure 5.22). Product determination will be accomplished primarily using NMR and gas chromatography (FID and MS coupled) techniques.

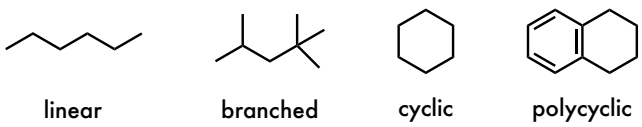

Figure 5.22. Examples of hydrocarbons for study in Phase I. Figure reproduced with permission by Julian West.

Simultaneous to our studies with [NiFe]-LDH, we propose testing the catalytic efficiency of zeolite-encapsulated ferrate. Before attempting electrocatalytic oxidation cycles, we plan to begin with stoichiometric oxidations, similar to the potassium permanganate work described above. These experiments will allow for proper screening of solvent, zeolite, and time conditions for maximum substrate turnover. Because the zeolite structure plays an important role in permanganate reactivity, we expect similar sensitivity with the ferrate system. It is also critical to determine experimental conditions that will limit the amount of ferrate that leaches out of the zeolite framework. Both oxidation conditions and adsorption techniques can be developed to minimize desorption. Finally, stoichiometric studies will determine the scope of the reaction, identifying which substrates can be successfully oxidized by the system at the reaction conditions.

Once optimal conditions have been established, oxidations will be carried out by forcing substrate solutions through activated cartridges of zeolite material by means of a pump or syringes. The ratio of graphite (for support and electrical conductivity) to zeolite material (for catalysis) will be modulated to ensure that solutions can flow freely through the columns while still retaining their structural stability. Solutions exiting the cartridge will be collected and solvent will be removed by evaporation. Products will be analyzed by conventional means (*e.g.*, NMR, GC/MS). Desorption of ferrate from the zeolite will be tested by UV-visible absorption spectroscopy of column washes.

The novelty of this system is ultimately based on the catalytic, reusable nature of the ferrate columns. There are two possible recharging cycles that are proposed here (Figure 5.23): (1) direct electro-regeneration of ferrate from the nominally iron(III) decomposition species or (2) reduction of the iron(III) species to iron(0), followed by a secondary oxidation to ferrate(VI) *in situ*. In early work, regeneration will be performed in standard, 3-component electrochemical cells.

Cycle I depends on the direct oxidation of iron(III) oxides (rust) to ferrate at the anode. Preliminary electrochemical synthesis experiments indicate that this is not a straightforward task; because the iron(III) products dimerize and form μ-oxo species in aqueous solution, the mononuclear iron(VI) product is not observed. Cycle I may remain a

feasible model, however, because the iron(III) oxides will be immobilized inside the pores of the zeolite, preventing aggregation and the formation of bridging oxos.

In Cycle II, the Fe_2O_3 is initially reduced to iron metal (there is precedent for electrochemical reduction of rust to Fe_3O_4)[68] inside the zeolite pores. Although the lattice structure of iron rust generally prevents its direct reduction to Fe(0), the unique environment

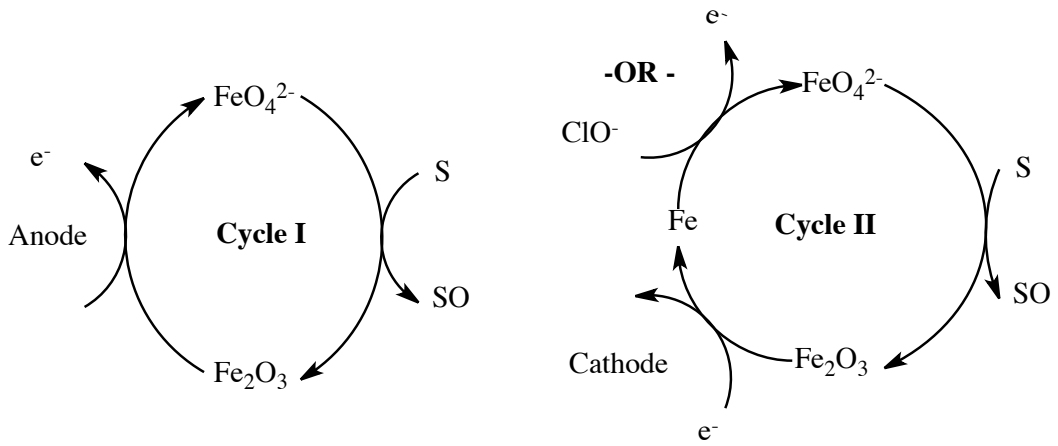

Figure 5.23. Two possible electrocatalytic cycles for zeolite supported ferrate cartridges. In Cycle I (left), the iron(III) decay product is directly re-oxidized to ferrate at the anode after substrate has been oxidized (S → SO). In Cycle II, the iron(III) decay product is first reduced to iron(0) at the cathode before being oxidized back to ferrate. Cycle II requires electrochemical "pulsing" of the electrode. In Cycle II, the second oxidation step could be performed chemically by hypochlorite.

of the zeolite pores may again prove useful here. Following a cathodic sweep, the electrode will be poised anodically, regenerating ferrate. The electrochemical synthesis of ferrate from Fe(0) has been accomplished as a preliminary result.

The regeneration of ferrate *in situ* may prove challenging electrochemically due to the high potentials that are needed. Specifically, the graphite/carbon paste would need to be robust at such high potentials. One alternative method is shown in Cycle II of Figure 5.23, where the wet chemical synthesis (*i.e.* bleach method, *vide supra*) is utilized instead of the direct oxidation at the electrode.

Following initial studies, our goal is to develop a continuous-flow electrocatalytic cartridge for organic oxidations. Although the mechanism is identical to that detailed above,

significant mechanical engineering would need to take place to ensure that organic substrates are not present in the cell when cartridge regeneration occurs. A pump valve, interfaced with the voltage source, could force substrate out of the column with aqueous base to prepare for regeneration. Following regeneration of the packing material, another valve could dispose of (or recycle) the aqueous waste, clearing the column for refilling with organic substrate. An automated system as described could find use in industry for large-scale oxidations.

For the [NiFe]-LDH material, which can be immobilized on conductive glass, a prototype flow-through device has been designed and built (Figure 5.24.). The device, which features a 100μm substrate channel, is intended to oxidize substrate as it passes over the anodized catalyst layer. We plan to work with industry partners to scale this device up to medium- and large-scale reactions.

Figure 5.24. Flow-through cell.

Phase II: Oxidation of mixtures of hydrocarbons

While selective oxidation of a single substrate is itself useful, the capacity of the catalyst to distinguish between similar components in a complex mixture for selective oxidation could also be of high interest. We propose reacting mixtures of the previously studied hydrocarbons and assaying the proportion of oxidized products. An example is provided in Figure 5.25.

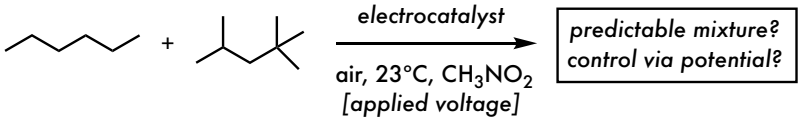

Figure 5.25. An example competition experiment for the oxidation of two hydrocarbons, as proposed in Phase II. Figure reproduced with permission by Julian West.

Phase III: Oxidation of partially oxidized hydrocarbons

The controlled oxidation of partially oxidized hydrocarbons while avoiding mineralization could be synthetically valuable, particularly true if secondary oxidation occurs predictably in response to the existing oxidation (whether through electronic effects or directivity). Additionally, the existing C–H oxidation literature[15,18,22] typically involves this substrate class, allowing us to compare and contrast our method using substrates such as in Figure 5.26; these are the substrates generally targeted by the pharmaceutical industry.

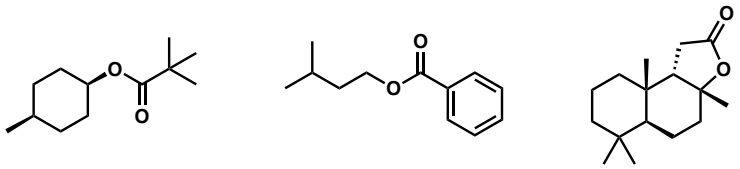

Figure 5.26. Example of partially oxidized hydrocarbons to be studied during Phase III. Figure reproduced with permission by Julian West.

5.6.4. Aim 3: Mechanistic Investigation

We will build on our synthetic observations with mechanistic insight to better understand and improve our oxidation system. Toluene is oxidized only to benzyl alcohol at low potentials with benzaldehyde becoming accessible at high potentials. The spectroscopic studies suggest that this divergent reaction outcome results from the formation of different oxidizing species under the electrocatalytic conditions, with an Fe(IV) terminal oxo site proposed for oxidations at low potentials and an Fe(VI) ferrate-like terminal site emerging under high potentials. We propose to use these same techniques to assay the speciation of the catalyst under relevant C–H oxidation conditions and interrogate this hypothesis.

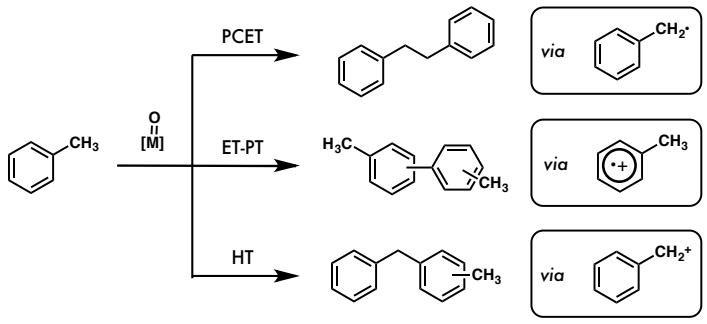

Figure 5.27. Differentiated products from the oxidation of toluene by metal-oxo catalysts, with bibenzyl, biaryl, and diarylmethane implicating PCET, ET-PT, and HT, respectively. Figure reproduced with permission by Julian West.

We also aim to determine which NOCHA mechanism(s) is(are) operative: ET-PT, PCET, or HT. Seminal studies by Mayer[69] on metal-oxo C–H oxidations have revealed that the oxidation of toluene, a compatible substrate with this method can provide characteristic side products depending on mechanism, with biphenyl (PCET/HAT), biaryl (ET-PT), and diarylmethane (HT) being highly suggestive of some mechanistic contribution from each possibility (Figure 5.27). KIE results can also help distinguish between PCET and ET-PT oxidations of alkanes. Concerted O-atom insertion and OH^+ insertion can be elucidated by the judicious use of stereochemical and radical clock probes. Together, these results could help inform what other synthetic applications would be most effective to target with this C–H activation electocatalyst. Additionally, we will pursue experiments to test for the presence of Fenton-type reaction pathways.

5.7. Conclusion

The development of a "green," sustainable, and selective hydrocarbon oxidation catalyst would be of great importance. It is proposed to utilize a high-performing, earth-abundant water oxidation catalyst to drive a robust, heterogeneous electrocatalytic system based on the immobilized ferrate anion (FeO_4^{2-}). The primary goal will be assaying and tuning the selectivity of this reaction for a variety of hydrocarbon feedstocks, a pursuit will be informed by concurrent mechanistic study. This experience and understanding will then allow us to

extend this approach to the development of new, useful C–H functionalization reactions of hydrocarbons, with C–H fluorination being our starting point.

5.8. References and Notes

(1) Arndtsen, B. A.; Bergman, R. G.; Mobley, T. A.; Peterson, T. H. *Acc. Chem. Res.* **1995**, *28*, 154.

(2) Shilov, A. E.; Shul'pin, G. B. *Chem. Rev.* **1997**, *97*, 2879.

(3) Labinger, J. A.; Bercaw, J. E. *Nature* **2002**, *417*, 507.

(4) Yu, J.-Q. *Adv. Synth. Catal.* **2014**, *356*, 1393.

(5) Godula, K.; Sames, D. *Science* **2006**, *312*, 67.

(6) Gutekunst, W. R.; Baran, P. S. *Chem. Soc. Rev.* **2011**, *40*, 1976.

(7) Goldshleger, N.; Tyabin, M.; Shilov, A.; Shteinman, A. *Russian Journal of Physical Chemistry* **1969**, *43*, 1222.

(8) Janowicz, A. H.; Bergman, R. G. *J. Am. Chem. Soc.* **1982**, *104*, 352.

(9) Hoyano, J. K.; Graham, W. A. *J. Am. Chem. Soc.* **1982**, *104*, 3723.

(10) Waterman, R. *Organometallics* **2013**, *32*, 7249.

(11) Mayer, J. M.; Larsen, A. S.; Bryant, J. R.; Wang, K.; Lockwood, M.; Rice, G.; Won, T.-J.; ACS Publications: 2004.

(12) Yan, M.; Lo, J. C.; Edwards, J. T.; Baran, P. S. *J. Am. Chem. Soc.* **2016**, *138*, 12692.

(13) Que, L.; Tolman, W. B. *Nature* **2008**, *455*, 333.

(14) Shilov, A. E.; Shteinman, A. A. *Acc. Chem. Res.* **1999**, *32*, 763.

(15) Groves, J. T.; Nemo, T. E. *J. Am. Chem. Soc.* **1983**, *105*, 6243.

(16) Barona-Castaño, J. C.; Carmona-Vargas, C. C.; Brocksom, T. J.; de Oliveira, K. T. *Molecules* **2016**, *21*, 310.

(17) Que Jr, L. *Acc. Chem. Res.* **2007**, *40*, 493.

(18) Chen, M. S.; White, M. C. *Science* **2007**, *318*, 783.

(19) Bigi, M. A.; Reed, S. A.; White, M. C. *Nat. Chem.* **2011**, *3*, 216.

(20) *Oxidation in Organic Chemistry: Part A*; Wiberg, K. B., Ed.; Academic Press: New York, 1965.

(21) Joglekar, M.; Nguyen, V.; Pylypenko, S.; Ngo, C.; Li, Q.; O'Reilly, M. E.; Gray, T. S.; Hubbard, W. A.; Gunnoe, T. B.; Herring, A. M. *J. Am. Chem. Soc.* **2015**, *138*, 116.

(22) Horn, E. J.; Rosen, B. R.; Chen, Y.; Tang, J.; Chen, K.; Eastgate, M. D.; Baran, P. S. *Nature* **2016**.

(23) Reidies, A. H. In *Ullmann's Encyclopedia of Industrial Chemicals*; Wiley-VCH: Weinheim, 2002.

(24) Hoppe, M. L.; Schlemper, E. O.; Murmann, R. K. *Acta Crystallogr.* **1982**, *B38*, 2237.

(25) Ockerman, L. T.; Schreyer, J. M. *J. Am. Chem. Soc.* **1951**, *73*, 5478.

(26) Thompson, G. W.; Ockerman, L. T.; Schreyer, J. M. *J. Am. Chem. Soc.* **1951**, *73*, 1379.

(27) Sharma, V. K.; O'Brian, B.; Smith, J. O. *J. Am. Chem. Soc.* **1997**, *213*, 238.

(28) Carr, J. D. In *Ferrates*; Sharma, V. K., Ed.; American Chemical Society: 2008; Vol. 985, p 189.

(29) Hrostowski, H. J.; Scott, A. B. *J. Chem. Phys.* **1950**, *18*, 105.

(30) Caddick, S.; Murtagh, L.; Weaving, R. *Tetrahedron* **2000**, *56*, 9365.

(31) Macova, Z.; Bouzek, K.; Hives, J.; Sharma, V. K.; Terryn, R. J.; Baum, J. C. *Electrochimica Acta* **2009**, *54*, 2673.

(32) Lapique, F.; Valentin, G. *Electrochem. Comm.* **2002**, *4*, 764.

(33) He, W.; Wang, J.; Shao, H.; Zhang, J.; Cao, C. *Electrochem. Comm.* **2005**, *7*, 607.

(34) Herren, M.; Güdel, H. U. *Inorg. Chem.* **1992**, *31*, 3683.

(35) Brunold, T. C.; Hauser, A.; Güdel, H. U. *J. Lumin.* **1994**, *59*, 321.

(36) Brunold, T. C.; Güdel, H. U.; Kuck, S.; Huber, G. *J. Lumin.* **1995**, *65*, 293.

(37) Wagner, W. F.; Gump, J. R.; Hart, E. N. *Anal. Chem.* **1952**, *24*, 1497.

(38) Audette, R. J.; Quail, J. W.; Smith, P. J. *Tet. Lett.* **1971**, *12*, 279.

(39) Bemiller, J. N.; Kumari, V. G.; Darling, S. D. *Tet. Lett.* **1972**, *36*, 4143.

(40) Tsuda, Y.; Nakajima, S. *Chem. Lett.* **1978**, *7*, 1397.

(41) Sharma, V. K.; Burnett, C. R.; Rivera, W.; Joshi, V. N. *Langmuir* **2001**, *17*, 4598.

(42) Ho, C.-M.; Lau, T.-C. *New J. Chem.* **2000**, *24*, 587.

(43) Wood, R. H. *J. Am. Chem. Soc.* **1957**, *80*, 2038.

(44) Delaude, L.; Laszlo, P. *J. Org. Chem.* **1996**, *61*, 6360.

(45) Regen, S. L.; Koteel, C. *J. Am. Chem. Soc.* **1977**, *99*, 3837.

(46) Quici, S.; Regen, S. L. *J. Org. Chem.* **1979**, *44*, 3436.

(47) Sreekumar, R.; Padmakumar, R. *Tet. Lett.* **1997**, *38*, 5143.

(48) Davis, M. E.; Lobo, R. F. *Chem. Mater.* **1992**, *4*, 756.

(49) Bielski, B. H. J.; Thomas, M. J. *J. Am. Chem. Soc.* **1987**, *109*, 7761.

(50) Rush, J. D.; Zhao, Z.; Bielski, B. H. J. *Free Rad. Res.* **1996**, *3*, 187.

(51) Rush, J. D.; Bielski, B. H. J. *Inorg. Chem.* **1989**, *28*, 3947.

(52) Sarma, R.; Angeles-Boza, A. M.; Brinkley, D. W.; Roth, J. P. *J. Am. Chem. Soc.* **2012**, *37*, 15371.

(53) Lee, D. G.; Gai, H. *Can. J. Chem.* **1993**, *71*, 1394.

(54) Mayer, J. M. *Acc. Chem. Res.* **1999**, *31*, 441.

(55) Bordwell, F. G.; Cheng, J.; Ji, G.; Satish, A. V.; Zhang, X. *J. Am. Chem. Soc.* **1991**, *113*, 9790.

(56) Green, M. T.; Dawson, J. H.; Gray, H. B. *Science* **2004**, *304*, 1653.

(57) Holm, R. H.; Donahue, J. P. *Polyhedron* **1993**, *12*, 571.

(58) Corrigan, D. A. *J. Electrochem. Soc.*, *132*, 377.

(59) Hunter, B. M.; Blakemore, J. D.; Deimund, M.; Gray, H. B.; Winkler, J. R.; Müller, A. M. *J. Am. Chem. Soc.* **2014**, *136*, 13118.

(60) Bonhote, P.; Dias, A.-P.; Papageorgiou, N.; Kalyanasudaram, K.; Graetzel, M. *Inorg. Chem.* **1996**, *35*, 1168.

(61) Mann, C. In *Electroanalytical Chemistry: A Series of Advances*; Bard, A. J., Ed.; Marcel Dekker: New York, 1969, p 57.

(62) Ossola, F.; Pistoia, G.; Seeber, R.; Ugo, P. *Electrochim. Acta* **1988**, *33*, 47.

(63) Tinker, L. A.; Bard, A. J. *J. Am. Chem. Soc.* **1978**, *101*, 2316.

(64) Bagster, L. S.; Steele, B. D. *Chem. News* **1912**, *105*, 157.

(65) Alvaro, M.; Cabeza, J. F.; Fabuel, D.; Garcia, H.; Guijarro, E.; Martinez de Juan, J. L. *Chem. Mater.* **2005**, *18*, 26.

(66) Pereira-Ramos, J.-P.; Messina, R.; Perichon, J. *J. Electroanal. Chem.* **1982**, *146*, 157.

(67) U.S. Energy Information Administration. Table 4.1 Technically Recoverable Crude Oil and Natural Gas Resource Estimates, 2009 https://www.eia.gov/totalenergy/data/annual/showtext.php?t=ptb0401 (accessed Jan 15, 2016).

(68) Suzuki, I.; Masuko, N.; Hisamatsu, Y. *Corrosion Science* **1979**, *19*, 521.

(69) Larsen, A. S.; Wang, K.; Lockwood, M. A.; Rice, G. L.; Won, T.-J.; Lovell, S.; Sadílek, M.; Tureček, F.; Mayer, J. M. *J. Am. Chem. Soc.* **2002**, *124*, 10112.

6 LOOKING FORWARD: THE FUTURE OF HETEROGENEOUS WATER OXIDATION CATALYSTS

6.1. Where are we at?

The current high-performing, earth-abundant materials are generally made from iron, cobalt, and nickel. We have finally reached overpotentials and current densities which justify incorporating these catalysts into electrolysis devices and researching their stability and efficiency. Moving forward with these materials, incremental changes in morphologies and attachment strategies will provide small improvements in overall device efficiency; these efforts will mirror the ongoing efforts to increase the efficiency of silicon-based photovoltaics.

6.2. The Future

Major advances in device efficiency that will allow solar-driven water splitting to compete with traditional photovoltaics must come from the development of a new class of heterogeneous water oxidation catalyst. These new materials will have exceptionally low overpotentials, ultrafast kinetics, and be stable both intrinsically and in their attachment to photoanodes. Below, I share my final thoughts on what these materials might look like, based on my experience exploring the [NiFe]-LDH material.

6.3. Electronic Considerations

6.3.1. Straddle the "Oxo Wall"

The stabilities of metal-oxo complexes with tetragonal (four-fold) symmetry decrease across the periodic table due to the addition of *d* electrons to formally π* orbitals.[1] Correspondingly, oxo ligands bound to metals with low *d*-counts (d^1, d^2) are strongly acidic, whereas those in d^4 complexes can be strongly basic.[2] Notably, an "oxo wall" separates the Fe-Ru-Os and Co-

Rh-Ir triads in the periodic table.[1] To the left of the wall, multiply-bonded metal oxos are common; to the right of the wall, they are very scarce.

Betley et al. have proposed an acid-base (AB) strategy for O-O bond formation, in which an oxygen nucleophile (*e.g.* water or hydroxide) attacks an electrophilic metal-oxo.[3] Notably, the AB strategy is one proposed mechanism for oxygenic photosynthesis is photosystem II.[4] It is also the microscopic reverse of the O-O bond heterolysis step in cytochrome P450.[5,6] If nucleophilic attack on a metal-oxo is indeed an operative mechanism in water oxidation catalysis, an oxo of moderate stability would be critical for catalysis.

In order to facilitate catalytic O-O bond formation, I propose two criteria for the active metal site: (1) a metal-oxo must be formed, and (2) the oxo must not remain triply-bonded to the metal. In (1), the species may be transient, but must exist long enough for attack (and bond formation) to take place. Condition (2) can be satisfied by either a high *d*-count ($>d^3$) or an elevated reduction potential for a high-valent metal center. Such a complex would be reduced upon attack, allowing for the formation of an O-O bond.

Considering the early transition metals (Sc-V), the *d*-counts are very low in all common oxidation states. Even by tuning the reduction potentials of the complexes, it is unlikely that triply-bonded oxos will be destabilized enough to form active heterogeneous catalysts for water oxidation. This prediction is realized experimentally in the materials developed featuring these metals: the addition of other, more active, metals is critical to their performance.

Materials containing chromium and manganese perform better, though the higher oxidation states are still too stabilizing. The key to improving the performance of these materials is the careful tuning of the 2-electron reduction potentials, e.g. E_{red}(Mn(V/III)), which reduce the metal to a d^4 configuration. This can be accomplished readily in a protein environment, but will be more difficult in a heterogeneous catalyst consisting primarily of oxide and hydroxide ligands.

Iron, cobalt, and nickel straddle the "oxo wall," which is perhaps a good explanation for their high activity for water oxidation. These oxos follow the Goldilocks principle, being neither too strong nor too weak. Based on these considerations, it may be prudent to stay

close to the oxo wall while developing new, highly active catalysts without extensive tuning of reduction potentials.

Finally, Cu and Zn show reduced activity because the d^9 and d^{10} configuration do not support oxos for long enough to observe catalysis. As such, it is proposed that many of the late first-row transition metals are poor water oxidation catalysts because they cannot reach a ~d^4 electron count at reasonable potentials.

6.3.2. An Exception: Move to Trigonal Ligand Fields

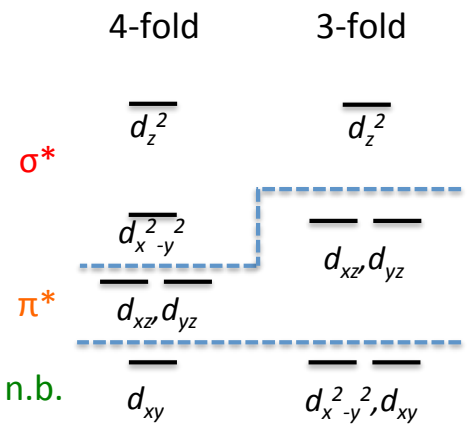

Figure 6.1. Electronic structures for complexes in tetragonal (four-fold) and trigonal (three-fold) ligand fields.

One strategy for activating mid-to-late transition metal-oxos would be to move to trigonal (three-fold) symmetry, as shown in Figure 6.1. In trigonally symmetric point groups, the lowest orbitals of *d* parentage are a non-bonding *e* set, which can be occupied by four electrons. Thus, a d^4 complex in tetragonal symmetry can be "isoreactive" to a d^6 complex in trigonal symmetry. For some of the late transition metals with high *d*-counts, moving to trigonal symmetry may be a considerable advantage; the non-bonding *e* set of molecular orbitals can hold twice as many electrons (as compared to tetragonal symmetry) before beginning to weaken the metal-oxo bond.

These electronic considerations have profound experimental ramifications: no terminal metal-oxos have been isolated beyond the "oxo wall" in tetragonal symmetry. In trigonal ligand frameworks, however, one can move past the wall (*e.g.* $(Mes)_3Ir^V(O)$).[8]

6.4. Kinetic Considerations

6.4.1. Operating at pH 7

Ultimately, a successful water splitting device must operate in *seawater* at pH 7, not in acid or base. Due to the high levels of chloride in seawater (often at concentrations greater than 0.5 *M*),[9] water oxidation will necessarily compete with the more kinetically facile oxidation of chloride to chlorine:

$$2Cl^- \rightarrow Cl_2(g) + 2e^- \qquad E^o = -1.36\ V \qquad \text{(Eq. 1)}.$$

The chlorine/chloride couple is proton- and pH-independent (Figure 6.2), so operation at higher pH is desirable. A low operating overpotential at pH 7 would be sufficient to exclude chloride oxidation, since $\Delta E = E(Cl_2/2Cl^-) - E(O_2/2H_2O) = 0.54$ V.

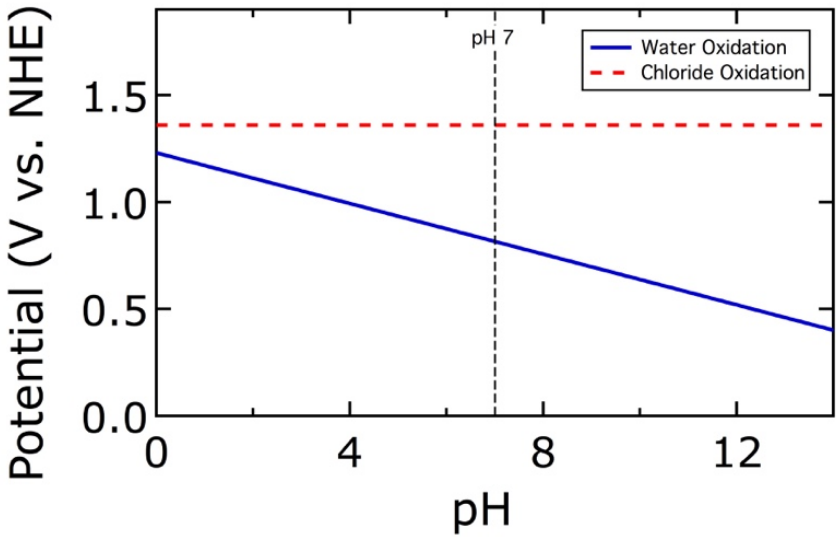

Figure 6.2. Potentials (V vs. NHE) for water oxidation (blue) and chloride oxidation (red) at pH 0-14. Note that water oxidation is pH-dependent while chloride oxidation is pH-independent. The dotted black line indicates pH 7.

6.5. A Prediction

My prediction is that the next generation of earth-abundant heterogeneous water oxidation catalysts will be mineralogical (hence, geologically stable) motifs in nanoparticulate form. I believe they will be late transition metals with mild 2-electron reduction potentials, but weakened metal-oxo bonding due to elevated *d* counts. These complexes will likely only be stable with trigonal symmetry.

6.6. Outlook

We have made considerable progress developing catalysts and beginning to understand how they operate. In the future, water splitting devices will provide electrons and protons to a myriad of "plug-and-play" fuel and material generators which will supply us with value-added chemicals on-the-spot, reducing transportation inefficiencies. Farmers will produce fertilizer, bottlers will produce ethylene, and fuel stations (previously known as gas stations)

will produce hydrogen on-site. It's an exciting time to be doing fundamental research in sustainable energy, and I encourage a dramatic increase in the amount of funding and attention being spent on these basic research projects.

A. CONTROLLED-POTENTIAL ELECTROMECHANICAL RESHAPING OF CARTILAGE

Reprinted with permission from Hunter, B. M.; Kallick, J.; Kissel, J.; Herzig, M.; Manuel, C.; Protsenko, D.; Wong, B. J. F.; Hill, M. G. Controlled-Potential Electromechanical Reshaping of Cartilage. *Angewandte Chemie* **2016**, *128*, 5587. DOI: 10.1002/ange.201600856.

A.1. Abstract

An alternative to conventional "cut-and-sew" cartilage surgery, electromechanical reshaping (EMR) is a molecular-based modality in which an array of needle electrodes is inserted into cartilage held under mechanical deformation by a jig. Brief (~2 min.) application of an electrochemical potential at the water-oxidation limit results in permanent reshaping of the specimen. Highly sulfated glycosaminoglycans within the cartilage matrix provide structural rigidity to the tissue via extensive ionic-bonding networks; this matrix is highly permselective for cations. Our studies indicate that EMR results from electrochemical generation of localized, low-pH gradients within the tissue: fixed negative charges in the proteoglycan matrix are protonated, resulting in chemically induced stress relaxation of the tissue. Re-equilibration to physiological pH restores the fixed negative charges, and yields remodeled cartilage that retains a new shape approximated by the geometry of the reshaping jig.

A.2. Introduction

Hyaline cartilage forms underlying structural features of the head and neck, and serves a critical functional role in the upper airway.[1] Congenital defects, trauma, and disease can damage cartilage tissue, necessitating surgical intervention to reshape (or replace) damaged (or missing) structures.[2] Conventional open surgery is characterized by long recovery times, significant tissue morbidity, and high cost; reshaping living tissue using less invasive

techniques is thus the subject of active research.[3,4] Most alternative methods focus on modifying the bulk mechanical properties of cartilage—*i.e.*, using laser- or RF-heat generation to denature and/or accelerate stress relaxation—by exploiting the thermoviscoelesticity common to collagenous tissues.[5] Our work instead focuses on novel electrochemical modalities that transiently alter the chemical properties of tissue, providing a molecular-based alternative to the scalpel and sutures.

Originally conceived as a thermal technique in which electrical current flow through cartilage would cause resistive heating,[6] "electromechanical reshaping" (EMR) was developed as a low-cost technique for reshaping cartilage. EMR combines mechanical deformation with the application of electric fields: in a typical embodiment, cartilage is held in mechanical deformation by a mold, needle electrodes are inserted into the tissue, and a constant voltage (*e.g.*, 5 V) is applied across the specimen for several minutes. When the electrodes and mold are removed, the cartilage assumes a new shape that approximates the geometry of the mold (*e.g.*, a 90° bend).[7]

Although effective shape change has been demonstrated in several animal models,[8,9] the process often is accompanied by tissue injury near the electrode-insertion sites; moreover, the relationship between shape change and the duration and magnitude of the applied voltage can be unpredictable. The lack of detailed mechanistic insight into the molecular changes that occur during EMR has impeded its development as a practical clinical tool. Indeed, careful measurements recorded during EMR reveal negligible tissue heating (< 2°C),[10] indicating a mechanism of action quite distinct from conventional thermoforming. Here, we report the results of simple electrochemical assays that indicate EMR-induced tissue remodeling is a chemical process that depends on the generation of highly localized pH gradients within cartilage under mechanical stress. Carefully controlling the electrolysis conditions has enabled us to reshape *ex vivo* tissue both predictably and reproducibly, with minimal cell mortality. These results position EMR as a potentially transformative, ultra-low-cost, chemical-based surgical therapy, suitable for point-of-care implementation.

A.3. Cartilage Structure and Permselectivity

Cartilage tissue is a polymer hydrogel (~75% water by weight) consisting of highly organized collagen fibrils surrounded by a proteoglycan matrix.[11] Highly sulfated and carboxylated glycosaminoglycans (GAGs) that are deprotonated under physiological conditions provide a substantial fixed negative charge to the tissue, resulting in an ionic-bond network that provides structural rigidity. Chondrocytes are sparsely populated within this extracellular matrix, governing homeostasis and repair processes; maintaining chondrocyte viability is particularly important, as inflammation following trauma can lead to unregulated production of fibrocartiliginous tissue, with subsequent susceptibility to scarring and loss of function.[12]

Given the analogous structural elements common both to cartilage and synthetic polyelectrolytes (*e.g.*, Nafion), we suspected that cartilage tissues might exhibit strong permselectivity to cations.[13] We thus prepared thin (~100 um) sections of costal cartilage[14] to serve as membranes between two concentration cells that contained different activities of sodium chloride. For a material that is ideally permselective, the membrane (Donnan) potential between two reference electrodes placed separately into these cells is given by:

$$E_{mem} = \frac{RT}{F} \ln\left(\frac{a_1}{a_2}\right),$$

where a_1 and a_2 are the respective activities of Na^+ in the two chambers. At 25°C, a plot of E_{mem} vs. $\log(a_1/a_2)$ should yield a straight line with slope equal to 59 mV per decade. As illustrated in Figure A.1, voltage measurements obtained across a cartilage membrane result in a slope (44±6 mV/decade)[15] that is remarkably close to that found in analogous experiments where Nafion is used instead;[16] as with the synthetic polyelectrolyte, the slightly lower-than-ideal slope suggests that some sodium ions are able to migrate through the tissue, likely as ion-pairs.

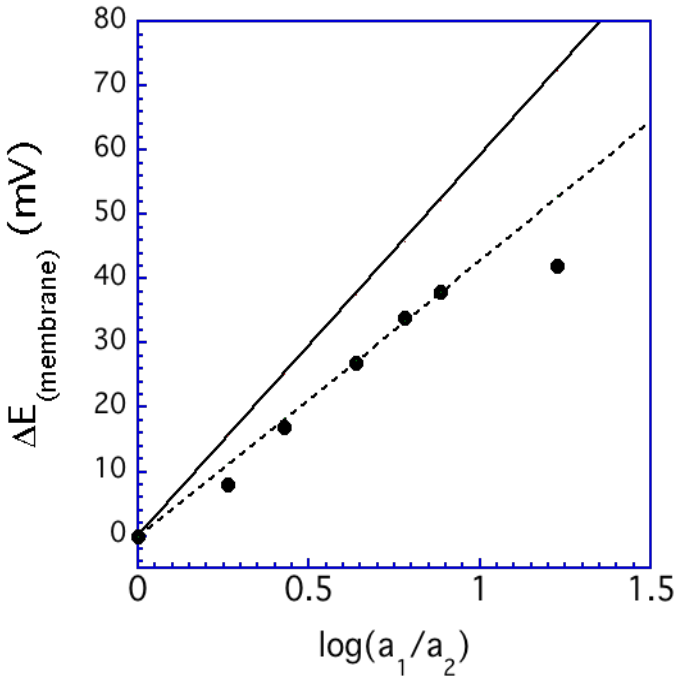

Figure A.1. Plot of potential difference (ΔE_{mem}) measured between two concentration cells featuring identical AgCl/Ag reference electrodes, separated by a ~100 um thick cartilage membrane. Solid line corresponds to ideal permselective response (59 mV/decade). The activity of Na^+ in chamber two was fixed at 0.0059 M. All solutions contained 5 mM sodium phosphate, adjusted to pH 7.4 with HCl.

Notably, the slope of the cartilage-membrane potential should begin to flatten out when the concentration of NaCl in one of the chambers approaches the fixed-charge density (FCD) within the tissue: at this point Donnan exclusion of anions is less complete and the membrane potential levels off. In our system, this flattening occurs at a salt concentration of ~0.15 M—a value fully consistent with the FCD of articular cartilage measured *via* MRI,[17,18] computed tomography (CT),[19,20] and fluorescence-labeling[21] methods. Evaluating the permselectivity response of cartilage membranes, therefore, provides an alternative for quantifying the FCD of tissue samples.

A.4. Molecular mechanism of EMR

We considered several modes of action for electromechanical tissue reconstruction: (i) dehydration of the hydrogel matrix followed by tissue denaturation; (ii) electrophoresis; and (iii) chemical modification of the GAG matrix. To distinguish between these possibilities, we carried out a series of electrolysis experiments using a biopotentiostat that featured two working-electrode arrays. Figure A.2 shows the cyclic voltammogram recorded at a platinum electrode inserted into rabbit septal cartilage immersed in phosphate-buffered saline (PBS), pH 7.4. The respective cathodic and anodic currents correspond to the solvent limits for hydrogen evolution and water oxidation recorded under identical conditions in the absence of cartilage. Notably, oxidation of chloride to chlorine (with subsequent conversion to hypochlorite) is also expected at the positive potential.

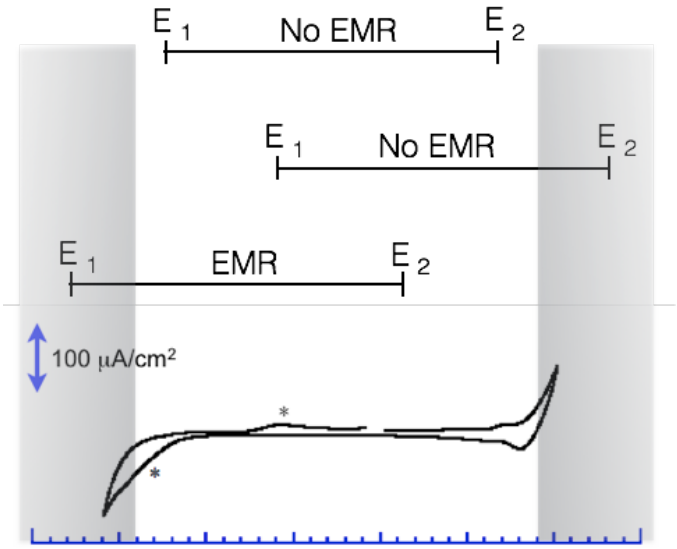

Figure A.2. Cyclic voltammogram recorded at a platinum electrode inserted into a ~ 2-mm thick section of rabbit septal cartilage submerged in PBS buffer. (Scan rate = 50 mV/sec; the response due to chloride oxidation and re-reduction is indicated by *.) Shaded areas mark respective potential thresholds for water oxidation (onset ~ 1.4 V *vs.* AgCl/Ag) and reduction (onset ~ -0.9 V *vs.* AgCl/Ag). Horizontal lines represent applied-potential gradients (E_1 and E_2 for EMR trials.

Using a 90°-reshaping jig[22] (Figure A.3), we next performed a series of reshaping experiments. To decouple the effects of voltage gradients, current flow, and applied potentials on the shape-changing process, the two sets of working electrodes were held at a constant potential difference (2 V), while the midpoint of those potentials was scanned between ± 1 V (*vs.* AgCl/Ag). Because the bipotentiostat directs electron flow between the working electrodes and a remote auxiliary electrode, current does not pass directly through the tissue.

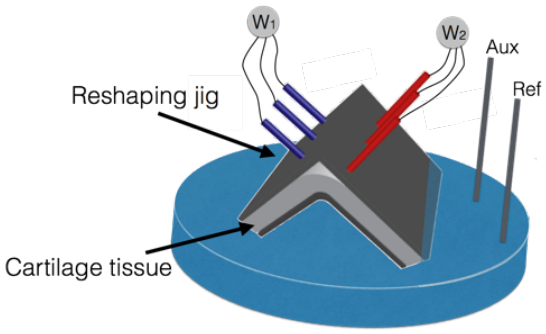

Figure A.3. Illustration of the EMR apparatus. W_1 and W_2 correspond to the two arrays of platinum-needle working electrodes.

Significantly, EMR occurs *only* when the potential of at least one set of working electrodes is held positive of the anodic limit. No potential gradient across the tissue is required; indeed, reshaping is measurably more effective when both sets of working electrodes are held positive of the water-oxidation threshold.

As illustrated in Figure A.4.A, the cartilage bend angle, θ, plotted for multiple trials *vs.* the applied potential during EMR reveals reshaping efficiencies that vary widely from run to run (albeit with a trend toward greater shape change (smaller θ) at higher potentials). However, re-plotting θ *vs.* the charge passed during each experiment (Figure A.4.B) shows

that the magnitude of EMR correlates directly with the total charge transferred, regardless of the applied potential.

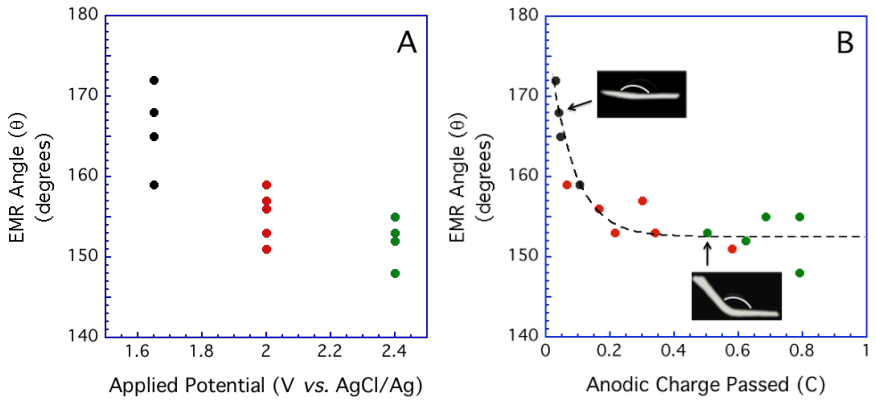

Figure A.4. (A) EMR "bend angle", θ, for multiple samples of rabbit-septal cartilage following a 2-minute electrolysis at 1.65 V (black), 2.0 V (red), and 2.4 V (green) *vs.* AgCl/Ag. Note the range of bend angles at each applied potential. (B) The same θ data re-plotted *vs.* the anodic charge passed during each run. Insets: images of reshaped cartilage following 0.05 C and 0.5 C passed.

We propose that acidification at the anode (a consequence of water oxidation) and subsequent diffusion of protons into the tissue is the dominant process responsible for shape change. Protonation of immobilized anions within the GAG matrix disrupts the ionic-bonding network that provides structural integrity to the tissue. This, in turn, relieves the stress imposed by mechanical deformation. Re-equilibration to physiological pH restores the FCD after molecules have locally "shifted" and reestablishes the ionic-bonding matrix, resulting in sustained shape change of the tissue. It is noteworthy that this mechanism explains our observation that EMR persists *ex vivo* only if the pH is re-equilibrated in neutral buffer for several minutes following electrolysis; if the specimen is instead removed from the jig immediately after electrolysis, the tissue is noticeably more malleable near the electrode placements.

This mechanism also explains why the maximum EMR-bend angles in Figure A.4 are significantly larger than (the ideal) 90°. Bending the tissue induces both tensile and compressive stress localized within the matrix;[23] chemically induced stress relaxation occurs only when the fixed negative charges at those loci lie within the diffusion radius of protons generated *via* electrolysis (~1 mm). It is evident from the plots of θ *vs.* charge that under these experimental conditions the maximum shape change is reached by ~0.5 C passed. That charge is sufficient to generate a pH gradient low enough to fully neutralize the FCD proximal to the individual electrodes in the array: stressed tissue outside of the diffusion radius remains unaffected by the EMR process and is therefore not remodeled. Indeed, placing electrodes above *and* below the axis of inertia of bent tissues results in more effective cartilage remodeling, as both tension and compression are chemically relaxed.

A.5. pH Dependence of Shape Change

Given this model, the pH threshold for inducing shape change should correspond to the pK_a of the sulfonic and carboxylic acid functional groups of the GAGs.[24] It follows that neutralizing the FCD would cause a loss of permselectivity, and that loss would be reflected in smaller Donnan potentials across the cartilage membrane. This is precisely what we find. Figure 4A shows several plots of E_{mem} vs. $\log(a_1/a_2)$ recorded as a function of pH. The slopes depend strongly on the pH of the solution, approaching zero at ~ pH 1. Plotting the slopes *vs.* the solution pH produces a sigmoidal response (Figure 4B), from which we calculate an effective tissue pK_a of ~3.5.

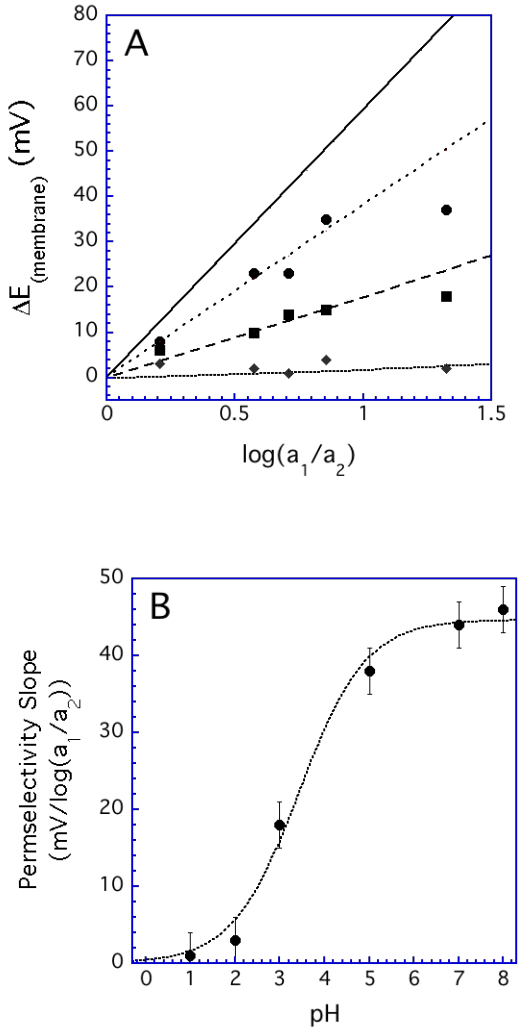

Figure A.5. (A) Plot of E_{mem} between two AgCl/Ag reference electrodes placed into concentration cells separated by a ~100 um cartilage membrane, recorded at different pH values. (●) pH 5; (■) pH 3; (▲) pH 1. Tissues were equilibrated at the given pH for 5 minutes before data collection. Solid line corresponds to an ideal permselective response. (B) Plot of the "Permselectivity Slope" as a function of solution pH.

A.6. Conclusions

In contrast to conventional surgical procedures that rely on carving, cutting, suturing, or morselizing cartilage to produce physically altered structures, EMR exploits chemical reactions (water oxidation/proton diffusion) that are both highly localized *and* highly

reversible to remodel tissue. By restoring physiological pH following EMR, remodeled cartilage regains its FCD and exhibits physical properties indistinguishable from untreated tissues.[26] Combined with previously developed finite-element models that map the internal stress within mechanically deformed tissues, coulometric analysis can be used to "dose" the EMR process to ensure maximal shape change while avoiding over-oxidation (and over-acidification). These experiments thus provide a roadmap for developing EMR as a chemical-based surgical therapy that operates by reversibly altering the inherent physical properties of tissue at the molecular level.

A.7. Experimental Section

Electrochemical measurements were carried out using a Princeton Applied Research VersaSTAT 4/3F bipotentiostat/galvanostat. Potentials are reported *vs.* AgCl/Ag in 1M KCl.

Polycarbonate concentration cells (~20 mL) featured matching 1-cm diameter holes surrounded by o-ring fittings. Cartilage membranes were positioned between the two o-rings, and the cells were clamped together prior to permselectivity assays. Donnan potentials were measured by recording the potential difference between two AgCl/Ag reference electrodes placed into each cell, using a Keithley Model 2000 digital voltmeter. 100-um thick cartilage membranes were cut from fresh porcine costal cartilage.

EMR experiments were carried out using a needle-based reshaping jig. Rabbit septal cartilage was harvested from specimens obtained from a local abattoir. Samples were loaded into the reshaping jig and partially submerged in PBS prior to electrolysis. The jig was then transferred into a large beaker containing fresh PBS and soaked for five minutes. The specimen was removed from the jig, digitally photographed, and the reshaping angle was measured using commercial software (Screen Protractor, Iconico).

Chondrocyte viability was monitored using a "live/dead" assay as previously described.[26] Specimens subjected to potential-controlled EMR exhibited only minimal chondrocyte mortality compared to untreated samples.

A.8. References and Notes

[1] Hanson, J.T. *Netter's Clinical Anatomy, Third Edition*; Elsevier Saunders: Philadelphia, PA, 2014.

[2] Lorenz, R.R. *Curr. Op. in Otolaryngology & Head & Neck Surgery* **2003**,*11*, 467.

[3] V. Oswal, M. Remacle, *Lasers in Otorhinolaryngology and Head and Neck Surgery, 2nd Ed.*, Kugler Publications: Amsterdam, 2014.

[4] Wormald, J.C.R.; Fishman, J.M.; Juniat, S.; Tolley, N.; Birchall, M.A. *J. Laryngol. Oto*. **2015**, *129*, 732.

[5] Baek, S.; Wells, P.B.; Rajagopal, K.R.; Humphrey, J.D. *J. Biomech. Eng*. **2005**, *127*, 580.

[6] Protsenko, D.E.; Ho, K.; Wong, B.J.F. *Annals Biomed. Eng*. **2006**, *34*, 455.

[7] Manuel, C.T.; Foulad, A.; Protsenko, D.E.; Sepehr, A.; Wong, B.J.F. *Ann. Biomed. Eng*. **2010**, *38*, 3389.

[8] Hussain, S.; Manuel, C.T.; Protsenko, D.E.; Wong, B.J.F. *Laryngoscope* **2015**, *125*, 1628.

[9] Animal models show that memory effects result in some shape recidivism (both acute and longer-term) of cartilage treated by EMR. Clinical procedures would likely require "over correction" to achieve the desired long-term shape. See, for example: Badran, K.W.; Manuel, C.T.; Loy, A.C.; Conderman, C.; Yau, Y.Y; Lin, J.; Tjoa, T.; Su, E.; Protsenko, D.; Wong, B.J.F.*Laryngoscope* **2015**, *125*, 2058.

[10] Ho, K.H.K.; Valdes, S.H.D.; Protsenko, D.E.; Aguliar, G.; Wong, B.J.F. *Laryngoscope* **2003**, *113*, 1916.

[11] Poole, A.R.; Kojima, T.; Yasuda, T.; Mwale, F.; Kobayashi, M.; Leverty, S. *Curr. Ortho. Prac.* **2001**, *391*, S26.

[12] Loeser, R.F. *Arthritis Rheum.* **2006**, *54*, 1357.

[13] Naegeli, R.; Redepenning, J.; Anson, F.C. *J. Phys. Chem.* **1986**, *90*, 6227.

[14] Fouland, A.; Manuel, C.; Wong, B.J.F. *Arch. Facial Plast. Surg.* **2011**, *13*, 259.

[15] Error in the permselectivity response (i.e., the slope of ΔE_{mem} vs. $\log(a_1/a_2)$) for any given run was typically quite small, cf., Figure A.1. There was, however, considerable sample-to-sample variability: at pH 7.4 individual slopes ranged from ~ 40 – 50 mV/decade depending on the individual specimen.

[16] Redepenning, J.; Anson, F.C. *J. Phys. Chem.* **1989**, *91*, 4549.

[17] Kneeland, J.B.; Reddy, R. 2007, *J. Magn. Reson. Im.* **2007**, *25*, 339.

[18] Freedman, J.D.; lusic, H.; Wiewiorski, M.; Farley, M.; Snyder, B.D.; Grinstaff, M.W. *Chem. Commun.* **2015**, *51*, 11166.

[19] Bansal, P.N.; Joshi, N.S.; Entezari, V.; Malone, B.C.; Stewart, R.C.; Snyder, B.D.; Grinstaff, M.W. *J. Ortho. Res*. **2011**, *29*, 704.

[20] Freedman, J.D.; Lusic, H.; Snyder, B.D.; Grinstaff, M.W. *Angew. Chem. Int. Ed*. **2014**, *53*, 8406.

[21] Hyun, H.; Owens, E.A.; Wada, H.; Levitz, A.; Park, G.; Park, M.H.; Frangioni, J.V.; Henary, M.; Choi, H.S. *Angew. Chem. Int. Ed*. **2015**, *54*, 8648.

[22] Wu, E.C.; Protsenko, D.E.; Khan, A.Z.; Dubin, S.; Karimi, K.; Wong, B.J.F. *IEEE T. Bio-Med. Eng.* **2011**, *58*, 2378.

[23] Protsenko, D.E.; Wong, B.J.F. *Laser. Surg. Med.* **2007**, *39*, 245.

[24] Du, Y.; Taga, A.; Suzuki, S.; Liu, W.; Honda, S. *J. Chromatogr. A* **2002**, *947*, 287.

[25] This value is slightly higher than analogous solution pK_a's of the GAG functional groups (~2.5 – 3),[24] suggesting a more hydrophobic environment inside of the tissue that renders the groups slightly less acidic.

[26] Protsenko, D.E.; Ho, K.; Wong, B.J.F. *Ann. Biomed. Eng.* **2011**, *39*, 66.

B. M-M BOND-STRETCHING ENERGY LANDSCAPES FOR $M_2(DIMEN)_4^{2+}$ (M = Rh, Ir; DIMEN = 1,8-diisocyanomenthane) COMPLEXES

Reprinted with permission from Hunter, B. M.; Villahermosa, R. M.; Exstrom, C. L.; Hill, M. G.; Mann, K. R.; Gray, H. B. M-M Bond-Stretching Energy Landscapes for $M_2(dimen)_4^{2+}$ (M = Rh, Ir ; dimen = 1,8-diisocyanomenthane) Complexes. *Inorganic Chemistry* **2012**, *51*, 6898. DOI: 10.1021/ic300716q.

B.1. Abstract:

Isomers of $Ir_2(dimen)_4^{2+}$ (dimen = 1,8-diisocyanomenthane) exhibit different Ir-Ir bond distances in 2:1 MTHF:EtCN solution (MTHF = 2-methyltetrahydrofuran). Variable-temperature absorption data suggest that the isomer with the shorter Ir-Ir distance is favored at room temperature [K = ~8; $\Delta H° = -0.8$ kcal/mol; $\Delta S° = 1.44$ cal mol^{-1} K^{-1}]. We report calculations that shed light on $M_2(dimen)_4^{2+}$ (M = Rh, Ir) structural differences: (1) metal-metal interaction favors short distances; (2) ligand deformational-strain energy favors long distances; and (3) an out-of-plane (A_{2u}) distortion promotes twisting of the ligand backbone at short metal-metal separations. Calculated potential-energy surfaces reveal a double minimum for $Ir_2(dimen)_4^{2+}$ (~4.1 Å Ir-Ir with 0° twist angle and ~3.6 Å Ir-Ir with ±12° twist angle), but not for the rhodium analogue (~4.5 Å Rh-Rh with no twisting). As both the ligand strain and A_{2u} distortional energy are virtually identical for the two complexes, the strength of the metal-metal interaction is the determining factor. Based on the magnitude of this interaction, we obtain the following results: (1) a single-minimum (along the Ir-Ir coordinate), harmonic potential-energy surface for the triplet electronic-excited state of $Ir_2(dimen)_4^{2+}$ ($R_{e,Ir-Ir} = 2.87$ Å, $F_{Ir-Ir} = 0.99$ mdyne/Å); (2) a single-minimum, anharmonic surface for the ground state of $Rh_2(dimen)_4^{2+}$ ($R_{e,Rh-Rh} = 3.23$ Å, $F_{Rh-Rh} = 0.09$ mdyne/Å); and

(3) a double-minimum (along the Ir-Ir coordinate) surface for the ground state of $Ir_2(dimen)_4^{2+}$ ($R_{e,Ir-Ir}$ = 3.23 Å, F_{Ir-Ir} = 0.16 mdyne/Å).

B.2. Introduction

Binuclear complexes of square-planar Rh(I), Ir(I), and Pt(II) centers have been extensively investigated, owing in part to their spectroscopic, photophysical, and photochemical properties.[1-7] The electronic structures of these d^8-d^8 complexes feature a d_z^2-derived HOMO that is σ-antibonding and a p_z-derived LUMO that is σ-bonding (Figure B.1),[8] giving rise to a broad dσ* → pσ absorption whose position in the spectrum depends strongly on the metal-metal separation.[9-11]

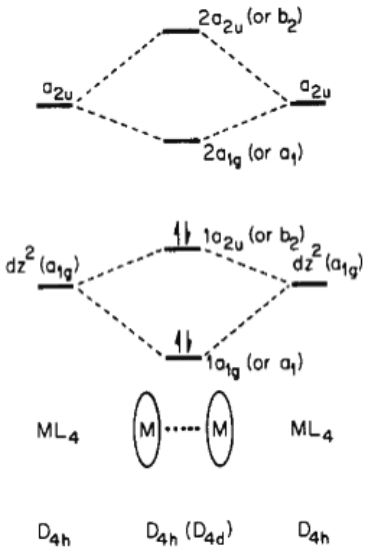

Figure B.1. Molecular-orbital scheme for d^8-d^8 face-to-face dimers, derived from the a_{1g} (d_z^2) and a_{2u} (p_z) monomer functions for $[Rh(CNPh)_4]_2^{2+}$. Reproduced from ref. 8.

It has been known since 1975 that the Rh(I) tetrakis(phenylisocyanide) cation dimerizes in concentrated solutions through the formation of an unsupported Rh-Rh bond.[8] In accord with a d^8-d^8 molecular-orbital model,[8] as well as a recent DFT analysis,[12] the Rh-Rh bond in $[Rh(CNPh)_4]_2^{2+}$ is relatively weak in the ground state (on the order of ~10

kcal/mol).[9,12] In contrast, Rh-Rh bonding in the $^{1,3}A_{2u}$ ($d\sigma^* \rightarrow p\sigma$) excited states is much stronger,[13] as confirmed by excited-state Raman and time-resolved X-ray diffraction investigations.[14]

Since the $d\sigma^* \rightarrow p\sigma$ transition normally gives rise to a symmetric band in the visible absorption spectrum of a d^8-d^8 complex, we suggested that the decidedly *asymmetric* system observed for a Rh(I) dimer bridged by four dimen (1,8-diisocyanomenthane) ligands (Figure B.2) logically must be related to an extended Rh-Rh

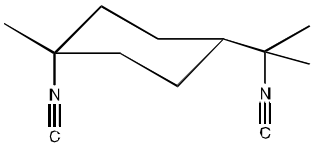

Figure B.2. Dimen ligand.

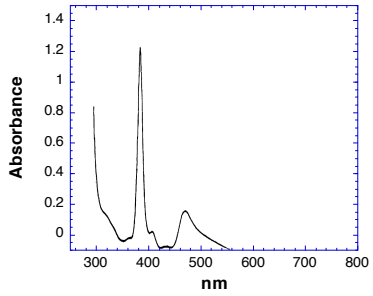

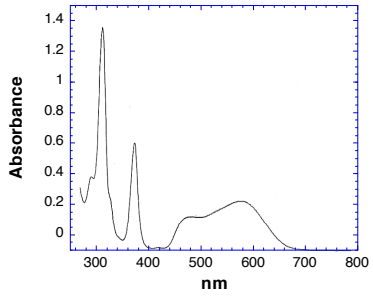

Figure B.3. UV-vis absorption spectra: $Rh_2(dimen)_4^{2+}$ (top); and $Ir_2(dimen)_4^{2+}$ (bottom) in CH_3CN solution.

separation imposed by the relatively rigid cyclohexyl unit:[4] the natural bridging distance of dimen is ~5 Å *versus* the ~3.3-Å separation[15] observed for $Rh_2(TM4)_4^{2+}$, where TM4 = 2,5-diisocyano-2,5-dimethylhexane, a flexible bridging ligand. For $Rh_2(dimen)_4^{2+}$, then, there is a very shallow, anharmonic ground-state potential-energy profile along the Rh-Rh coordinate: dimen strain dominates an energy landscape that is distorted by weak Rh-Rh attraction, giving rise to an asymmetric $d\sigma^* \rightarrow p\sigma$ absorption system.

The spectrum of $Ir_2(dimen)_4^{2+}$ is even richer, showing two distinct absorption maxima (~470 and 580 nm) at room temperature in fluid solutions.[16] Based on (1) our serendipitous observation that the color of the Ir(I) complex changes reversibly from purple to blue as a function of temperature; (2) the strong correlation between solid-state Ir-Ir distance and the position of the $d\sigma^* \rightarrow p\sigma$ absorption band for $Ir_2(dimen)_4^{2+}$ salts containing different counterions;[16] and (3) solution Raman data that revealed resonance enhancement of two different Ir-Ir stretching frequencies (12 cm^{-1} and 48 cm^{-1}) upon respective excitation into the high- *vs*. low-energy regions of the absorption system,[17] we suggested that $Ir_2(dimen)_4^{2+}$ exists as an equilibrium mixture of two isomers with different Ir-Ir separations in room-temperature solutions. Very recently, this model was supported by independent investigations, one involving ultrafast laser spectroscopy by Gaffney and coworkers,[18] and another based on time-resolved X-ray scattering by Haldrup *et al.*[19] Thus $Ir_2(dimen)_4^{2+}$ is a rare example of "deformational" isomerism.[20-24]

Noting the head-to-tail asymmetry of the dimen ligand, Haldrup and coworkers suggested that the two Ir-Ir distances of $Ir_2(dimen)_4^{2+}$ arise from different geometric isomers that result from the various head-to-tail arrangements of the ligands.[19] Although we cannot rule out this proposal, we favor an alternative explanation here supported by calculations in which the structural elements of $M_2(dimen)_4^{2+}$ have been factored into separate metal- and ligand-based distortions. Overlaying these individual potentials yields composite potential-energy surfaces for $Rh_2(dimen)_4^{2+}$ and $Ir_2(dimen)_4^{2+}$ that are in accord with all the experimental data: the Rh(I) surface shows a single minimum along the Rh-Rh coordinate, whereas the Ir(I) analogue exhibits distinct minima at two different Ir-Ir spacings. Our calculations indicate that the inherent energy required to distort four dimen ligands along the

various deformational coordinates (rather than the specific geometric arrangements of the ligands around the d^8 metal centers) can be offset by d^8-d^8 M-M interactions with the result that there is either a single or double minimum in the potential profile along the M-M coordinate.

B.3. Experimental

The compounds $[Ir_2(dimen)_4][Y]_2$ (Y = PF_6^-, TFPB (tetrakis[3,5-bis(trifluoromethyl)phenyl]borate), and $B(C_6H_5)_4^-$) were prepared according to previously reported procedures.[25] UV/vis spectra were obtained on a Tracor Northern TN-6500 diode array apparatus employing a Xe arc lamp as the light source. Samples were prepared in a 2:1 mixture of 2-methyltetrahydrofuran (MTHF) to ethyl cyanide (EtCN), which formed a clear, glassy matrix at low temperatures. Variable temperature measurements were obtained using an Air Products Model APD-E temperature indicator/controller. Density functional theory (DFT) calculations were carried out using the commercial *Gaussian* software package[26] at the B3LYP/6-311G level.[27]

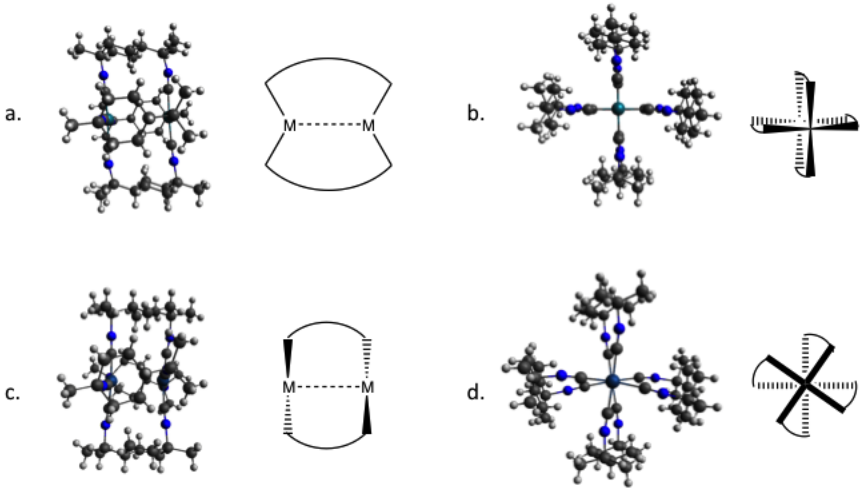

Figure B.4. Structural diagrams for the deformational motifs of $Ir_2(dimen)_4^{2+}$: (a) side-view of eclipsed geometry; (b) end-view of eclipsed geometry; (c) side-view of twisted geometry; (d) end-view of twisted geometry.

B.4. Results and Discussion

The crystal structures of $[M_2(dimen)_4][Y]_2$ (M = Rh or Ir; Y = PF_6^-, TFPB (tetrakis[3,5-bis(trifluoromethyl)phenyl]borate), and $B(C_6H_5)_4^-$) salts reveal a remarkable range of M-M spacings (3.6-4.5 Å, depending on the identity of M and Y).[16] Moving along the M-M coordinate, the dimen ligands accommodate distances shorter than ~5 Å *via* two distinct and sequential deformational modes: first, a bending motion in which the isocyano moieties remain eclipsed but "pinch" together; then, at distances < ~3.9 Å, a twisting motion in which the isocyano groups stagger by dihedral angle θ, thereby distorting the ligand backbone (Figure B.4). Two geometric motifs therefore emerge for $Ir_2(dimen_4)^{2+}$: an eclipsed "paddle wheel" conformation (Ir-Ir > ~3.9 Å); and a twisted "propeller" conformation (Ir-Ir < ~3.9 Å).

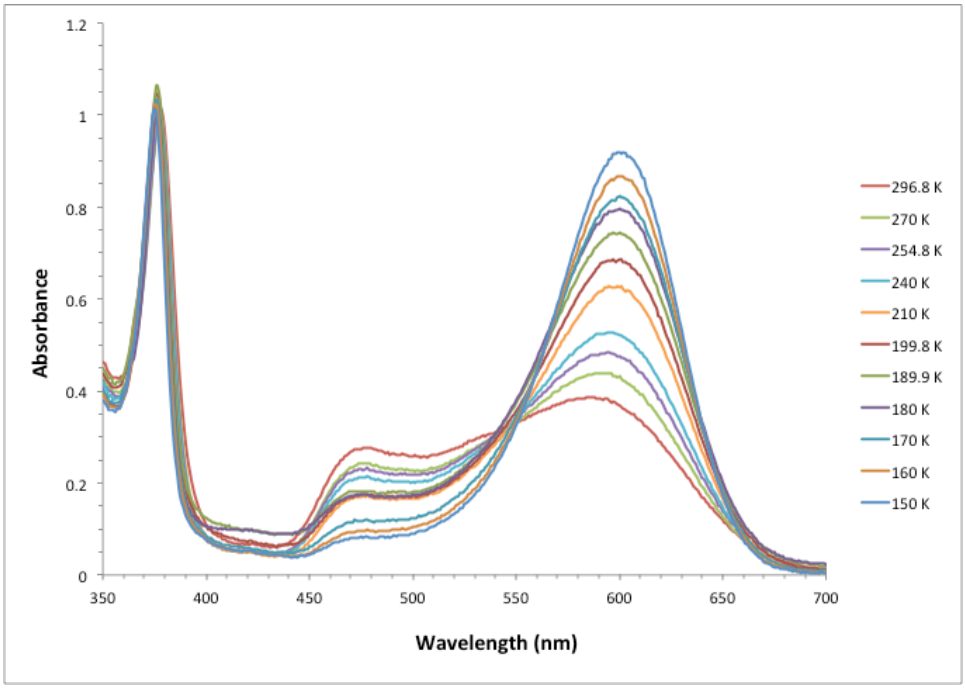

Figure B.5. UV-vis absorption spectra of $Ir_2(dimen)_4^{2+}$ in 2:1 MTHF:EtCN recorded between 296.8 and 150 K. Spectra have been corrected for changes in solvent density and index of refraction.

Notably, the solution absorption spectrum of $Ir_2(dimen)_4^{2+}$ exhibits two maxima that are temperature dependent (Figure B.5). The absorption at 470 nm decreases in intensity as the temperature is lowered, while the 580-nm absorption increases. At temperatures lower than ~120 K, only a single maximum (580 nm) is observed. This process is completely reversible, consistent with rapid equilibration of two isomers, "long" and "short" with respect to Ir-Ir distance, each with its signature absorption. Based on the solid-state absorption maxima of the PF_6^- and $B(C_6H_5)_4^-$ salts (λ_{max} = 468, 580 nm, respectively), we assign the 470-nm band to a paddle-wheel structure that resembles the PF_6^- salt ("long" Ir-Ir distance and eclipsed dimen ligands) and the 580-nm band to a propeller structure resembling the $B(C_6H_5)_4^-$ salt ("short" Ir-Ir distance and twisted dimen ligands). Analyzing these data yields values of $\Delta H°$ and $\Delta S°$ of -0.8 kcal/mol and 1.44 cal mol^{-1} K^{-1} for the long $\Leftrightarrows$ short equilibrium. Based on X-ray structural data,[16] we estimate that the long isomer has an Ir-Ir separation of ~4.5 Å (dihedral twist angle of 0°), while the short isomer has an Ir-Ir distance of ~3.6 Å (twist angle near ~17°).[28,29]

A vibrational wavepacket analysis by Gaffney *et al.* based on ultrafast transient-absorption data confirms that there are indeed two ground-state Ir-Ir stretches in acetonitrile solution.[18] To aid in their analysis, these workers also carried out DFT calculations on $Ir_2(dimen)_4^{2+}$. In their simulations, the $[Ir_2(dimen)_4][PF_6]_2$ X-ray structure was optimized under forced C_{2v} and C_2 symmetries, resulting in geometries qualitatively similar to those seen experimentally: C_{2v}, long Ir-Ir distance, eclipsed ligands; C_2, short Ir-Ir distance, twisted ligands (it is of interest that similar findings were reported by Coppens *et al*. for a related Rh complex).[30] Although the computations correctly predicted two optimized geometries, the authors noted that they differed quantitatively from the actual (X-ray) structures.[18]

From a structural point of view, the whole-molecule DFT analysis leaves several important questions unanswered. For example, why are there distinct flexing *vs.* twisting ligand distortions for the long and short isomers? Perhaps more fundamentally, which factors lead to the energetic balance between the two deformational isomers in the first place? In an attempt to answer these questions, we have examined four separate elements of the overall

potential surface: (1) a pure metal-metal stretch; (2) an out-of-square-plane bending mode of A_{2u} symmetry; (3) a ligand flexing motion; and (4) a twisting of the square planes about the M-M axis. Although we rely on DFT calculations to estimate the energies involved in distorting the dimen ligands, the other deformational energies can be obtained from spectroscopic data.

B.4.1. Metal-Metal Interaction

We first considered the ground-state d^8-d^8 M-M interaction. Previous resonance-Raman studies of the $M_2(TM4)_4^{2+}$ analogues of $M_2(dimen)_4^{2+}$ revealed a ground-state ν(M-M) frequency of 55 cm^{-1} for $Rh_2(TM4)_4^{2+}$ and 53 cm^{-1} for $Ir_2(TM4)_4^{2+}$.[10,13] These values yield respective ν(Rh-Rh) and ν(Ir-Ir) force constants of 0.09 and 0.16 mdyne/Å. As expected, ν(Ir-Ir) is much larger in the $Ir_2(TM4)_4^{2+}$ $^3A_{2u}$ state (132 cm^{-1}).[10] TM4 features a flexible alkane bridge that allows the metal centers to adopt their preferred "bond" distances. These distances were calculated using Woodruff's relationship,[29] which gives R_e = 3.23 Å for both Rh(I) and Ir(I) (the calculated Ir-Ir distance in electronically excited ($^{1,3}A_{2u}$) $Ir_2(dimen)_4^{2+}$ is 2.87 Å). We previously estimated the Rh-Rh bond strength to be 12 ± 6 kcal/mol,[9] and experience suggests that the $5d^8$-$5d^8$ Ir-Ir bond will be stronger (~ 25 kcal/mol).

The Morse potential curves for d^8-d^8 Rh(I) and Ir(I) are shown in Figure 5. Clearly, this potential favors short M-M distances, and Ir(I) has a deeper well than Rh(I).

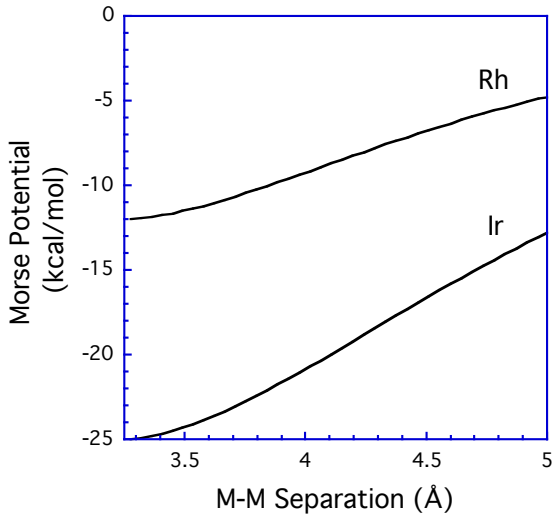

Figure B.6. Calculated Morse potentials for the M(I)-M(I) interaction. Force constants were calculated from experimental Raman frequencies (Rh=0.09 and Ir=0.16 mdyne/Å) and equilibrium bond distances were estimated from Woodruff's relationship (3.23 Å). The Rh(I) and Ir(I) well depths were estimated to be 12 and 25 kcal/mol respectively.

B.4.2. Ligand Strain

Balancing the attraction of the metal centers is the energy required to distort four dimen ligands to accommodate a short M-M separation. Indeed, owing to the relatively weak "bond" between the metal centers, it seemed likely that ligand strain might be the dominant force in determining the optimal M-M separation.

The effect of dimen ligand deformation was explored by performing constrained DFT optimizations on a free ligand. Initially, the isocyano groups were restricted to the same plane. By further constraining the distance between the two terminal carbon atoms of the isocyano groups (the "bridging C---C" distance), the extent of bending of the ligand was controlled. The C---C parameter was scanned from 3.8-4.8 Å, corresponding to a range of 3.2-5.0 Å along the M-M axis (this assumes an average Ir-C bond length of 1.93 Å). Structures were optimized at 0.025 Å increments, and the calculated energy for each structure was multiplied by four to account for the entire set of ligands. The relative energies of this

"pinching" distortion are plotted *vs.* the corresponding M-M distance in Figure B.7 (solid line). The lowest-energy conformation of the ligand occurs at an M-M distance of ~5 Å, which is close to that of the experimentally determined "long" form of $Ir_2(dimen)_4^{2+}$. The energy required to distort the ligands to accommodate an M-M distance of 3.5 Å *via* this pinching mode is ~6 kcal/mol.

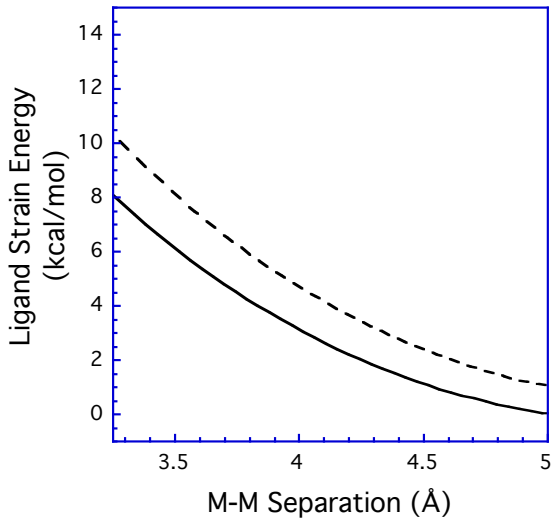

Figure B.7. Calculated ligand-strain energy as a function of M-M separation for $M_2(dimen)_4^{2+}$ complexes constrained such that the square planes are either eclipsed (0° twist angle, solid line) or twisted (10° dihedral angle, dashed line).

In addition to "pinching", dimen ligands also exhibit a pronounced "twisting" about the M-M axis at shorter M-M distances (< ~3.9 Å). Interestingly, this second mode of ligand deformation is not predicted by ligand-based DFT calculations. A second set of optimizations was performed in which the ligand was constrained to a twist angle of 10° while the M-M coordinate was again scanned. The energy of this "twisting" distortion *vs.* M-M distance (Figure B.7, dashed line) shows that the twisted geometry is higher in energy than the corresponding eclipsed geometry *at every metal-metal distance*. Consequently, the ligand-based calculations suggest that the complex should never twist, regardless of the M-M distance.

To address this problem, we examined the localized structural effects of ligand "pinching" *vs.* "twisting" at the metal centers. Based on the backbone length of dimen, the individual Ir(I) units of an eclipsed (paddle wheel) dimer can be perfectly planar only at an Ir-Ir spacing of ~4.5 Å. At shorter (or longer) spacings, the dimen ligands pinch (or expand), causing out-of-plane distortions along the A_{2u} bending normal mode at the metal centers. On the other hand, twisting the dimen ligands as the M-M separation becomes shorter allows the ML_4 geometry to retain a *quasi*-planar structure. As such, it is likely that the dimen ligands twist in order to reduce the strain associated with distortion along the A_{2u} bending coordinate.

To quantify this out-of-plane distortional energy, the DFT-optimized structures from the ligand-strain calculations were used to estimate the extent that each ML_4 center would be deformed under the imposed ligand geometry. The out-of-plane deformational energy was calculated according to:

$$E_{A2u} = F\phi^2,$$

where F is the force constant given by normal-mode analysis and ϕ is the magnitude of the distortion from planarity. Because the relevant vibrational frequencies are not known for $Ir_2(dimen)_4^{2+}$, we used the value calculated by Kubas and Jones for the A_{2u} normal mode of $Pt(CN)_4^{2-}$ (0.65 mdyne Å rad^{-2}, 93.5 kcal mol^{-1} rad^{-2})[31] as an estimate for F. The rather large force constant for this bending mode presumably originates from disrupting π-bonding to CN as the ligands move out-of-plane along the A_{2u} coordinate.

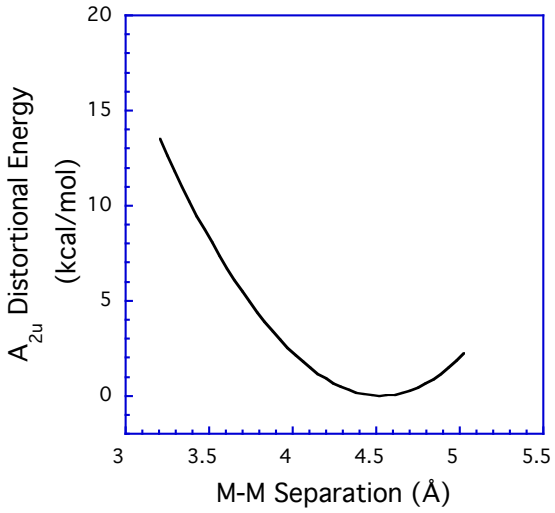

Figure B.8. Out-of-plane distortional energy (A_{2u} bending mode with local D_{4h} symmetry) as a function of M-M distance, calculated for $M_2(dimen)_4^{2+}$ constrained in an eclipsed configuration.

Figure B.8 shows a plot of this A_{2u} distortional energy as a function of M-M separation, assuming a perfectly-eclipsed dimen geometry. The magnitude of the A_{2u} out-of-plane bending term is comparable in size to ligand strain, reinforcing the preference for a long M-M distance when the isocyano groups are eclipsed.

B.4.3. Potential Energy Profiles

The structural elements that determine the preferred M-M separation in $Ir_2(dimen)_4^{2+}$ are: (1) an M-M interaction that favors short distances; (2) ligand deformational strain that favors long distances; and (3) an out-of-plane distortional potential that promotes twisting of the dimen backbone at short M-M distances.

Because the ligand-pinching motion is coupled with out-of-plane A_{2u} dynamics, we can revise the Ir-Ir Morse curve to obtain a 2D potential-energy profile for distortion of the eclipsed (0° dihedral) (paddle-wheel) structure of $Ir(dimen)_4^{2+}$ along the M-M coordinate. Likewise, we can combine the (higher) deformational-strain energy of the twisted dimen ligands (10° dihedral) with the same Ir-Ir Morse potential to construct the analogous 2D

profile that corresponds to the twisted (propeller) form of the complex. These potential profiles are shown along with similarly-constructed ones for the paddle-wheel and propeller forms of $Rh_2(dimen)_4^{2+}$ in Figure B.9.

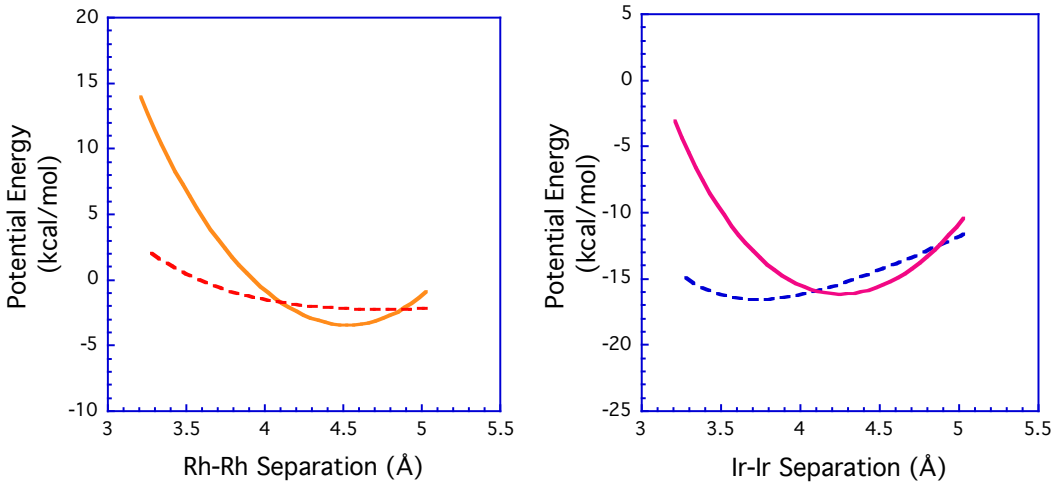

Figure B.9. Calculated ground-state potential profiles for $Rh_2(dimen)_4^{2+}$ (top) and $Ir_2(dimen)_4^{2+}$ (bottom). Solid lines indicate eclipsed (0° dihedral angle) ligand conformations and dashed lines indicate twisted (10° dihedral angle) ligand arrangements. For Ir(I), the eclipsed geometry features a minimum at ~4.3Å while the twisted geometry has a well at ~3.7Å. There is a small barrier where the two geometries cross at ~4.1Å, which is approximately where twisting occurs in the crystal structures. For Rh(I), the twisted (dashed) potential energy curve is not sufficiently deep to produce a second minimum at short Rh-Rh distances. Notably, this $Rh_2(dimen)_4^{2+}$ profile is remarkably similar to the surface we predicted[4] based on extensive spectroscopic measurements; and it is nearly identical with the surface calculated by DFT.[35]

Not only do these potential energy curves reveal the emergence of a double-potential-energy minimum for the Ir(I) complex, they also explain why the phenomenon is not observed for the Rh(I) analogue. At long Ir-Ir distances, ligand geometry and out-of-plane distortional energy dominate the total potential energy, resulting in a "long" isomer with an Ir-Ir distance of ~4.5 Å, close to the A_{2u} surface minimum. At shorter M-M distances, however, a second region exists in which twisted dimen structures are able to minimize the

out-of-plane distortion while maximizing the M-M bonding interaction. These curves cross at an intermediate Ir-Ir separation near 4.1 Å, remarkably close to that observed for $Ir_2(dimen)_4^{2+}$ X-ray structures that reveal square-plane twisting. In the case of the Rh(I) analogue, the Rh-Rh interaction is too weak to produce a second minimum in the short distance region. Thus, the relatively greater strength of the Ir(I) interaction is responsible for the second, low-energy structure, which turns out to be the preferred isomeric form.

B.4.4. 3D Potential Energy Surfaces

Two-dimensional slices of far more complicated potential-energy surfaces are shown in Figure B.9. As we would like to look more closely at transition states, we attempted to calculate a three-dimensional (3D) surface for $Ir_2(dimen)_4^{2+}$ as a function of Ir-Ir separation and ligand dihedral-twist angle.

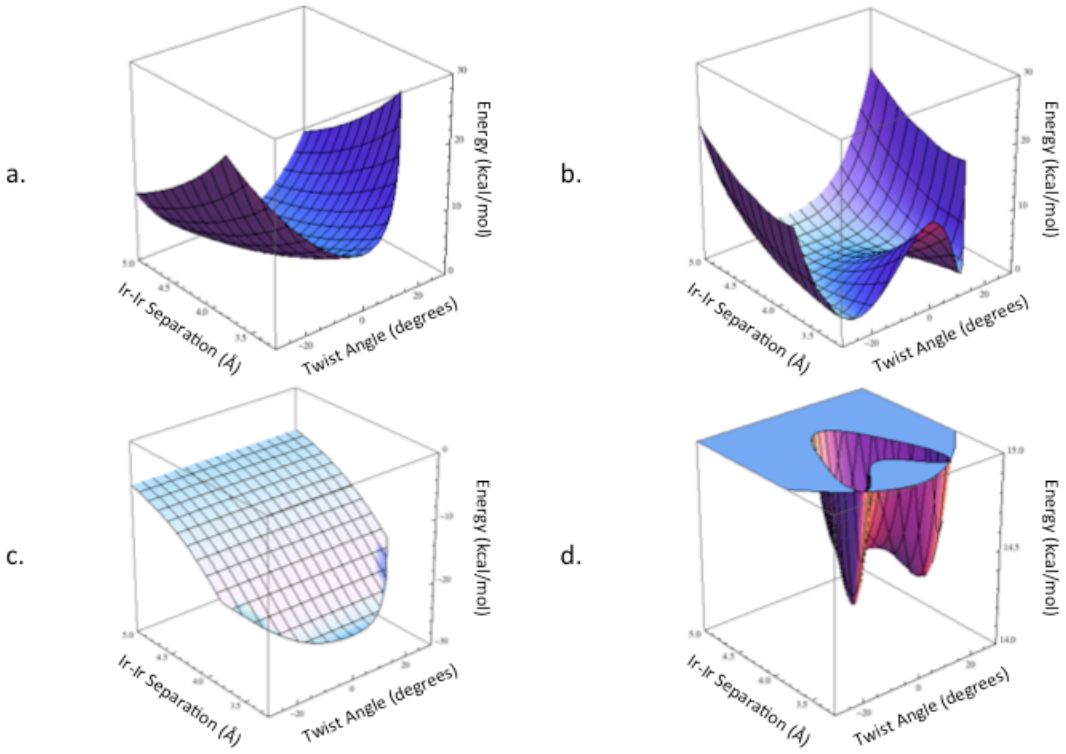

Figure B.10. Potential-energy surfaces for $Ir_2(dimen)_4^{2+}$ as a function of Ir-Ir distance (3.2-5.0 Å) and dihedral twist angle (-30-30°). Vertical axis units are kcal/mol: (a) ligand deformation energy; (b) A_{2u} out-of-plane distortional energy; (c) Morse potential; (d) total-energy surface.

Ligand geometries were independently constrained along both the bending and dihedral-twisting coordinates across the range of values found in crystal structures (Ir-Ir 3.2-5.0 Å, dihedral twist 0-30°). These geometries were then optimized, and the deformational energy of four dimen ligands in each of the configurations was plotted as a function of the M-M distance and twist angle (Figure B.10a). Utilizing symmetry, positive and negative twist angles were assumed to have the same deformational energy, and the surface was mirrored for -30-0°.

Each optimized ligand structure was used to determine the out-of-plane distortion, ϕ, of an ML_4 center constrained to that geometry. The calculated A_{2u} out-of-plane distortional energy was included in the potential-energy surface shown in Figure B.10b. The energetic cost of

distorting the metal square planes is substantial, and it is largest for eclipsed-ligand structures. We clearly see the benefit of propeller-type geometries; a horseshoe-shaped minimum traces out a set of structures with small out-of-plane distortions that require ligand twisting, thereby demonstrating that this structural element is primarily responsible for the geometrical change from the long to short Ir-Ir form.

The ligand and A_{2u} surfaces were combined with a modified Morse potential for $Ir_2(dimen)_4^{2+}$ (Figure B.10c)[32] to produce the potential energy surface Figure B.10d (a topographical contour map of B.10d is in Figure B.11b) that shows three distinct local minima (two are equivalent structures differing only by the twist direction) corresponding to long and short M-M distances. Furthermore, the short form is favored by less than 1 kcal/mol, and the barrier between the two states is predictably very small. The minima are located approximately at the values expected from the experimental data: ~4.1 Å / 0° twist; and ~3.6 Å / ± 12° twist.

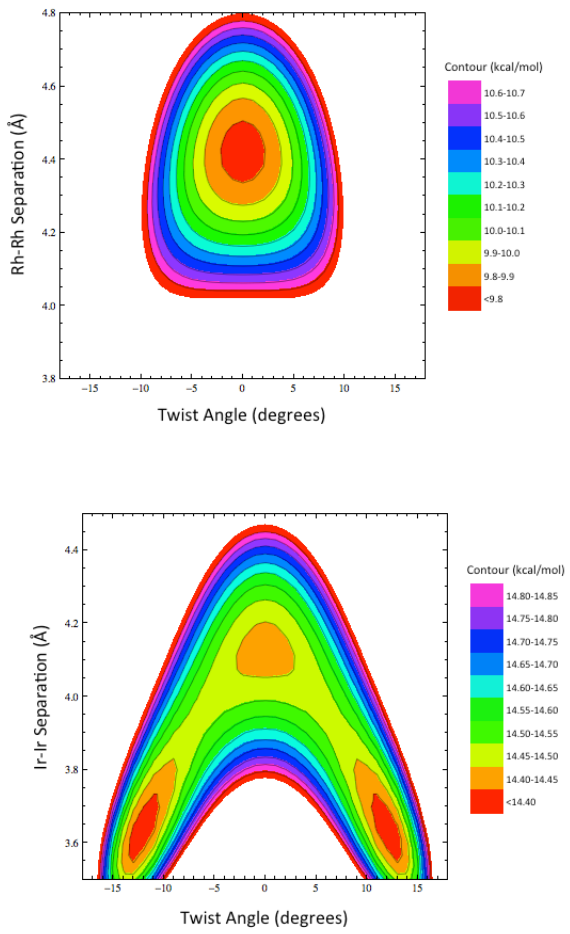

Figure B.11. Contour plots of potential-energy surfaces for $Rh_2(dimen)_4^{2+}$ (top) and $Ir_2(dimen)_4^{2+}$ (bottom).

A contour map of the calculated $Rh_2(dimen)_4^{2+}$ surface is shown in Figure B.11a. Since the weaker Rh-Rh interaction is insufficient to overcome the substantial ligand strain and/or A_{2u} deformational energy, the surface features a single minimum at a relatively long Rh-Rh separation (~4.5 Å) and 0° twist angle. Consistent with our previous spectroscopic analysis, the surface is highly anharmonic.[33]

B.5. Conclusion

In comparing our model to the proposal that head-to-tail ligand arrangements are responsible for conformational isomerism, we emphasize that the explanation offered here is consistent with the temperature dependence of equilibrium $Ir_2(dimen)_4^{2+}$ isomer populations. Nuclear magnetic resonance spectroscopic data show that there is a statistical distribution of ligands at room temperature.[34] Clearly, if the head-to-tail ligand arrangement determines the lowest-energy structure, this distribution would have to change at low temperatures, and it would have to change very rapidly. Ligand substitution on the timescale that we see equilibration is unlikely.

Our proposed model is also predictive, explaining both the ground-state spectroscopy of $Rh_2(dimen)_4^{2+}$, and the excited-state spectroscopy of $Ir_2(dimen)_4^{2+}$. Electronic absorption data indicate that $Rh_2(dimen)_4^{2+}$ has a single, anharmonic potential-energy surface in the ground state, while $Ir_2(dimen)_4^{2+}$ features minima at two different Ir-Ir distances, a finding that can be attributed to a weaker Rh-Rh interaction. Additionally, because $M_2(dimen)_4^{2+}$ $d\sigma^* \rightarrow p\sigma$ excitation leads to a formal M-M bond, we expect that the increased M-M interaction in the excited state will dominate the surface, thereby eliminating minima at longer M-M distances. The single, symmetric emission band in each of the Ir(I) and Rh(I) complexes is fully in line with this interpretation.

B.6. References and Notes

[1] (a) Mann, K.R.; Lewis, N.S.; Miskowski, V.M.; Erwin, D.K.; Hammond, G.S.; Gray, H.B. *J. Am. Chem. Soc.* **1977**, *99*, 5525. (b) Dallinger, R.F.; Miskowski, V.M.; Gray, H.B.; Woodruff, W.H. *J. Am. Chem. Soc.* **1981**, *103*, 1595.

[2] Rodman, G.S.; Daws, C.A.; Mann, K.R. *Inorg. Chem.* **1988**, *27*, 3347.

[3] (a) Smith, D.C.; Gray, H.B. *Coord. Chem. Rev.* **1990**, *100*, 169. (b) Mann, K.R.; Gray, H.B. *Adv. Chem. Ser.* **1979**, *173*, 225. (c) Rice, S.F.; Milder, S.J.; Goldbeck, R.A.; Kliger, D.S.; Gray, H.B. *Coord. Chem. Rev.* **1982**, *42*, 349. (d) Roundhill, D.M.; Gray, H.B.; Che, C.-M. *Acc. Chem. Res.* **1989**, *22*, 55.

[4] Miskowski, V.M.; Rice, S.F.; Gray H.B.; Dallinger, R.F.; Milder, S.J.; Hill, M.G.; Exstrom, C.L.; Mann, K.R. *Inorg Chem.* **1994,** *33*, 2799.

[5] Connick, W.B.; Marsh, R.E.; Schaefer, W.P.; Gray, H.B. *Inorg. Chem.* **1997**, *36*, 913.

[6] Leung, S.Y.-L.; Lam, W.H.; Zhu, N.; Yam, V.W.-W. *Organometallics* **2010**, *29*, 5558.

[7] (a) Hill, M.G.; Mann, K.R. *Inorg. Chem.* **1991**, *30*, 1429. (b) Hill, M.G.; Mann, K.R. *Inorg. Chim. Acta* **1994**, *243*, 219.

[8] Mann, K.R.; Gordon, J.G.; Gray, H.B. *J. Am. Chem. Soc.* **1975**, *97*, 3553.

[9] Rice, S.F.; Miskowski, V.M.; Gray, H.B. *Inorg. Chem.* **1988**, *27*, 4704.

[10] Smith, D.C.; Miskowski, V.M.; Mason, W.R.; Gray, H.B. *J. Am. Chem. Soc.* **1990**, *112*, 3759.

[11] Miskowski, V.M.; Rice, S.F.; Gray, H.B.; Milder, S.J. *J. Phys. Chem.* **1993**, *97*, 4277.

[12] Grimme, S.; Djukic, J.-P. *Inorg. Chem.* **2011**, *50*, 2619.

[13] Dallinger, R.F.; Carlson, M.J.; Miskowski, V.M.; Gray, H.B. *Inorg. Chem.* **1998**, *37*, 5011.

[14] Coppens, P.; Gerlits, O.; Vorontsov, I.; Kovarlevsky, A.; Chen, Y.; Graber, T.; Gembicky, M.; Novozhilova, I. *Chem. Commun.* **2004**, *19*, 2144.

[15] Mann, K.R.; Thich, J.A.; Bell, R.A.; Coyle, C.L.; Gray, H.B. *Inorg. Chem.***1980**, *19*, 2462.

[16] Exstrom, C.L.; Britton, D.; Mann, K.R.; Hill, M.G.; Miskowski, V.M.; Schaefer, W.P; Gray, H.B. *Inorg. Chem.* **1996**, *35*, 549.

[17] Villahermosa, R. and Miskowski, V.M. Unpublished work.

[18] Hartsock, R.W.; Zhang, W.; Hill, M.G.; Sabat, B.; Gaffney, K.J. *J. Phys. Chem. A* **2011**, *115*, 2920.

[19] Haldrup, K.; Harlang, T.; Christensen, M.; Dohn, A.; Brandt van Driel, T.; Skov Kjaer, K.; Harrit, N.; Vibenholt, J.; Guerin, L.; Wulff, M.; Nielsen, M.M. *Inorg. Chem.* **2011**, *50*, 9329.

[20] Kolle, U.; Kossakowski, J.; Klaff, N.; Wesemann, L.; Englert, U.; Heberich, G. E. *Angew. Chem., Int. Ed. Engl.* **1991**, *30*, 690.

[21] Rohmer, M.M.; Benard, M. *Chem. Soc. Rev.* **2001**, *30*, 340.

[22] Comba, P.; Pandian, S.;Wadepohl, H.; Wiesner, S. *Inorg. Chim. Acta* **2011**, *374*, 422.

[23] Petrov, K.T.; Pinter, B.; Veszpremi, T. *J. Organomet. Chem.* **2012**, *706*, 84..

[24] Franzen, S.; Miskowski, V.M.; Shreve, A.P.; Wallace-Williams, S.E.; Woodruff, W.H.; Ondrias, M.R.; Barr, M.E.; Moore, L.; Boxer, S.G. *Inorg. Chem.* **2001**, *40*, 6375.

[25] (a) Smith, T.P. Ph.D. Dissertation, California Institute of Technology, 1989. (b) Sykes, A.G. Ph.D. Dissertation, University of Minnesota, 1990. (c) Hill, M.G. Ph.D. Dissertation, University of Minnesota, 1992.

[26] Frisch, M.J.; *et. al. Gaussian 03,* revision C.02; Gaussian Inc.; Wallingford, CT. 2004.

[27] (a) Becke, A.D. *J. Chem. Phys.* **1993**, *98*, 5648. (b) Lee, C.; Yang, W.; Parr, R.G. *Phys. Rev. B.* **1988**, *37*, 785. (c) Stephens, P.J.; Devlin, F.J.; Chabalowski, C.F.; Frisch, M.J. *J. Phys. Chem.* **1994**, *98*, 11623.

[28] We could, in theory, estimate the M-M separation based on the vibrational frequencies measured by resonance Raman or wavepacket analysis (Ref. 18) and the correlations developed by Woodruff (Ref. 28); however, these correlations break down for very weak M-M interactions, especially at the limit of the long M-M conformational isomer. For the short M-M isomer, we would predict a 3.25 Å Ir-Ir distance. We expect that the actual value lies somewhere between 3.25 and 3.6 Å.

[29] Miskowski, V.M.; Dallinger, R.F.; Christoph, G.G.; Morris, D.E.; Spies, G.H.; Woodruff, W.H. *Inorg. Chem.* **1987**, *26*, 2127.

[30] Novozhilova, I.V.; Volkov, A.V.; Coppens, P. *Inorg. Chem.* **2004**, *43*, 2299. For computational reasons, the symmetries in this analysis were lowered from ideal C_4/C_{4v} to C_2/C_{2v}.

[31] Kubas, G.J.; Jones, L.H. *Inorg. Chem.* **1974**, *13*, 2816.

[32] For 3D potential energy surface calculations, the Ir-Ir interaction was estimated to be 18.5 kcal/mol and the force constant was 0.65 mdyne/Å (the latter is approximately four times larger than the experimentally determined value). The need to increase the Ir-Ir force constant may be related to an overestimation of the A_{2u} distortional energy for twisted geometries.

[33] The calculated surface for the excited triplet of $Ir_2(dimen)_4^{2+}$ shows a single minimum along the Ir-Ir coordinate (see Supporting Information, Figure S8) corresponding to an Ir-Ir separation of ~3Å and a dihedral twist angle of ± 16°.

[34] Sykes, A.G.; Mann, K.R. *Inorg. Chem.* **1990**, *29*, 4449.

[35] Coppens, P.; Benedict, J.; Messerschmidt, M.; Novozhilova, I.; Graber, T.; Chen, Y.-S.; Vorontsov, I.; Scheins, S.; Zheng, S.-L. *Acta Cryst. A.* **2010**, *66*, 179.

C. REDUCED AND SUPERREDUCED DIPLATINUM COMPLEXES

Reprinted with permission from Darnton, T. V; Hunter, B. M.; Hill, M.G.; Záliš, S.; Vlček Jr, A.; Gray, H.B. Reduced and Superreduced Diplatinum Complexes. *Journal of the American Chemical Society* **2016**, *138*, 5699. DOI: 10.1021/jacs.6b02559.

C.1. Abstract

A d^8-d^8 complex $[Pt_2(\mu\text{-}P_2O_5(BF_2)_4]^{4-}$ (abbreviated $Pt(pop\text{-}BF_2)^{4-}$) undergoes two $1e^-$ reductions at $E_{1/2}$ = -1.68 and E_p = -2.46 V (*vs*. Fc^+/Fc) producing reduced $Pt(pop\text{-}BF_2)^{5-}$ and superreduced $Pt(pop\text{-}BF_2)^{6-}$ species, respectively. The EPR spectrum of $Pt(pop\text{-}BF_2)^{5-}$ and UV-vis spectra of both the reduced and superreduced complexes, together with TD-DFT calculations, reveal successive filling of the 6pσ orbital accompanied by gradual strengthening of Pt–Pt bonding interactions and, because of 6pσ delocalization, of Pt–P bonds in the course of the two reductions. Mayer-Millikan Pt–Pt bond orders of 0.173, 0.268, and 0.340 were calculated for the parent, reduced, and superreduced complexes, respectively. The second (5–/6–) reduction is accompanied by a structural distortion that is experimentally manifested by electrochemical irreversibility. Both reduction steps proceed without changing either d^8 Pt electronic configuration, making the superreduced $Pt(pop\text{-}BF_2)^{6-}$ a very rare $6p^2$ σ-bonded binuclear complex. However, the Pt–Pt σ bonding interaction is limited by the relatively long bridging-ligand-imposed Pt–Pt distance accompanied by repulsive electronic congestion. $Pt(pop\text{-}BF_2)^{4-}$ is predicted to be a very strong photooxidant (potentials of +1.57 and +0.86 V are estimated for the singlet and triplet dσ*pσ excited states, respectively).

C.2. Introduction

The prototypal d^8-d^8 binuclear complex $Pt_2(P_2O_5H_2)_4^{4-}$ (abbreviated $Pt(pop)^{4-}$) and its perfluoroborated derivative $Pt_2(P_2O_5(BF_2)_2)_4^{4-}$ ($Pt(pop\text{-}BF_2)^{4-}$) have similar electronic structures and UV-vis absorption spectra, but profoundly different photophysics.[1,2] The

HOMO is a Pt–Pt σ-antibonding orbital (dσ*); interestingly, the LUMO is Pt–Pt bonding (pσ), albeit ~50% delocalized over the phosphorous ligands.[2] These two frontier orbitals are well separated from lower-lying occupied and higher unoccupied orbitals (Figure C.1). In $Pt(pop\text{-}BF_2)^{4-}$, pairs of bridging ligands are covalently connected by BF_2 groups, forming a rigid cage around the photo- and electroactive Pt–Pt unit that features outward facing fluorine atoms. This extra rigidity and shielding likely are responsible for the dramatically enhanced lifetime of the lowest dσ*→pσ singlet excited state (1.6 ns *vs*. ca. 3 ps for $Pt(pop)^{4-}$).[1,3] Electron excitation into the pσ orbital strengthens the Pt–Pt interaction, as evidenced by 0.18 Å bond shortening (calc'd for $Pt(pop\text{-}BF_2)$;[2] 0.21-0.31 Å determined[4-7] by X-ray and optical techniques for Pt(pop)) and a 38-45 cm^{-1} increase of the Pt–Pt stretching frequency in both Pt(pop) and $Pt(pop\text{-}BF_2)$.[3,6-9] In analogy to optical excitation, reduction is expected to fill the pσ orbital, forming a weak Pt–Pt bond in $Pt(pop\text{-}BF_2)^{5-}$. Although reversible electrochemical reduction of $Pt(pop)^{4-}$ has not been reported,[10] $Pt(pop)^{5-}$ with a 34 μs lifetime was generated by pulse radiolysis in aqueous solution.[11] What is more, transient generation of a reduced species was indicated by observation of electrochemiluminescence at a platinum electrode in MeCN upon high-frequency potential switching.[12,13] As reducible –O–H···O– hydrogens are absent in $Pt(pop\text{-}BF_2)^{4-}$, we thought it likely that the complex could be reduced reversibly, and we have observed a two-step sequential reduction of $Pt(pop\text{-}BF_2)^{4-}$. The electronic structures of the two reduced forms have been investigated by DFT as well as spectroelectrochemical methods.

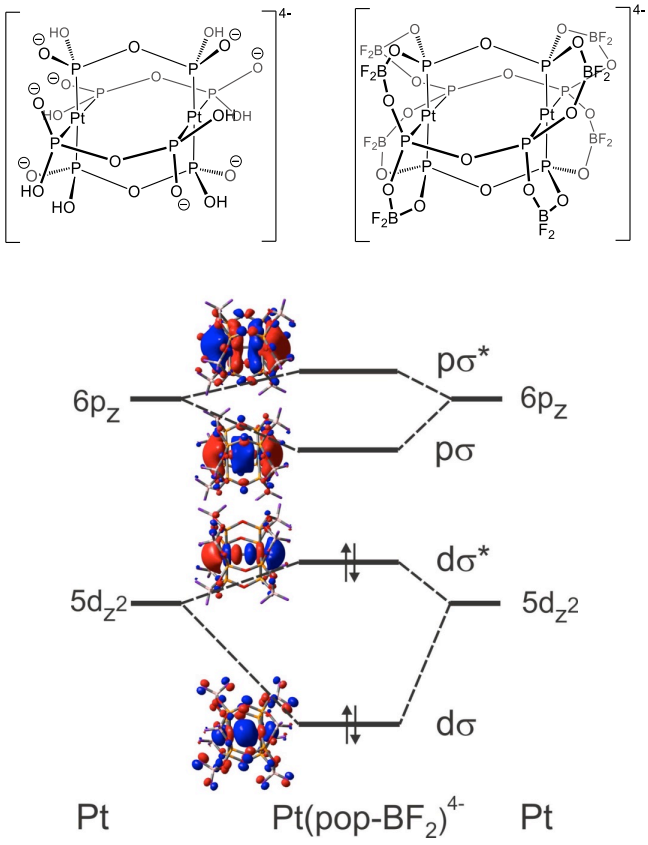

Figure C.1. Structural representations of $Pt(pop)^{4-}$ and $Pt(pop\text{-}BF2)^{4-}$ along with a qualitative σ-MO scheme.

C.3. Results

$Pt(pop\text{-}BF_2)^{4-}$ in MeCN at 273 K undergoes one-electron reductions at $E_{1/2}$ = -1.68 and E_p = -2.46 V *vs*. Fc^+/Fc (Figure C.2.2). The first wave is chemically reversible and electrochemically quasireversible at a scan rate of 50 mV/s (ΔE_p = 155 mV; compared with ~100 mV obtained for Fc^+/Fc under virtually identical conditions). The second wave is electrochemically irreversible and chemically reversible, indicating formation of a superreduced complex $Pt(pop\text{-}BF_2)^{6-}$, stable at least at 273 K. At room temperature, the peak-current ratio of the second wave is less than unity and two small shoulders appear at its positive site, attributable to decomposition products. Scanning over the anodic region reveals a 2-electron chemically irreversible oxidation at +0.94 V (*vs*. Fc^+/Fc).

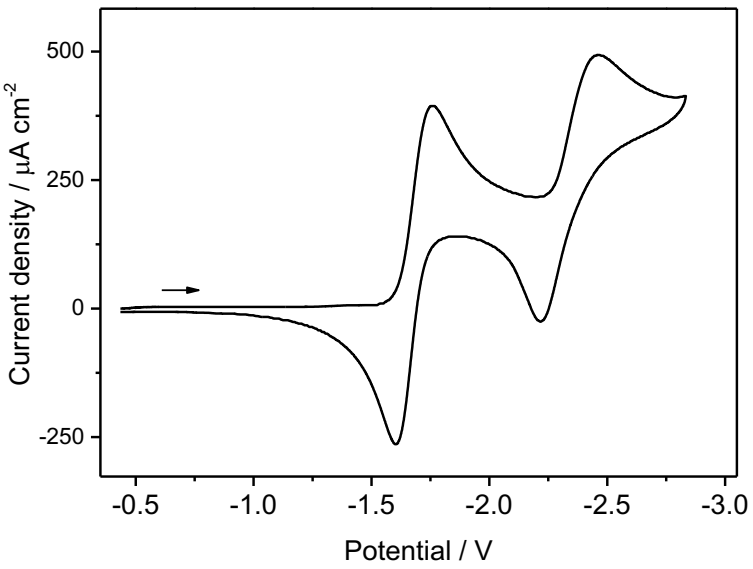

Figure C.2. Cyclic voltammogram of $Pt(pop\text{-}BF_2)^{4-}$ in MeCN containing 0.1 M Bu_4NPF_6 at 273 K. Potentials vs. Fc+/Fc. Scan rate 50 mV/s.

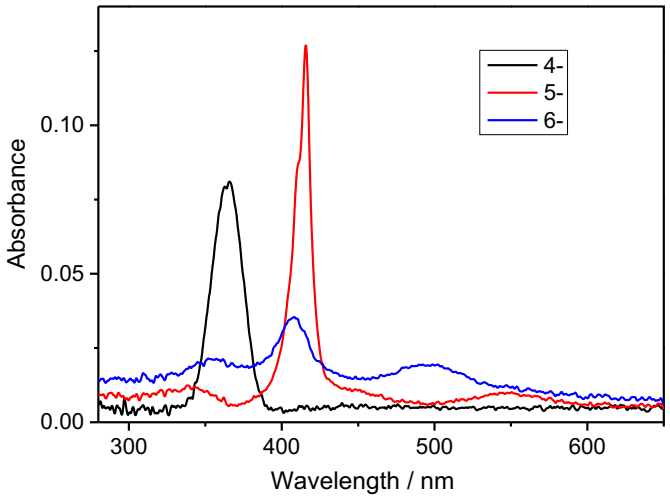

Figure C.3. UV-vis absorption spectra of $Pt(pop\text{-}BF_2)^{4-}$ (black) and in-situ spectroelectrochemically produced $Pt(pop\text{-}BF_2)^{5-}$ (red) and $Pt(pop\text{-}BF_2)^{6-}$ (blue, contains ca. 20% of $Pt(pop\text{-}BF_2)^{5-}$). Conditions: glassy carbon working electrode, MeCN, 0.1 M Bu_4NPF_6, 273 K. Binomial smoothing applied.

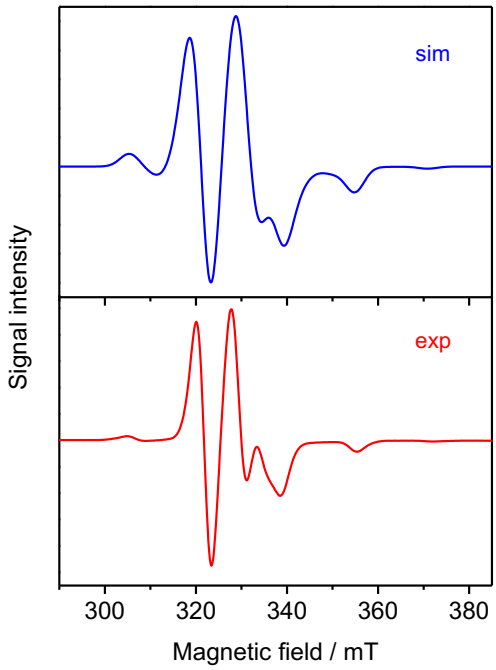

Figure C.4. Experimental (bottom) and simulated (top) EPR spectra of $Pt(pop\text{-}BF_2)^{5-}$ obtained after $Pt(pop\text{-}BF_2)^{4-}$ reduction with Na/Hg in MeCN at room temperature. Simulated parameters: g_1 = 1.98, g_2 = 2.03, g_3 = 2.04; A(Pt) = 550, 550, 900 MHz; A(Pt') = 350, 500, 900 MHz.

UV-vis spectroelectrochemistry in MeCN at 273 K carried out at the potential of the first reduction wave shows a decrease in intensity of the 365-nm band of $Pt(pop\text{-}BF_2)^{4-}$ accompanied by a rise of a sharp band at 416 nm with shoulders at ca. 411 and ~450 nm, and broad weak bands at ~550 and 338 nm, all attributable to $Pt(pop\text{-}BF_2)^{5-}$ (C.3). The parent complex is nearly quantitatively recovered upon anodically switching the potential. Further reduction at more negative potentials yields a spectrum with three distinct features (356, 408 and 496 nm; Figure C.3). Spectra measured in the course of the second reduction show an isosbestic point, indicating conversion to the superreduced species $Pt(pop\text{-}BF_2)^{6-}$. Reoxidation at more positive potentials initially recovers $Pt(pop\text{-}BF_2)^{5-}$ at 273 K, whereas an unidentified species strongly absorbing at 350 nm is formed at room temperature. Experimental spectra of both the reduced and superreduced species match those calculated by TD-DFT, supporting their assignments as $Pt(pop\text{-}BF_2)^{5-}$ and $Pt(pop\text{-}BF_2)^{6-}$, respectively.

The reduced species $Pt(pop\text{-}BF_2)^{5-}$ also was characterized by EPR, after reduction with Na/Hg and freezing to 77 K. Both experimental and simulated spectra are shown in Figure B.4. The EPR spectrum is characteristic of a spin-doublet state with an axial spin distribution ($g_2 \cong g_3 \neq g_1$). Hyperfine splitting constants due to the two ^{195}Pt nuclei are similar, indicating a nearly symmetrical spin density distribution. The g values are similar to those determined for Pt(II) complexes with radical-anion ligands.[14,15] In contrast, "platinum blue" species, where the unpaired electron is delocalized over four Pt atoms in a molecular orbital with predominantly 5d-character, also exhibit axial EPR spectra but with much larger g values as well as pronounced anisotropy.[16,17] Still larger g-values have been reported for Pt(I) d^9 sites.[18] The EPR data for $Pt(pop\text{-}BF_2)^{5-}$ suggest that the unpaired electron is delocalized over the two Pt atoms as well as the ligands in a molecular orbital of 6p-character. Our interpretation is supported by DFT spin-density calculations (Figure C.5), which accurately reproduce the g-values.

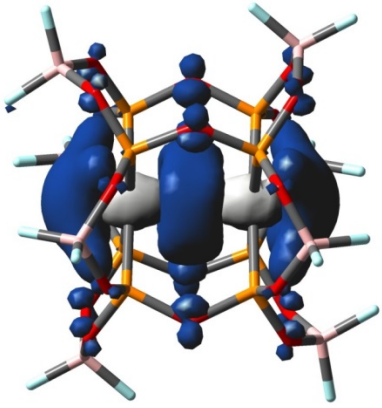

Figure C.5. DFT(PBE0/PCM-MeCN) calculated spin-density distribution in $Pt(pop\text{-}BF_2)^{5-}$ in MeCN solution.

C.3.1. Molecular and electronic structures: DFT calculations

DFT optimizations of the reduced and superreduced species in MeCN were performed without symmetry constraints. Calculations started from several different initial structures, including asymmetric ones, to ensure that the absolute energy minimum was found. Structural optimization shows successive Pt-Pt and Pt-P bond shortening upon each one-electron reduction (Table C-1). The P_4Pt units, which are almost planar in $Pt(pop\text{-}BF_2)^{4-}$, bend slightly outwards upon the first reduction. The two platinum atoms remain approximately equivalent, as evidenced by nearly identical Pt(1)–P and Pt(2)–P distances. The inclusion of five Me_4N^+ cations in the calculation did not change the symmetrical molecular structure of $Pt(pop\text{-}BF_2)^{5-}$, although the cations adopted an asymmetric distribution around the 5– anion.

Two stable structures were calculated for superreduced $Pt(pop\text{-}BF_2)^{6-}$. The slightly asymmetric conformation (denoted **6**) is the more stable one with small angular distortions around the Pt atoms (Table C-1). The other calculated conformation (**6'**) is nearly symmetrical, much like the 5– species, with the Pt atoms displaced inwards with respect to the surrounding P_4 planes. The calculated free energy of **6'** is 0.096 eV higher than that of **6** and the Pt–Pt and Pt–P bonds are shorter relative to $Pt(pop\text{-}BF_2)^{5-}$ in both conformations. Structural optimization in the presence of six Me_4N^+ cations yields a structure similar to **6**, with an asymmetrical distribution of cations.

Table C-1: Selected bond lengths (Å) of $Pt(pop\text{-}BF_2)^{n-}$ (n = 4, 5, 6) calculated by DFT(PBE0/PCM-MeCN).

n =	4	5	Δ(5 – 4)	6	Δ(6 – 5)	6'	Δ(6' – 5)
Pt-Pt	2.887	2.803	-0.084	2.739	-0.058	2.745	-0.058
Pt-P (average)	2.301	2.278	-0.025	2.255	-0.023	2.255	-0.023
P-O(-P) (average)	1.625	1.634	0.009	1.643	0.010	1.644	0.010
P-Pt-P (average)	178.8[a]	177.1[a]	-1.7	166.8[a] -175.7[b]	-10.3 7.2	176.0[a]	-1.1

[a] The P→Pt vectors point inwards to the Pt–Pt unit. [b] The P→Pt vectors point outwards from the Pt–Pt unit. The Pt–P directions are reversed at the other PtP_4 unit.

The two reduction steps correspond to successive filling of the pσ orbital (Figure C.1), whose calculated Pt character increases from 43% in the parent complex to about 59% in both the 5– and 6– species. Accordingly, the calculated spin density in $Pt(pop\text{-}BF_2)^{5-}$ is nearly symmetrically distributed between and around the two Pt atoms (Figure C.5). The strong narrow band in the $Pt(pop\text{-}BF_2)^{5-}$ UV-vis absorption spectrum is due to a transition of predominantly βHOMO→βLUMO (dσ*→pσ) character (Table C-2, Figure C.6); it is red-shifted relative to the corresponding band of the parent complex (416 vs. 365 nm[1]), but of comparable integrated intensity (Figure C.3). The high-energy shoulder is attributable to vibronic structure: corresponding peak wavenumbers of 24050 and 24380 cm^{-1}, separated by 330 cm^{-1}, were obtained by Gaussian decomposition. (The absorption band can be decomposed into four Gaussians with an average separation of 270 cm^{-1}.) Several mixed δ(POP)/ν(PtPt) vibrations are expected[3] to occur in this frequency range. The lowest absorption band (550 nm) of $Pt(pop\text{-}BF_2)^{5-}$ has no counterpart in the $Pt(pop\text{-}BF_2)^{4-}$ spectrum. The transition in question predominantly involves excitation from a pσ orbital (αHOMO) to a ligand-localized molecular orbital that also contains a dσ* admixture (αLUMO). This

transition gains intensity from the 23% contribution of βHOMO→βLUMO (dσ*→pσ) excitation (Table C-2).

Table C-2: TD-DFT (PBE0/PCM-MeCN) calculated lowest doublet excitation energies for $Pt(pop\text{-}BF_2)^{5-}$. The MOs (spin-orbitals) involved in the lowest excitations are depicted in Figure 6; αLUMO+6 and αLUMO+7 are mostly localized on pop-BF_2.

State	Main contributing excitations (%)	Transition energy eV (nm)	Oscillator strength	Exptl. nm
b^2A	99 (αHOMO → αLUMO+1)	2.32 (533)	0.0[a]	
c^2A	70 (αHOMO → αLUMO) 23 (βHOMO → βLUMO)	2.43 (509)	0.036	~550
d^2A	99 (αHOMO → αLUMO+2)	2.46 (505)	0.0[a]	~450
e^2A	74 (βHOMO → βLUMO) 25 (αHOMO → αLUMO)	3.02 (411)	0.285	416
f^2A	90 (αHOMO → αLUMO+6)	3.82 (325)	0.009	338
g^2A	99 (αHOMO → αLUMO+7)	3.82 (325)	0.015	

[a] Oscillator strengths become nonzero (~2×10^{-4}) when spin-orbit coupling is approximately included.

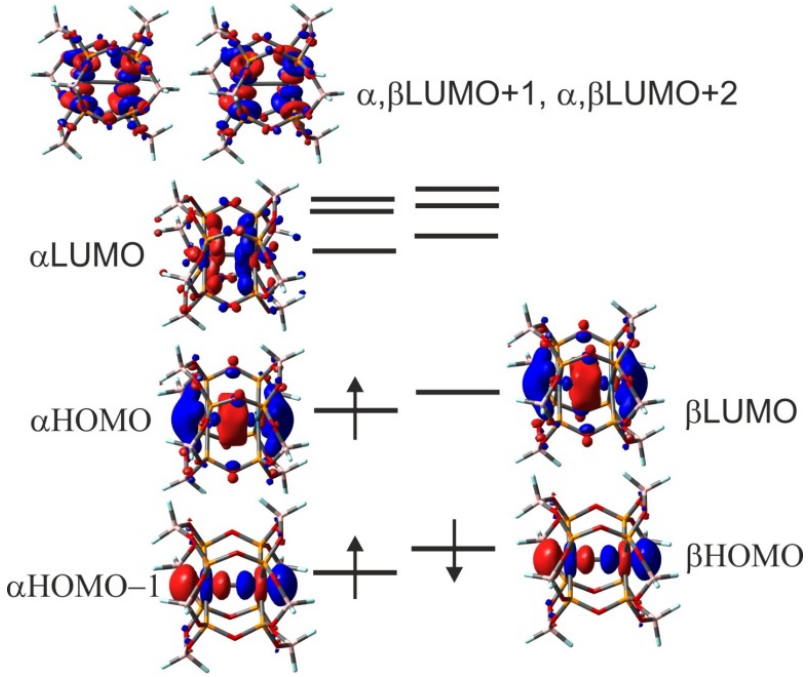

Figure C.6. Frontier molecular orbitals (spin-orbitals) involved in the lowest electronic transitions of $Pt(pop\text{-}BF_2)^{5-}$.

The doubly occupied pσ HOMO in the superreduced species **6** is polarized toward one of the Pt atoms (Figure C.7), making the electron distribution slightly asymmetric. Each Pt atom in **6** formally keeps its $5d^8$ electron configuration, while the two Pt atoms are connected by a 2-electron σ-bond arising from $6p_z$–$6p_z$ orbital overlap. With a $(d\sigma^*)^2(p\sigma)^2$ configuration, spectroscopically relevant electronic transitions are unrelated to those of the parent complex. These transitions, which originate from the pσ HOMO, are directed into higher unoccupied orbitals of mixed metal/ligand character (Table C-3). The lowest broad band due to the HOMO→LUMO transition involves a small electron-density shift between the Pt atoms; the transition weakens the Pt–Pt bond both because of HOMO(pσ) depopulation and the partial pσ* character of the LUMO. The absorption spectrum calculated for the more symmetrical configuration **6'** shows only one principal band. It is very different from both the experimental spectrum and the spectrum calculated for **6**.

Table C-3: TD-DFT (PBE0/PCM-MeCN) calculated lowest singlet excitation energies (eV) for $Pt(pop\text{-}BF_2)^{6-}$/conformation **6**. The relevant MOs are depicted in Figure B.7.

State	Main contributing excitations (%)	Transition energy eV (nm)	Oscillator strength	Exptl. eV (nm)
b^1A	90 (HOMO → LUMO)	2.53 (490)	0.184	496
c^1A	80 (HOMO → LUMO+1) 10 (HOMO → LUMO+4)	3.07 (404)	0.075	408
d^1A	87 (HOMO → LUMO+4) 12 (HOMO → LUMO+1)	3.53 (350)	0.081	356
e^1A	92 (HOMO → LUMO+6)	4.00 (310)	0.016	
f^1A	70 (HOMO → LUMO+7)	4.08 (304)	0.013	

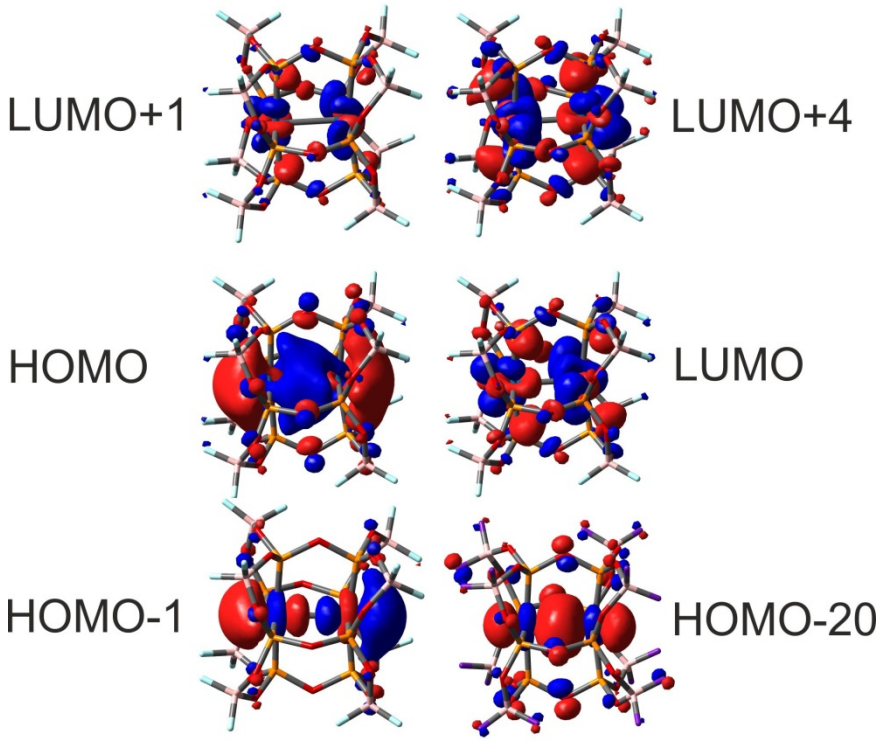

Figure C.7. Frontier molecular orbitals involved in the lowest electronic transitions of $Pt(pop\text{-}BF_2)^{6-}$/conformer **6**. HOMO is the 6pσ orbital; HOMO-1 and HOMO-20 are the 5dσ* and 5dσ orbitals, respectively.

C.4. Discussion

Perfluoroboration strongly stabilizes reduced forms of $Pt(pop)^{4-}$. The reduced $Pt(pop\text{-}BF_2)^{5-}$ and superreduced $Pt(pop\text{-}BF_2)^{6-}$ are stable in MeCN solution at least on the order of minutes, compared with μs-ms times[11,12] in the case of $Pt(pop)^{5-}$ (and it is not likely that $Pt(pop)^{6-}$ can be isolated[19]). The enhanced stability of the reduced and superreduced forms is attributable to the lack of reducible hydrogen atoms in the covalently linked inorganic cage around the Pt–Pt unit. The large potential difference (~0.7 V) between the first and second reductions indicates that disproportionation of $Pt(pop\text{-}BF_2)^{5-}$ is disfavored.

The first reduction of $Pt(pop\text{-}BF_2)^{4-}$ occurs at -1.68 V (vs Fc^+/Fc), as compared with ca. -1.8 V for Pt(pop). (The Pt(pop) value was estimated[20] from excited-state reductive

quenching kinetics in MeOH. No electrochemical reduction wave was reported.) This redox-potential difference is attributable to the electron-withdrawing effect of BF_2, transmitted to the Pt–Pt unit by pσ delocalization over the P donor atoms (Figures B.1, B.6, B.7). It follows that electronically excited $Pt(pop\text{-}BF_2)^{4-}$ is a very strong oxidant: potentials of +1.57 and +0.86 V (vs Fc^+/Fc) can be estimated for $*^1Pt(pop\text{-}BF_2)^{4-/5-}$ and $*^3Pt(pop\text{-}BF_2)^{4-/5-}$ redox couples, respectively (using spectroscopically determined excited-state energies[3]). Owing to the stability of the reduced species and the shielding effect of the eight BF_2 groups, reductive quenching of excited $Pt(pop\text{-}BF_2)^{4-}$ should be reversible and occur with a high cage-escape yield (80% was reported[20] for quenching of $*^3Pt(pop)$ by dimethylaniline). $Pt(pop\text{-}BF_2)^{4-}$ thus emerges as a promising photooxidant that could be employed to drive steps in organic reactions.

The reduced species $Pt(pop\text{-}BF_2)^{5-}$ can be generated by electrochemical or chemical reduction and also by irradiating the parent complex in the presence of an irreversible reductive quencher.[21] It could reduce substrates in reactions involving both outer and inner sphere activation. However, the radical-like reactivity typical for $*^3Pt(pop)$[22-24] is not expected for the reduced species, since the outward-oriented dσ* orbital is doubly occupied, unlike the excited state. The superreduced $Pt(pop\text{-}BF_2)^{6-}$ can only be produced electrochemically or by using very strong chemical reductants. In a preliminary experiment, we found $Pt(pop\text{-}BF_2)^{6-}$ to be much more reactive toward CH_2Cl_2 than $Pt(pop\text{-}BF_2)^{5-}$. Rates of outer-sphere electron transfer reactions of $Pt(pop\text{-}BF_2)^{6-}$ will be limited by large reorganization energies, as indicated by the electrochemical irreversibility of the 5-/6- CV wave at the 50 mV/s scan rate (Figure B.2). The relatively slow second reduction step correlates with increasing structural reorganization, as revealed by DFT (Table B-1).

Spectroscopic changes recorded in the course of the reduction together with DFT calculations point to successive filling of the pσ molecular orbital: the strong, sharp $d\sigma^* \rightarrow p\sigma$ band is the lowest-energy feature in the spectrum of the parent complex. It also is present in the reduced (5–) species with a $(d\sigma^*)^2(p\sigma)^1$ configuration but preceded in energy by a weaker band attributable to pσ excitation (Table B-2). The UV-vis spectral pattern changes

completely in the superreduced complex, as the pσ orbital becomes fully occupied. The dσ*→pσ transition vanishes and the spectrum exhibits a series of transitions from the pσ HOMO to higher unoccupied orbitals (Table B-3).

Successive filling of the pσ orbital formally generates a Pt–Pt σ bond without changing the Pt $5d^8$ electronic configuration, making $Pt(pop\text{-}BF_2)^{6-}$ a very rare $6p^2$ σ-bonded binuclear complex. The DFT-calculated Mayer-Mulliken bond orders[25] show strengthening of the Pt–Pt bonding interaction upon reduction (Table B-4), whereby the bond order increases about two-fold on going from the 4– parent (0.17) to the 6– superreduced complex (0.34). While significant, the Pt–Pt bonding in $Pt(pop\text{-}BF_2)^{6-}$ is far from a full σ-bond. The Pt–Pt bonding interaction is limited by several structural and electronic factors: the rigid pop-BF_2 ligand cage does not allow the metal-metal distance to shorten very much, disfavoring effective orbital overlap; the $(5d\sigma)^2(5d\sigma^*)^2(6p\sigma)^2$ configuration places six σ electrons in spatial proximity with one another, producing repulsive electronic congestion along the Pt–Pt axis; and the pσ molecular orbital is only 59% $6p_z$ in character, being delocalized over the Pt-P bonds (Figures B.1, B.6, B.7). Accordingly, Pt–P bond orders also gradually increase upon reduction (Table B-4). The EPR spectrum of $Pt(pop\text{-}BF_2)^{5-}$ confirms the delocalized nature of the singly occupied 6pσ molecular orbital, showing axial spin density distribution.

Table C-4: DFT-calculated Mayer-Mulliken bond orders for $Pt(pop\text{-}BF_2)^{n-}$ complexes. Atom P5 is in alignment with atom P1, etc.

bond \ n	4	5	6/conf. **6**
Pt - Pt	0.173	0.268	0.340
Pt – P1	1.119	1.181	1.175
Pt – P2	1.122	1.173	1.309
Pt – P3	1.122	1.173	1.167
Pt – P4	1.119	1.182	1.312
Pt – P5	1.119	1.183	1.320
Pt – P6	1.121	1.174	1.175
Pt – P7	1.121	1.175	1.328
Pt – P8	1.119	1.183	1.168

The Pt–Pt distance was calculated to shorten by 0.08 and 0.06 Å upon the first and second reductions, respectively, while the calculated Pt–Pt stretching frequency ν(Pt–Pt) increases from 128 cm^{-1} in the parent complex to 146 (5–) and 170 cm^{-1} (6–). The reduced species essentially keeps the high symmetry of the parent complex, which is manifested both by the calculation and the EPR spectrum. The most stable conformer of $Pt(pop\text{-}BF_2)^{6-}$ shows a small asymmetry, both between the two Pt centers and within each PtP_4 unit, where one pair of *trans* Pt-P bonds is shorter than the other. The HOMO also is distributed slightly asymmetrically, perhaps due to the "frustrated" pσ interaction mentioned above. Nevertheless, the calculated natural charges at the two Pt atoms differ by only 0.035 e^-, in accordance with the $(5d\sigma)^2(5d\sigma^*)^2(6p\sigma)^2$ configuration. This behavior contrasts with that of doubly-reduced $5d^8$-$5d^8$ $Ir_2(dimen)_4^{2+}$ (dimen = 1,8-diisocyano-*p*-menthane) that adopts a d^8-

d^{10} (Ir^{II}-Ir^{0}) mixed-valence configuration. In this case, one iridium center maintains a square planar local geometry, while the other distorts toward tetrahedral.[26] Such a distortion avoids the congested $(5d\sigma)^2(5d\sigma^*)^2(6p\sigma)^2$ electronic structure and its stabilizing effect is manifested by the much smaller difference between the first and second reduction potentials of $Ir_2(dimen)_4^{2+}$ (0.19 V),[26] as compared with Pt(pop-BF2) (~0.7 V). Such a distortion toward a mixed-valence structure is possible in the $Ir_2(dimen)_4^{2+}$ case because of the structural flexibility of the dimen bridge,[27] whereas the rigid pop-BF_2 ligand cage of $Pt(pop\text{-}BF_2)^{6-}$ enforces a nearly symmetrical structure, producing the unusual partial 6pσ metal-metal bond. We plan to map the reactivity patterns of this powerful $(6p)^2$ σ-bond reductant.

C.5. Experimental

Materials and procedures. $[Bu_4N]_4[Pt_2(P_2O_5(BF_2)_2)_4]$ was prepared as described previously.[1,21] All measurements were performed under an argon atmosphere in dry, degassed acetonitrile (HPLC grade, Fisher) that was passed through a solvent purification column. Bu_4NPF_6 (Fluka) was used as received. Electrolyte solutions were prepared and stored over activated alumina and 4-Å molecular sieves.

All electrochemical experiments were performed with a CH Instruments Model 650A electrochemical analyzer. Cyclic voltammetry (CV) at ambient temperature was measured in a three-electrode configuration consisting of a highly polished glassy-carbon-disk working electrode (A = 0.07 cm^2), a Pt wire auxiliary electrode, and a 1.0 M KCl AgCl/Ag reference electrode, separated by a modified Luggin capillary. Low temperature CV was carried out using a nonisothermal cell configuration, in which the reference electrode was held at ambient temperature, separated from the working compartment by a long glass tube filled with electrolyte, and connected by a Luggin capillary. The temperature was monitored by a thermocouple placed in the working compartment. Potentials in the figures are reported vs. aqueous AgCl/Ag, not corrected for the junction potential. The ferrocenium/ferrocene couple has $E^{0'}$ = 0.434 V, measured at identical experimental conditions. All potentials in the text are reported vs. Fc^+/Fc.

Thin-layer spectroelectrochemistry was carried out in a specular-reflectance mode using a modified IR cell. An Ocean Optics UV-vis light source (DH-2000) and spectrometer (USB2000) were connected to the Y-arms of a bifurcated fiber-optic cable; the end of the cable was connected through a lens housing containing a semi-spherical collimating lens to the front-face window of the spectroelectrochemical cell at a 90 degree angle. A drop of mineral oil between the fiber optic and front-face quartz window of the cell ensures refractive-index matching. Spectra were not corrected for front-face reflection. The error in intensity at an absorbance of 0.5 is less than 1%. The glassy-carbon working electrode of the spectroelectrochemical cell was attached with silver epoxy to a brass cooling tube, connected to a circulating variable-temperature bath.

EPR spectra were recorded on a Bruker EMS spectrometer at 9.39 GHz. Samples at ~10 mM concentration were prepared by reduction with Na/Hg in dry acetonitrile under an N_2 atmosphere and frozen with liquid nitrogen prior to the measurements. Spectral simulations were performed with MATLAB using the EasySpin MATLAB toolbox (version 4.5.5). Simulation parameters obtained: g = [2.04, 2.03, 1.98]; HStrain = [180, 120, 100] MHz; A_{Pt1} = [550, 550, 900] MHz; A_{Pt2} = [350, 500, 900] MHz.

DFT Calculations. Electronic structures of $Pt(pop\text{-}BF_2)^{n-}$ (n = 4, 5, 6) complexes were calculated by density functional theory (DFT) methods using Gaussian 09[28] (G09) and ADF 2014.06[29] program packages. All calculations employed the hybrid Perdew, Burke and Ernzerhof[30,31] (PBE0) exchange and correlation functional. The following basis sets were used within G09: 6-311g(3d) polarized triple-ζ basis sets[32] for P and O; 6-31g(d) double-ζ for remaining first row atoms, and quasi-relativistic small-core effective core pseudopotentials and the corresponding optimized set of basis functions for Pt.[33,34] Mayer-Mulliken bond orders and natural charges were calculated by NBO 6.0 program.[35]

The solvent was included using the polarizable calculation model (PCM).[36] Geometry optimizations, which were performed without any symmetry constraints, included the PCM solvent correction.[36] They were followed by vibrational analysis: no imaginary frequencies

were found for energy minima. Open-shell systems were treated by the unrestricted Kohn–Sham (UKS) procedure. For comparison of spectra in different redox states, Me_4N^+ counter-ions corresponding to the negative charge of the complex anion were added. ADF calculations employed Slater-type orbital (STO) basis sets of triple-ζ quality with two polarization functions for the Pt atom, triple-ζ with polarization functions for O, P, and H atoms, and double-ζ with one polarization function for the remaining atoms. The basis set was represented by a frozen core approximation (1s for B, N, O, 1s-2p for P and 1s-4d for Pt were kept frozen). The scalar relativistic (SR) zero order regular approximation (ZORA) was used. Solvent effect corrections were calculated using the COSMO model.[37] The *g* tensor was obtained from a spin-nonpolarized wave function after incorporating spin-orbit (SO) coupling.[38] EPR parameters were calculated by single point procedures at optimized structures.

C.6. References and Notes

(1) Durrell, A. C.; Keller, G. E.; Lam, Y.-C.; Sýkora, J.; Vlček, A., Jr.; Gray, H. B. *J. Am. Chem. Soc.* **2012**, *134*, 14201−14207.

(2) Záliš, S.; Lam, Y. C.; Gray, H. B.; Vlček, A., Jr. *Inorg. Chem.* **2015**, *54*, 3491−3500.

(3) Hofbeck, T.; Lam, Y. C.; Kalbáč, M.; Záliš, S.; Vlček, A.; Yersin, H. *Inorg. Chem., submitted* **2016**.

(4) van der Veen, R. M.; Milne, C. J.; El Nahhas, A.; Lima, F. A.; Pham, V.-T.; Best, J.; Weinstein, J. A.; Borca, C. N.; Abela, R.; Bressler, C.; Chergui, M. *Angew. Chem. Int. Ed.* **2009**, *48*, 2711 –2714.

(5) Christensen, M.; Haldrup, K.; Bechgaard, K.; Feidenhans'l, R.; Kong, Q.; Cammarata, M.; Lo Russo, M.; Wulff, M.; Harrit, N.; M.M., N. *J. Am. Chem. Soc.* **2009**, *131*, 502–508.

(6) Rice, S. F.; Gray, H. B. *J. Am. Chem. Soc.* **1983**, *105*, 4571-4575.

(7) Che, C.-M.; Butler, L. G.; Gray, H. B.; Crooks, R. M.; Woodruff, W. H. *J. Am. Chem. Soc.* **1983**, *105*, 5492-5494.

(8) Stiegman, A. E.; Rice, S. F.; Gray, H. B.; Miskowski, V. M. *Inorg. Chem.* **1987**, *26*, 1112-1116.

(9) Fordyce, W. A.; Brummer, J. G.; Crosby, G. A. *J. Am. Chem. Soc.* **1981**, *103*, 7061-7064.

(10) Bryan, S. A.; Schmehl, R. H.; Roundhill, D. M. *J. Am. Chem. Soc.* **1986**, *108*, 5408–5412.

(11) Che, C.-M.; Atherton, S. J.; Butler, L. G.; Gray, H. B. *J. Am. Chem. Soc.* **1984**, *106*, 5143–5145.

(12) Vogler, A.; Kunkely, H. *Angew. Chem. Int. Ed. Engl.* **1984**, *23*, 316-317.

(13) Kim, J.; Fan, F. F.; Bard, A. J.; Che, C.-M.; Gray, H. B. *Chem. Phys. Lett.* **1985**, *121*, 543-546.

(14) Braterman, P. S.; Song, J.-I.; Vogler, C.; Kaim, W. *Inorg. Chem.* **1992**, *31*, 222-224.

(15) Hirani, B.; Li, J.; Djurovich, P. I.; Yousufuddin, M.; Oxgaard, J.; Persson, P.; Wilson, S. R.; Bau, R.; Goddard III, W. A.; Thompson, M. E. *Inorg. Chem.* **2007**, *46*, 3865-3875.

(16) Matsunami, J.; Urata, H.; Matsumoto, K. *Inorg. Chem.* **1995**, *34*, 202-208.

(17) Arrizabalaga, P.; Castan, P.; Geoffroy, M.; Laurent, J.-P. *Inorg. Chem.* **1985**, *24*, 3656-3660.

(18) Schmauke, T.; Einar Möller, E.; Roduner, E. *Chem. Commun.* **1998**, 2589–2590.

(19) Reaction of Pt(pop) with two equivalents of Cr^{2+} in aqueous solution produced a stable species that was tentatively assigned as $Pt(pop)^{6-}$.[39] However, this assignment cannot be correct, since the Cr^{3+}/Cr^{2+} potential (ca. -1.1 V) is more positive than the estimated $E(Pt(pop)^{4-/5-})$ value of -1.8 V. Moreover, the Raman spectrum of the product has a ν(Pt-Pt) band at lower wavenumber than in the Pt(pop) parent.[39]

(20) Heuer, W. B.; Totten, M. D.; Rodman, G. S.; Hebert, E. J.; Tracy, H. J.; Nagle, J. K. *J. Am. Chem. Soc.* **1984**, *106*, 1163-1164.

(21) Lam, Y. C., PhD Dissertation, California Institute of Technology, 2015.

(22) Vlček, A., Jr.; Gray, H. B. *J. Am. Chem. Soc.* **1987**, *109*, 286-287.

(23) Vlček, A., Jr.; Gray, H. B. *Inorg. Chem.* **1987**, *26*, 1997-2001.

(24) Smith, D. C.; Gray, H. B. In *ACS Symposium Series 394. The Challenge of d and f Electrons.*; Salahub, D. R., Zerner, M. C., Eds.; American Chemical Society: Washington, DC, 1989, pp 356-365.

(25) Bridgeman, A. J.; Cavigliasso, G.; Ireland, L. R.; Rothery, J. *J. Chem. Soc., Dalton Trans.* **2001**, 2095–2108.

(26) Hill, M. G.; Sykes, A. G.; Mann, K. R. *Inorg. Chem.* **1993**, *32*, 783–784.

(27) Hunter, B. M.; Villahermosa, R. M.; Exstrom, C. L.; Hill, M. G.; Mann, K. R.; Gray, H. B. *Inorg. Chem.* **2012**, *51*, 6898−6905.

(28) Frisch, M. J.; Trucks, G. W.; Schlegel, H. B.; Scuseria, G. E.; Robb, M. A.; Cheeseman, J. R.; Scalmani, G.; Barone, V.; Mennucci, B.; Petersson, G. A.; Nakatsuji, H.; Caricato, M.; Li, X.; Hratchian, H. P.; Izmaylov, A. F.; Bloino, J.; Zheng, G.; Sonnenberg, J. L.; Hada, M.; Ehara, M.; Toyota, K.; Fukuda, R.; Hasegawa, J.; Ishida, M.; Nakajima, T.; Honda, Y.; Kitao, O.; Nakai, H.; Vreven, T.; Montgomery, J. A., Jr.; Peralta, J. E.; Ogliaro, F.; Bearpark, M.; Heyd, J. J.; Brothers, E.; Kudin, K. N.; Staroverov, V. N.; Kobayashi, R.; Normand, J.; Raghavachari, K.; Rendell, A.; Burant, J. C.; Iyengar, S. S.; Tomasi, J.; Cossi, M.; Rega, N.; Millam, J. M.; Klene, M.; Knox, J. E.; Cross, J. B.; Bakken, V.; Adamo, C.; Jaramillo, J.; Gomperts, R.; Stratmann, R. E.; Yazyev, O.; Austin, A. J.; Cammi, R.; Pomelli, C.; Ochterski, J. W.; Martin, R. L.; Morokuma, K.; Zakrzewski, V. G.; Voth, G. A.; Salvador, P.; Dannenberg, J. J.; Dapprich, S.; Daniels, A. D.; Farkas, O.; Foresman, J. B.; Ortiz, J. V.; Cioslowski, J.; Fox, D. J.; Gaussian 09, Revision C.01, Gaussian, Inc.: Wallingford CT, 2009.

(29) *ADF2014.06, SCM, Theoretical Chemistry, Vrije Universiteit, Amsterdam, The Netherlands, http://www.scm.com*.

(30) Perdew, J. P.; Burke, K.; Ernzerhof, M. *Phys. Rev. Lett.* **1996**, *77*, 3865-3868.

(31) Adamo, C.; Scuseria, G. E.; Barone, V. *J. Chem. Phys.* **1999**, *111*, 2889-2899.

(32) Raghavachari, K.; Binkley, J. S.; Seeger, R.; Pople, J. A. *J. Chem. Phys.* **1980**, *72*, 650-654.

(33) Andrae, D.; Häussermann, U.; Dolg, M.; Stoll, H.; Preuss, H. *Theor. Chim. Acta* **1990**, *77*, 123-141.

(34) Martin, J. M. L.; Sundermann, A. *J. Chem. Phys.* **2001**, *114*, 3408.

(35) Glendening, E. D.; Badenhoop, J. K.; Reed, A. E.; Carpenter, J. E.; Bohmann, J. A.; Morales, C. M.; Landis, C. R.; Weinhold, F. Theoretical Chemistry Institute, University of Wisconsin, Madison, USA, 2013.

(36) Cossi, M.; Rega, N.; Scalmani, G.; Barone, V. *J. Comput. Chem.* **2003**, *24*, 669-681.

(37) Klamt, A.; Schüürmann, G. *J. Chem. Soc., Perkin Trans. 2* **1993**, 799 - 805.

(38) van Lenthe, E.; Ehlers, A.; Baerends, E. J. *J. Chem. Phys.* **1999**, *110*, 8943-8953.

(39) Alexander, K. A.; Paul Stein; Hedden, D. B.; Roundhill, D. M. *Polyhedron* 1983, 2, 1389-1392.

D. ELECTRONIC STRUCTURES OF REDUCED AND SUPERREDUCED Ir_2(1,8-diisocyanomenthane)$_4^{n+}$ COMPLEXES

Reprinted with permission from Záliš, S; Hunter, B. M.; Gray, H. B.; Vlček Jr, A. Electronic Structures of Reduced and Superreduced Ir_2(1,8-diisocyanomenthane)$_4^{n+}$ Complexes. *Inorganic Chemistry*, **2017**, *56*, 2874. DOI: 10.1021/acs.inorgchem.6b03001.

D.1. Abstract

Molecular and electronic structures of Ir_2(1,8-diisocyanomenthane)$_4^{n+}$ (Ir(dimen)$^{n+}$) complexes have been investigated by DFT for n = 2, 1, 0 (abbreviated **2+**, **1+**, **0**). Calculations reproduced the experimental structure of **2+**, ν(C≡N) IR, and visible absorption spectra of all three oxidation states, as well as the EPR spectrum of **1+**. We have shown that the two reduction steps correspond to successive filling of the Ir–Ir pσ orbital. Complexes **2+** and **1+** have very similar structures with **1+** having a shorter Ir–Ir distance. The unpaired electron density in **1+** is delocalized along the Ir–Ir axis and over N atoms of the eight C≡N– ligands. The second reduction step **1+** → **0** changes the Ir(CN–)$_4$ coordination geometry at each Ir site from approximately planar to seesaw whereby one –N≡C–Ir–C≡N– moiety is linear and the other bent at the Ir (137°) as well as N (146°) atoms. Although complex **0** is another example of a rare $(p\sigma)^2$ dimetallic species (after $[Pt_2(\mu\text{-}P_2O_5(BF_2)_2)_4]^{6-}$, *J. Am. Chem. Soc.* **2016**, *138*, 5699), the redistribution of lower-lying occupied molecular orbitals increases electron density predominantly at the bent C≡N– ligands whose N atoms are predicted to be nucleophilic reaction centers.

D.2. Introduction

Although the electronic excited states of binuclear complexes of d^8 metals (Pt^{II}, Ir^{I}, Rh^{I}) are versatile redox agents,[1,2,3,4,5,6,7,8,9,10] d^8-d^8 electrochemistry has not been studied in depth.[3,11,12,13,14,15,16,17,18,19,20] Investigating electrochemical reduction of d^8-d^8 complexes is challenging, owing to negative reduction potentials and slow heterogeneous electron transfer, as well as complications attributable to product reactivity. Indeed, reversible electrochemical reductions along with characterization of products have only been reported for $[Ir_2(1,8\text{-diisocyanomenthane})_4]^{2+}$ ($Ir(dimen)^{2+}$, abbreviated **2**+)[12] and $[Pt_2(P_2O_5(BF_2)_2)_4]^{4-}$ ($Pt(pop\text{-}BF_2)^{4-}$).[11] Notably, the $Ir(dimen)^{2+}$ complex was found to catalyze electrochemical reduction of CO_2.[13]

Both complexes are reduced in two chemically reversible 1-electron steps: **2**+ at -1.36 and -1.54 V vs. Ag/AgCl (ca. -1.75, -1.93 V vs. Fc^+/Fc);[12,13] $Pt(pop\text{-}BF_2)^{4-}$ at -1.68 and -2.46 V (vs. Fc^+/Fc).[11] For both complexes, the first reduction is chemically reversible, whereas the second one is quasireversible. A combined spectroelectrochemical (UV-vis absorption, EPR) and DFT-computational study of the $Pt(pop\text{-}BF_2)^{n-}$ redox series (n = 4, 5, 6) revealed that the two reduction processes correspond to successive filling of a Pt-Pt bonding pσ orbital (the LUMO of the parent complex).[11] Therefore, the Pt-Pt bonding strengthens upon the first and, even more, the second reduction. The superreduced complex is a very rare $6p^2$ σ-bonded binuclear complex; formally it is a dimer of Pt^{I} ($5d^86p^1$) rather than ($5d^9$).[11] While the calculations revealed small angular distortions around the metal atoms, the two Pt centers were found to be essentially equivalent with respective natural charges differing by only 0.035 e^-.[11]

By analogy, similar localization accompanying reduction processes could be expected for the $Ir(dimen)^{n+}$ redox series (n = 2, 1, 0). Indeed, the EPR spectrum of $Ir(dimen)^+$ (**1**+) and its IR spectrum in the range of C≡N– stretching vibrations, ν(C≡N), point to a $(p\sigma)^1$ configuration with an axial spin density distribution and an increased Ir→C≡N– π back donation, the latter manifested by a 66 cm^{-1} downshift of the ν(C≡N) IR band, from 2156

cm^{-1} in **2+** to 2090 cm^{-1} in **1+**.[12] The second reduction, however, was accompanied by a large (~189 cm^{-1}) splitting of the ν(C≡N) band into two new features (2058 and 1869 cm^{-1}).[12] Such behavior signals a loss of symmetry and formation of two distinct sets of isocyanide groups in the superreduced complex $Ir(dimen)^0$ (**0**). It was interpreted[12] as indicating asymmetry between the two metal centers; and **0** was formulated as a d^8-d^{10} ($Ir^{I}\cdots Ir^{-I}$) mixed-valence complex with approximately square planar and tetrahedral coordination geometries around Ir^{I} and Ir^{-I} centers, respectively.[12] The experimentally demonstrated asymmetry and the mixed-valence formulation of **0** are in stark contrast with the nearly symmetrical $(p\sigma)^2$ bond established[11] for $Pt(pop\text{-}BF_2)^{6-}$, thereby challenging our understanding of the electronic structures of superreduced d^8-d^8 complexes. We have therefore addressed the problem of bonding and electron localization in the $Ir(dimen)^{n+}$ redox series by DFT calculations.

D.3. Computational details

Electronic structures of $Ir(dimen)^n$ (n = 0, 1 and 2) in various oxidation states were calculated by DFT using the Gaussian 09 (G09) program package. The open shell system **1+** was calculated by the UKS approach. Geometry optimization was followed by vibrational analysis in order to characterize stationary states. Calculations performed without any symmetry constraints provided real energy minima for all investigated isomers and oxidation states. The short/twisted **2+** isomer was also optimized within the D_2 symmetry and the results were used to characterize the approximate symmetries of ν(C≡N) modes. DFT calculations employed the Perdew, Burke, Ernzerhof (PBE0) hybrid functional,[21,22] with the D3 version of Grimme's dispersion correction added.[23] (The choice of the PBE0 functional was motivated by the good results it has provided for Pt d^8-d^8 dimers and other heavy-metal complexes.[11,24,25,26]) The MeCN solvent was described by the polarizable conductor model (PCM).[27] The following basis sets were used: for H double ζ 6-31g(d) basis set,[28] for C, N, and O atoms polarized triple ζ basis sets 6-311g(d)[29,30], and quasirelativistic effective core pseudopotentials and corresponding optimized set of basis functions for Ir.[31,32] Electronic transitions were calculated by time-dependent DFT (TDDFT). Mayer-Mulliken bond orders

were obtained by the NBO 6 program. Reported vibrational frequencies were scaled[33,34] by a factor of 0.956 that provided the best match with the experimental ν(CN) band of **2**+. the same scaling factor was used for all there oxidation states.

D.4. Results

Isomerism

Two kinds of isomerism should be considered when dealing with Ir(dimen)^n complexes: deformational and orientational. Deformational isomerism arises from two possible combinations of Ir-Ir bond-lengths and ligand conformations, giving rise to long/eclipsed and short/twisted configurations[35,36,37] (Figure D.1) with distinctly different visible absorption spectra.[36,37] As both isomers are present in solution at room temperature,[36,37] they must be considered separately. Calculations were therefore performed on both deformational isomers in MeCN (modeled as a dielectric continuum). Gibbs free energies of the two **2**+ isomers were comparable (in MeCN, 298 K), with the long/eclipsed one more stable by 0.105 eV. However, its zero-point corrected electronic energy was calculated to be 0.029 eV higher than that of the short/twisted isomer, indicating stabilization of the short/twisted form with decreasing temperature, in agreement with experiment[36] ($\Delta H^o_{\text{long-short}} = +0.035$ eV).

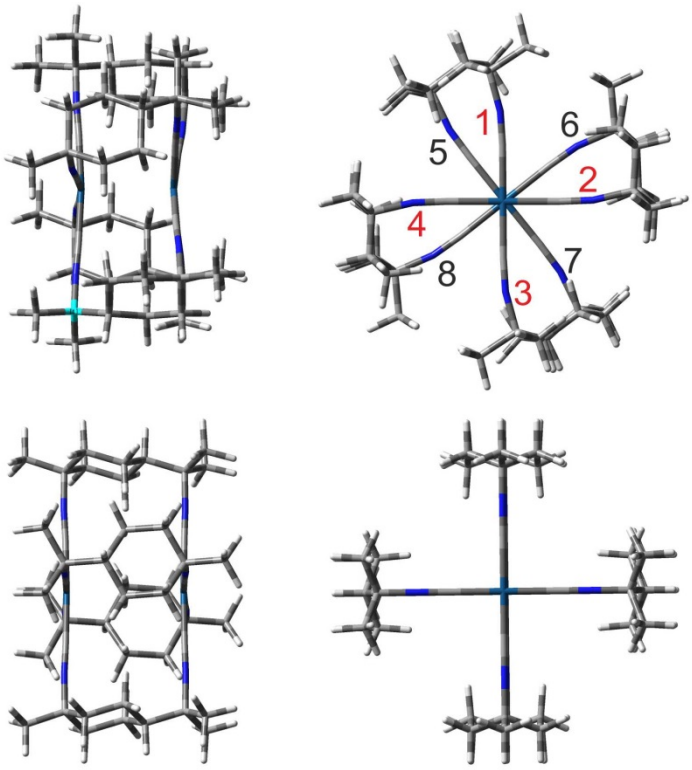

Figure D.1. DFT-optimized solution structures of short/twisted (top) and long/eclipsed (bottom) deformational isomers of the *trans*-2:2 orientational isomer of Ir(dimen)$^{2+}$ (further abbreviated **2**+). Left: side views; right: front views along the Ir-Ir (*z*) axis. The CN groups labeled 1,2,3,4 (red) are in the front, the 5,6,7,8 (black) ones are in the back.

Structure optimization of the short/twisted **2**+ isomer required the dispersion correction GD3,[38] otherwise the calculation did not converge. Hence, the GD3 correction was used throughout this work. A good match between calculated (Table D-1) and experimental[39] (3.60 and 4.3 Å, in MeCN solution) Ir–Ir distances was obtained for the two **2**+ deformational isomers. (Only the structure of the long/eclipsed isomer was successfully optimized without dispersion but the calculated bond length of 4.78 Å grossly overestimated the Ir–Ir distance. This result further underlines the importance of including dispersion in calculations of isocyanide d^8-d^8 complexes.[10,40])

Since the dimen ligand is asymmetric, the individual bridging ligands can adopt different "head-to-tail" relative orientations: 4:0 (all aligned), 3:1, *cis*-2:2, and *trans*-2:2. The respective DFT-calculated free energies of **2**+ orientational isomers (relative to the most stable isomer, MeCN, 293 K) are 0.077, 0.011, 0.003, and 0.0 eV for the long/eclipsed deformational isomer and 0.005, 0.0, 0.049, and 0.032 eV for the short/twisted isomer. The actual solution composition is not known and may vary with synthetic conditions. Crystal structures[35] show disordered dimen orientations, which correspond to mixtures of orientational isomers. Below, we present computational results for the *trans*-2:2 isomer obtained without any symmetry constraints. Calculations on other orientational isomers yielded very similar electronic structures, UV-vis and IR spectra.

Molecular structures

Both **2**+ isomers have typical d^8-d^8 structures, as there are two parallel, almost planar IrC_4 moieties (Figure D.1, Table D-1). The long/eclipsed and short/twisted isomers differ in the Ir–Ir distance and the twist angle between the two planes, calculated as 4.319 Å/0° and 3.244 Å/38.4°, respectively. The Ir-Ir distances match well the corresponding experimental values of 4.3 and 3.60 Å determined[39] in MeCN solution by X-ray scattering. The calculated twist angle is about twice as large as in the crystal structures,[35] indicating constraints imposed in the solid state. The deviation of IrC_4 units from planarity was calculated to be slightly larger in the long/eclipsed isomer (2.6-3.4°), which is different for the two *trans* pairs of dimen ligands (Table 1). The Ir–C≡N– units are essentially linear around the carbon atom but slightly bent at nitrogen atoms (more in the short/twisted isomer due to higher ligand strain).

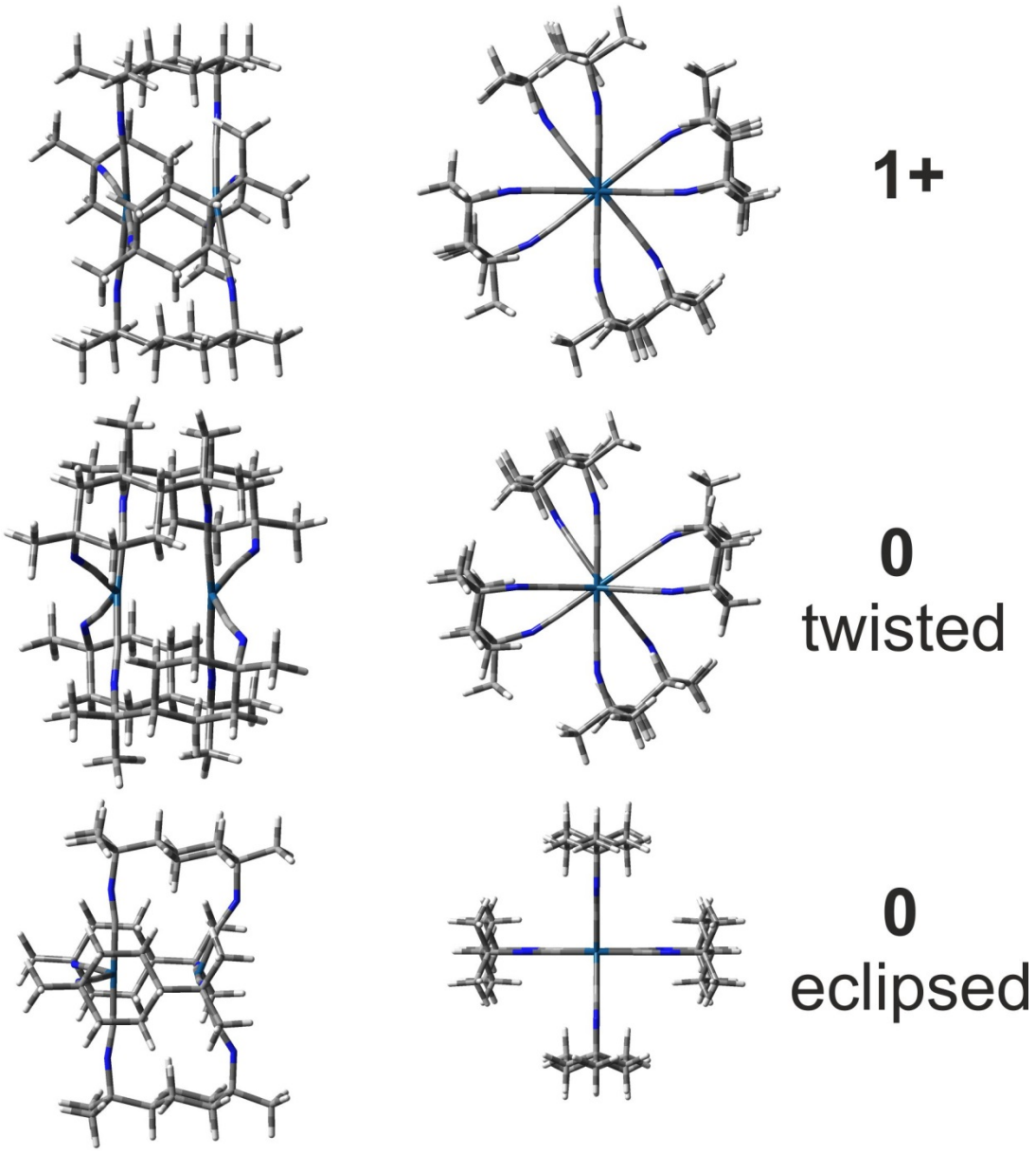

Figure D.2. Optimized molecular structures of $Ir(dimen)^{+}$ (top, further abbreviated **1**+) and the two deformational isomers of $Ir(dimen)^{0}$ (middle and bottom, further abbreviated **0**). Left: side views; right: front views along the Ir-Ir (*z*) axis.

Only a single stable structure (Figure D.2) was found for **1**+, whether or not optimization started from the short/twisted or long/eclipsed **2**+ structure. The first reduction triggers only small structural changes, especially when compared to the short/twisted isomer

of the parent. The IrC_4 units of **1+** remain nearly planar and parallel, although the deviation from planarity increases slightly to 3.7-5.1° (Table 1). The Ir–Ir distance shortens by 0.16 and 1.23 Å relative to the short/twisted and long/eclipsed **2+** isomers. The twist angle stays nearly the same. All the C≡N bonds lengthen and Ir–C bonds shorten by ca. 0.01 Å upon the first reduction.

The second reduction is accompanied by profound structural changes (Figure D.2, Table D-1). The IrC_4 geometry changes at each center from approximately square planar to seesaw. Two sets of $Ir(C{\equiv}N{-})_2$ units with different C-Ir-C angles as well as Ir–C and C≡N bond lengths occur in the **0** structure: axial, which are nearly linear and comparable to those in **1+**; and equatorial with a 137° angle between the Ir–C bonds. Equatorial Ir–C and C≡N bonds are ~0.03 Å shorter and longer, respectively, than in the axial unit. Moreover, equatorial isocyanide ligands are bent at the N atoms, with C≡N– angles ~20° smaller than in the axial ligands. DFT optimization yielded two stable isomeric structures of **0** that differ in the relative orientation of axial and equatorial positions at the two Ir centers (Figure B.2). In the twisted isomer, the IrC_4 units are twisted by 37.3°. The eclipsed isomer has the two seesaw sites perpendicular to each other, which leads to aligned –N≡C–Ir–C≡N– bonds when viewed along the Ir–Ir axis (Figure D.2). (In particular, the axial –N≡C–Ir–C≡N– moiety at one Ir is aligned with the equatorial unit at the other.) The calculated Ir–Ir bond length is similar in eclipsed (3.088 Å) and twisted (2.988 Å) isomers. In both cases, one C≡N– group of each dimen ligand is bound equatorially to one Ir atom while the other is bound axially to the second Ir. The twisted isomer was calculated to be more stable by 0.029 eV in MeCN at 298 K.

Table D-1: DFT-calculated Ir(dimen)$^{n+}$ structural parameters. Bond lengths in Å. Atom numbering is shown in Figure B.1.

Bond / n	**2+$_{long/ecl}$**	**2+$_{short/tw}$**	**1+**	**0$_{eclipsed}$**	**0$_{twisted}$**
Ir1-Ir2	4.319	3.251	3.087	3.088	2.988
Ir-C1	1.959	1.959	1.949	1.945 [ax]	1.943 [ax]
Ir-C2	1.959	1.959	1.949	1.917 [eq]	1.923 [eq]
Ir-C3	1.959	1.959	1.949	1.945 [ax]	1.943 [ax]
Ir-C4	1.959	1.959	1.949	1.917 [eq]	1.923 [eq]
Ir-C5	1.959	1.959	1.949	1.945 [ax]	1.943 [ax]
Ir-C6	1.959	1.959	1.949	1.917 [eq]	1.923 [eq]
Ir-C7	1.959	1.959	1.949	1.945 [ax]	1.943 [ax]
Ir-C8	1.959	1.959	1.949	1.917 [eq]	1.923 [eq]
C_a-N_a	1.161 [a]	1.163 [a]	1.171 [a]	1.197 [ax]	1.196 [ax]
C_b-N_b	1.161 [b]	1.163 [b]	1.170 [b]	1.174 [eq]	1.175 [eq]
angle					
Ir2-Ir1-C1	90.8	92.6	93.8	89.7 [ax]	87.2 [ax]
Ir2-Ir1-C2	90.8	93.4	94.5	111.5 [eq]	109.2 [eq]
Ir2-Ir1-C3	90.8	92.6	93.7	89.7 [ax]	87.2 [ax]
Ir2-Ir1-C4	90.8	93.4	94.6	111.5 [eq]	109.2 [eq]
Ir2-Ir1-C5	90.8	92.6	95.1	111.5 [eq]	109.2 [eq]
Ir2-Ir1-C6	90.8	93.4	94.0	89.7 [ax]	87.2 [ax]

Ir2-Ir1-C7	90.8	92.6	95.2	111.5 [eq]	109.2 [eq]
Ir2-Ir1-C8	90.8	93.4	94.0	89.7 [ax]	87.2 [ax]
C_a-N_a-C	176.9 [a]	168.2 [a]	165.2 [a]	165.2 [ax]	161.5 [ax]
C_b-N_b-C	177.4 [b]	168.8 [b]	166.0 [b]	145.2 [eq]	146.2 [eq]
C_a-Ir1-Ir2-$C_{a'}$ [c]	0.0	38.4	40.4	0.0	37.3
C_b-Ir1-Ir2-$C_{b'}$ [d]	0.0	38.4	39.9	0.0	37.3

[a] Average of C1N1, C3N3, C5N5, and C7N7 distances or corresponding C-N-C angles. [b] Average of C2N2, C4N4, C6N6, and C8N8 distances or corresponding C-N-C angles. [c] Average of C1Ir1Ir2C5 and C3Ir1Ir2C7 angles. [d] Average of C2Ir1Ir2C6 and C4Ir1Ir2C8 angles. Superscript ax refers to the axial –N≡C–Ir–C≡N– linkage of the seesaw structure (Figure D.2); eq refers to the equatorial (bent, 137°) Ir(C≡N–)$_2$ moiety of the seesaw structure (Figure D.2).

Infrared spectra: ν(C≡N) vibrations

DFT-calculations closely reproduced experimental IR spectra in the ν(C≡N) region of all three redox states of Ir(dimen)$^{n+}$, in terms of peak wavenumbers as well as relative intensities and, hence, also the isosbestic points (Figure D.3 and Table D-2). Corresponding vibrational motions are depicted in Figure D.4. Experimental IR bands are broader and show several weak shoulders, usually on their low-energy sides (Figure D.3-left). These features are attributable to the presence of several nearly degenerate modes, the two deformational isomers, as well as to contributions from various orientational isomers whose IR spectra were calculated to be very similar.

The single ν(C≡N) band displayed by **2**+ arises from almost degenerate B_3 and B_2 vibrations in the approximate D_2 symmetry (originating from an E_u mode in D_{4h}). These

vibrations correspond to antisymmetric combinations of C≡N stretchings (Figure D.4). The first reduction shifts[12] this band by -66 cm^{-1}, which is matched by the calculated shift of -59 cm^{-1} relative to the short/twisted isomer (-74 cm^{-1} with respect to the long/eclipsed isomer). The calculated **1**+ spectrum shows a peak at 2094 cm^{-1} and a shoulder at 2122 cm^{-1} that also is apparent on the high-energy side of the experimental band (Figure D.3). The main peak results from downshifted B_3 and B_2 ν(C≡N) vibrations, while the shoulder is due to a mode calculated for **2**+ at 2212 cm^{-1} that gains IR intensity owing to a small distortion upon reduction.

As in the spectroelectrochemical experiment,[12] the DFT-simulated IR spectral pattern changes upon reduction to **0**. Two ν(C≡N) bands emerge at ca. 2068 and 1897 cm^{-1} with a distinct shoulder at ~1920 cm^{-1} that match experimental features at 2058 and 1867-1883 cm^{-1}, together with a ~1915 cm^{-1} shoulder (Figure D.3). The higher band is due to closely spaced C≡N stretching vibrations of axial (linear) –N≡C–Ir–C≡N– moieties at both Ir centers, whereas the lower band corresponds to similar vibrations of equatorial (bent) $Ir(C{\equiv}N{-})_2$ units. The calculations indicated only very little mixing between stretching motions of the two kinds of C≡N– ligands. The most IR-active vibrations of both deformational isomers are shown in Figure B.4. The calculated splitting of the two main ν(C≡N) IR features (172 cm^{-1}, on the average) is very near the experimental value of 189 cm^{-1}.[12]

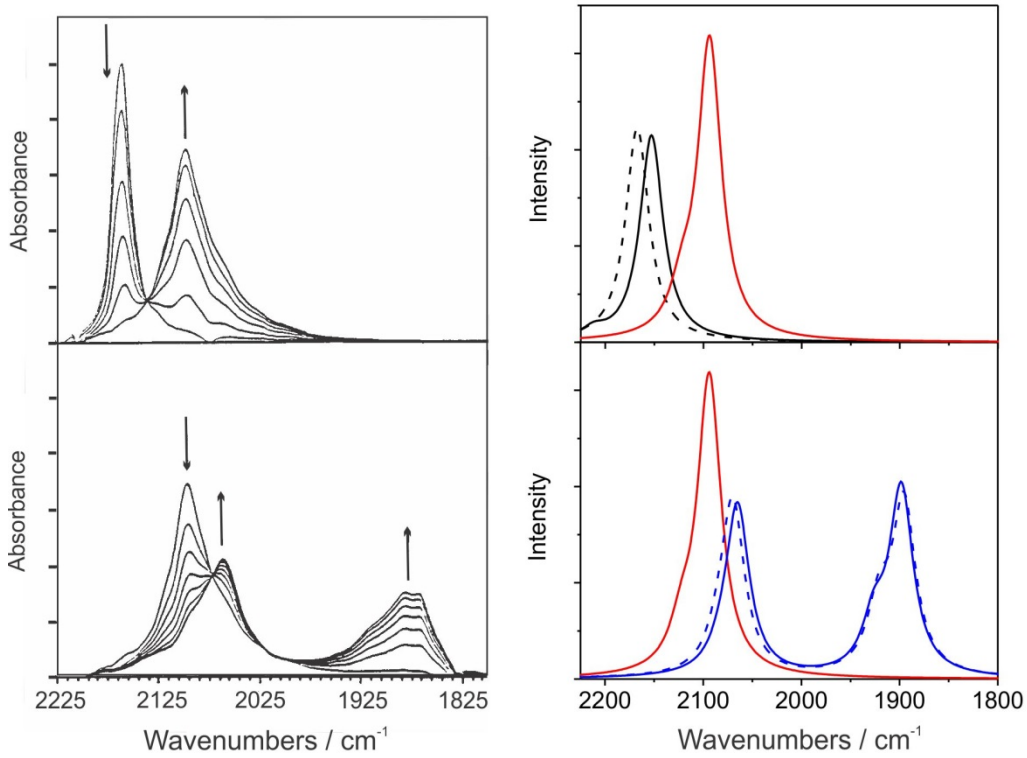

Figure D.3 Left: Experimental spectra recorded in MeCN during **2**+ → **1**+ (top) and **1**+ → **0** (bottom) electrochemical reductions. (Adapted with permission from ref.[12] Copyright (1993) American Chemical Society.) Right: calculated ν(C≡N) IR spectra of **2**+ (black), **1**+ (red), and **0** (blue) in MeCN. Full lines: short/twisted isomers, dashed lines: long/eclipsed isomers. Simulated spectra assumed fwhm of 30 cm^{-1}.

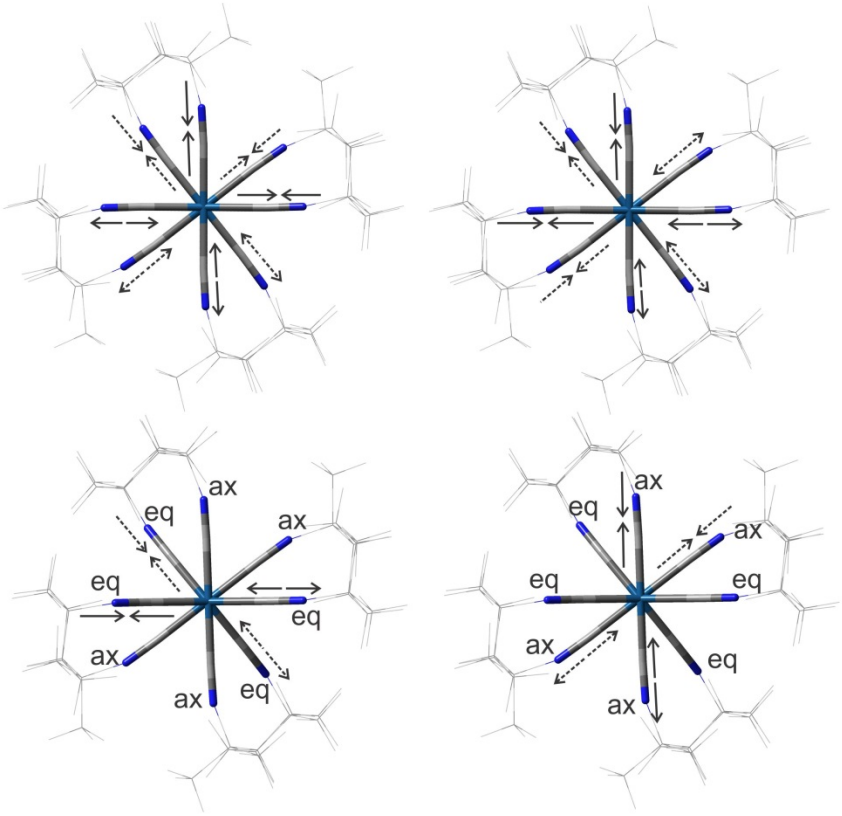

Figure D.4. Top: Schematic representation of DFT-calculated B_3 and B_2 ν(C≡N) vibrations of short/twisted **2**+, both calculated at 2168 cm^{-1}. Bottom: most intense ν(C≡N) vibrations of twisted **0** calculated at 1897 cm^{-1} (left) and 2066 cm^{-1} (right). Views of the structures are in the direction of the Ir–Ir bond. Labels ax, eq denote the axial (linear) and equatorial (bent) ligands, respectively. Full and dashed arrows indicate vibrational motions of the front and back parts of the molecule, respectively.

Table D-2: DFT calculated ν(C≡N) wavenumbers (cm^{-1}) and intensities (in parenthesis, 10^3 km/mol) of **2**+, **1**+, and **0**. Wavenumbers are scaled by 0.956. Experimental data from ref.[12]

2+			**1**+		**0**		
long/ecl	short/tw	Exp.	Calc.	Exp.	eclipsed	twisted	Exp.
2164 (0.2)	2147 (0.0)		2088		1896 (4.8)	1897 (8.4)	1867-1883[a]
2164 (0.0)	2147 (0.0)		2088 (0.7)		1896 (4.8)	1902 (2.2)	
2168 (6.0)	2153 (5.7)	2156	2092 (0.0)		1921 (3.6)	1926 (2.8)	1915 sh
2168 (5.9)	2153 (5.9)		2094 (8.3)	2090	1938 (0.0)	1944 (0.0)	
2188 (0.0)	2170 (0.0)		2095 (7.9)		2070 (4.8)	2063 (2.8)	2058
2190 (0.0)	2172 (0.0)		2096 (0.0)		2070 (4.8)	2066 (6.9)	
2240 (0.0	2212 (0.5)		2122 (2.1)	sh	2084 (1.2)	2082 (0.7)	sh
2243 (0.0)	2231 (0.0)		2187 (0.0)		1896 (0.0)	2132 (0.0)	

[a] Broad band with several apparent maxima, see Figure B.3-left. sh: shoulder apparent in the experimental spectrum.

Electronic structure: molecular orbitals and bonding

The MO diagram of **2**+ (Figure D.5) matches the qualitative bonding model proposed for d^8-d^8 complexes in 1975.[41] The $5d_z^2$ orbitals from each Ir atom combine in bonding and antibonding fashion producing dσ and dσ* (HOMO) orbitals that are both occupied. A similar interaction between $6p_z$ orbitals leads to pσ (LUMO) and pσ* orbitals. The splitting between σ bonding and antibonding orbitals is very small in the long/eclipsed isomer but increases on going to the short/twisted isomer, as the Ir–Ir distance shortens. A manifold of occupied 5dπ/π(CN) orbitals is at lower energies (Figure D.5). Although Ir–Ir σ bonding and

antibonding pairs of orbitals are either occupied or empty and no net bonding is expected, the Mayer-Mulliken bond orders indicate a weak bonding interaction: 0.072 (long/eclipsed) and 0.156 (short/twisted). Dispersion forces between the two parallel $Ir(C{\equiv}N{-})_4$ planes further stabilize the dimeric structure,[10,40] as discussed above.

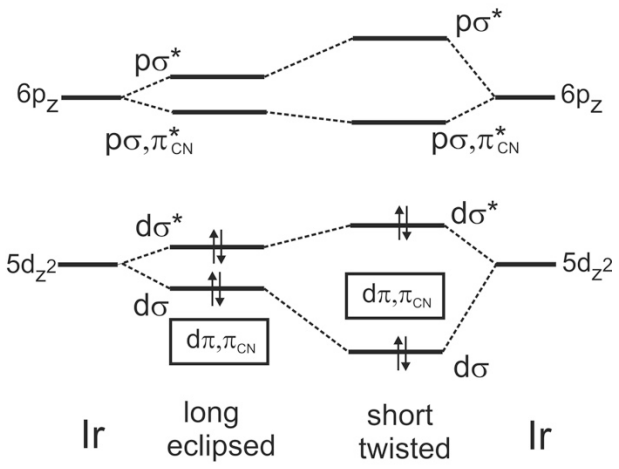

Figure D.5. Qualitative MO scheme of **2+**. dπ orbitals are π bonding or antibonding with respect to the Ir–Ir bond.

The MOs relevant to Ir–Ir bonding are shown in Figure D.6. Importantly, the **2**+ pσ LUMO is delocalized over the C≡N– groups whose π* orbitals contribute ca. 60 % while the $6p_z$ contribution was calculated to be ca. 35%. (A calculation with forced molecular symmetries indicated even larger delocalization with ~20% $6p_z$ participation.[36]) DFT calculations of the reduced and superreduced forms show that both reduction steps involve successive filling of the pσ LUMO orbital, with only minor changes in its composition.

For **1**+, the pσ-localization of the extra electron is supported by the calculated spin density distribution that approximately coincides with the pσ SOMO shape and produces EPR parameters (g_1 = 2.047, g_2 = 2.043, g_3 = 1.991) close to the experimental values[12] (g_1 = 2.064, g_2 = 2.060, g_3 = 2.01), maintaining the relation $g_1 \approx g_2 > g_3$ that reflects axial symmetry.

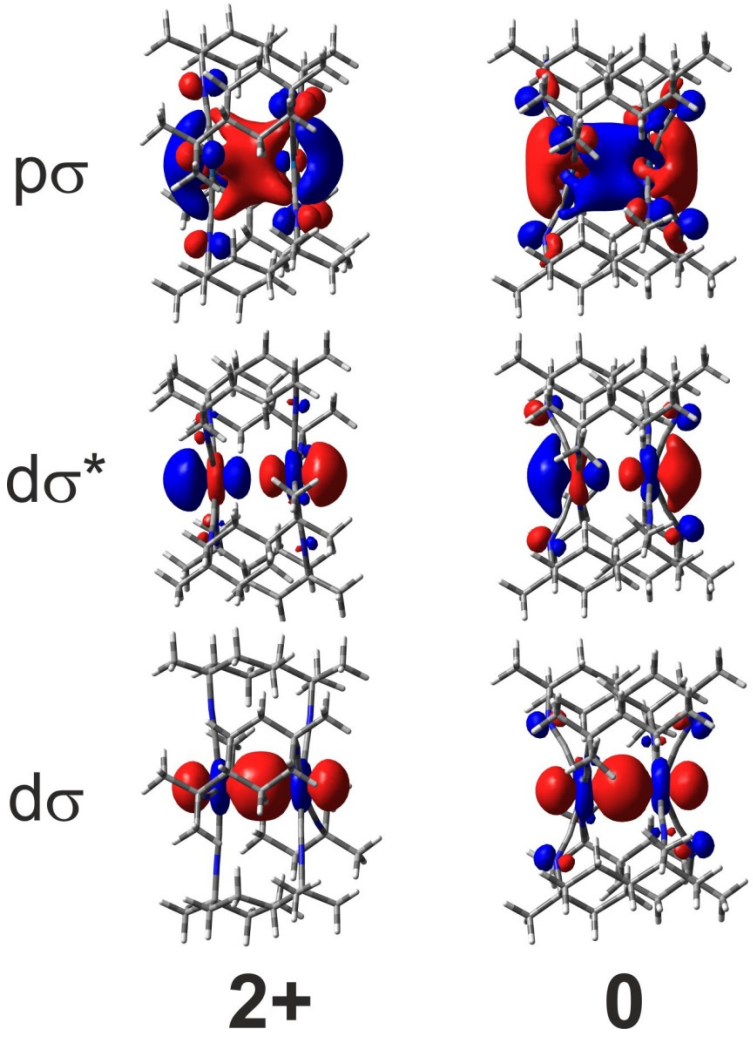

Figure D.6. Shapes of dσ, dσ*, and pσ orbitals of short/twisted isomers of **2**+ and **0**.

Lower-lying occupied orbitals of **2**+ and **1**+ are predominantly Ir 5d in character, π or π* with respect to the Ir-Ir bond. They are partly delocalized over the ligands, much more on N than C atoms. Whereas the delocalization over the eight C≡N– groups is nearly even in **2**+ and **1**+, large differences between axial and equatorial C≡N– π orbitals were found for **0**, whereby C and N atoms of the equatorial C≡N– groups participate in HOMO-1,2,3 almost equally (~15%). The involvement of axial ligands is much smaller, and mostly through the N atoms, as in **2**+ and **1**+.

Further insight into bonding changes upon reduction is provided by Mayer-Mulliken bond orders (Table D-3). The Ir–Ir bond order slightly increases upon the first reduction: by 0.045 relative to short/twisted **2**+, whereas a larger change (0.129) was calculated with respect to the long/eclipsed isomer. Filling the pσ orbital in the course of the second reduction is accompanied by further Ir–Ir bond-order increase of ca. 0.1. All three redox states show an alternating pattern of Ir–C and C–N bond orders whereby the equatorial –N≡C–Ir–C≡N– moieties are characterized by higher Ir–C and lower C–N bond orders than the axial ones. While these differences are negligible in **2**+ and **1**+, they become pronounced in both superreduced isomers. Bond-order changes and corresponding axial/equatorial alternation thus indicate that the second reduction mainly affects equatorially-bound pairs of C≡N– groups at both Ir centers.

Table D-3: Mayer-Mulliken bond orders of Ir(dimen)$^{n+}$ (**2+**, **1+**, **0**) complexes. Labels ax, eq denote the axial (linear) and equatorial (bent) ligands, respectively.

bond \ n	**2+** long/eclipsed	**2+** short/twisted	**1+**	**0** twisted	**0** Eclipsed
Ir – Ir	0.072	0.156	0.201	0.286	0.311
Ir1 – C1	0.526	0.558	0.618	0.594 ^{ax}	0.622 ^{ax}
Ir1 – C2	0.523	0.568	0.635	0.940 ^{eq}	0.928 ^{eq}
Ir1 – C3	0.526	0.559	0.618	0.594 ^{ax}	0.622 ^{ax}
Ir1 – C4	0.523	0.568	0.635	0.940 ^{eq}	0.928 ^{eq}
C1 – N1	2.374	2.345	2.237	2.170 ^{ax}	2.193 ^{ax}
C2 – N2	2.375	2.345	2.236	2.035 ^{eq}	2.038 ^{eq}
C3 – N3	2.375	2.345	2.236	2.170 ^{ax}	2.193 ^{ax}
C4 – N4	2.374	2.345	2.450	2.035 ^{eq}	2.038 ^{eq}
Ir2 – C5	0.523	0.558	0.647	0.940 ^{eq}	0.928 ^{eq}
Ir2 – C6	0.526	0.568	0.621	0.594 ^{ax}	0.622 ^{ax}
Ir2 – C7	0.523	0.559	0.647	0.940 ^{eq}	0.928 ^{eq}
Ir2 – C8	0.524	0.568	0.622	0.594 ^{ax}	0.622 ^{ax}
C5 – N5	2.374	2.345	2.231	2.035 ^{eq}	2.038 ^{eq}
C6 – N6	2.375	2.345	2.237	2.170 ^{ax}	2.193 ^{ax}
C7 – N7	2.375	2.345	2.238	2.035 ^{eq}	2.038 ^{eq}
C8 – N8	2.374	2.345	2.436	2.170 ^{ax}	2.193 ^{ax}

Localization of the reduction steps can be examined by comparing changes of Mulliken charges upon the first and second reduction steps (Table D-4). The first reduction is delocalized over the Ir_2 unit (0.39 e^-, 0.2 e^- per Ir atom) and the eight C≡N– groups, where the electron density increases by 0.31 e^- (mainly at N, 0.23 e^-, 0.03 e^- per atom). There is virtually no difference between the two $Ir(C{\equiv}N{-})_4$ units and between axial and equatorial C≡N– groups. On the other hand, upon second reduction, the charge decreases by 0.15 e^- on both Ir atoms and by 0.48 e^- on all eight C≡N– units (twisted isomer), with a large difference between axial (-0.17 e^-) and equatorial (-0.31 e^-) ligands. This difference is even more pronounced in the eclipsed isomer: -0.08 vs. -0.37 e^-, respectively; and the charge on the two Ir atoms decreases by 0.19 e^-. The DFT-calculated charge changes also show that the electron density added in each reduction step is nearly equally distributed over the two $Ir(CN{-})_4$ units. In particular, the increases in electron density at Ir1 and Ir2 upon second reduction are virtually identical.

Table D-4: Changes of DFT-calculated Mulliken charges at individual atoms accompanying the two reduction steps of **2**+. The isomers are specified in parenthesis. Labels ax, eq denote the axial (linear) and equatorial (bent) ligands, respectively.

	2(sh/tw)→1	1→0(tw)	1→0(ecl)
Ir1	-0.194	-0.072	-0.092
C[a]	-0.011	-0.012 [ax]	-0.003 [ax]
N[a]	-0.029	-0.031 [ax]	-0.017 [ax]
C[b]	-0.009	-0.033 [eq]	-0.054 [eq]
N[b]	-0.030	-0.042 [eq]	-0.036 [eq]
Ir2	-0.193	-0.074	-0.093
C[c]	-0.005	-0.037 [eq]	-0.058 [eq]
N[c]	-0.030	-0.042 [eq]	-0.036 [eq]
C[d]	-0.011	-0.012 [ax]	-0.002 [ax]
N[d]	-0.028	-0.031 [ax]	-0.018 [ax]

[a] Average for C1 and C3, N1 and N3. [b] Average for C2 and C4, N2 and N4. [c] Average for C5 and C7, N5 and N7. [d] Average for C6 and C8, N6 and N8.

UV-vis absorption spectra

TDDFT-calculated electronic transitions for both **2**+ deformational isomers as well as for reduced and superreduced forms match the experimental spectra (Figure D.7 and Table D-5). The lowest absorption band of each **2**+ isomer originates from the HOMO→LUMO transition and, given the delocalized LUMO character, can be described as

$d\sigma^* \rightarrow p\sigma$/MMLCT (MMLCT = metal-metal to ligand charge transfer). The strong sharp bands in the UV region are $d\pi \rightarrow p\sigma$(LUMO), predominantly MMLCT. The position of the lower UV band (377-378 nm) matches the calculated triplet transitions at 367 and 384 nm while no spin-allowed transitions were calculated to fall in this region. We conclude that this band is attributable to a pair of close-lying spin-forbidden $^3d\pi \rightarrow p\sigma$ transitions, in accord with polarized absorption and MCD spectra of an analogous complex Ir_2(2,5-diisocyano-2,5-dimethylhexane)$_4^{2+}$.[42] As with $Pt(pop\text{-}BF_2)^{4-}$,[25] a full assignment of the Ir(dimen) UV spectrum will require calculation that includes spin-orbit coupling explicitly.

Electronic transitions of the open-shell complex **1**+ are described in terms of spin-orbitals. A weak low-energy band at 800 nm that appears upon the first reduction[12] is attributable to a βHOMO($d\sigma^*$)$\rightarrow\beta$LUMO($p\sigma$) transition (calculated at 713 nm). This feature is the counterpart of the $d\sigma^* \rightarrow p\sigma$ visible band of **2**+. A second, stronger band at 595 nm (calculated at 532 nm) is due to a αHOMO($p\sigma$)$\rightarrow\alpha$LUMO($p\sigma^*$/CN(π^*) transition of mixed MMLCT/intraligand character. In the UV region, **1**+ exhibits a band at 320 nm arising from two strongly mixed transitions. The experimental absorption spectrum of **0** exhibits[12] features at 432 nm (calculated at 411-425 nm) due to a HOMO($p\sigma$)$\rightarrow$LUMO($p\sigma^*$) transition and at 300 nm that include several transitions from HOMO($p\sigma$) and HOMO-1($d\sigma^*$) to LUMO and other high-lying orbitals (calculated at 306-328 nm).

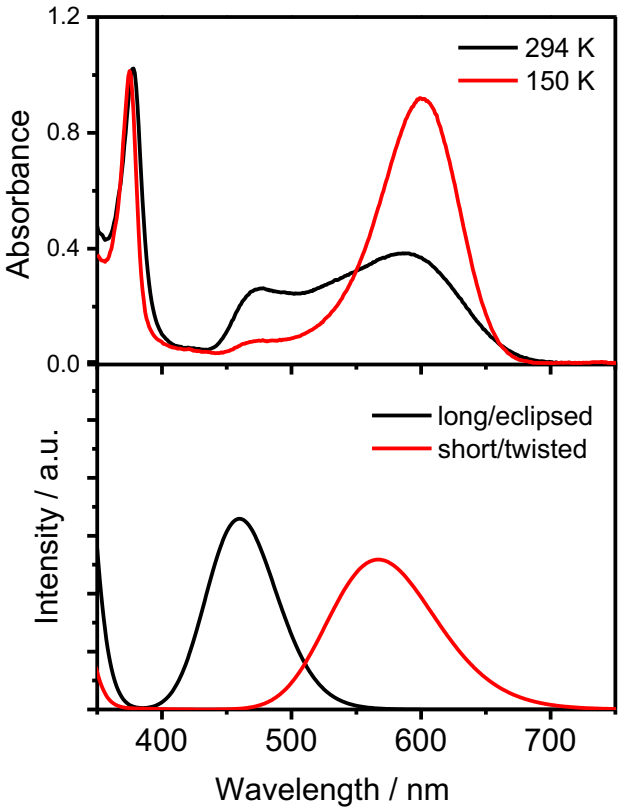

Figure D.7. Experimental UV-vis absorption spectra of **2**+ at 293.5 and 150 K (top) and simulated visible spectra of the long/eclipsed and short/twisted isomer (bottom). Simulated spectra assumed fwhm of 3000 cm^{-1}.

Table D-5: Calculated and experimental UV-vis spectra of $Ir(dimen)_4^n$ in MeCN. Transitions with oscillator strengths larger than 0.01 and spectroscopically relevant[42] triplet transitions (^3A) are listed.

Compound	Main contributing excitations (%)	Wavelength nm	Oscillator strength	Experiment λ, nm (ε, $M^{-1}cm^{-1}$)
2+ long/eclipsed	HOMO→LUMO (95)	460	0.227	475 [a]
	HOMO-4 →LUMO (95) ^3A	384	-	378 [a,d]
	HOMO-5 →LUMO (95) ^3A	384	-	
	HOMO-4 →LUMO (95)	326	0.376	327 [b] (36600)
	HOMO-5 →LUMO (95)	326	0.376	
2+ short/twisted	HOMO→LUMO (99)	567	0.178	598 [c] (7300 [b])
	HOMO-3 →LUMO (99) ^3A	367	-	377 [c,d] (18000 [b])
	HOMO-4 →LUMO (99) ^3A	366	-	
	HOMO-3 →LUMO (99)	321	0.177	327 [b] (36600)
	HOMO-4 →LUMO (99)	320	0.201	
1+	βHOMO→βLUMO (86)	713	0.019	800 [b] (3700)
	αHOMO→αLUMO (81)	534	0.211	595 [b] (12300)
	αHOMO→αLUMO+8 (60)	350	0.019	
	mixed	320	0.204	320 [b] (20900)
	mixed	320	0.246	
0 twisted	HOMO→LUMO+2 (96)	443	0.014	432 [b] (14400)
	HOMO→LUMO (98)	425	0.305	
	HOMO→LUMO+5 (94)	384	0.019	
	HOMO→LUMO+4 (97)	383	0.013	

	HOMO→LUMO+7 (89)	334	0.021	
	HOMO→LUMO+8 (89)	328	0.138	300 [b] (25100)
	HOMO→LUMO+10 (95)	317	0.037	
	HOMO-1→LUMO (90)	306	0.093	
0 eclipsed	HOMO→LUMO (99)	441	0.347	432 [b] (14400)
	HOMO→LUMO+2 (96)	411	0.011	
	HOMO→LUMO+5 (94)	368	0.008	
	HOMO→LUMO+4 (97)	368	0.009	
	HOMO→LUMO+8 (89)	322	0.113	300 [b] (25100)
	HOMO-1→LUMO (90)	322	0.113	
	HOMO→LUMO+10 (95)	317	0.037	

[a] 293.5 K; from ref.[39], [b] room temperature; from ref.[12], [c] 150 K; from ref.[39], [d] Assigned as $d_{xz,yz} \rightarrow p\sigma\ ^3E_u$ transition.[42]

D.5. Discussion

Our DFT calculations account for spectral changes in the **2+**, **1+**, **0** redox series; they also reveal changes of the molecular and electronic structures accompanying the two reduction steps. The reduction process can be interpreted as a sequential filling of the **2+** pσ LUMO. It is accompanied by large molecular and electronic relaxation upon addition of the second electron in the **1+** → **0** step.

The first reduction **2+** → **1+** amounts to simple electron addition to the pσ orbital in accord with the axial EPR spectrum of **1+**. The extra electron (spin) density is localized along the Ir-Ir linkage (Figure S2) and the eight N atoms. The UV-vis spectrum retains the dσ*→pσ band accompanied by a new feature at higher energy due to excitation of the pσ

electron to the pσ* orbital. The ν(C≡N) IR spectral pattern of **2**+ (single band) is preserved in **1**+, in agreement with the calculated **1**+ structure (Table D-1). The 66 cm^{-1} downshift of the ν(C≡N) band is attributable to electron delocalization over the isocyanide ligands that arises from overlap of the Ir $6p_z$ with π*(C≡N–) orbitals. It also accords with the ~0.01 Å lengthening of C≡N bonds. Bond orders (Table D-3) indicate that the eight Ir–C≡N– units are very similar.

Addition of the second electron to the pσ orbital causes a major change in both molecular and electronic structures although the character of the pσ orbital changes very little on going to **0** and its double occupancy amounts to formation of a $(p\sigma)^2$ bond as in $[Pt(pop\text{-}BF_2)]^{6-}$.[11] Accordingly, the Ir-Ir distance in **0** is shorter and the bond order is larger than in **1**+. Of importance is that the planar $Ir(C{\equiv}N{-})_4$ arrangement is unstable upon the second reduction; and a seesaw geometry is adopted at both Ir centers. (Alternatively, each Ir site can be viewed as trigonal bipyramidal, whereby the two axial and two of the equatorial positions are occupied by C≡N– groups and the other Ir atom occupies the third equatorial site.) Two nonequivalent –N≡C–Ir–C≡N– groups are at each Ir center: axial (linear), and equatorial that are bent at both Ir and N atoms and characterized by relatively large Ir–C and low C≡N bond orders (Table D-3). Axial bonds essentially retain their Ir–C≡N– character, only slightly modified by increased π back donation due to full pσ occupation. The nonequivalence of the two kinds of C≡N– groups in **0** accounts for the most striking spectroelectrochemical feature in the $Ir(dimen)^{n+}$ series: the large splitting of the ν(C≡N) IR band upon second reduction. The two IR bands of **0** correspond to antisymmetric stretching vibrations of axial and equatorial –N≡C–Ir–C≡N– moieties. Relative to the single ν(C≡N) feature of **1**+, the axial and equatorial vibrations in **0** shift lower by 32 and ca. 215 cm^{-1}, respectively, reflecting larger electron density localization at equatorial C≡N– groups.

Despite the pσ localization of the extra electron in **0**, the electron density increase relative to **1**+ is much larger on the equatorial than on the axial CN– groups and the Ir atoms (Table D-4). This is because the **1**+ → **0** reduction is accompanied by enhanced

delocalization of some of the lower-lying occupied MOs over the equatorial CN– groups. In consequence, the overall electron density increase on the four equatorial CN– ligands is more than two times larger than on both Ir atoms. It is worth noting that both reduction steps are accompanied by large electron density increases at the N atoms, especially on the bent equatorial ligands (0.07 e^- at each N_{eq}, relative to **2**+). The superreduced complex **0** thus possesses two kinds of nucleophilic centers (Ir and N_{eq}) that could play roles in substrate activation. Indeed, electrochemical CO_2 and H_2O reduction catalyzed by **2**+ has been reported.[13]

Relaxation of molecular and electronic structures upon the second reduction stabilizes the superreduced species **0** by delocalizing electron density over the whole molecule. The structural flexibility of the dimen ligand and the π-accepting ability of isocyanide groups are key factors in allowing this stabilization. In the case of isoelectronic $Pt(pop\text{-}BF_2)^{6-}$, such relaxation is limited by the rigidity of the pop-BF_2 ligand cage.[11] The lack of stabilizing reorganization of the superreduced Pt complex leads to a larger difference between the first and second reduction potentials (ΔE = -0.78 V) as well as the much more negative second reduction potential (E_2 = -2.46 V) than in the case of the Ir complex (ΔE = -0.18, E_2 = -1.93 V, respectively, even though the first reduction potentials are similar: -1.68 V (Pt), -1.75 V (Ir)).

D.6. Conclusions

Our DFT calculations accord with the experimental structure of **2**+, as well as the EPR spectrum of **1**+ and the ν(C≡N) IR and visible absorption spectra of all three $Ir(dimen)^{n+}$ complexes (**2**+, **1**+, **0**). We have found that dispersion forces between the $Ir(CN–)_4$ planes contribute to the stability of the dimeric structure. The two reduction steps correspond to successive filling of a pσ orbital that is delocalized over the C≡N– ligands. **0** is another example of a $(p\sigma)^2$-bonded dimer, after $Pt(pop\text{-}BF_2)^{6-}$.[11]

Structural changes accompanying **2**+ to **1**+ reduction are very small. The extra electron density (spin density) is delocalized in the direction of the molecular axis between the two Ir

atoms, at the outer sides of the IrC_4 planes, and over the N atoms of the eight C≡N– groups. The second reduction (**1+** to **0**) triggers a profound structural change that produces two non-equivalent sets of C≡N– ligands, axial and equatorial, but maintains the near-equivalence of the two Ir centers. The extra electron density is delocalized mainly over the four equatorial C≡N– groups that are bent at the N atoms. The prediction that equatorial N atoms could act together with Ir atoms as nucleophilic centers provides motivation for our forthcoming electrocatalytic studies employing $Ir(dimen)^{n+}$ complexes.

D.7. References and Notes

1. Yam, V. W.-W.; Au, V. K.-M.; Leung, S. Y.-L., Light-Emitting Self-Assembled Materials Based on d^8 and d^{10} Transition Metal Complexes. *Chem. Rev.* **2015** *115*, 7589−7728.

2. Roundhill, D. M.; Gray, H. B.; Che, C.-M., Pyrophosphito-Bridged Diplatinum Chemistry. *Acc. Chem. Res.* **1989,** *22*, 55-61.

3. Harvey, P. D., Chemistry, properties and applications of the assembling 1,8-diisocyano-p-menthane, 2,5-dimethyl-2,5-diisocyanohexane and 1,3-diisocyanopropane ligands and their coordination polynuclear complexes. *Coord. Chem. Rev.* **2001,** *219–221*, 17–52.

4. Sweeney, R. J.; Harvey, E. L.; Gray, H. B., Photoreactions of tetrakis(m-pyrophosphito)diplatinate(II) with alcohols and hydrocarbons. *Coord. Chem. Rev.* **1990,** *105*, 23-34.

5. Smith, D. C.; Gray, H. B., Photochemistry of Binuclear d^8 Complexes. *Coord. Chem. Rev.* **1990,** *100*, 169-181.

6. Marshall, J. L.; Stiegman, A. E.; Gray, H. B., Photochemistry of Dinuclear d^8-d^8 Iridium and Platinum Complexes. In *Excited States and Reactive Intermediates. ACS Symposium Series.*, Lever, A. B. P., Ed. American Chemical Society: Washington, DC, 1986; Vol. 307, pp 166-176.

7. Peterson, J. R.; Kalyanasundaram, K., Energy- and Electron-Transfer Processes of the Lowest Triplet Excited State of Tetrakis(diphosphito)diplatinate(II). *J. Phys. Chem.* **1985,** *89*, 2486-2492.

8. Heuer, W. B.; Totten, M. D.; Rodman, G. S.; Hebert, E. J.; Tracy, H. J.; Nagle, J. K., Electron-Transfer Reactions and Luminescent Quantum Yield of the Triplet Excited State of Tetrakis[m-diphosphito(2-)-*P*,*P*′]diplatinate(II). *J. Am. Chem. Soc.* **1984,** *106*, 1163-1164.

9. Milder, S. J.; Goldbeck, R. A.; Kliger, D. S.; Gray, H. B., Studies of Energy-Transfer and Electron-Transfer Processes Involving the $^3A_{2u}$ Excited States of Binuclear Rhodium Isocyanide Complexes. *J. Am. Chem. Soc.* **1980,** *102*, 6761-6764.

10. Gray, H. B.; Záliš, S.; Vlček, A., Electronic structures and photophysics of d^8-d^8 complexes *Coord. Chem. Rev.* **2017**, http://dx.doi.org/10.1016/j.ccr.2017.1001.1008.

11. Darnton, T. V.; Hunter, B. M.; Hill, M. G.; Záliš, S.; Vlček, A., Jr.; Gray, H. B., Reduced and Superreduced Diplatinum Complexes. *J. Am. Chem. Soc.* **2016,** *138*, 5699−5705.

12. Hill, M. G.; Sykes, A. G.; Mann, K. R., Spectroelectrochemical Characterization of $Ir_2(dimen)^{4+}$ and $Ir_2(dimen)_4^0$ (dimen = 1,8-Diisocyanomenthane). *Inorg. Chem.* **1993,** *32*, 783–784.

13. Cheng, S. C.; Blaine, C. A.; Hill, M. G.; Mann, K. R., Electrochemical and IR Spectroelectrochemical Studies of the Electrocatalytic Reduction of Carbon Dioxide by $[Ir_2(dimen)_4]^{2+}$ (dimen = 1,8-Diisocyanomenthane). *Inorg. Chem.* **1996,** *35*, 7704-7708.

14. Rodman, G. S.; Bard, A. J., Electrogenerated Chemiluminescence. 52. Binuclear Iridium(I) Complexes. *Inorg. Chem.* **1990,** *29*, 4699-4702.

15. Miskowski, V. M.; Smith, T. P.; Loehr, T. M.; Gray, H. B., Properties of Metal-Metal Single Bonds. Vibrational and Electronic Spectra of Binuclear Rhodium(II) and Iridium(II) Isocyanide Complexes with Comparisons to $Mn_2(CO)_{10}$. *J. Am. Chem. Soc.* **1985,** *107*, 7925-7934.

16. Che, C.-M.; Butler, L. G.; Grunthaner, P. J.; Gray, H. B., Chemistry and Spectroscopy of Binuclear Platinum Diphosphite Complexes. *Inorg. Chem.* **1985,** *24*, 4662-4665.

17. Bryan, S. A.; Schmehl, R. H.; Roundhill, D. M., Electrochemical oxidation of the tetrakis(m-pyrophosphito-*P*,*P'*)diplatinum(II) complex $Pt_2(m\text{-}P_2O_5H_2)_4^{4-}$ both in the presence and the absence of halide ions and reduction of the axially substituted halodiplatinum(III) complexes $Pt_2(m\text{-}P_2O_5H_2)_4X_2^{4-}$ *J. Am. Chem. Soc.* **1986,** *108*, 5408–5412.

18. Rhodes, M. R.; Mann, K. R., Electrochemical Oxidation of Tetrakis(1,8-diisocyanomenthane)dirhodium(2+) in Nonaqueous Solutions: A Net Two-Electron Oxidation Process. *Inorg. Chem.* **1984,** *23*, 2053-2058.

19. Kim, J.; Fan, F. F.; Bard, A. J.; Che, C.-M.; Gray, H. B., Electrogenerated chemiluminescence on the electrogenerated chemiluminescence (ECL) of tetrakis(pyrophosphito)diplatinate(II), $Pt_2(P_2O_5H_2)_4^{4-}$. *Chem. Phys. Lett.* **1985,** *121*, 543-546.

20. Vogler, A.; Kunkely, H., Electrochemiluminescence of Tetrakis(diphosphonato)diplatinate(II). *Angew. Chem. Int. Ed. Engl.* **1984,** *23*, 316-317.

21. Perdew, J. P.; Burke, K.; Ernzerhof, M., Generalized Gradient Approximation Made Simple. *Phys. Rev. Lett.* **1996,** *77*, 3865-3868.

22. Adamo, C.; Barone, V., Toward reliable density functional methods without adjustable parameters: The PBE0 model. *J. Chem. Phys.* **1999,** *110*, 6158-6170.

23. Grimme, S.; Antony, J.; Ehrlich, S.; Krieg, H., A consistent and accurate ab initio parameterization of density functional dispersion correction (DFT-D) for the 94 elements H-Pu. *J. Chem. Phys.* **2010,** *132*, 154104.

24. Záliš, S.; Ben Amor, N.; Daniel, C., Influence of the Halogen Ligand on the Near-UV-Visible Spectrum of [Ru(X)(Me)$(CO)_2$(a-diimine)] (X = Cl, I, a-Diimine = Me-DAB, iPr-DAB, DAB = 1,4-Diaza-1,3-butadiene): An ab Initio and TD-DFT Analysis. *Inorg. Chem.* **2004,** *43*, 7978-7985.

25. Záliš, S.; Lam, Y. C.; Gray, H. B.; Vlček, A., Jr., Spin−Orbit TDDFT Electronic Structure of Diplatinum(II,II) Complexes. *Inorg. Chem.* **2015,** *54*, 3491−3500.

26. Kvapilová, H.; Sattler, W.; Sattler, A.; Sazanovich, I. V.; Clark, I. P.; Towrie, M.; Gray, H. B.; Záliš, S.; Vlček, A., Electronic Excited States of Tungsten(0) Arylisocyanides. *Inorg. Chem.* **2015,** *54*, 8518−8528.

27. Tomasi, J.; Mennucci, B.; Cammi, R., Quantum Mechanical Continuum Solvation Models. *Chem. Rev.* **2005,** *105*, 2999-3093.

28. Ditchfield, R.; Hehre, W. J.; Pople, J. A., Self-Consistent Molecular Orbital Methods. 9. Extended Gaussian-type basis for molecular-orbital studies of organic molecules. *J. Chem. Phys.* **1971,** *54*, 724-728.

29. Raghavachari, K.; Binkley, J. S.; Seeger, R.; Pople, J. A., Self-consistent molecular orbital methods. XX. A basis set for correlated wave functions *J. Chem. Phys.* **1980,** *72*, 650-654.

30. McLean, A. D.; Chandler, G. S., Contracted Gaussian-basis sets for molecular calculations. 1. 2nd row atoms, Z=11-18. *J. Chem. Phys.* **1980,** *72*, 5639-5648.

31. Andrae, D.; Häussermann, U.; Dolg, M.; Stoll, H.; Preuss, H., Energy-adjusted ab initio pseudopotentials for the second and third row transition elements. *Theor. Chim. Acta* **1990,** *77*, 123-141.

32. Martin, J. M. L.; Sundermann, A., Correlation consistent valence basis sets for use with the Stuttgart–Dresden–Bonn relativistic effective core potentials: The atoms Ga–Kr and In–Xe. *J. Chem. Phys.* **2001,** *114*, 3408-3420.

33. Laury, M. L.; Carlson, M. J.; Wilson, A. K., Vibrational Frequency Scale Factors for Density Functional Theory and the Polarization Consistent Basis Sets. *J. Comput. Chem.* **2012,** *33*, 2380–2387.

34. Merrick, J. P.; Moran, D.; Radom, L., An Evaluation of Harmonic Vibrational Frequency Scale Factors. *J. Phys. Chem. A* **2007,** *111*, 11683-11700.

35. Exstrom, C. L.; Britton, D.; Mann, K. R.; Hill, M. G.; Miskowski, V. M.; Schaefer, W. P.; Gray, H. B.; Lamanna, W. M., Structures of $[M_2(dimen)_4](Y)_2$ (M = Rh, Ir; dimen = 1,8-Diisocyanomenthane; Y = PF_6, Tetrakis[3,5-bis(trifluoromethyl)phenyl]borate, $B(C_6H_5)_4$) Crystals Featuring an Exceptionally Wide Range of Metal-Metal Distances and Dihedral Twist Angles. *Inorg. Chem.* **1996,** *35*, 549-550.

36. Hunter, B. M.; Villahermosa, R. M.; Exstrom, C. L.; Hill, M. G.; Mann, K. R.; Gray, H. B., M−M Bond-Stretching Energy Landscapes for $M_2(dimen)_4^{2+}$ (M = Rh, Ir; dimen = 1,8-Diisocyanomenthane) Complexes. *Inorg. Chem.* **2012,** *51*, 6898−6905.

37. Hartsock, R. W.; Zhang, W.; Hill, M. G.; Sabat, B.; Gaffney, K. J., Characterizing the Deformational Isomers of Bimetallic $Ir_2(dimen)_4^{2+}$ (dimen = 1,8-diisocyano-p-menthane) with Vibrational Wavepacket Dynamics. *J. Phys. Chem. A* **2011,** *115*, 2920–2926.

38. Grimme, S.; Antony, J.; Ehrlich, S.; Krieg, H., A consistent and accurate ab initio parametrization of density functional dispersion correction (DFT-D) for the 94 elements H-Pu. *J. Chem. Phys.* **2010,** *132*, 154104.

39. Haldrup, K.; Harlang, T.; Christensen, M.; Dohn, A.; van Driel, T. B.; Kjær, K. S.; Harrit, N.; Vibenholt, J.; Guerin, L.; Wulff, M.; Nielsen, M. M., Bond Shortening (1.4 A) in the Singlet and Triplet Excited States of $[Ir_2(dimen)_4]^{2+}$ in Solution Determined by Time-Resolved X-ray Scattering. *Inorg. Chem.* **2011,** *50*, 9329–9336.

40. Grimme, S.; Djukic, J.-P., Cation-Cation "Attraction": When London Dispersion Attraction Wins over Coulomb Repulsion. *Inorg. Chem.* **2011,** *50*, 2619–2628.

41. Mann, K. R.; Gordon II, J. C.; Gray, H. B., Characterization of Oligomers of Tetrakis(phenyl isocyanide)rhodium(I) in Acetonitrile Solution. *J. Am. Chem. Soc.* **1975,** *97*, 3553-3555.

42. Smith, D. C.; Miskowski, V. M.; Mason, W. R.; Gray, H. B., Electronic Absorption and MCD Spectra of $M_2(TMB)_4^{2+}$, M = Rh and Ir. A Valence-Bond Description of the Upper Electronic Excited States. *J. Am. Chem. Soc.* **1990,** *112*, 3759-3767.